Adam Szymkiewicz

Modelling Water Flow in Unsaturated Porous Media

Accounting for Nonlinear Permeability and Material Heterogeneity

Springer

GeoPlanet: Earth and Planetary Sciences

For further volumes:
http://www.springer.com/series/8821

Adam Szymkiewicz

Modelling Water Flow in Unsaturated Porous Media

Accounting for Nonlinear Permeability and Material Heterogeneity

Springer

Adam Szymkiewicz
Faculty of Civil and Environmental Engineering
Gdansk University of Technology
Gdansk
Poland

The GeoPlanet: Earth and Planetary Sciences Book Series is in part a continuation of Monographic Volumes of Publications of the Institute of Geophysics, Polish Academy of Sciences, the journal published since 1962 (http://pub.igf.edu.pl/index.php).

ISSN 2190-5193 ISSN 2190-5207 (electronic)
ISBN 978-3-642-23558-0 ISBN 978-3-642-23559-7 (eBook)
DOI 10.1007/978-3-642-23559-7
Springer Heidelberg New York Dordrecht London

Library of Congress Control Number: 2012945473

Printed on acid-free paper

Springer is part of Springer Science+Business Media (www.springer.com)

Series Editors

Managing Editor

Advisory Board

Kon-Kee Liu
Institute of Hydrological
and Oceanic Sciences
National Central University Jhongli
Jhongli, Taiwan

Teresa Madeyska
Research Centre in Warsaw
Institute of Geological Sciences
Warszawa, Poland

Stanisław Massel
Institute of Oceanology
Polish Academy of Sciences
Sopot, Polska

Antonio Meloni
Instituto Nazionale di Geofisica
Rome, Italy

Evangelos Papathanassiou
Hellenic Centre for Marine Research
Anavissos, Greece

Kaja Pietsch
AGH University of Science and
Technology
Kraków, Poland

Dušan Plašienka
Prírodovedecká fakulta, UK
Univerzita Komenského
Bratislava, Slovakia

Barbara Popielawska
Space Research Centre
Polish Academy of Sciences
Warszawa, Poland

Tilman Spohn
Deutsches Zentrum für Luft-
und Raumfahrt
in der Helmholtz Gemeinschaft
Institut für Planetenforschung
Berlin, Germany

Krzysztof Stasiewicz
Swedish Institute of Space Physics
Uppsala, Sweden

Roman Teisseyre
Earth's Interior Dynamics Lab
Institute of Geophysics
Polish Academy of Sciences
Warszawa, Poland

Jacek Tronczynski
Laboratory of Biogeochemistry
of Organic Contaminants
IFREMER DCN_BE
Nantes, France

Steve Wallis
School of the Built Environment
Heriot-Watt University
Riccarton, Edinburgh
Scotland, UK

Wacław M. Zuberek
Department of Applied Geology
University of Silesia
Sosnowiec, Poland

Acknowledgments

I owe very special thanks to Prof. Rainer Helmig, Head of the Department of Hydromechanics and Modeling of Hydrosystems in the Institute for Modeling Hydraulic and Environmental Systems, University of Stuttgart, who invited me several times to work with his research group. His help and advice were essential for the preparation of the present book. During my stay in Stuttgart I was supported by the German Research Foundation (DFG), in the framework of the Cluster of Excellence in Simulation Technology (SimTech, EXC 310/1), as well as by the International Training Group *Non-linearities and Upscaling in Porous Media* (NUPUS). The aid received from these two institutions is kindly acknowledged here.

A significant part of this book is based on the research work which I carried out together with Prof. Jolanta Lewandowska and I very much appreciate our long lasting cooperation. I also greatly benefitted from the collaboration with Prof. Insa Neuweiler, Prof. Kazimierz Burzyński, Prof. Michel Vauclin, Prof. Jean-Louis Auriault, Prof. Rafael Angulo-Jaramillo, Prof. Sorin Pop, Dr. Joanna Butlańska, and Dr. Alexandru Tatomir.

I am much indebted to Prof. Paweł Rowiński, editor of the Springer Geoplanet series, for the possibility of publishing my manuscript. Moreover, I would like to acknowledge the support and encouragement received from Prof. Zbigniew Sikora, Head of the Department of Geotechnics, Geology and Marine Engineering at the Faculty of Civil and Environmental Engineering, Gdańsk University of Technology, Prof. Ireneusz Kreja, dean of the Faculty, Prof. Eugeniusz Dembicki, Prof. Henryk Zaradny, and Prof. Jarosław Napiórkowski. Thanks to all the colleagues from the Department of Geotechnics in Gdańsk and from the Department of Hydromechanics in Stuttgart for a friendly atmosphere, which helped me substantially in my work.

I am very grateful to Prof. Rainer Helmig, Prof. Insa Neuweiler, Prof. Zbigniew Sikora and my father, Prof. Romuald Szymkiewicz, for careful reading of the manuscript and many helpful suggestions. Any remaining errors are entirely my

own responsibility. I also greatly appreciate the help received from Ms. Agata Oelschlager, Ms. Anna Dziembowska, Mr. Gowrishankar Chakkravarthy and his team in the preparation of this book.

Last, but not least, many thanks are to my wife Maria, my daughter Lidia and my parents Iwona and Romuald, for their constant love and support.

Contents

1 Introduction 1
References 6

2 Mathematical Models of Flow in Porous Media 9
2.1 Fundamental Concepts 10
2.1.1 Wettability and Capillarity 10
2.1.2 Volume Fractions and Saturations 13
2.1.3 Fluid Potentials 14
2.1.4 Capillary Function 16
2.1.5 Darcy Equation 21
2.1.6 Relative Permeability Functions 23
2.1.7 Density and Viscosity of Fluids 26
2.2 Governing Equations for Fluid Flow 27
2.2.1 Two-Phase Flow 27
2.2.2 Richards Equation 30
2.2.3 Single-Phase Flow 35
2.3 Auxiliary Conditions 36
2.3.1 Initial Conditions 36
2.3.2 Boundary Conditions 39
2.3.3 Conditions at Material Interfaces 41
References 44

3 Numerical Solution of Flow Equations 49
3.1 Basic Properties of Numerical Discretization Schemes 50
3.2 Spatial Discretization 53
3.2.1 Finite Difference Method 53
3.2.2 Finite Element Method 57
3.2.3 Cell-Centred Finite Volume Method 66
3.2.4 Vertex-Centred Finite Volume Method 70

3.3 Solution of Semi-Discrete Equations 75
3.3.1 Discretization in Time 75
3.3.2 Linearization 77
3.3.3 Selection of Time Step Size 84
3.3.4 Solution of Linear Systems 85
References 86

4 Computation of Inter-Nodal Permeabilities for Richards Equation 91
4.1 Overview of Averaging Approaches for One-Dimensional Flow 91
4.1.1 Simple Averaging Methods 92
4.1.2 Direction Dependent Methods 94
4.1.3 Darcian Means 96
4.2 Improved Approximation Scheme 100
4.2.1 Infiltration 102
4.2.2 Drainage 105
4.2.3 Capillary Rise 107
4.2.4 Implementation Issues 109
4.2.5 Evaluation for Steady Flow 110
4.2.6 Evaluation for Unsteady Flow 114
4.3 Saturated–Unsaturated Transition 118
4.4 Heterogeneous Medium 120
4.5 Multidimensional Problems 129
4.6 Two-Phase Flow 133
References 136

5 Upscaling from Darcy Scale to Field Scale 139
5.1 Heterogeneity Patterns 140
5.2 Overview of Upscaling Approaches 142
5.3 Permeability Upscaling for Steady Single-Phase Flow 145
5.3.1 Algebraic Averaging 146
5.3.2 Effective Medium Theory 149
5.3.3 Direct Solution of Steady Flow Equation 153
5.4 Upscaling of Transient Two-Phase Flow 160
5.4.1 Local Equilibrium and Quasi Steady-State Models 160
5.4.2 Local Non-Equilibrium Models 164
References 170

6 Flow in Binary Media with Heterogeneous Hydraulic Diffusivity 177
6.1 Periodic Homogenization Method 177
6.2 Basic Assumptions 179

6.3 Upscaled Models for Different Diffusivity Ratios 183
6.3.1 Moderately Heterogeneous Medium 183
6.3.2 Weakly Permeable Inclusions: Local Equilibrium 186
6.3.3 Weakly Permeable Inclusions: Local Non-Equilibrium 188
6.3.4 Quasi-Impermeable Inclusions 190
6.3.5 Highly Permeable Inclusions 191
6.4 Generalized Formulation 192
6.5 Numerical Implementation 194
6.6 Comparison with Darcy-Scale Numerical Solutions 199
6.7 Comparison with Experiment 205
6.7.1 Experimental Setup 205
6.7.2 Material Parameters. 206
6.7.3 Results. 210
References 212

7 Flow in Binary Media with Heterogeneous Air-Entry Pressure . . . 215
7.1 Upscaled Model of Two-phase Capillary Flow 215
7.1.1 Basic Assumptions 215
7.1.2 Capillary Flow without Entry Pressure Effects 217
7.1.3 Infiltration with Entry Pressure Effects 218
7.1.4 Drainage with Entry Pressure Effects 221
7.1.5 Modified Richards Equation 223
7.2 Numerical simulations 224
7.2.1 Geometry and Material Parameters 225
7.2.2 Example 1: Fluctuating Water Table 227
7.2.3 Example 2: Two-Dimensional Infiltration 231
References 234

8 Summary. 235

Notations

Subscripts related to fluid phases:

a	Air,
w	Water,
α	Generic fluid phase.

Subscripts related to the components of vectors and tensors (Einstein summation convention is implied only for these subscripts): i, j, k, l, m, n.

Superscripts related to spatial discretization (in parentheses)

(i) to (m)	Indices of grid entities: nodes, elements, volumes or faces,
(ij)	Average value between nodes i and j,
(e)	Average value in a finite element,
(fc)	Average value at a finite volume face,
(τ)	Time step index,
(v)	Iteration index.

Superscripts related to components of a heterogeneous medium:

I	Fracture system or background material
II	Rock matrix or inclusions

Superscripts related to averaged field-scale properties:

eff	Effective parameter,
eq	Equivalent parameter.

Superscripts related to homogenization analysis:

$*$	Dimensionless variable,
(c)	Characteristic value.

Symbols (physical units specified where appropriate):

Uppercase Latin letters:

$A_\alpha^{(ij)}$ Coefficients in spatially discretized flow equations for phase α at node j,

B_{ij}^{high} Geometry-dependent constant for calculating the effective water permeability in a medium with highly permeable inclusions,

B_{ij}^{low} Geometry-dependent constant for calculating the effective water permeability in a medium with weakly permeable inclusions,

$C_{\text{it}}^{\text{dec}}$ Coefficient decreasing the time step size,

$C_{\text{it}}^{\text{inc}}$ Coefficient increasing the time step size,

C_{ch} Specific water capacity in the pressure head based form of the Richards equation, (m^{-1}),

C_{wh} Storage coefficient in the pressure head based form of the Richards equation, (m^{-1}),

C_{wp} Storage coefficient in the pressure based form of the Richards equation, (Pa^{-1}),

D Hydraulic diffusivity tensor, ($\text{m}^2\,\text{s}^{-1}$),

D_{e} Energy dissipation for fluid flow in porous medium, (Pa^2),

D_L Characteristic diffusivity at the field scale (m),

D_l Characteristic diffusivity at the Darcy scale (m),

$E^{(n)}$ nth finite element,

$F^{(n)}$ nth face of a finite volume grid,

$G_\alpha^{(j)}$ Gravity term in spatially discretized flow equation for phase α at node j,

H_α Total potential head of fluid phase α, (m),

$K_{\text{s}\alpha}$ Hydraulic conductivity of phase α at apparent saturation, ($\text{m}\,\text{s}^{-1}$),

K_α Hydraulic conductivity of phase α, ($\text{m}\,\text{s}^{-1}$),

L Characteristic length at the field scale, (m),

M_α Mass density of fluid phase α with respect to the bulk volume of porous medium, $M_\alpha = \rho_\alpha \phi_\alpha S_{\alpha,}$, ($\text{kg}\,\text{m}^{-3}$),

$Q_\alpha^{(\text{fc})}$ Total mass flux of phase α at a control volume face, ($\text{kg}\,\text{s}^{-1}$),

R_{b} Characteristic dimension of a matrix block or inclusion, (m),

R_{gas} Universal gas constant, $(\text{J}(\text{mol}\,^\circ\text{K})^{-1})$,

$S_{\text{a}}^{\text{trap}}$ Effective air saturation for a heterogeneous medium in trapped-air regime,

$S_{\text{w}}^{\text{trap}}$ Effective water saturation for a heterogeneous medium in trapped-air regime,

S_α Saturation of fluid phase α,

$S_{\text{e}\alpha}$ Normalized saturation of phase α,

$S_\alpha^{\max}$ Maximum attainable saturation of phase α,

$S_\alpha^{\min}$ Minimum attainable saturation of phase α,

$S_{r\alpha}$	Saturation of phase α at residual state,
T_{α}^{m}	Non-equilibrium mass flow rate between fractures and matrix, or between background material and inclusions, $(\mathrm{kg}(\mathrm{m}^3\,\mathrm{s})^{-1})$,
T_{α}^{v}	Non-equilibrium volumetric flow rate between fractures and matrix, or between background material and inclusions, (s^{-1}),
U	Domain of a representative elementary volume at the pore scale,
U_{α}	Part of a pore-scale representative elementary volume occupied by phase α,
V_{b}	Matrix block domain,
$V^{(i)}$	ith finite volume,
W	Solution domain at the Darcy scale,
Z_{k}	Auxiliary parameter in the formula for inter-nodal permeability,
Z_{s}	Auxiliary parameter in the formula for relating parameters of the Brook-Corey and van Genuchten functions.

Calligraphic Latin letters:

$\mathscr{D}^{(j)}$	Spatial discretization operator for node j,
$\mathscr{E}^{(j)}$	Set of finite elements sharing node j,
$\mathscr{H}$	Relative air humidity,
$\mathscr{M}_{\alpha}$	Mole mass of fluid phase α, $(\mathrm{kg\ mol}^{-1})$,
$\mathscr{N}_{\mathrm{elem}}^{(n)}$	Set of nodes belonging to n-th finite element,
$\mathscr{N}_{\mathrm{nod}}^{(j)}$	Set of nodes connected to node j, including j,
$\mathscr{O}(u)$	Order of magnitude of number u,
$\mathscr{R}_{c}$	Dimensionless gravity–capillarity ratio,
$\mathscr{R}_{d}$	Dimensionless hydraulic diffusivity ratio between inclusions and background,
$\mathscr{R}_{k}$	Dimensionless permeability ratio between inclusions and background,
$\mathscr{R}_{t}^{\iota}$	Dimensionless time scale for Darcy-scale flow in porous material ι,
$\mathscr{T}$	Kelvin temperature, (°K).

Lowercase Latin letters:

a_i	Length of the ellipsoidal inclusion in ith spatial direction, (m),
a', a'_{10}, a'_{11}, a'_{2}	Parameters in the Gasto et al. formula for the inter-nodal permeability,
b', b'_{01}, b'_{02}, b'_{1}	Parameters in the Gasto et al. formula for the inter-nodal permeability,
c', c'_{0}	Parameters in the Gasto et al. formula for the inter-nodal permeability,
d_i	Ellipsoid depolarisation coefficient in ith spatial direction,
f_{α}	Fractional flow function for fluid phase α,
g	Magnitude of the gravitational acceleration vector, $(\mathrm{m\ s}^{-2})$,

$\mathbf{g}$	Gravitational acceleration vector, (m s^{-2}),
h_α	Pressure head of fluid phase α, (Pa),
h_c	Capillary pressure head, (Pa),
h_e	Air-entry pressure head, (Pa),
h_g	Pressure head scaling parameter, (Pa),
$k_{ca}^{(ij)}$	Average relative water permeability for the capillary-driven flow between nodes i and j,
$k_{gr}^{(ij)}$	Average relative water permeability for the gravity-driven flow between nodes i and j,
$k_{int}^{(ij)}$	Integrated average relative water permeability between nodes i and j,
k_{ii}^{cpl}	Cardwell and Parsons lower bound for the equivalent permeability in ith direction, $i = 1, 2, 3$, (m^2),
k_{ii}^{cpu}	Cardwell and Parsons upper bound for the equivalent permeability in ith direction, $i = 1, 2, 3$, (m^2),
$k_{rw}^{(el)}$	Average relative water permeability in a finite element,
k_{rw}^{fm}	Relative water permeability at the fracture–matrix interface,
$k_{rw}^{(ij)}$	Average relative water permeability between nodes i and j,
$k_{r\alpha}$	Relative permeability of phase α,
k_s	Intrinsic permeability tensor, (m^2),
k_s^{eq}	Equivalent intrinsic permeability tensor of heterogeneous medium, (m^2),
k_s^{eff}	Effective intrinsic permeability tensor of a heterogeneous medium, (m^2),
k_t	Total permeability tensor in fractional flow formulation, ($m^2(Pa\,s)^{-1}$),
k_α	Permeability tensor of phase α, (m^2),
k_α^{eff}	Effective permeability tensor of a heterogeneous medium for phase α, (m^2),
k_w^{high}	Effective water permeability tensor for a heterogeneous medium with highly permeable inclusions, (m^2),
k_w^{low}	Effective water permeability tensor for a heterogeneous medium with weakly permeable inclusions, (m^2),
k_w^{trap}	Effective water permeability tensor for a heterogeneous medium in trapped-air regime, (m^2),
l	Characteristic length at the Darcy scale, (m),
l_h	Characteristic dimension of Darcy-scale heterogeneities, (m),
l_v	Characteristic dimension of the averaging volume, (m),
m_g	Exponent in the van Genuchten capillary function,
n_b	Exponent in the Brooks–Corey capillary function,
n_g	Exponent in the van Genuchten capillary function,

$\boldsymbol{n}_E$	Unit vector normal to the boundary of a finite element,
$\boldsymbol{n}_V$	Unit vector normal to the boundary of a finite volume,
$\boldsymbol{n}_W$	Unit vector normal to the boundary of the porous domain,
$\boldsymbol{n}$	Unit vector normal to the interface separating two porous materials,
p_{atm}	Atmospheric pressure, (Pa),
p_{c}	Capillary pressure, (Pa),
p_{e}	Air-entry pressure, (Pa),
$p_{\mathrm{e}}^{\mathrm{drain}}$	Air-entry pressure during drainage, (Pa),
$p_{\mathrm{e}}^{\mathrm{wet}}$	Air-entry pressure during wetting, (Pa),
p_{g}	Capillary pressure scaling parameter in the Gardner and van Genuchten functions, (Pa),
p_α	Pressure in fluid phase α, (Pa),
p_α^{ref}	Reference pressure for fluid phase α, (Pa),
p_{glob}	Global pressure in the fractional flow formulation, (Pa),
$\tilde{p}_i$	Fluctuation of the fluid pressure for steady flow in ith spatial direction, (Pa),
q_{ev}	Cumulative evaporation flux at the soil surface, (m),
q_{inf}	Cumulative infiltration flux at the soil surface, (m),
r_{b}	Local spatial coordinate in a matrix block or inclusion, (m),
r_{c}	Radius of a capillary tube, (m),
$r_{\mathrm{c}1}, r_{\mathrm{c}2}$	Main curvature radii of the air–water interface, (m),
s_{abs}	Absolute error tolerance in the solution of nonlinear algebraic equations,
s_{rel}	Relative error tolerance in the solution of nonlinear algebraic equations,
t	Time, (s),
t_{dry}	Surface drying time in the evaporation simulation, (s),
t_{pond}	Surface ponding time in the infiltration simulation, (s),
u	Generic variable,
$\mathbf{u}$	Vector of unknown nodal values in the numerical solution,
v_L	Characteristic advective velocity at the field scale, ($\mathrm{m\,s^{-1}}$),
v_l	Characteristic advective velocity at the Darcy scale, ($\mathrm{m\,s^{-1}}$),
$v_{\mathrm{st}}^{(ij)}$	Steady-state volumetric water flux between nodes i and j, ($\mathrm{m\,s^{-1}}$),
$v_{\mathrm{w}}^{\mathrm{top}}$	Volumetric water flux at the soil surface, ($\mathrm{m\,s^{-1}}$),
$\mathbf{v}_\alpha$	Volumetric flux of fluid phase α with respect to the solid phase (Darcy velocity), ($\mathrm{m\,s^{-1}}$),
$\mathbf{v}_{\mathrm{t}}$	Total volumetric flux in the fractional flow formulation, ($\mathrm{m\,s^{-1}}$),
w	Volumetric fraction of a porous material,
$\mathbf{x}$	Spatial coordinate vector, (m),
$\mathbf{y}$	Spatial coordinate vector associated with a periodic cell, (m),
z	Elevation above the reference level, (m).

Uppercase Greek letters:

Γ	Interface between two porous materials,
$\Delta x^{(ij)}$	Distance between nodes i and j, (m),
$\Delta x'$	Normalized distance between nodes,
Δt	Time step, (s),
Θ	Weighting coefficient in the time discretization scheme,
Λ^{b}	External surface of a matrix block,
$\Lambda^{(i+1/2)}$	Interface between nested matrix blocks i and $i+1$ in MINC method,
Υ	Weighting function in the finite element method,
Φ_{h}	Flux potential with respect to the water pressure head, (m),
Φ_{p}	Flux potential with respect to the water pressure, (Pa),
$\Psi^{(i)}$	Shape function for node i in the finite element method,
$\Psi_{\mathrm{e}}^{(i)}$	Element shape function for node i in the finite element method,
Ω	Domain of a periodic cell,
Ω^{I}	Part of a periodic cell occupied by the background material,
Ω^{II}	Part of a periodic cell occupied by the inclusions.

Lowercase Greek letters:

α_{g}	Inverse of the scaling pressure (or pressure head) in the capillary function, (Pa^{-1}) or (m^{-1}),
$\alpha_{p,q}$	Coefficients in the modified equation,
β_{α}	Relative compressibility coefficient for fluid phase α, (Pa^{-1}),
β^{fm}	Shape coefficient for the fracture–matrix transfer term,
β'	Parameter in the averaging formula for the inter-nodal permeability,
$\beta_{p,q}$	Coefficients in the modified equation,
γ^{fm}	Scaling coefficient for the fracture–matrix transfer term,
$\gamma_{p,q}$	Coefficients in the modified equation,
$\delta\mathbf{u}$	Increment of the vector of unknown values in the iterative solution procedure,
ε	Scale parameter,
ζ	Gravity coefficient, cosine of the angle between x axis and the gravity vector in one-dimensional problems,
ζ'	Modified gravity coefficient,
η_{α}	Exponent in the power-law relative permeability function for phase α,
$\eta_1, \eta_2, \eta_3, \eta_4$	Exponents in the Mualem and Burdine relative permeability functions,
θ_{α}	Volumetric content of phase α,

$\theta_{r\alpha}$	Volumetric content of phase at the residual state α,
$\theta_{s\alpha}$	Volumetric content of phase α at the state of apparent saturation,
θ_a^{trap}	Effective volumetric air content for a heterogeneous medium in trapped-air regime,
θ_w^{trap}	Effective volumetric water content for a heterogeneous medium in trapped-air regime,
κ	Connectivity parameter in the Mualem and Burdine relative permeability functions,
λ_α	Mobility of phase α, $(\mathrm{Pa\,s})^{-1}$,
μ_α	Dynamic viscosity coefficient of fluid phase α, (Pa s),
$\boldsymbol{\xi}$	Local spatial coordinate in the finite element scheme,
π_i	Weighting coefficient in the generalized power average formula for the equivalent permeability in ith spatial direction,
ρ_α	Intrinsic mass density of fluid phase α, (kg m^{-3}),
ρ_α^{ref}	Reference intrinsic mass density of fluid phase α, (kg m^{-3}),
$\sigma_{\alpha\beta}$	Surface tension between phases α and β, ($\mathrm{N\,m}^{-1}$),
υ	Small number used in numerical differentiation,
ϕ	Porosity,
χ_i	Auxiliary variable used to define the effective permeability in ith spatial direction,
	Wetting angle,
ω_k	Weighting parameter in the averaging scheme for fracture–matrix permeability,
ω_v	Weighting parameter in the averaging formula for the inter-nodal relative permeability,
ω_w	Weighting parameter in the averaging formula for the inter-nodal relative permeability.

Chapter 1
Introduction

The unsaturated zone, also called vadose zone, is located between the soil surface and the groundwater table. Its depth is variable and depends on geological and climatic factors. As the name implies, soils and rocks in the unsaturated zone are only partially filled with water, the rest of the pore space being occupied by air. The vadose region constitutes a vital link between groundwater, atmospheric water and surface water. It is a place of intense human activity of various kinds, including civil and environmental engineering and agriculture. Therefore, flow and transport phenomena occurring in the unsaturated zone can be studied from different viewpoints, as shown schematically in Fig. 1.1.

A distinct scientific specialization, soil physics, is entirely devoted to the study of physical processes in soils, including the water flow in unsaturated conditions, e.g. [17, 20, 47]. Soil physics developed in a close relationship to agronomy and hydrology. In agricultural applications, emphasis is put on the availability of water and dissolved nutrition substances to plants, which motivates the development of comprehensive models to describe the soil-plant-atmosphere system, e.g. [8, 9]. Accurate evaluation of water infiltration into the soil and evapotranspiration from the soil is also important for hydrological models. For instance, the infiltration capacity of soils has a direct influence on the formation of runoff, and thus is an important factor in predicting the risk of flood. Consequently, a trend towards explicit coupling of the surface and shallow subsurface flow in hydrological models can be observed, e.g. [11, 48].

On the other hand, the water flow processes in the unsaturated zone have significant impact on groundwater flow in saturated aquifers, which constitute a major source of drinking water. Even more importantly, the vadose zone is a buffer between groundwater and various sources of pollutants located at the soil surface or in the shallow subsurface. Reliable prediction of the fate of contaminants dissolved in water requires the knowledge of water flow velocities in the unsaturated zone, which are in general highly variable in space and time. Therefore, increasing attention is paid to coupled saturated-unsaturated models of groundwater flow and contaminant transport, e.g. [43, 44, 50]. Moreover, accounting for the unsaturated flow allows for

A. Szymkiewicz, *Modelling Water Flow in Unsaturated Porous Media*,
GeoPlanet: Earth and Planetary Sciences, DOI: 10.1007/978-3-642-23559-7_1,

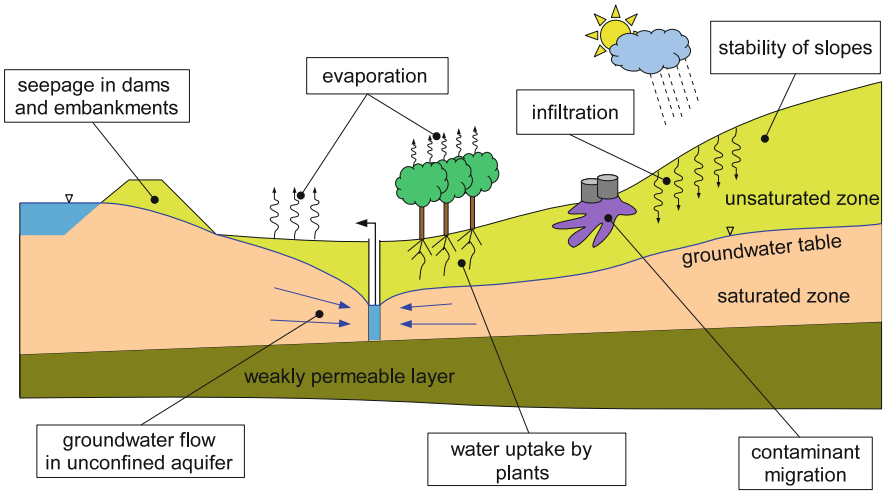

Fig. 1.1 Typical problems related to water flow in the vadose zone

improved estimation of parameters related to the hydraulics of phreatic aquifers, such as the recharge rate [18], the specific yield [35] or the height of the seepage face in wells [5].

Water flow in the vadose zone has important implications also for geotechnical engineering. Traditionally, soil mechanics focused mostly on completely dry or fully saturated non-cohesive soils, and fully saturated cohesive soils. However, a wide range of problems can be more accurately modelled, if the variability in the soil water saturation is taken into account. This is particularly necessary for soils that swell, shrink or collapse due to the changes in water saturation, but there is an increasing awareness of the importance of unsaturated flow also for other applications, including soil compaction, slope stability, flow in dams and embankments, protection of landfills, tunneling or interpretation of penetration tests, e.g. [30, 31, 51]. Unsaturated soil mechanics is still an emerging and very active field of research, which developed substantially during the last twenty years, e.g. [10, 25, 28].

In all the applications mentioned above a crucial issue is the ability to accurately model water flow in soils, or—more generally—partially saturated porous media. This, however, is a challenging task, due to the multi-phase and multi-scale nature of porous media, especially the ones formed by natural processes. Porous soils and rocks in the vadose zone consist of several deformable solid and fluid phases, separated by clearly distinguishable interfaces, representing sharp discontinuities in physical and chemical properties [16, 33]. In general, each of the phases consists of multiple chemical components, which can move between phases. Pore air, for instance, is a mixture of gases, including water vapor, while pore water contains many dissolved substances, including gases. The number of phases and components included in the mathematical model depends on the problem under consideration. In many applications focusing on the water flow, a sufficient accuracy can be achieved with

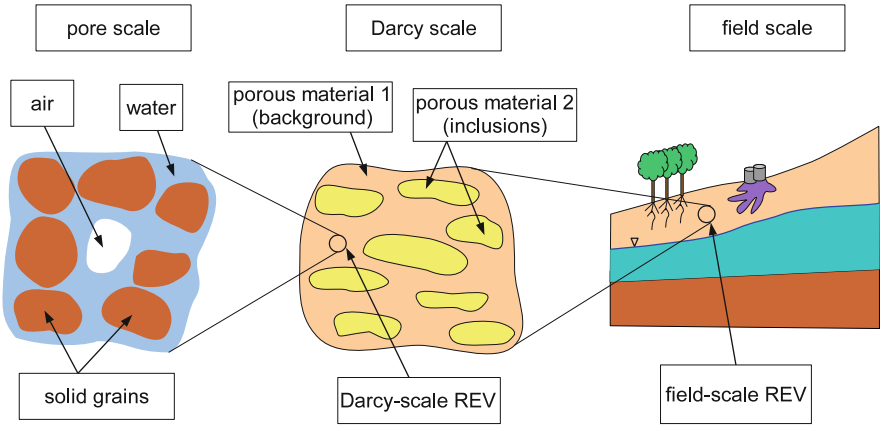

Fig. 1.2 Observation scales in a porous medium

a simplified model, where both air and water are considered as immiscible single-component phases and the deformation of the solid skeleton is neglected. Such an approach is adopted in the present work.

Modelling of flow in porous media is further complicated by the fact that the relevant physical processes can be described at various observation scales. Mathematical models applied at each scale typically represent the principles of conservation of basic quantities such as mass, momentum and energy, but the exact form of the governing equations may differ substantially between the scales. In some cases the model describing processes at a larger scale can be derived directly from the equations relevant at a smaller scale by an appropriate averaging procedure. This process is known as upscaling. Alternatively, the governing equations can be formulated directly at the larger scale, based on phenomenological considerations. Two basic scales, typically distinguished in porous media, are the pore scale and the Darcy scale, Fig. 1.2. In the former case, the characteristic spatial dimension is the size of a single pore, which in granular media is approximately proportional to the grain size. At this scale, each phase occupies a distinct spatial domain, and each point of space can be associated with a specific phase. On the other hand, it is assumed that each phase can be regarded as a continuum within its own spatial sub-domain, i.e. the size of the pores is much larger than the size of fluid molecules. The flow of fluid phases can be described by the Navier-Stokes equations with appropriate conditions at the fluid-solid and fluid-fluid interfaces. However, the pore scale description is not suitable for practical problems, which involve spatial domains having dimensions larger than the pore size by many orders of magnitude. Therefore, the governing equations describing behaviour of various phases are usually formulated at a much larger scale, which in the present work will be referred to as the Darcy scale, from the name of H. Darcy, who developed the well-known formula for the water seepage velocity in a porous medium [7]. At this scale, each spatial point corresponds to a representative elementary volume (REV), containing a sufficiently large number of pores, occupied

by multiple fluid phases. Thus, in contrast to the pore scale description, at the Darcy scale each phase forms a continuum over the entire spatial domain.

The most commonly used two-phase model of air and water flow at the Darcy scale is a combination of the mass conservation equation for each fluid with the semi-empirical equation for flow velocity, based on an extension of the Darcy formula for the case of multi-phase flow. One of key components of the model is the capillary function, describing the relationship between the water saturation and the capillary pressure, defined as the difference between pressures in the air and water phases. A complementary constitutive relationship is given by the relative permeability function, which describes the ability of each fluid phase to flow in the porous medium as a function of the phase saturation. Both functions are strongly nonlinear. Their form depends principally on the geometrical characteristic of the pore space and on the properties of the fluid-fluid and fluid-solid interfaces (surface tension). The mathematical model of two-phase flow is often formulated as two coupled partial differential equations of parabolic type, with the two phase pressures or saturations as the primary unknown variables.

The two-phase model can be simplified, if one assumes that the air phase is continuously distributed in pores, it is connected to the atmospheric air and much more mobile than the water phase. Accordingly, the pressure in the air phase can be considered constant and equal to the atmospheric pressure, and the equation describing air flow is eliminated. The remaining equation for the water flow is called the unsaturated flow equation or the Richards equation [34]. Similarly to the full two-phase flow model, the Richards equation is based on semi-empirical concepts of the capillary and relative permeability functions, introduced at the Darcy scale to account for a number of pore scale phenomena, which at present are not fully understood. These constitutive relationships are difficult to associate with the Darcy-scale processes in a manner that is both physically rigorous and easy to implement practically. While a number of improved formulations for the two-phase and unsaturated flow have been proposed, e.g. [3, 14, 26, 29, 32, 49], the Richards equation remains a useful and well-established tool in the unsaturated zone modelling, and is the basis of the present analysis.

The present book focuses on two aspects of the application of the Richards equation. The first one is related to its numerical solution. Although significant development of the numerical algorithms occurred in the last twenty years, e.g. [4, 27], solution of the Richards equation remains a challenging task due to the afore-mentioned strongly nonlinear constitutive relationships, which must be appropriately represented in the discretized space-time domain. A particularly important issue is the approximation of the relative permeability between the nodes of a spatial grid, which is a necessary to estimate water fluxes, according to a discrete version of the Darcy formula. As the relative permeabilities may differ by several orders of magnitude (for example, during infiltration in a dry soil, or evaporation), the choice of the averaging method is often essential for the overall accuracy of the approximate solution. Several simple averaging schemes have been proposed, e.g. arithmetic mean, geometric mean and upstream weighting, but each of them may lead to large errors for particular combinations of the initial and boundary conditions, grid size and the form of

functional relationship between the relative permeability and the capillary pressure, e.g. [1, 2, 15]. On the other hand, more accurate methods often require significantly larger computational effort, e.g. [46]. In this work an averaging scheme is presented, that is relatively easy to implement and significantly improves the solution accuracy for a wide range of one- and two-dimensional problems. The method was proposed in the paper [36], and further developed in [37, 38]. Extension of the method for unstructured grids and implications for the solution of the full two-phase model are also discussed. The analysis is carried out for a simple form of the Richards equation, which does not account for soil compressibility nor water uptake by plant roots. While these two factors are very important in many applications related to the unsaturated zone and must be properly treated numerically, they have no direct influence on the development of the averaging schemes for inter-nodal permeabilities.

The second topic considered in this book deals with flow in porous media showing material heterogeneity at the Darcy scale. Heterogeneity may be related to various physical and chemical properties of the porous medium. The focus of this work is on porous formations composed of sub-domains characterized by distinct textural properties, which imply differences in pore geometry, and consequently in the physical parameters such as permeability, hydraulic diffusivity or air entry pressure (defined as the value of the capillary pressure above which the pore air flow is possible). The important issue of chemical heterogeneity, for instance related to the wettability and adsorption properties of the solid phase is not considered here. If the number of heterogeneous regions in the considered spatial domain is large, their explicit representation on a numerical grid becomes difficult or even impossible. Therefore, a new observation scale can be introduced, which for the purposes of this work will be called the field scale, Fig. 1.2. At this scale the relevant representative elementary volume encompasses sufficiently large number of Darcy scale heterogeneities to allow for the development of an upscaled model. The heterogeneous structure can be described in either deterministic or stochastic terms. In particular the stochastic models for flow and transport in unsaturated heterogeneous porous media have been a subject of intense research, e.g. [6, 12, 52]. In this book the deterministic viewpoint is adopted and a specific heterogeneity pattern is considered: a binary porous medium with disconnected porous inclusions (lenses) embedded in a continuous porous background material. While such a structure is relatively simple, it is representative of a number of natural porous formations, such as fluvial or coastal sediments, or sandstone-shale sequences, e.g. [19]. On the other hand, this type of pattern can be conveniently parametrized and analysed from the theoretical point of view, allowing for a good general understanding of local heterogeneities on the large-scale behaviour of the medium. The second part of this work presents an extended discussion of several models based on the Richards equation, which were developed for such type of media using the asymptotic homogenization approach [21–24, 39, 41]. These works showed that the macroscopic behaviour of the medium depends on the ratio between the permeabilities of the inclusions and the background material. A generalized model, valid for a wide range of inclusion-to-background permeability ratio, was proposed [39], and its preliminary experimental verification was carried out [40]. It can be also shown that the Richards approximation is not valid for media

characterized by higher value of the air-entry pressure in the matrix than in inclusions. In porous media showing heterogeneity with respect to the air-entry pressure the assumption of the continuity of air phase in porous medium, which underlies the Richards equation, may not be satisfied [41]. However, the accuracy of the Richards equation can be improved, if the large-scale capillary and permeability functions are appropriately modified [42].

The field scale discussed in this book represents an intermediate level in the hierarchy of scales relevant to the modeling of water flow in the vadose zone, with the characteristic length of the order of meters to dekameters. Significant research has been devoted to the description of unsaturated zone processes at regional scale, corresponding to hydrological watersheds, with the horizontal dimensions of many kilometers, e.g. [13, 45]. At such a scale, simplified mathematical models of the black-box type are routinely used and an important question is how to relate their parameters to the more detailed characteristics of the porous media available at smaller scales. While regional-scale hydrological modelling is of high practical importance, it is not considered in this book.

The book is structured as follows. Chapter 2 presents the mathematical formulation of flow in unsaturated porous medium. The governing equations for the two-phase model and the Richards model are discussed, together with various analytical formulae for capillary and permeability functions. In Chap. 3 a numerical algorithm to solve the governing flow equations is developed. The algorithm is formulated in general terms and can be applied to both the two-phase model and the Richards equation. Various methods of spatial discretization are discussed, including the control volume–finite difference and control volume–finite element approaches. The approximation of the average permeability in spatially discretized Richards equation is considered in detail in Chap. 4. Chapter 5 introduces basic concepts of upscaling. In Chap. 6 the upscaled models developed for flow in binary media without air-entry pressure effects are presented. The model accounting for air-entry effects is discussed in Chap. 7. The final chapter summarizes the contents of the book and outlines some open problems related to the discussed topics.

References

1. Baker D (1995) Darcian weighted interblock conductivity means for vertical unsaturated flow. Ground Water 33(3):385–390. doi:10.1111/j.1745-6584.1995.tb00294.x
2. Belfort B, Lehmann F (2005) Comparison of equivalent conductivities for numerical simulation of one-dimensional unsaturated flow. Vadose Zone J 4(4):1191–1200. doi:10.2136/vzj2005.0007
3. Bentsen R (2001) The physical origin of interfacial coupling in two-phase flow through porous media. Transp Porous Media 44(1):109–122. doi:10.1023/A:1010791526239
4. Celia M, Bouloutas E, Zarba R (1990) A general mass-conservative numerical solution for the unsaturated flow equation. Water Resour Res 26(7):1483–1496. doi:10.1029/WR026i007p01483
5. Chenaf D, Chapuis R (2007) Seepage face height, water table position, and well efficiency at steady state. Ground Water 45(2):168–177. doi:10.1111/j.1745-6584.2006.00277.x

6. Dagan G (1989) Flow and transport in porous formations. Springer, New York
7. Darcy H (1856) Les fontaines publiques de la ville de Dijon. Dalmont, Paris
8. Evett S (2002) Water and energy balances at soil-plant-atmosphere interfaces. In: Soil physics companion, CRC Press, Boca Raton, pp 127–188
9. Feddes R, Kowalik P, Zaradny H (1978) Simulation of field water use and crop yield. Wageningen, PUDOC
10. Fredlund D, Rahardjo H (1993) Soil mechanics for unsaturated soils. Wiley, New York
11. Furman A (2008) Modeling coupled surface-subsurface flow processes: a review. Vadose Zone J 7(2):741–756. doi:10.2136/vzj2007.0065
12. Gelhar L (1993) Stochastic subsurface hydrology. Prentice Hall, Engelwood Cliffs
13. Harter T, Hopmans J (2004) Role of vadose-zone flow processes in regional-scale hydrology: review, opportunities and challenges. In: Unsaturated zone modelling: progress, challenges and applications, Kluwer, Dordrecht
14. Hassanizadeh M, Gray W (1993) Toward an improved description of the physics of two-phase flow. Adv Water Resour 16(1):53–67. doi:10.1016/0309-1708(93)90029-F
15. Haverkamp R, Vauclin M (1979) A note on estimating finite difference interblock hydraulic conductivity values for transient unsaturated flow. Water Resour Res 15(1):181–187. doi:10.1029/WR015i001p0018
16. Helmig R (1997) Multiphase flow and transport processes in the subsurface: a contribution to the modeling of the hydrosystems. Springer, Berlin
17. Hillel D (1998) Environmental soil physics. Academic Press, San Diego
18. Hunt R, Prudic D, Walker J, Anderson M (2008) Importance of unsaturated zone flow for simulating recharge in a humid climate. Ground Water 46(4):551–560. doi:10.1111/j.1745-6584.2007.00427.x
19. Knudby C, Carrera J, Bumgardner J, Fogg G (2006) Binary upscaling—the role of connectivity and a new formula. Adv Water Resour 29(4):590–604. doi:10.1016/j.advwatres.2005.07.002
20. Kowalik P (2007) Zarys fizyki gruntów (Fundamentals of soil physics). Wydawnictwa Politechniki Gdańskiej, Gdańsk
21. Lewandowska J, Auriault JL (2004) Modeling of unsaturated water flow in soils with highly permeable inclusions. C R Mec 332(1):91–96
22. Lewandowska J, Laurent JP (2001) Homogenization modeling and parametric study of moisture transfer in an unsaturated heterogeneous porous medium. Transp Porous Media 45(3):321–345. doi:10.1023/A:1012450327408
23. Lewandowska J, Szymkiewicz A, Burzyński K, Vauclin M (2004) Modeling of unsaturated water flow in double-porosity soils by the homogenization approach. Adv Water Resour 27(3):283–296. doi:10.1016/j.advwatres.2003.12.004
24. Lewandowska J, Szymkiewicz A, Auriault JL (2005) Upscaling of Richards equation for soils containing highly conductive inclusions. Adv Water Resour 28(11):1159–1170. doi:10.1016/j.advwatres.2005.03.006
25. Lu N, Likos W (2004) Unsaturated soil mechanics. Wiley, Hoboken
26. Manthey S, Hassanizadeh M, Helmig R (2005) Macro-scale dynamic effects in homogeneous and heterogeneous porous media. Transp Porous Media 58(1–2):121–145. doi:10.1007/s11242-004-5472-6
27. Miller C, Abhishek C, Farthing M (2006) A spatially and temporally adaptive solution of Richards' equation. Adv Water Resour 29(4):525–545. doi:10.1016/j.advwatres.2005.06.008
28. Murray E, Sivakumar V (2010) Unsaturated soils. A fundamental interpretation of soil behaviour. Wiley-Blackwell, Chichester
29. Niessner J, Hassanizadeh S (2008) A model for two-phase flow in porous media including fluid-fluid interfacial area. Water Resour Res 44:W08439. doi:10.1029/2007WR006721
30. Oettl G, Stark R, Hofstetter G (2004) Numerical simulation of geotechnical problems based on a multi-phase finite element approach. Comput Geotech 31(8):643–664. doi:10.1016/j.compgeo.2004.10.002
31. Ossowski R, Sikora Z (2004) Numeryczne modelowanie sondowania statycznego CPTU (Numerical modeling of static CPTU tests). Politechnika Gdańska, Gdańsk

32. Pachepsky Y, Timlin D, Rawls W (2003) Generalized Richards equation to simulate water transport in unsaturated soils. J Hydrol 272(1–4):3–13. doi:10.1016/S0022-1694(02)00251-2
33. Pinder G, Gray W (2008) Essentials of multiphase flow and transport in porous media. Wiley, Hoboken
34. Richards L (1931) Capillary conduction of liquids through porous medium. Physics 1:318–333
35. Shah N, Ross M (2009) Variability in specific yield under shallow water table conditions. J Hydrol Eng 14(12):1290–1298. doi:10.1061/(ASCE)HE.1943-5584.0000121
36. Szymkiewicz A (2009) Approximation of internodal conductivities in numerical simulation of 1D infiltration, drainage and capillary rise in unsaturated soils. Water Resour Res 45:W10403. doi:10.1029/2008WR007654
37. Szymkiewicz A, Burzyński K (2011) Computing internodal conductivities in numerical modeling of two dimensional unsaturated flow on rectangular grid. Arch Civil Eng 57(2):215–225. doi:10.2478/v.10169-011-0016-2
38. Szymkiewicz A, Helmig R (2011) Comparison of conductivity averaging methods for one-dimensional unsaturated flow in layered soils. Adv Water Resour 34(8):1012–1025. doi:10.1016/j.advwatres.2011.05.011
39. Szymkiewicz A, Lewandowska J (2006) Unified macroscopic model for unsaturated water flow in soils of bimodal porosity. Hydrol Sci J 51(6):1106–1124
40. Szymkiewicz A, Lewandowska J, Angulo-Jaramillo R, Butlańska J (2008) Two-scale modeling of unsaturated water flow in a double-porosity medium under axi-symmetric conditions. Can Geotech J 45(2):238–251. doi:10.1139/T07-096
41. Szymkiewicz A, Helmig R, Kuhnke H (2011) Two-phase flow in heterogeneous porous media with non-wetting phase trapping. Trans Porous Media 86(1):27–47. doi:10.1007/s11242-010-9604-x
42. Szymkiewicz A, Helmig R, Neuweiler I (2012) Upscaling unsaturated flow in binary porous media with air entry pressure effects. Water Resour Res 48:W04522. doi:10.1029/2011WR010893
43. Thoms R, Johnson R, Healy R (2006) Users guide to the variably saturated flow (VSF) process for MODFLOW. Technical Report, USGS
44. Twarakavi N, Simunek J, Seo S (2008) Evaluating interactions between groundwater and vadose zone using the HYDRUS-based flow package for MODFLOW. Vadose Zone J 7(2):757–768. doi:10.2136/vzj2007.0082
45. Vereecken H, Kasteel R, Vanderborght J, Harter T (2007) Upscaling hydraulic properties and soil water flow processes in heterogeneous soils: a review. Vadose Zone J 6(1):1–28. doi:10.2136/vzj2006.0055
46. Warrick A (1991) Numerical approximation of Darcian flow through unsaturated soil. Water Resour Res 27(6):1215–1222. doi:10.1029/91WR00093
47. Warrick A (2002) Soil physics companion. CRC Press, Boca Raton
48. Weill S, Mouche E, Patin J (2009) A generalized Richards equation for surface/subsurface flow modelling. J Hydrol 366(1–4):9–20. doi:10.1016/j.jhydrol.2008.12.007
49. Whitaker S (1986) Flow in porous media II: the governing equations for immiscible, two-phase flow. Transp Porous Media 1(2):105–125. doi:10.1007/BF00714688
50. Xu T, Sonnenthal E, Spycher N, Pruess K (2008) TOUGHREACT user's guide: A simulation program for non-isothermal multiphase reactive geochemical transport in variably saturated geologic media, v1.2.1. Technical Report, Lawrence Berkeley National Laboratory
51. Xu YQ, Unami K, Kawachi T (2003) Optimal hydraulic design of earth dam cross section using saturated-unsaturated seepage flow model. Adv Water Resour 26(1):1–7. doi:10.1016/S0309-1708(02)00124-0
52. Zhang D (2002) Stochastic methods for flow in porous media: coping with uncertainties. Academic Press, San Diego

Chapter 2
Mathematical Models of Flow in Porous Media

In this chapter a general model for the two-phase fluid flow in porous media is presented, together with its simplified form, known as the Richards equation, which is applicable (under specific assumptions) to describe water flow in the vadose zone. In each case the governing equations are formulated at the Darcy scale, using the capillary pressure–saturation relationship and an empirical extension of the Darcy equation for the multiphase flow. The validity of these concepts, and the models based on them, is a subject of ongoing scientific debate, due to unclear connections between the pore-scale and Darcy-scale physical quantities, e.g. [25, 29, 32, 56, 66, 88]. Nevertheless, the models described here can be used to simulate many practical cases of multiphase flow in the subsurface with sufficient accuracy, e.g. [17, 31]. Therefore, they have been assumed as the starting point for the analysis presented in this work.

The two-phase flow model considered here is based on the following assumptions:

1. Pore air and pore water are single-component fluids.
2. Mass transfers between the fluids, i.e. the dissolution of air in water and the evaporation of water, are neglected.
3. The flow is isothermal.
4. Both fluid phases are barotropic, i.e. each phase density depends only on the pressure in the respective phase.
5. The solid phase is homogeneous, materially incompressible and does not react with the pore fluids.
6. The solid skeleton is rigid.
7. The flow of each fluid can be described by the extended Darcy formula including the relative permeability coefficient.

Additional assumptions underlying the Richards equation are discussed in Sect. 2.2.2. Fluid compressibility and soil skeleton deformation are not essential for the range of problems considered in this book. However, fluid compressibility is included in order to retain parabolic character of the governing equations for single phase flow. For a description of more comprehensive modeling approaches, which take into account the deformation of porous medium, see e.g. [20, 24, 47, 59, 70]. In the following

A. Szymkiewicz, *Modelling Water Flow in Unsaturated Porous Media*,
GeoPlanet: Earth and Planetary Sciences, DOI: 10.1007/978-3-642-23559-7_2,

sections the key components of the model are briefly outlined, based to a large extent on the works [31, 33, 63].

2.1 Fundamental Concepts

2.1.1 Wettability and Capillarity

When two fluids are present in the pore space, one of them is preferentially attracted by the surface of the solid skeleton. It is called the wetting fluid (or phase), while the other fluid phase is called non-wetting. Here we consider only hydrophilic porous media, showing greater affinity to water than to air, which are more widespread in nature [33]. In the following the term wetting phase will be used as a synonym for water and the term non-wetting phase—as a synonym for air.

Immiscible fluids are separated by a well defined interface, which, if observed at a scale much larger than the molecule size, can be considered infinitely thin. Since the cohesion between fluid molecules at one side of the interface is different from that at the other side, the interface is characterized by some surface energy (or surface tension), which is a measure of the forces that must be overcome to change its shape. One consequence of the existence of the surface tension is the difference in the equilibrium pressures of air and water, separated by a curved interface, due to unbalanced tangential forces at the dividing surface. The pressure drop between the air and water phases can be calculated from the Laplace equation [63]:

$$\Delta p = p_{\mathrm{a}} - p_{\mathrm{w}} = \sigma_{\mathrm{aw}} \left(\frac{1}{r_{\mathrm{c1}}} + \frac{1}{r_{\mathrm{c2}}} \right), \tag{2.1}$$

where the subscripts a and w denote the air and water phases, respectively, σ_{aw} is the surface tension of the air–water interface, and r_{c1} and r_{c2} are the main curvature radii of the interface. The value of air-water surface tension at the temperature of 20 °C is equal to 0.0726 $\mathrm{N\,m^{-1}}$ and decreases with increasing temperature [63]. The pressure is always smaller in the fluid occupying the concave side of the interface. In the absence of any external forces, the interface of a droplet of one fluid contained in another fluid tends to assume a spherical shape, which minimizes the surface energy.

In the presence of a solid surface the shape of the interface is determined by the relative magnitude of the surface tensions between all three phases, Fig. 2.1a:

$$\sigma_{\mathrm{aw}} \cos\psi = \sigma_{\mathrm{sa}} - \sigma_{\mathrm{sw}} , \tag{2.2}$$

where σ_{sa} and σ_{sw} are the values of the surface tension between the solid phase and air and water, respectively, and ψ is called the wetting angle. For a perfectly wetting fluid, $\psi = 0°$, i.e. the fluid tends to spread evenly over the whole solid surface. For

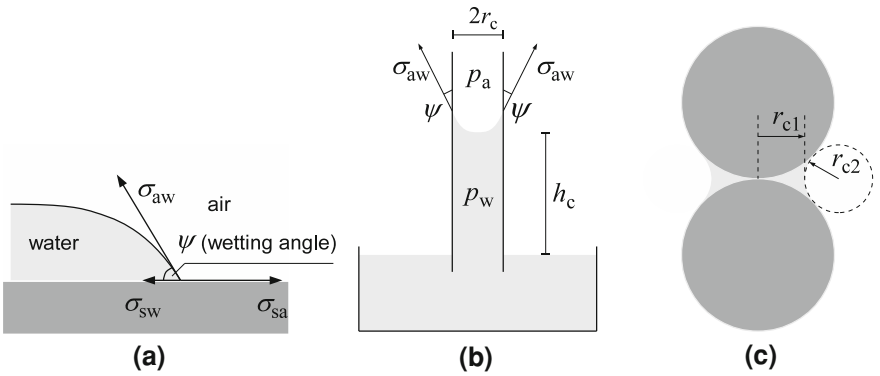

Fig. 2.1 Surface tension effects: **a** equilibrium position of the fluid–fluid interface near the solid surface, **b** rise of the wetting fluid in a capillary tube, **c** pendular ring around the contact point of two solid grains

a perfectly non-wetting fluid, $\psi = 180°$, which results in the formation of spherical droplets on the solid surface.

The existence of surface tension is at the origin of the capillary rise observed in small tubes, Fig. 2.1b. The molecules of the wetting fluid are attracted by the tube wall, and a meniscus (curved interface) forms between water and air above the free surface of water in the recipient. The pressure drop across the interface is denoted in this context as the capillary pressure and can be calculated for a cylindrical tube as:

$$\Delta p = p_c = p_a - p_w = \frac{2\,\sigma_{aw}\,\cos\psi}{r_c}\,, \tag{2.3}$$

where r_c is the tube radius. Assuming that the value of the surface tension between air and water corresponds to the temperature of 20 °C, the tube material is perfectly wettable ($\psi = 0°$), air is at constant atmospheric pressure everywhere, and water is incompressible, one obtains the well known formula for the height of the capillary rise:

$$h_c = \frac{1.5 \times 10^{-5}}{r_c}\,, \tag{2.4}$$

where both h_c and r_c are in meters. Equation (2.4) is often used to approximate the height of capillary rise in natural porous media, which are characterized by small wettability angles. However, as the geometry of pores in natural porous media is much more complex, the representation of pore system as a bundle of capillary tubes does not hold in many situations, and more complex configurations of air and water in the pore space are encountered, which will be discussed on the example of a granular porous medium.

Since water molecules are preferentially attracted to the surface of the solid phase, they can be adsorbed from the vapour present in the pore air. Thus, small amounts

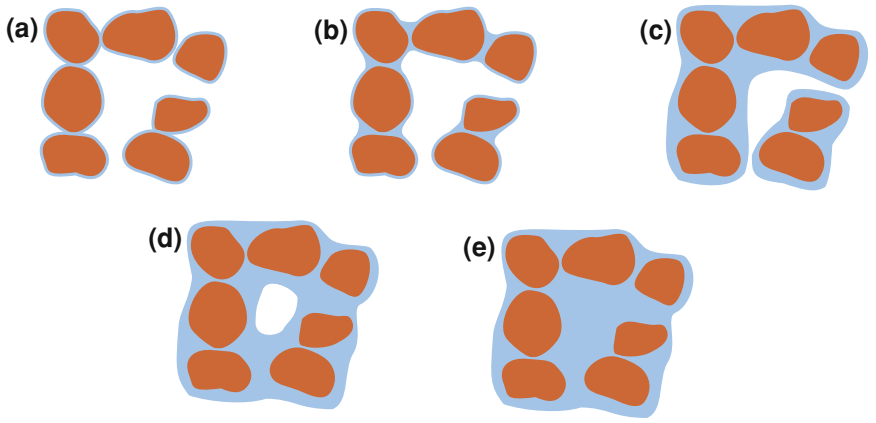

Fig. 2.2 Spatial configurations of water and air in an unsaturated granular porous medium: **a** adsorbed regime, **b** capillary pendular regime, **c** capillary funicular regime, **d** occluded air bubble regime, **e** fully saturated regime

of water are always present in the form of thin films covering the surface of the solid skeleton, Fig. 2.2a. The thickness of this layer depends on the strength of molecular level interactions between solid and water and on the relative air humidity. Due to the tight bonding of the adsorbed water to the solid surface, in many practical problems it is considered as immobile [62]. As the amount of water in a porous medium increases, it is attracted to the water adsorbed at the solid surface by the cohesion forces, but on the other hand tends to minimize the area of the water–air interface. This form of water is known as the capillary water, and occurs initially in acute corners of the pores. If the porous skeleton is made of grains, water forms pendular rings around the contact points, Figs. 2.1c and 2.2b. The corresponding water–air configuration is known as the pendular stage. Pendular water is less tightly bound by the solid phase, but it occurs in isolated regions, and does not form continuous flowpaths, so it can be considered as macroscopically immobile [62]. The pressure drop at the interface between pendular water and pore air can be theoretically calculated from Eq. (2.1), assuming a negative value for r_{c1} and a positive value for r_{c2} (Fig. 2.1c). If more water is added to the system, the regions occupied by pendular water coalesce and continuous thicker films are formed along the pore walls. At this stage, known as the funicular stage, the flow of liquid water is possible, Fig. 2.2c. For all three water configurations mentioned above, air occupies continuously the central part of the pores. As the amount of water in the system increases further, the water films become thicker and pores can be entirely filled with water at the points where their cross-section is smaller. The air phase loses its continuity and no macroscopic air flow is possible. This is called the occluded air bubbles stage. With time the air can dissolve in water and full water saturation is reached. Since in this work evaporation and dissolution are neglected, the considerations presented in the following chapters are applicable to funicular, occluded air, and fully water saturated stages.

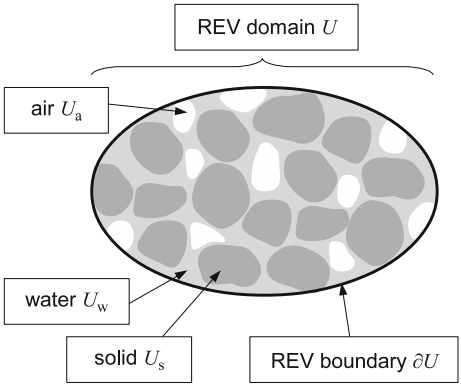

Fig. 2.3 Pore-scale representative elementary volume

2.1.2 Volume Fractions and Saturations

Continuum description of a multiphase porous medium at the Darcy scale implies that the relevant physical quantities defined at a given point **x** represent averages taken over a pore-scale representative elementary volume (REV) associated with that point, Fig. 2.3. At the Darcy scale the same point can be occupied simultaneously by all three phases, which is represented by the concepts of volume fractions and saturations. The volume fraction of phase α is defined as the ratio of the volume of the part of the REV occupied by phase α to the total volume of the REV:

$$\theta_\alpha = \frac{|U_\alpha|}{|U|} \, . \tag{2.5}$$

Porosity is defined as the volume fraction of pores, and it is equal to the sum of the volume fractions of the two pore fluids:

$$\phi = \frac{|U_w| + |U_a|}{|U|} = \theta_a + \theta_w \, . \tag{2.6}$$

Moreover, it is convenient to define the saturation of each phase, which is equal to the fraction of the pore space occupied by a given fluid:

$$S_\alpha = \frac{\theta_\alpha}{\phi} \, . \tag{2.7}$$

The sum of the air and water saturations must be equal to one:

$$S_a + S_w = 1 \, . \tag{2.8}$$

In general, each saturation can vary from 0 to 1. However, in most practical problems the range of variability is smaller. For instance, if a fully water-saturated medium is drained, at some point the mobile water (not adsorbed to the solid phase) looses its continuity and the liquid flow will not be possible (transition from the funicular to pendular state). The corresponding value of the water saturation is called residual or irreducible values, and denoted by S_{rw}, respectively. However, it should be noted that the value of water saturation can be further decreased by natural evaporation or oven drying. Similarly, during imbibition in a dry medium in natural conditions, it is generally not possible to achieve full water saturation, as a part of the pores will be occupied by isolated air bubbles. The corresponding residual air saturation is denoted as S_{ra}, respectively. However, the water saturation can increase above the value of $1 - S_{\mathrm{ra}}$, for example if the air is compressed or dissolves in water. Therefore, the residual saturations must be considered as problem-specific parameters, not material parameters [31].

For practical purposes, the fluid saturations are often normalized with respect to the range of values occurring in the problem under consideration. The resulting normalized (effective) saturations are defined as:

$$S_{\mathrm{e}\alpha} = \frac{S_\alpha - S_\alpha^{\min}}{S_\alpha^{\max} - S_\alpha^{\min}} \ , \tag{2.9}$$

where $S_\alpha^{\max}$ and $S_\alpha^{\min}$ are the maximum and minimum saturation values occurring for a given problem.

In soil physics and hydrology it is more common to quantify the relative amount of fluid phases in soil using the volumetric fractions θ_α. If the compressibility of the solid skeleton is neglected ($\phi = const$), the volumetric phase contents are uniquely defined by phase saturations. In field conditions the volumetric fraction of water varies between the residual water content:

$$\theta_{\mathrm{rw}} = \phi \, S_{\mathrm{rw}} \ , \tag{2.10}$$

and the so-called saturated water content:

$$\theta_{\mathrm{sw}} = \phi \ (1 - S_{\mathrm{ra}}) \ . \tag{2.11}$$

The latter value refers to the state of maximum attainable water saturation. Equivalent limit values can be defined also for the volumetric air content.

2.1.3 Fluid Potentials

At the Darcy scale, the energy state of each of the two fluids present in the pore space is commonly characterized using the concept of energy potential. The energy

potential is related to the forces acting on the fluid. It is defined as the negative integral of the force over the path taken by an infinitesimally small volume of water, when it moves from a reference location to the point under consideration [58]. The reference point is commonly assumed to be at the surface of a free water body located at the same elevation as the considered volume of the pore fluid, and subjected to normal atmospheric pressure. Thus, the values of the fluid potentials are relative to the normal atmospheric pressure. Potentials can be expressed as energy per unit mass ($\mathrm{J\,kg^{-1}}$), energy per unit volume ($\mathrm{Jm^{-3}} = \mathrm{Pa}$) or energy per unit weight ($\mathrm{Jkg^{-1}m^{-1}s^2} = \mathrm{m}$).

Assuming that the fluid density depends only on its pressure and that the only mass force is the gravity, acting in the direction of decreasing elevation z, the potential of each pore fluid can be conveniently expressed in terms of the total hydraulic head:

$$H_\alpha = \int_{p_\alpha^{\mathrm{ref}}}^{p_\alpha} \frac{\mathrm{d}\hat{p}}{\rho_\alpha(\hat{p})g} + z = h_\alpha + z, \tag{2.12}$$

where p_α^{ref} is the reference pressure, ρ_α is the fluid density, $\hat{p}$ is the integration variable, g is the magnitude of gravitational acceleration, z is the elevation above the reference level, and h_α is the pressure head. As far as the water phase is considered, in the fully water-saturated conditions the variable p_w represents the pressure exerted by unsupported water phase overlying the point of interest, while in partially saturated conditions it accounts for the effect of capillary and adsorption forces binding water molecules to the solid skeleton. These interactions include short range van der Waals forces between water and solid, cohesion through hydrogen bonds in water and ion hydration and binding of water in diffuse double layers [48, 58]. In the case of the air phase (or the non-wetting fluid in general) the variable p_a represents only the pressure, as the interaction between this phase and the solid skeleton is typically neglected.

The difference between the pressure potentials of air and water in unsaturated conditions, caused by the action of capillary and adsorption forces, is often called the capillary pressure, by analogy to the pore-scale capillary pressure defined by Eq. (2.3). The capillary pressure at the Darcy scale is assumed to be a function of the water saturation:

$$p_\mathrm{a} - p_\mathrm{w} = p_\mathrm{c}(S_\mathrm{w})\ . \tag{2.13}$$

In hydrophilic porous media the capillary pressure is always nonnegative. If the pore air pressure is constant, p_c increases with decreasing water saturation, while the water pressure potential decreases correspondingly. This is caused by the fact that as the water saturation decreases, the relative amount of water molecules bound by strong short range forces to the solid surface increases.

There are important differences between the pore-scale and Darcy-scale capillary pressure. According to Eq. (2.3), the pressure is larger in the fluid occupying the concave side of the interface. Therefore, from the pore scale point of view, the water pressure is lower than the air pressure in pendular rings or in capillary tubes, but it is higher

than the air pressure in the thin water layers around spherical solid grains, or around occluded air bubbles. However, in each of these situations the Darcy-scale capillary pressure is defined as a nonnegative value. Due to this discrepancy, some authors prefer to use the term suction potential, instead of the capillary potential, and the term matric potential, instead of the water pressure in the unsaturated zone, e.g. [58]. Indeed, the values of the water pressure potential at low saturations, measured with respect to the atmospheric pressure, are often well below −100 kPa, which would indicate negative absolute pressures. In this work, the terms capillary pressure and water pressure are used, with a full recognition of the fact that in unsaturated conditions they refer to the average energy state of water within a representative elementary volume, rather than the physical pressure in the liquid water.

2.1.4 Capillary Function

The relationship between Darcy-scale capillary pressure and water saturation is known under a number of names, such as the capillary function, suction function, retention function, or soil water characteristic function [41, 48, 58, 63]. Figure 2.4 presents its basic features, in relation to various configurations of air and water in a porous medium. Usually, if the medium is fully water-saturated, it can be invaded by the air phase only if the air pressure exceeds the water pressure by a specific value. The corresponding value of p_c is called air-entry pressure or bubbling pressure [41, 58]. This effect can be explained if the medium is conceptualized as a bundle of capillary tubes. According to the Laplace law, Eq. (2.3), all tubes remain saturated, if the water pressure is lower than the pressure of the surrounding air, but the capillary pressure $(p_a - p_w)$ does not exceed the maximum possible value for the largest tube. After this value has been exceeded, the largest tube drains and the overall saturation of the system becomes smaller than one. In natural porous media the value of the air entry pressure corresponds to the diameter of the largest pore forming a connected path through the system. The air entry pressure is more often observed in granular media with relatively uniform grain size, and may be not pronounced in fine-textured media [41]. Above the value of the air entry pressure, the water saturation decreases with the increasing value of the capillary potential. The slope of the curve is determined by the uniformity of the size of pores. If the pores have very similar size, most of them drain quickly above the entry pressure and the slope of the curve is very steep. If the pores show large variability in size, at each increment of the potential only a small part of the pores will be drained, and the decrease in saturation is much more gradual. At some point, the value of the residual water saturation is reached, and further liquid flow is inhibited by the lack of connectivity of the pendular capillary water. The saturation can be further decreased by evaporation, but this requires very large increments of the potential. The capillary pressure can be related to the air relative humidity by the Kelvin equation [58]:

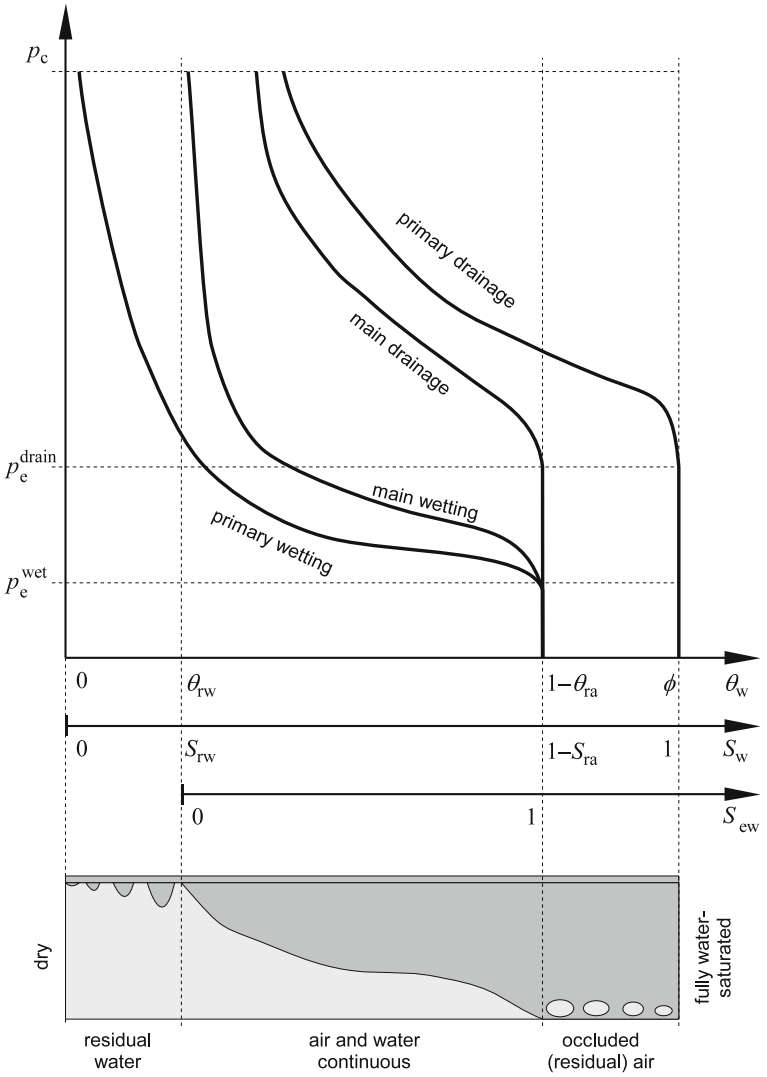

Fig. 2.4 Capillary pressure–water saturation relationship for various air and water flow regimes

$$p_c = -\frac{R_{gas}\,\mathscr{T}\,\rho_w}{\mathscr{M}_w}\ln(\mathscr{H})\ , \tag{2.14}$$

where R_{gas} is the universal gas constant $\left(R_{gas} = 8.31\,\mathrm{J\,mol^{-1}\,K^{-1}}\right)$, $\mathscr{T}$ is the Kelvin temperature, $\mathscr{M}_w$ is the mole mass of water $\left(\mathscr{M}_w = 0.018\,\mathrm{kg\,mol^{-1}}\right)$, and $\mathscr{H}$ is the relative air humidity. For oven dry conditions the potential value of about 10^6 kPa is

reported in the literature, which corresponds to the relative air humidity of 0.01 % [21, 45].

It is important to note that the capillary pressure–saturation relationship shows hysteresis and depends on the history of the flow. The drying process described above corresponds to the so-called primary drainage curve. A complementary relationship, i.e. the primary imbibition curve, can be obtained by increasing the water saturation, starting from oven-dry conditions. During imbibition the values of the capillary potential corresponding to a given water saturation are smaller than during the primary drainage. Moreover, it is in general not possible to reach full water saturation during imbibition, due to the trapping of air bubbles. The maximum possible water saturation $1 - S_{\mathrm{ra}}$ can be achieved for a value of the capillary potential larger than zero. This value is the counterpart of the air-entry pressure at the primary drainage curve, and is sometimes called the water-entry pressure [41]. As the latter term has also other meanings, in this work the term air-entry pressure, or simply entry pressure is consistently used for the characteristic value of the capillary pressure above which air flow is possible, in relation to both imbibition and drainage. The entry pressure at the imbibition curve is smaller than at the drainage curve, and sometimes does not appear at all, i.e. the maximum saturation is reached only at $p_{\mathrm{c}} = 0$. In many practical problems the water saturation varies between the residual value S_{rw} and the maximum value $1 - S_{\mathrm{ra}}$. The drainage process from $1 - S_{\mathrm{ra}}$ to S_{rw} is described by the main drainage curve, while the corresponding imbibition process by the main imbibition (or wetting) curve. If the flow direction is reversed before the limit saturation is reached, the capillary pressure and saturation follow a so-called scanning curve, which is a path in the area enclosed by the main curves.

The hysteresis is usually explained by the variations in the value of the wetting angle between advancing and receding fluid at the solid surface, by the pore-scale trapping of air and by the ink-bottle effect, e.g. [41, 63]. The latter one is related to the fact that during imbibition the possibility of capillary flow is controlled by the widest cross-section of the pore, while during drainage it is controlled by the smallest cross-section. In this work the hysteresis of the capillary function at the Darcy scale is not considered. However, in Chap. 7 it will be shown that a quasi-hysteresis may occur in the field-scale capillary function for a porous medium that shows a specific heterogeneous structure at the Darcy scale.

For practical purposes it is convenient to express the capillary function, for either imbibition or drainage, as an analytical function. A large number of such analytical formulae can be found in the literature. In this section only the ones used in the following part of this book are presented. For a more detailed reviews of various propositions, see [38, 43, 45]. Typically, the formulae are expressed in terms of the normalized water saturation, Eq. (2.9). The choice of the parameters $S_{\mathrm{w}}^{\mathrm{min}}$ and $S_{\mathrm{w}}^{\mathrm{max}}$ depends on the problem under consideration. For the primary drainage with subsequent drying $S_{\mathrm{w}}^{\mathrm{max}} = 1$ and $S_{\mathrm{w}}^{\mathrm{min}} = 0$, for the primary imbibition $S_{\mathrm{w}}^{\mathrm{max}} = 1 - S_{\mathrm{ra}}$ and $S_{\mathrm{w}}^{\mathrm{min}} = 0$, while for the main drainage and imbibition curves $S_{w}^{\mathrm{max}} = 1 - S_{\mathrm{ra}}$ and $S_{\mathrm{w}}^{\mathrm{min}} = S_{\mathrm{rw}}$.

For the sake of consistency all the following functions have the capillary pressure p_{c} as their argument. In fact some of them were originally written in terms of the

capillary pressure head h_c. Transition to the pressure head based form is straightforward and requires only that the parameters p_e and p_g are replaced by the corresponding pressure heads.

One of the most often used analytical models, proposed by Brooks and Corey [7], can be written in the following form:

$$S_{ew} = \begin{cases} (p_c/p_e)^{-n_b} & \text{if} \quad p_c > p_e \\ 1 & \text{if} \quad p_c \le p_e \end{cases} , \tag{2.15}$$

$$p_c = p_e \, (S_{ew})^{-1/n_b} , \tag{2.16}$$

where p_e is the air-entry pressure and n_b is a parameter related to the pore-size distribution, generally ranging from 0.2 to 5. Large values of n_b correspond to a rapid decrease of the saturation above the entry pressure, which is typical for media having uniformly sized pores. Smaller values of n_b characterize media with non-uniform pore size distributions. This model is useful for porous media having a distinct air entry pressure and relatively uniform pore sizes, however it cannot reproduce the inflection point in the capillary function, characteristic for many finely textured soils [41].

Another well-known model, introduced by van Genuchten [79], has the following form:

$$S_{ew} = \left[1 + (p_c/p_g)^{n_g}\right]^{-m_g} , \tag{2.17}$$

$$p_c = p_g \left[(S_{ew})^{-1/m_g} - 1\right]^{1/n_g} , \tag{2.18}$$

where p_g is a pressure scaling parameter, related to the average size of the pores (in the original paper its inverse $\alpha_g = 1/p_g$ was used). The value of p_g approximately corresponds to the position of the inflection point at the capillary curve described by Eq. (2.17). The exponents m_g and n_g are related to the pore size distribution, and in principle can be considered as independent of each other. However, in order to reduce the number of independent parameters, and to develop analytical formulae for the relative permeability (discussed later in Sect. 2.1.6), it is often assumed that $m_g = 1 - 1/n_g$ or $m_g = 1 - 2/n_g$. The van Genuchten function does not account explicitly for the air-entry pressure, although for some values of n_g and m_g saturations very close to unity can be obtained for a certain range of the capillary pressures above zero. Some authors proposed to introduce the air-entry pressure as an additional explicit parameter in the van Genuchten model [34, 81]. In the special case of $m_g = 1$ the van Genuchten function reduces to the Gardner function [23]:

$$S_{ew} = \frac{1}{1 + \left(p_c/p_g\right)^{n_g}} , \tag{2.19}$$

$$p_c = p_g \, (S_{ew} - 1)^{1/n_g} . \tag{2.20}$$

Table 2.1 Parameters of the van Genuchten ($m_g = 1-1/n_g$) and Brooks–Corey capillary functions for various types of soil (van Genuchten function parameters from [10])

	p_g (Pa)	n_g (–)	p_e (Pa)	n_b (–)	θ_{sw} (–)	θ_{rw} (–)	K_{sw} ($m\,s^{-1}$)
sand	677	2.68	440	1.124	0.43	0.045	8.25E−5
loamy sand	791	2.28	498	0.908	0.41	0.057	4.05E−5
sandy loam	1308	1.89	814	0.908	0.41	0.065	1.23E−5
loam	2725	1.56	1779	0.719	0.43	0.078	2.89E−6
silt	6131	1.37	4462	0.710	0.46	0.034	6.94E−7
clay	12263	1.09	12203	0.090	0.38	0.068	5.56E−7

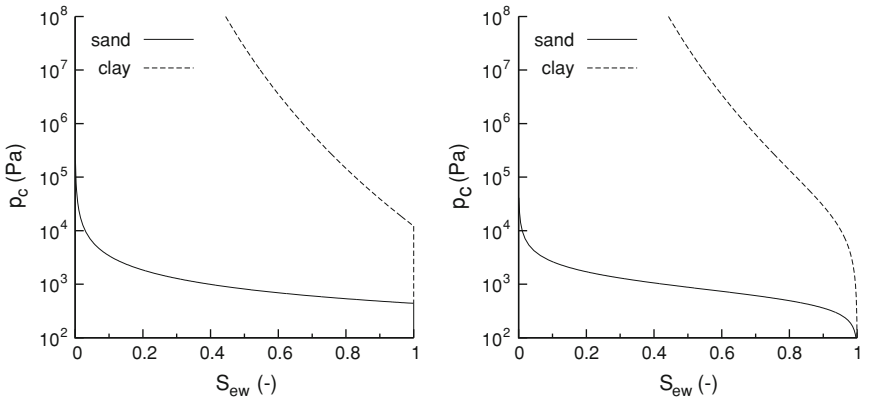

Fig. 2.5 Typical capillary functions for sand and clay

Lenhard et al. [44] established analytical relationships between the parameters of Brooks–Corey function and van Genuchten function (with $m_g = 1 - 1/n_g$) for the same porous material, based on the slope of the curves at normalized saturation equal to 0.5. They are given by the following formulae:

$$n_b = (n_g - 1)\left(1 - 0.5^{n_g/(n_g-1)}\right), \tag{2.21}$$

$$Z_s = 0.72 - 0.35\,\exp\left(-(n_g)^4\right), \tag{2.22}$$

$$p_e = p_g\,(Z_s)^{1/n_b}\left[(Z_s)^{n_g/(1-n_g)} - 1\right]^{1/n_g}, \tag{2.23}$$

where Z_s is an auxiliary parameter. Typical values of the parameters of the van Genuchten and Brooks–Corey models for several types of soil are listed in Table 2.1. The van Genuchten function parameters were taken from [10]. The corresponding Brooks–Corey function parameters were calculated using the above formulae. Figure 2.5 shows the capillary functions for sand and clay, according to both models.

A relatively simple exponential formula is often used in the development of analytical solutions for the Richards equation, e.g. [3, 68]:

$$S_{\mathrm{ew}} = \begin{cases} \exp\left(-\dfrac{p_{\mathrm{c}} - p_{\mathrm{e}}}{p_{\mathrm{g}}}\right) & \text{if} \quad p_{\mathrm{c}} > p_{\mathrm{e}} \\ 1 & \text{if} \quad p_{\mathrm{c}} \leq p_{\mathrm{e}} \end{cases} , \tag{2.24}$$

$$p_c = p_{\mathrm{e}} - p_{\mathrm{g}} \ln(S_{\mathrm{ew}}) , \tag{2.25}$$

where p_{e} is the air entry pressure and p_{g} is a pressure scaling parameter. This formula can be considered as a complementary relationship to the Gardner exponential relative permeability function (introduced later in Sect. 2.1.6).

Note that all the above formulae predict infinite value of the capillary pressure as the normalized saturation approaches zero, which is not consistent with the fact mentioned earlier, that even for oven-dry conditions the capillary pressure has a finite value of about 10^6 kPa. Therefore, Eqs. (2.15)–(2.24) should be considered valid only in the range of normalized water saturations significantly larger than zero. For the dry range the capillary functions should be appropriately modified, to ensure a finite value of the capillary pressure at zero water saturation [21, 37].

2.1.5 Darcy Equation

At the pore scale, the momentum conservation principle for each fluid phase is represented by the Navier-Stokes equations. In the case of steady, laminar flow of incompressible newtonian fluid α in a horizontal tube having a uniform circular cross-section, the Navier-Stokes equations reduce to the Poiseuille equation, which gives the following formula for the average fluid velocity v_α [4]:

$$v_\alpha = -\frac{r_{\mathrm{c}}^2}{8\,\mu_\alpha} \frac{\mathrm{d}\,p_\alpha}{\mathrm{d}\,x} , \tag{2.26}$$

where r_{c} is the tube radius and μ_α is the dynamic viscosity coefficient of the fluid. An important feature of this relationship is that the average velocity is directly proportional to the pressure gradient, and the proportionality coefficient depends on the geometric parameters and the fluid viscosity. In a more general case of three-dimensional single-phase fluid flow in a medium characterized by arbitrary pore geometry, a mathematically rigorous averaging of the pore scale Navier-Stokes equations yields the following result, e.g. [2, 4, 28, 86]:

$$\mathbf{v}_\alpha = -\frac{\mathsf{k}_{\mathrm{s}}}{\mu_\alpha} \left(\nabla p_\alpha - \rho_\alpha\, \mathbf{g}\right) , \tag{2.27}$$

where k_s is the absolute (or intrinsic) permeability tensor and $\mathbf{g}$ is the gravity vector. Intrinsic permeability has dimension of m^2 and depends only on the geometric characteristics of the pores. Its value can be computed for a given geometry of pores, by solving Stokes equations in a representative elementary volume [77]. Alternatively, it can be estimated using many empirical or semi-empirical formulae, developed particularly for granular media, for instance those proposed by Hazen or Kozeny and Carman [39, 82]. For practical purposes, however, the most reliable estimation of permeability is obtained from laboratory or field measurements. Equation (2.27) was derived from the pore-scale flow equations by several authors, e.g. [4, 28, 86]. The most important assumptions introduced in the derivation of Eq. (2.27) can be summarized as follows [31]:

- Inertial effects are neglected, i.e. quasi-steady fluid flow is assumed.
- The flow is laminar.
- The viscous part of the stress tensor in fluid behaves according to the Newton law.

Equation (2.27) can be rewritten it terms of the hydraulic head as:

$$\mathbf{v}_\alpha = -\frac{\mathsf{k}_s\, \rho_\alpha\, g}{\mu_\alpha} \nabla H_\alpha = -\mathsf{K}_{s\alpha}\, \nabla H_\alpha \ , \tag{2.28}$$

where $\mathsf{K}_{s\alpha}$ is the hydraulic conductivity tensor for single-phase flow, which depends on the properties of porous medium and the pore fluid. Equations (2.27) and (2.28) represent an extension to three dimensions of the linear flow law, which was established experimentally for the one-dimensional case by Darcy [14]. The head-based form of the Darcy formula is often used in groundwater flow simulations, when the variations of fluid density and viscosity are negligible, and the hydraulic conductivity with respect to water K_{sw} can be considered constant.

If two fluids flow within the pore space, it is often assumed that their velocities can be expressed by the following extended form of the Darcy formula, e.g. [63]:

$$\mathbf{v}_\alpha = -\frac{\mathsf{k}_\alpha\,(S_\alpha)}{\mu_\alpha} \left(\nabla p_\alpha - \rho_\alpha\, \mathbf{g}\right) = -\mathsf{K}_\alpha\,(S_\alpha)\ \nabla H_\alpha \ , \tag{2.29}$$

where k_α and K_α are permeability and conductivity tensors, which depend on the saturation of phase α. In a general case of anisotropic porous medium, the relationship between permeability and saturation will be different for each component of the permeability tensor. However, for practical purposes a simplified relationship is often postulated in the following form:

$$\mathsf{k}_\alpha\,(S_\alpha) = \mathsf{k}_s\, k_{r\alpha}\,(S_\alpha) \ , \tag{2.30}$$

where $k_{r\alpha}$ is a scalar relative permeability coefficient, assuming values from zero to one. The equivalent relationship for the hydraulic conductivity tensor is:

$$\mathsf{K}_\alpha\,(S_\alpha) = \mathsf{K}_{s\alpha}\, k_{r\alpha}\,(S_\alpha) \ , \tag{2.31}$$

The maximum value $k_{r\alpha} = 1$ corresponds to the case of full saturation with fluid phase α. The minimum value $k_{r\alpha} = 0$ occurs when the fluid phase becomes immobilized, which corresponds to the fluid saturations below the residual saturation $S_\alpha \leq S_{r\alpha}$. Alternatively, the extended Darcy formula can be rewritten in the following form:

$$\mathbf{v}_\alpha = -\mathsf{k}_s \, \lambda_\alpha \left(S_\alpha\right) \left(\nabla p_\alpha - \rho_\alpha \, \mathbf{g}\right) \, , \tag{2.32}$$

where $\lambda_\alpha \left(S_\alpha\right) = k_{r\alpha} \left(S_\alpha\right) / \mu_\alpha$ is the phase mobility.

In contrast to Eq. (2.27), the extension of Darcy equation for multiphase flow given by Eq. (2.29) should be considered as purely phenomenological. As shown by several authors, e.g. [1, 29], in the case of two fluid phases a rigorous averaging of pore-scale momentum conservation leads to coupled Darcy-scale equations, where the flow velocity of each phase depends on the potential gradients in both fluid phases. Such results are consistent with the Onsager reciprocity theorem [66]. These limitations notwithstanding, in the present work Eq. (2.29) is assumed to be a valid approximation of two-phase flow in porous media at the Darcy scale.

2.1.6 Relative Permeability Functions

Since the relative permeability of fluid phase α varies from $k_{r\alpha} = 0$ for $S_\alpha = S_{r\alpha}$ to $k_{r\alpha} = 1$ for $S_\alpha = 1$, it can be conveniently represented by a function of the normalized saturation of each phase, as given by Eq. (2.9), assuming $S_\alpha^{\min} = S_{r\alpha}$ and $S_\alpha^{\max} = 1$. However, in order to simplify the model formulation, the capillary function and permeability functions for both fluids are typically defined with respect to the water saturation normalized in the range between $S_w^{\min} = S_{rw}$ and $S_w^{\max} = 1 - S_{ra}$. In such a case, the relative permeability equals unity for the actual fluid saturation smaller than one. In order to keep the physical consistency of the model, k_s is interpreted as the maximum permeability attainable for the considered problem, which can be different for each phase, and is generally smaller than the permeability tensor for single phase flow. In soil hydrology and soil physics the maximum attainable value of the water conductivity:

$$\mathsf{K}_{sw} = \mathsf{k}_s \, \frac{\rho_w \, g}{\mu_w} \, , \tag{2.33}$$

is often referred to as the saturated hydraulic conductivity. However, it corresponds to the state of apparent saturation, with the corresponding volumetric water content θ_{sw} smaller than the porosity ϕ. The formulae for relative permeability presented below can be used in conjunction with various definitions of the normalized water saturation S_{ew}.

Simple power-type relationships between the normalized saturation and the relative permeabilities are often postulated, e.g. [42, 63]:

$$k_{rw} = \left(S_{ew}\right)^{\eta_w} \, , \tag{2.34}$$

$$k_{ra} = \left(1 - S_{ew}\right)^{\eta_a} \, , \tag{2.35}$$

Table 2.2 Parameters used in Burdine and Mualem relative permeability models

	κ	η_1	η_2	η_3	η_4
Mualem	0.5	1.0	2.0	$2.5 + 2.0/n_{bc}$	$1.0 + 1.0/n_{bc}$
Burdine	2.0	2.0	1.0	$3.0 + 2.0/n_{bc}$	$1.0 + 2.0/n_{bc}$

where the exponents η_w and η_a are fitting parameters. Relationships of this type can be obtained on the theoretical basis, for simple models of laminar flow in bundles of capillary tubes [54]. As it is the wetting fluid, water tends to move along the solid phase surface and preferentially fills smaller pores. Therefore, at the same saturation of each fluid the resistance of the medium to the flow of water is larger than the resistance to the flow of air. Thus, the exponent η_w is typically larger than η_a.

More sophisticated models of the relative permeability are based on the consideration of statistical distribution of the pore size within the medium, and the connectivity between pores of various sizes. The pore size distribution can be computed from the capillary function, due to the inverse relationship between the capillary radius and the capillary pressure, as given by the Laplace law, Eq. (2.3). The connectivity parameter is more difficult to derive theoretically and is often used as a fitting parameter in the resulting model. Two well known statistical models were proposed by Burdine [9] and Mualem [53]. They can be written in the following generalized form:

$$k_{rw}\left(S_{ew}\right) = \left(S_{ew}\right)^{\kappa} \left[\frac{\int_0^{S_{ew}} p_c(\hat{S})^{-\eta_1}\, \mathrm{d}\hat{S}}{\int_0^1 p_c(\hat{S})^{-\eta_1}\, \mathrm{d}\hat{S}} \right]^{\eta_2}, \tag{2.36}$$

$$k_{ra}\left(S_{ew}\right) = \left(1 - S_{ew}\right)^{\kappa} \left[\frac{\int_{S_{ew}}^1 p_c(\hat{S})^{-\eta_1}\, \mathrm{d}\hat{S}}{\int_0^1 p_c(\hat{S})^{-\eta_1}\, \mathrm{d}\hat{S}} \right]^{\eta_2}, \tag{2.37}$$

where $\hat{S}$ denotes the integration variable and the values of the connectivity parameter κ and the exponents η_1 and η_2 are listed in Table 2.2.

In a general case the application of these models to an arbitrary $p_c(S_{ew})$ function requires numerical integration. In some cases, however, the integrals can be evaluated analytically. In particular, it is possible for the Brooks–Corey capillary function, for which the following formulae are obtained:

$$k_{rw}\left(S_{ew}\right) = \left(S_{ew}\right)^{\eta_3}, \tag{2.38}$$

$$k_{rw}\left(S_{ew}\right) = \left(1 - S_{ew}\right)^{\kappa} \left[1 - \left(S_{ew}\right)^{\eta_4}\right]^{\eta_2}, \tag{2.39}$$

where the exponents η_3 and η_4 are given in Table 2.2. Note that the relative permeability of the water phase is given by a simple power law, similarly as in Eq. (2.34). In the case of van Genuchten capillary function, the Mualem formula can be integrated analytically if $m_g = 1 - 1/n_g$, leading to the following result:

$$k_{\mathrm{rw}}(S_{\mathrm{ew}}) = S_{\mathrm{ew}}^{\kappa}\left[1-\left(1-(S_{\mathrm{ew}})^{1/m_{\mathrm{g}}}\right)^{m_{\mathrm{g}}}\right]^2, \tag{2.40}$$

$$k_{\mathrm{ra}}(S_{\mathrm{ew}}) = (1-S_{\mathrm{ew}})^{\kappa}\left[1-(S_{\mathrm{ew}})^{1/m_{\mathrm{g}}}\right]^{2m_{\mathrm{g}}}. \tag{2.41}$$

In general, the connectivity factor κ can be treated as a fitting parameter of the model. Improved agreement with laboratory measurements was reported for negative values ranging from -1.28 for sands to -5.96 for clays [69]. The value of $\kappa = 1/3$ was suggested for the non-wetting phase relative permeability [49].

The Burdine approach provides a closed-form analytical result for the van Genuchten capillary function if $m_{\mathrm{g}} = 1 - 2/n_{\mathrm{g}}$:

$$k_{\mathrm{rw}}\,(S_{\mathrm{ew}}) = S_{\mathrm{ew}}^{\kappa}\left[1-\left(1-(S_{\mathrm{ew}})^{1/m_{\mathrm{g}}}\right)^{m_{\mathrm{g}}}\right], \tag{2.42}$$

$$k_{\mathrm{ra}}\,(S_{\mathrm{ew}}) = (1-S_{\mathrm{ew}})^{\kappa}\left[1-(S_{\mathrm{ew}})^{1/m_{\mathrm{g}}}\right]^{m_{\mathrm{g}}}. \tag{2.43}$$

All the above formulae can be rearranged using the relevant analytical expressions for $S_{\mathrm{ew}}(p_{\mathrm{c}})$ functions, in order to express the relative permeability of each phase as a function of the capillary pressure. Typical relative permeability functions for sand and clay according to Brooks–Corey–Burdine and van Genuchten–Mualem models are shown in Fig. 2.6. Parameters of the porous media are taken from Table 2.1. Significant differences between the two models are observed for clay. The van Genuchten–Mualem model predicts a rapid decrease of the relative water permeability and a rapid increase of the relative air permeability as the capillary pressure increases only slightly from 0 to 100 Pa, which is inconsistent with the fact that the water saturation in this range remains virtually constant and very close to 1. The reason for this discrepancy is related to the integrals in formulae (2.36) and (2.37), where, in the absence of the air-entry pressure, the inverse of the capillary pressure tends to infinity as the water saturation tends to one. As a remedy, introduction of the air-entry pressure as an additional parameter in the van Genuchten model is recommended [34, 81].

Some empirical models define the relative permeability directly as a function of the capillary pressure. Such approaches are typically used for the Richards equation, where the assumption of constant air pressure allows to express the relative water permeability as a function of the water pressure only. To this group belongs the widely used exponential formula, originally suggested by Gardner [23] and modified by Philip [61]:

$$k_{\mathrm{rw}}(p_{\mathrm{c}}) = \begin{cases} \exp\left(-\dfrac{p_{\mathrm{c}}-p_{\mathrm{e}}}{p_{\mathrm{g}}}\right) & \text{if} \quad p_c > p_e \\ 1 & \text{if} \quad p_{\mathrm{c}} \le p_{\mathrm{e}} \end{cases}, \tag{2.44}$$

where p_{e} and p_{g} have the same meaning as in Eq. (2.24). Another well-known formula was also proposed by Gardner [23]:

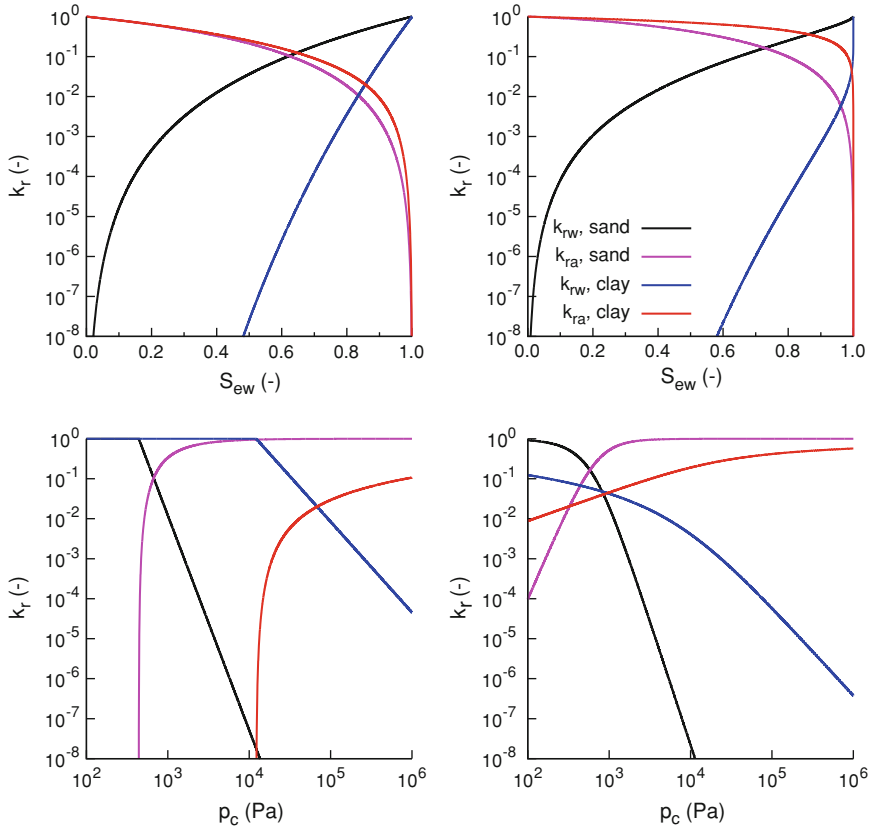

Fig. 2.6 Typical relative permeability functions for sand and clay according to Brooks–Corey–Burdine model (*left*) and van Genuchten–Mualem model (*right*). At the *top* $k_r(S_{ew})$ functions, at the *bottom* $k_r(p_c)$ functions

$$k_{rw}(p_c) = \frac{1}{1 + \left(p_c / p_g\right)^{\eta_w}} \,. \tag{2.45}$$

The above analytical expression has the same form as the formula for the capillary function in Eq. (2.19). Equations (2.44) and (2.45) can be alternatively expressed in terms of the capillary pressure head.

2.1.7 Density and Viscosity of Fluids

In general, the density of the water phase depends on the temperature, pressure and the concentration of dissolved substances. For pure water in isothermal conditions, the dependence of density on the pressure can be expressed as follows [31]:

$$\rho_{\mathrm{w}}(p_{\mathrm{w}}) = \rho_{\mathrm{w}}^{\mathrm{ref}} \exp\left[\beta_{\mathrm{w}}\left(p_{\mathrm{w}} - p_{\mathrm{w}}^{\mathrm{ref}}\right)\right] , \tag{2.46}$$

where $\rho_{\mathrm{w}}^{\mathrm{ref}}$ is the reference water density (1000 kg m^{-3} at 20 °C), $p_{\mathrm{w}}^{\mathrm{ref}}$ is the standard atmospheric pressure (101325 Pa) and β_{w} is the isothermal relative compressibility coefficient. For the range of temperatures from 10 to 50 °C and pressures from 0 to 10^6 Pa, β_{w} is approximately constant and equal to 4.5×10^{-10} Pa^{-1}. This value of β_{w} corresponds to a change of density of approximately 0.5 kg m^{-3}, if the pressure changes by 10^6 Pa.

While in many practical applications water is considered incompressible, its compressibility is included in this work, in order to keep consistency in the presentation of the governing equations for both fluid phases, and in order to maintain parabolic character of the governing equation for the water flow in fully saturated rigid porous medium. Application of the above formula is questionable for unsaturated conditions, where p_{w} is a measure of the energy potential rather than the actual pressure of the water phase and assumes very large negative values [25]. In the examples considered in this work the values of p_{w} do not fall below -10^6 Pa, and the discrepancy is neglected. Similarly to the density, the viscosity of water depends on the temperature, pressure and chemical composition. For the purposes of the present analysis, these dependencies are neglected, and a constant value of water viscosity is assumed $\mu_w = 10^{-3}$ Pa s, which corresponds to the temperature of 20 °C.

The density of dry air can be obtained from the ideal gas law [31]:

$$\rho_{\mathrm{a}} = \frac{\mathscr{M}_{\mathrm{a}}\, p_{\mathrm{a}}}{R_{\mathrm{gas}}\, \mathscr{T}} = c_{\mathrm{a}}\, p_{\mathrm{a}} , \tag{2.47}$$

where p_{a} is the air pressure, $\mathscr{M}_{\mathrm{a}}$ is the molecular mass of air (0.0029 kg mol^{-1}), R_{gas} is the universal gas constant (8.314 J mol^{-1} K^{-1}), $\mathscr{T}$ is temperature in degrees Kelvin and c_{a} is the absolute compressibility coefficient for air. In the temperature of 20 °C = 293.16 °K and at the normal atmospheric pressure the density of dry air is $\rho_{\mathrm{a}} = 1.206$ kg m^{-3}. The density of pore air varies according to the changes in the content of water vapour, but this effects are neglected in the present work. The viscosity of air is assumed constant and equal to $\mu_{\mathrm{a}} = 1.83 \times 10^{-5}$ Pa s.

2.2 Governing Equations for Fluid Flow

2.2.1 Two-Phase Flow

The governing equations for two-phase flow in a porous medium are derived from the mass conservation principle, applied to a Darcy-scale representative elementary volume, as shown in Fig. 2.3. In the absence of source/sink terms, the change in the total mass of fluid phase α inside the REV must be balanced by the total mass flux across the REV boundary. For a rigid solid phase this can be written as:

$$\frac{\partial}{\partial t} \int\limits_{U} \rho_\alpha \, S_\alpha \, \phi \, \mathrm{d}U = \int\limits_{\partial U} \rho_\alpha \, \mathbf{v}_\alpha \, \mathbf{n}_U \, \mathrm{d}\partial U \ , \tag{2.48}$$

where ∂U is the boundary of the REV and $\mathbf{n}_U$ is a unit vector normal to ∂U and directed outwards. Using the Gauss-Ostrogradski theorem and assuming immovable REV boundaries, Eq. (2.48) can be transformed to a differential (strong) form:

$$\frac{\partial}{\partial t} \left(\rho_\alpha \, S_\alpha \, \phi \right) + \nabla \left(\rho_\alpha \, \mathbf{v}_\alpha \right) = 0 \ . \tag{2.49}$$

The velocity of each fluid phase with respect to the solid phase is given by the extended Darcy formula, Eq. (2.29). Substitution of the Darcy equation into the mass balance equation for each phase results in the following system of two coupled partial differential equations:

$$\frac{\partial}{\partial t} \left(\rho_\mathrm{w} \, S_\mathrm{w} \, \phi \right) - \nabla \left[\frac{\rho_\mathrm{w} \, \mathbf{k}_\mathrm{s} \, k_\mathrm{rw}}{\mu_\mathrm{w}} \left(\nabla \, p_\mathrm{w} - \rho_\mathrm{w} \, \mathbf{g} \right) \right] = 0 \ , \tag{2.50}$$

$$\frac{\partial}{\partial t} \left(\rho_\mathrm{a} \, S_\mathrm{a} \, \phi \right) - \nabla \left[\frac{\rho_\mathrm{a} \, \mathbf{k}_\mathrm{s} \, k_\mathrm{ra}}{\mu_\mathrm{a}} \left(\nabla \, p_\mathrm{a} - \rho_\mathrm{a} \, \mathbf{g} \right) \right] = 0 \ . \tag{2.51}$$

Using the chain differentiation rule the storage term for each phase can be expanded to show explicitly the contributions related to the fluid compressibility and saturation change:

$$\begin{aligned} \frac{\partial}{\partial t} \left(\rho_\alpha \, S_\alpha \, \phi \right) &= S_\alpha \, \phi \, \frac{\partial \, \rho_\alpha}{\partial \, t} + \rho_\alpha \, \phi \, \frac{\partial \, S_\alpha}{\partial \, t} \\ &= S_\alpha \, \phi \, c_\alpha \, \frac{\partial \, p_\alpha}{\partial \, t} + \rho_\alpha \, \phi \, \frac{\partial \, S_\alpha}{\partial \, t} \ , \end{aligned} \tag{2.52}$$

where $c_\alpha = \mathrm{d}\rho_\alpha / \mathrm{d}p_\alpha$ is the compressibility coefficient for phase α. For water $c_\mathrm{w} = \rho_\mathrm{w} \, \beta_\mathrm{w}$. For air c_a is defined by Eq. (2.47). In order to obtain a closed system, one has to make use of the additional relationships discussed in the previous sections. The air saturation is uniquely defined by the water saturation (or vice versa), Eq. (2.8). The water saturation is a function of the capillary pressure, i.e. the difference between the air and water pressures, Eq. (2.13). The relative permeabilities depend on the fluid saturations, and the densities on the fluid pressures, Eqs. (2.46)–(2.47). As a result, a system of two equations with two unknowns is obtained.

Several possibilities exist with respect to the choice of the primary unknown variables. For instance, one can choose the two pressures, p_a and p_w, and compute the capillary pressure and the corresponding fluid saturations accordingly. However, such a formulation is not suitable for the numerical solution, when the air phase disappears completely from the porous medium. In such a situation, the derivatives of the discrete form of the air flow equation are equal to zero. Therefore, it is recommended to choose one of the fluid pressures and one of the saturations as the primary unknowns, e.g.

[31]. As this work focuses on water flow, the water pressure p_w and water saturation S_w are chosen as the primary variables.

Equations (2.50)–(2.51) can be rewritten in order to show explicitly the dependence of each term on the chosen primary variables:

$$\frac{\partial}{\partial t}\left[\rho_w(p_w)\, S_w\, \phi\right] - \nabla\left[\frac{\rho_w(p_w)\, \mathsf{k}_s\, k_{rw}(S_w)}{\mu_w}\left(\nabla p_w - \rho_w(p_w)\, \mathbf{g}\right)\right] = 0\,, \tag{2.53}$$

$$\frac{\partial}{\partial t}\left[\rho_a(p_w, S_w)\,(1 - S_w)\,\phi\right] - \nabla\left[\frac{\rho_a(p_w, S_w)\, \mathsf{k}_s\, k_{ra}(S_w)}{\mu_a}\left(\nabla p_w + \nabla p_c(S_w) - \rho_a(p_w, S_w)\, \mathbf{g}\right)\right] = 0\,. \tag{2.54}$$

If the compressibility of the fluids and the porous medium can be neglected, a simplified form of the governing equations is obtained:

$$\phi\, \frac{\partial S_w}{\partial t} - \nabla\, \mathbf{v}_w = 0\,, \tag{2.55}$$

$$-\phi\, \frac{\partial S_w}{\partial t} - \nabla\, \mathbf{v}_a = 0\,. \tag{2.56}$$

Alternatively, the above equations can be transformed to the fractional flow formulation, e.g. [6]. To this order the mass balance equations are added to each other:

$$\nabla\, (\mathbf{v}_w + \mathbf{v}_a) = \nabla\, \mathbf{v}_t = 0\,, \tag{2.57}$$

where $\mathbf{v}_t = \mathbf{v}_w + \mathbf{v}_a$ is the total fluid velocity. Equation (2.57) can be rewritten in terms of the fractional flow function f_w and the global pressure p_{glob} defined as follows:

$$f_w = \frac{\lambda_w}{\lambda_w + \lambda_a}\,, \tag{2.58}$$

$$p_{glob} = \frac{1}{2}\,(p_w + p_a) - \int_{S_w^{max}}^{S_w} \left(f_w - \frac{1}{2}\right) \frac{\mathrm{d}p_c}{\mathrm{d}S_w}\, \mathrm{d}S_w\,, \tag{2.59}$$

where S_w^{max} is the maximum water saturation, $p_c(S_w^{max}) = 0$. Equation (2.57) then becomes an elliptic one with respect to the global pressure:

$$\nabla\, \left\{\mathsf{k}_t\, \left[\nabla\, p_{glob} - (f_w\, \rho_w + (1 - f_w)\, \rho_a)\, \mathbf{g}\right]\right\} = 0\,, \tag{2.60}$$

where:

$$\mathsf{k}_t = \mathsf{k}_s\, (\lambda_w + \lambda_a)\,. \tag{2.61}$$

Using the definition of the total velocity, the water flux can be expressed as:

$$\mathbf{v}_\mathrm{w} = f_\mathrm{w}\,\mathbf{v}_\mathrm{t} + f_\mathrm{w}\,\lambda_\mathrm{a}\,\mathbf{k}_\mathrm{s}\,\left(\nabla p_\mathrm{c} + (\rho_\mathrm{w} - \rho_\mathrm{a})\,\mathbf{g}\right)\ . \tag{2.62}$$

Inserting Eq. (2.62) into Eq. (2.55) one obtains the following equation for the water saturation:

$$\phi\frac{\partial S_\mathrm{w}}{\partial t} + \nabla\left[f_\mathrm{w}\,\mathbf{v}_\mathrm{t} + f_\mathrm{w}\,\lambda_\mathrm{a}\,\mathbf{k}_\mathrm{s}\,(\rho_\mathrm{w} - \rho_\mathrm{a})\,\mathbf{g} + f_\mathrm{w}\,\lambda_\mathrm{a}\,\mathbf{k}_\mathrm{s}\,\frac{\mathrm{d}p_\mathrm{c}}{\mathrm{d}S_\mathrm{w}}\,\nabla S_\mathrm{w}\right] = 0\ . \tag{2.63}$$

The above equation has the form of an advection-diffusion one. The first two terms in brackets represent the advective transport. The first term corresponds to the viscous forces, while the second to the gravity forces. The diffusive transport, related to the action of capillary forces, is represented by the third term in brackets. If the capillary and gravity effects are neglected, Eq. (2.63) reduces to the Buckley-Leverett equation (nonlinear advection equation), well known in petroleum reservoir engineering literature, e.g. [13, 31]. In the unsaturated zone, the capillary and gravity forces can rarely be neglected, while the full fractional flow formulation poses problems in the implementation of various types of boundary conditions occurring in unsaturated zone modeling [6]. Moreover, in contrast to the phase pressures, the global pressure is not continuous at the interfaces separating porous materials characterized by different capillary functions. The fractional flow formulation is not used in the numerical simulations presented in the following chapters. However, it will be referred to in the discussion of the general properties of two-phase flow model.

2.2.2 Richards Equation

The two-phase model presented in the previous section can be considerably simplified under specific conditions occurring for air and water flow in the unsaturated zone. At the temperature of 20 °C the air viscosity is about 55 times smaller than the water viscosity, which means that the air mobility is greater than the water mobility by approximately the same factor, if the relative permeabilities of both fluids are similar. Therefore, it can be expected that any pressure difference in the air phase will be equilibrated much faster than in the water phase. On the other hand, it can be often assumed that the air phase is continuous in the pore space and that it is connected to the atmosphere. If the variations in the atmospheric pressure are neglected, one can consider the pore air to be essentially at a constant atmospheric pressure. These assumptions allow to eliminate the equation for the air flow from the system of governing Eqs. (2.50)–(2.51). The capillary pressure is now uniquely defined by the water pressure. For convenience it is often assumed that the reference atmospheric pressure $p_\mathrm{atm} = 0$, so one can write:

$$p_\mathrm{c} = p_\mathrm{atm} - p_\mathrm{w} = -p_\mathrm{w}\ . \tag{2.64}$$

Accordingly, the water saturation and the relative water permeability can be defined as functions of the water pressure. For the values of the water pressure smaller than the negative of the air entry pressure, $p_w < -p_e$ (where p_e can be zero if the van Genuchten capillary function is used), the water saturation and permeability can be computed from the analytical models described in Sect. 2.1.4 and 2.1.6, assuming $p_c = -p_w$. For the values of the water pressure which are larger than the negative of the air entry pressure, $p_w > -p_e$, the water saturation and water permeability are constant and equal to their maximum values.

The remaining equation for the water flow becomes:

$$\frac{\partial}{\partial t}\left(\rho_w \phi S_w(p_w)\right) - \nabla\left[\frac{\rho_w(p_w)\,\mathsf{k}_s\,k_{rw}(p_w)}{\mu_w}\left(\nabla p_w - \rho_w(p_w)\,\mathbf{g}\right)\right] = 0\,. \quad (2.65)$$

Taking into account Eq. (2.52) the storage term can be rewritten as:

$$\frac{\partial}{\partial t}\left(\rho_w \phi S_w\right) = \phi S_w \rho_w \beta_w \frac{\partial p_w}{\partial t} + \rho_w \phi \frac{\partial S_w}{\partial p_w}\frac{\partial p_w}{\partial t}\,. \quad (2.66)$$

Additionally, it is often assumed that the spatial gradients of the water density are negligible:

$$\nabla\left(\rho_w \mathbf{v}_w\right) \approx \rho_w \nabla \mathbf{v}_w\,.$$

Consequently, both sides of equation can be divided by ρ_w and one arrives at the following form:

$$C_{wp}(p_w)\frac{\partial p_w}{\partial t} - \nabla\left[\frac{\mathsf{k}_s\,k_{rw}}{\mu_w}\nabla\left(p_w + \rho_w\,\mathbf{g}\right)\right] = 0\,, \quad (2.67)$$

where C_{wp} is a storage coefficient:

$$C_{wp} = \theta_w\,\beta_w + \frac{\mathrm{d}\theta_w}{\mathrm{d}p_w}\,. \quad (2.68)$$

In hydrological and hydrogeological applications, Eq. (2.67) is often written in terms of the water pressure head:

$$C_{wh}(h_w)\frac{\partial h_w}{\partial t} - \nabla\left[\mathsf{K}_{sw}\,k_{rw}(h_w)\nabla\left(h_w + z\right)\right] = 0\,, \quad (2.69)$$

where $C_{wh} = \rho_w\,g\,C_{wp}$. Accordingly, the capillary and relative permeability functions are defined in terms of the capillary pressure head, which is equal to the negative water pressure head. Equations (2.67) and (2.69) describe transient water flow in both saturated and unsaturated conditions and are sometimes called generalized Richards equation.

By further neglecting the water compressibility one arrives at the following equation:

$$C_{\mathrm{ch}}(h_{\mathrm{w}})\,\frac{\partial h_{\mathrm{w}}}{\partial t} - \nabla\left[\mathsf{K}_{\mathrm{sw}}\,k_{\mathrm{rw}}(h_{\mathrm{w}})\nabla\,(h_{\mathrm{w}}+z)\right] = 0\,, \tag{2.70}$$

where the storage coefficient accounts only for the changes in water saturation:

$$C_{\mathrm{ch}}(h_{\mathrm{w}}) = \phi\,\frac{\mathrm{d}S_{\mathrm{w}}}{\mathrm{d}h_{\mathrm{w}}} = \frac{\mathrm{d}\theta_{\mathrm{w}}}{\mathrm{d}h_{\mathrm{w}}}\,. \tag{2.71}$$

This coefficient is often called specific water (or moisture) capacity, e.g. [85].

Equation (2.70) was originally developed by Richards [65], while the corresponding expression for the water flux in unsaturated conditions:

$$\mathbf{v}_{\mathrm{w}} = -\mathsf{K}_{\mathrm{sw}}\,k_{\mathrm{rw}}(h_{\mathrm{w}})\nabla\,(h_{\mathrm{w}}+z) \tag{2.72}$$

was suggested earlier by Buckingham [8] and is often called Darcy-Buckingham equation, e.g. [55]. In saturated conditions $C_{\mathrm{ch}} = 0$ and Eq. (2.70) degenerates to an elliptic equation describing steady flow. Thus a generalized form of the Richards equation, which includes water compressibility, Eq. (2.69), is preferable if parabolic character of the governing equation is to be retained during transition between saturated and unsaturated states. In geotechnical and hydrogeological applications, Eq. (2.69) is often modified by accounting for the compressibility of the solid skeleton in the storage term $\phi = \phi(p_{\mathrm{w}}, p_{\mathrm{a}})$. These effects are not considered here, as they are not essential for the analyses presented in the following chapters.

Equation (2.70) is often referred to as the pressure-based form of the Richards equation. Alternatively it can be rewritten in the so-called mixed form, which includes explicitly both the water content and the water pressure head:

$$\frac{\partial\theta(h_{\mathrm{w}})}{\partial\,t} - \nabla\left[\mathsf{K}_{\mathrm{sw}}\,k_{\mathrm{rw}}(h_{\mathrm{w}})\,\nabla\,(h_{\mathrm{w}}+z)\right] = 0\,. \tag{2.73}$$

It was shown that the mixed form has better properties with respect to the numerical solution, as it allows to minimize the mass balance error, persistent in the solutions employing the pressure-based form [12]. The third possible form is obtained by replacing the pressure head in all terms of Eq. (2.73) with the water content. To this order the hydraulic diffusivity tensor is introduced:

$$\mathsf{D}(\theta_{\mathrm{w}}) = \frac{\mathrm{d}h_{\mathrm{w}}}{\mathrm{d}\theta_{\mathrm{w}}}\,\mathsf{K}_{\mathrm{sw}}\,k_{\mathrm{rw}}(\theta_{\mathrm{w}})\,, \tag{2.74}$$

so that Eq. (2.73) becomes:

$$\frac{\partial \theta_w}{\partial t} - \nabla \left[\mathsf{D}\,(\theta_w)\,\nabla \theta_w \right] + \mathsf{K}_{sw}\, k_{rw}(\theta_w)\,\nabla z = 0\ . \tag{2.75}$$

Note that the above equation can be obtained as the limit case of the saturation equation in the fractional flow model, Eq. (2.63), assuming that the air phase is much more mobile than the water phase, $\lambda_a \gg \lambda_w$, and that the air phase density is much smaller than the water density $\rho_a \ll \rho_w$. In this case the relevant terms of Eq. (2.63) become:

$$f_w = \frac{\lambda_w}{\lambda_a + \lambda_w} \approx 0\ , \tag{2.76}$$

$$f_w\,\lambda_a = \frac{\lambda_w\,\lambda_a}{\lambda_a + \lambda_w} \approx \lambda_w = \frac{k_{rw}}{\mu_w}\ , \tag{2.77}$$

$$\phi \frac{\partial S_w}{\partial t} = \frac{\partial \theta_w}{\partial t}\ , \tag{2.78}$$

$$f_w\,\mathbf{v}_t \approx 0\ , \tag{2.79}$$

$$f_w\,\lambda_a\,\mathsf{k}_s\,(\rho_w - \rho_a)\,\mathbf{g} \approx \lambda_w\,\mathsf{k}_s\,\rho_w\,\mathbf{g} = -\mathsf{K}_{sw}\,k_{rw}\,\nabla z\ , \tag{2.80}$$

$$f_w\,\lambda_a\,\mathsf{k}_s \frac{\mathrm{d}p_c}{\mathrm{d}S_w}\nabla S_w \approx \lambda_w\,\mathsf{k}_s \frac{\mathrm{d}p_c}{\mathrm{d}S_w}\nabla S_w = -\mathsf{K}_{sw}\,k_{rw} \frac{\mathrm{d}h_w}{\mathrm{d}\theta_w}\nabla \theta_w\ . \tag{2.81}$$

The above assumptions lead to Eq. (2.75).

The water content (or saturation) based form is easier to solve numerically than the mixed or pressure based forms. Due to its similarity to the standard advection-diffusion equation it is often used to obtain analytical or semi-analytical solutions of the Richards equation, especially for one-dimensional flow, where the diffusivity and conductivity coefficients are scalars. The major drawback of the water-content based form is that it becomes indefinite in fully saturated conditions. Additional difficulty arises when the domain under consideration contains porous regions characterized by different capillary functions, because the water content is not continuous at such interfaces (see Sect. 2.3.3).

Yet another form of the Richards equation can be obtained for an isotropic medium using the Kirchhoff transform. The Kirchhoff variable, also called the flux potential can be defined as (e.g. [36, 85]):

$$\Phi_h(h_w) = \int_{-\infty}^{h_w} k_{rw}(\hat{h})\,\mathrm{d}\hat{h}\ , \tag{2.82}$$

where $\hat{h}$ is the integration variable. Using this transformation, the Richards equation can be rewritten as follows:

$$\phi \frac{\mathrm{d}S_\mathrm{w}}{\mathrm{d}\Phi_\mathrm{h}} \frac{\partial \Phi_\mathrm{h}}{\partial t} - \nabla \left(\mathsf{K}_\mathrm{sw} \nabla \Phi_\mathrm{h}\right) + \mathsf{K}_\mathrm{sw} k_\mathrm{rw}(\Phi_\mathrm{h}) \nabla z = 0 \,. \tag{2.83}$$

Alternatively, the flux potential can be also defined with respect to the water pressure as the primary variable:

$$\Phi_\mathrm{p}(p_\mathrm{w}) = \int_{-\infty}^{p_\mathrm{w}} k_\mathrm{rw}(\hat{p})\, \mathrm{d}\hat{p} \,. \tag{2.84}$$

Similarly to the water content, the flux potential is not continuous at material interfaces. Nevertheless, Eq. (2.83) is easier to solve numerically than the mixed and pressure-based forms of the Richards equation, and in contrast to the saturation-based form, can be used for fully saturated conditions. Several authors proposed efficient numerical algorithms based on this form of the Richards equation, e.g. [5, 36, 67]. Moreover, even if the mixed or pressure-based form of the Richards equation is solved, the Kirchhoff transform can be a useful tool to approximate the effective conductivity between the adjacent nodes (see Chap. 4).

While the Richards equation is a widely accepted model for the water flow in unsaturated soils and rocks, one has to be aware of its limitations. For obvious reasons, it cannot be used when there is an explicit interest in the simulation of air flow. Such applications include for example transport of volatile contaminants in the pore air, e.g. [11, 78], or dewatering by means of compressed air used in tunnel construction, e.g. [57]. However, even if the primary interest is in the water flow, the Richards equation can lead to inaccurate results, if one or more of the underlying assumptions is not fulfilled, as pointed out by several studies, e.g. [50, 51, 60, 80, 83, 84].

A number of sources for the possible discrepancies between the Richards model and the full two-phase model can be identified. The first one is related to the viscosity ratio between air and water. Numerical experiments [73] showed that the agreement between results obtained from the Richards equation and from the two-phase model is less than perfect for the water-to-air viscosity ratio smaller than 100. In natural conditions the viscosity of air can be expected to be only about 50 to 60 times smaller than the mobility of water. It should be noted that the phase mobility depends not only on its viscosity, but also on the relative permeability. Thus, further decrease in the mobility ratio can be expected if the relative permeability of air is much smaller than the permeability of water, which occurs as the air saturation approaches the residual value. For instance, it was shown that significant differences arise between the Richards model and the two-phase flow model if the relative permeabilities of water and air are proportional to the fourth power of the respective saturation, even assuming the viscosity ratio of the fluids equal to 100 [19].

The second factor limiting the applicability of the Richards equation is the presence of obstacles, which do not allow the pore air to contact freely with the atmospheric air. Examples of such obstacles include layers of porous media which are quasi-impermeable to air, either because they have very low intrinsic

permeability, or because they are saturated or nearly saturated with water. In this context, inadequacy of the Richards equation was demonstrated for various types of problems, such as infiltration in columns with sealed bottom [74–76], drainage of coarse sand overlaid by a layer of fine sand [40], field-scale infiltration with shallow groundwater table [27], increase of the water level in wells during ponded infiltration [26], or air trapping in flood embankments due to overtopping by flood wave [46]. The flowpaths of the pore air can also be blocked due to heterogeneous structure of the porous medium, especially if coarse-textured inclusions with low air entry pressure are embedded in a fine-textured background having high entry pressure. Such effects are investigated in Chap. 7.

2.2.3 Single-Phase Flow

Single phase flow occurs when the pores are completely filled with only one fluid phase, which in the context of this work is water. Since $S_\mathrm{w} = 1$ and $k_\mathrm{rw} = 1$, the governing equation for the water flow becomes:

$$\frac{\partial}{\partial t}\left(\rho_\mathrm{w}\,\phi\right) - \nabla\left[\frac{\rho_\mathrm{w}\,\mathsf{k}_\mathrm{sw}}{\mu_\mathrm{w}}\left(\nabla\, p_\mathrm{w} - \rho_\mathrm{w}\,\mathbf{g}\right)\right] = 0\,. \tag{2.85}$$

Similarly to the case of the Richards equation, saturated groundwater flow is usually described in terms of the water pressure head. Moreover, the spatial gradients of the water density are neglected, resulting in the following equation:

$$C_\mathrm{sat}\,\frac{\partial h_\mathrm{w}}{\partial t} - \nabla\left[\mathsf{K}_\mathrm{sw}\,\nabla\,\left(h_\mathrm{w} + z\right)\right] = 0\,, \tag{2.86}$$

where the saturated storage coefficient $C_\mathrm{sat} = \rho_\mathrm{w}\,\beta_\mathrm{w}\,g\,\phi$ is approximately constant. The above equation is valid for a rigid solid skeleton. In groundwater aquifers the compressibility of the skeleton is usually more important than the compressibility of water and has to be accounted for in the storage coefficient, e.g. [16].

It is important to note that when porous media are subject to imbibition in natural conditions, the transition from the unsaturated to fully saturated state occurs not directly, but via the occluded air bubble regime. At this stage the Darcy-scale capillary pressure is considered constant and equal to its minimum value ($p_\mathrm{e}^\mathrm{wet}$ in Fig. 2.4, which can be equal to zero in many cases), while the water pressure assumes values above $-p_\mathrm{e}^\mathrm{wet}$. However, the water saturation can further increase due to compressibility of the air bubbles, even though the macroscopic capillary pressure remains equal to zero for positive values of the water pressure. Moreover, the increase of the water saturation causes an increase in the relative permeability. While this effects are often neglected and the water saturation and permeability are assumed to be constant for the whole range of positive water pressures, the additional compressibility of the medium resulting from the presence of air bubbles can be important,

for example when considering soil liquefaction due to rapidly oscillating loading, e.g. [35].

2.3 Auxiliary Conditions

The governing equations for the two-phase (Eqs. (2.50)–(2.51)), unsaturated (Eq. (2.65)) or single-phase (Eq. (2.85)) unsteady flow in porous media are partial differential equations of parabolic type [31, 63]. These equations are solved in the spatial domain W, as shown schematically in Fig. 2.7 and for the time interval $\langle 0, t_{\max} \rangle$. The solution problem should be well-posed, which means that the following conditions are satisfied, e.g. [18, 71]:

- the solution exists,
- the solution is unique,
- the solution depends continuously on the initial and boundary conditions.

In order to obtain a well-posed problem, the initial and boundary conditions must be formulated in an appropriate manner. The initial conditions specify the state of the system at time $t = 0$, while the boundary conditions determine the behaviour of the unknown functions at the external boundaries ∂W of the considered spatial domain. For parabolic equations the boundary conditions can be in general time-dependent. In the case of steady flow, the derivatives with respect to time disappear from the governing equations and the equations become elliptic. For such type of equations, only boundary conditions are required and they are independent of time.

Moreover, porous materials in the solution domain may be heterogeneous with respect to the constitutive parameters and relationships such as the absolute permeability or the capillary and relative permeability functions. In general, one can assume either that the spatial domain is composed of several porous regions separated by internal boundaries (material interfaces), with uniform parameter distribution in each region, or that the parameters are continuously variable in space. In the first case the mathematical formulation must be complemented by additional conditions for the material interfaces, which allow to link the solutions from the neighbouring sub-domains. In the case of continuous distribution, a similar problem arises during numerical solution of the governing equations when spatial discretization is performed and specific material properties are assigned to each element of the grid.

2.3.1 Initial Conditions

The initial state of the system can be defined either in terms of the primary variables, or in terms of other variables, from which the primary ones can be calculated. For two-phase flow in the p_w–S_w formulation, the initial conditions can be specified as:

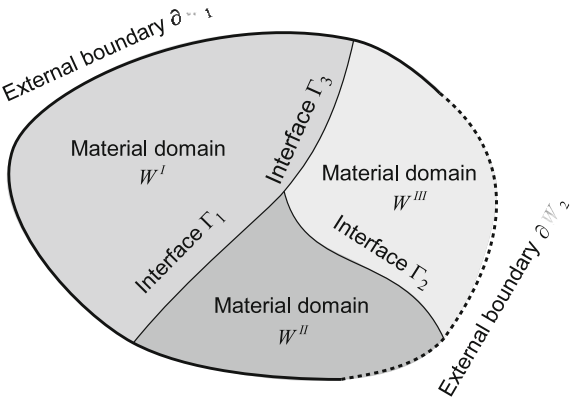

Fig. 2.7 Solution domain for flow equations with external and internal boundaries

$$p_{\mathrm{w}}(\mathbf{x}, t = 0) = p_{\mathrm{w}}^{\mathrm{init}}(\mathbf{x}) \ , \tag{2.87}$$

$$S_{\mathrm{w}}(\mathbf{x}, t = 0) = S_{\mathrm{w}}^{\mathrm{init}}(\mathbf{x}) \ . \tag{2.88}$$

In strictly unsaturated conditions, the initial water pressure can be replaced by the initial air pressure $p_{\mathrm{a}}^{\mathrm{init}}(\mathbf{x})$. However, if part of the domain is fully saturated with water, the air pressure cannot be meaningfully defined. On the other hand, it is also possible to define the initial conditions in terms of the two pressures:

$$p_{\mathrm{w}}(\mathbf{x}, t = 0) = p_{\mathrm{w}}^{\mathrm{init}}(\mathbf{x}) \ , \tag{2.89}$$

$$p_{\mathrm{a}}(\mathbf{x}, t = 0) = p_{\mathrm{a}}^{\mathrm{init}}(\mathbf{x}) \ . \tag{2.90}$$

The water saturation is then computed as $S_{\mathrm{w}}^{\mathrm{init}} = S_{\mathrm{w}}(p_{\mathrm{a}}^{\mathrm{init}} - p_{\mathrm{w}}^{\mathrm{init}})$. For the Richards model, only the initial value of the water pressure is necessary:

$$p_{\mathrm{w}}(\mathbf{x}, t = 0) = p_{\mathrm{w}}^{\mathrm{init}}(\mathbf{x}) \ . \tag{2.91}$$

In strictly unsaturated conditions it is possible to use initial distribution of saturation. The corresponding values of the water pressure are then obtained from the capillary function $p_{\mathrm{w}}^{\mathrm{init}} = -p_{\mathrm{c}}(S_{\mathrm{w}}^{\mathrm{init}})$.

While the initial distribution of the relevant variables can be obtained from measurements, it is common to assume some simple distribution schemes, for example:

- Uniform water and air pressures:

$$p_{\mathrm{w}}(\mathbf{x}, t = 0) = p_{\mathrm{w}}^{\mathrm{init}} \ , \tag{2.92}$$

$$p_{\mathrm{a}}(\mathbf{x}, t = 0) = p_{\mathrm{a}}^{\mathrm{init}} \ , \tag{2.93}$$

$$S_{\mathrm{w}}(\mathbf{x}, t = 0) = S_{\mathrm{w}}(p_{\mathrm{a}} - p_{\mathrm{w}}) \ . \tag{2.94}$$

In a homogeneous medium, uniform pressure distribution implies uniform distribution of the water saturation. In a heterogeneous medium, the values of water saturation will be different in each material region. If the gravity force is present in the system then some initial flow occurs due to the presence of gradient in the gravity potential. Otherwise the system is at equilibrium.

- Uniform water saturation:

$$S_{\mathrm{w}}(\mathbf{x}, t = 0) = S_{\mathrm{w}}^{\mathrm{init}}. \tag{2.95}$$

This condition must be completed by specifying either water or air pressure. Particular attention is required if such a condition is applied to a heterogeneous medium. For fully water saturated domain, a natural choice is to use $S_{\mathrm{w}}^{\mathrm{init}} = 1$ or $S_{\mathrm{w}}^{\mathrm{init}} = 1 - S_{\mathrm{ra}}$ and assume a uniform or hydrostatic distribution of the water pressure. If the medium is characterized by spatially varying entry pressure values, the corresponding distribution of the capillary pressure is discontinuous. On the other hand, in unsaturated conditions it is common to assume a uniform initial value of the air pressure equal to the atmospheric pressure. In this case spatial variability of the capillary function results in a discontinuous initial distribution of the water pressure and implies initial water flow between adjacent material regions.

- Hydrostatic water and air pressure distributions:

$$p_{\mathrm{w}}(\mathbf{x}, t = 0) = p_{\mathrm{w}}^{\mathrm{ref}} + \rho_{\mathrm{w}}\, g\, z \tag{2.96}$$

$$p_{\mathrm{a}}(\mathbf{x}, t = 0) = p_{\mathrm{a}}^{\mathrm{ref}} + \rho_{\mathrm{a}}\, g\, z \tag{2.97}$$

$$S_{\mathrm{w}}(\mathbf{x}, t = 0) = S_{\mathrm{w}}(p_{\mathrm{a}} - p_{\mathrm{w}}) \tag{2.98}$$

This case describes a system in equilibrium. It is often applied if the position of the groundwater table is known. The compressibility effects are assumed unimportant.

- Hydrostatic water pressure and uniform air pressure

$$p_{\mathrm{w}}(\mathbf{x}, t = 0) = p_{\mathrm{w}}^{\mathrm{ref}} + \rho_{\mathrm{w}}\, g\, z \tag{2.99}$$

$$p_{\mathrm{a}}(\mathbf{x}, t = 0) = p_{\mathrm{atm}} \tag{2.100}$$

$$S_{\mathrm{w}}(\mathbf{x}, t = 0) = S_{\mathrm{w}}(p_{\mathrm{a}} - p_{\mathrm{w}}) \tag{2.101}$$

Since the variations in the air pressure due to gravity are relatively small, they are often neglected. If the atmospheric air pressure is assumed everywhere in the domain, the vertical saturation profile above the water table corresponds exactly to the capillary function drawn in S_{w}–h_{c} coordinates. There is some initial air flow, but it is negligibly small.

2.3.2 Boundary Conditions

Boundary conditions provide information about the behaviour of the solution at physical boundaries of the domain. In general three types of the boundary conditions are distinguished, e.g. [63, 87]:

1. Dirichlet boundary conditions specify the values of the solution at a given part of the boundary;
2. Neumann boundary conditions specify the value of the spatial derivative of the solution. In the case of flow in porous media, this type of condition is usually written in terms of the fluid flux in the direction normal to the boundary;
3. Robin boundary conditions, which specify a relationship between the value of solution and its derivative, and can be viewed as a generalization of both Dirichlet and Neumann boundary conditions.

various boundary conditions can be specified on different parts of the domain boundary. For a steady flow problem, described by an elliptic equation, it is necessary to provide Dirichlet boundary conditions on at least one point of the boundary, otherwise the problem becomes ill-posed. For unsteady problems, described by parabolic equations, no such restriction exists. In the case of two-phase flow it is necessary to specify boundary conditions for each phase, and different types of condition can be used for each fluid at the same part of the boundary. Some examples of boundary conditions typically used in unsaturated flow modelling are listed below.

Dirichlet boundary conditions provide values of the pressures and/or saturations of the two fluid phases. They are typically applied when:

- the water pressure is known, e.g.:
  - the boundary corresponds to the groundwater table,
  - the distance between the boundary and the groundwater table is known, and a hydrostatic distribution of the water pressure between them can be assumed,
  - the boundary is in contact with a free water body assumed to be static, e.g. at the waterward slope of a dike or at the soil surface ponded by a water layer,
  - a specific negative value of the water pressure is applied, e.g. during infiltration or drainage experiments in controlled conditions,
- the air pressure is known, e.g. the boundary is exposed to the atmosphere and not fully water saturated,
- the water saturation is known, e.g. the boundary is fully saturated and the air pressure cannot be meaningfully specified,
- the boundary is far away from the region of interest and it can be assumed that the water and air pressures and saturations are constant and equal to the initial ones.

Neumann boundary conditions are typically used when the boundary is impermeable for one or both phases, $\rho_\alpha \, \mathbf{v}_\alpha \, \mathbf{n}_W = 0$, where $\mathbf{n}_W$ is a unit vector normal to the boundary of the domain W. This condition is also used to represent infiltration and evaporation fluxes at the soil surface.

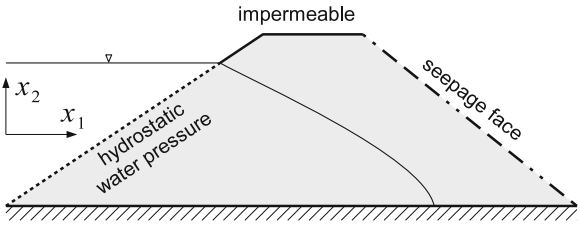

Fig. 2.8 Boundary conditions for a simple case of two-dimensional flow in a dike

Moreover, there are three specific sets of the boundary conditions widely applied in the unsaturated zone modelling. They include the free drainage condition, the seepage face condition and the soil-atmosphere interface condition e.g. [64, 72]. All of them are system-dependent, which means that the imposed value of the pressure of flux depends on the current state of the system. The free drainage condition represents vertical flow of water through the bottom of the soil profile towards a distant groundwater table. It is assumed that the water pressure gradient is zero and only the gravity component contributes to the flow:

$$\mathbf{v}_{\mathrm{w}}\,\mathbf{n}_W = \left(\frac{\rho_{\mathrm{w}}}{\mu_{\mathrm{w}}}\mathsf{k}_{\mathrm{w}}(S_{\mathrm{w}})\,\mathbf{g}\right)\mathbf{n}_W \tag{2.102}$$

Thus, the condition is of Neumann type, but the actual value of the flux depends on the solution at the specific boundary point.

The seepage face is a part of the outer surface of the porous medium which is exposed to the atmosphere and through which water can flow freely out of the porous domain. It typically occurs above the water level in wells and at the bottom of the landward slopes of earth dams or embankments, Fig. 2.8. The seepage face is considered impermeable to water as long as the adjacent part of the porous medium is unsaturated. If the pressure in the medium increases to the value of the atmospheric pressure water flows out freely from the medium and no build-up of positive pressure values is allowed. This is represented by assuming Neumann boundary condition $\mathbf{v}_{\mathrm{w}}\,\mathbf{n}_W = 0$ on the unsaturated part of the boundary and Dirichlet boundary condition $p_{\mathrm{w}} = 0$ on the saturated part. The position of the saturated-unsaturated interface is not known a priori and must be obtained iteratively during the numerical solution.

When modelling the infiltration and evaporation processes at the soil surface, it is often necessary to switch between Neumann and Dirichlet boundary condition, depending on the state of soil surface. During infiltration, at first a specific value of the water flux is applied at the boundary, Fig. 2.9a. As a result of the infiltration the water pressure at the soil surface increases from the initially negative value towards zero (atmospheric pressure). If the applied flux is larger than the soil infiltration capacity (equal to the saturated water conductivity) then positive values of the water pressure appear at the surface, which physically corresponds to the formation of a water layer on the ground surface (ponding). At this point the boundary condition for

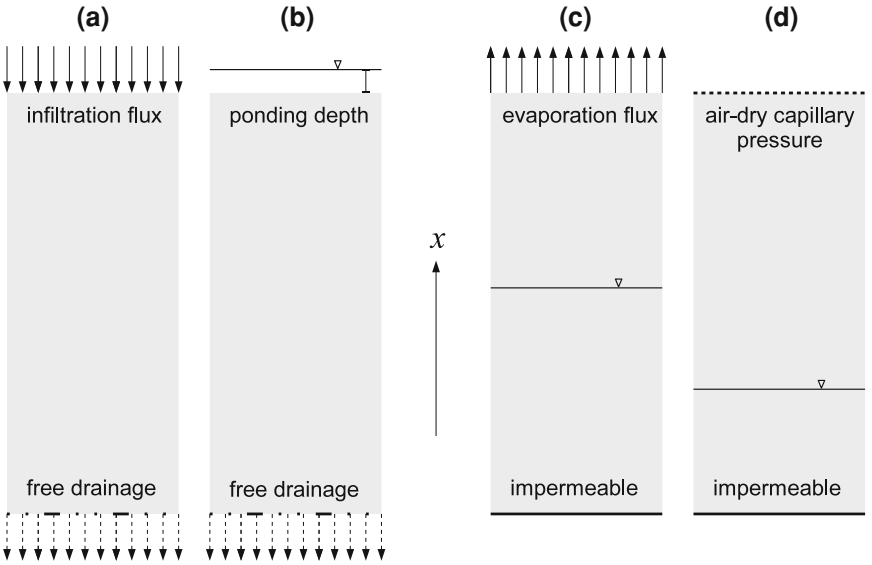

Fig. 2.9 Boundary conditions for typical one-dimensional flow problems: infiltration towards a distant groundwater table, **a** early stage, **b** late stage; evaporation from shallow groundwater table, **c** early stage, **d** late stage

the water phase is switched to Dirichlet type ($p_w = 0$ or some small positive value) and it is assumed that the excess precipitation forms the surface runoff, Fig. 2.9b. If the precipitation rate decreases below the soil infiltration capacity, the condition is switched back to Neumann type. A similar switch in the boundary conditions is performed when modelling evaporation. In this case the water pressure at the surface decreases as the water evaporates from soil at a specific rate, Fig. 2.9c. However, the water pressure cannot fall below a limit value defined by the temperature and relative humidity of the air, p_{dry}. If this value is reached, the boundary condition is switched to Dirichlet type with $p_{\mathrm{w}} = p_{\mathrm{dry}}$ and is maintained until the potential evaporation rate decreases or a rainfall occurs, Fig. 2.9d. It should be noted that such an approach provides only simplified description of the soil-atmosphere interface and is used primarily with the Richards model. More sophisticated modelling concepts are based on the coupling of air and water flow in porous medium with free flow of the surface water (after ponding) or atmospheric air above the soil-atmosphere interface, e.g. [22, 52].

2.3.3 Conditions at Material Interfaces

Porous media often consist of multiple regions, each of them having different properties such as porosity, intrinsic permeability, capillary function and relative

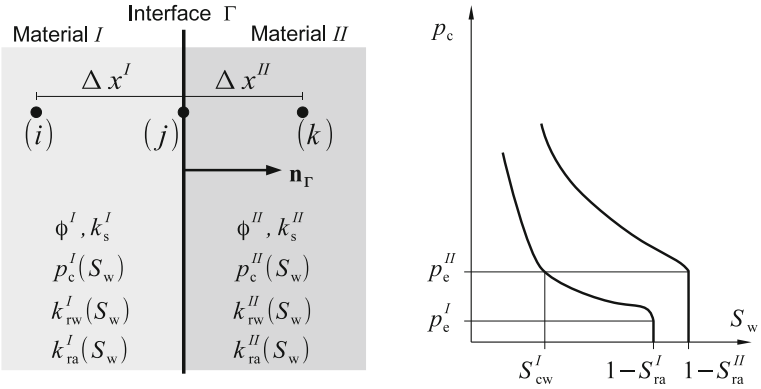

Fig. 2.10 Conditions at material interface separating two porous media

permeability functions. In each region the fluid flow is described by Eqs. (2.50)–(2.51), or by Eq. (2.65). The solutions in different subdomains must be connected to each other by appropriate interface conditions [30, 31].

Consider an interface between two porous materials, as shown in Fig. 2.10. At the Darcy's scale, the interface can be considered infinitely thin. Thus, the mass conservation principle implies that for each phase the components of the mass fluxes in the direction normal to the interface are equal:

$$(\rho_\alpha \mathbf{v}_\alpha)^I \mathbf{n}_\Gamma = (\rho_\alpha \mathbf{v}_\alpha)^{II} \mathbf{n}_\Gamma \tag{2.103}$$

where $\mathbf{n}_\Gamma$ is a unit vector normal to the interface Γ and oriented from material I to material II.

The second interface condition can be derived from the principle of momentum conservation [30], and states the continuity of the pressures in the two fluid phases, and consequently the continuity of the capillary pressure:

$$p_{\mathrm{w}}^I = p_{\mathrm{w}}^{II} \tag{2.104}$$

$$p_{\mathrm{a}}^I = p_{\mathrm{a}}^{II} \tag{2.105}$$

$$p_{\mathrm{c}}^I = p_{\mathrm{c}}^{II} \tag{2.106}$$

Note that the continuity of the capillary pressure implies that the water and air saturations are discontinuous, except for the case of two media characterized by the same capillary function. Moreover, if the saturation on one side of the interface is known, the saturation at the opposite side can be computed from the capillary pressure continuity condition:

$$S_{\mathrm{w}}^I = S_{\mathrm{w}}^I \left(p_{\mathrm{c}}^{II} \left(S_{\mathrm{w}}^{II}\right)\right) \tag{2.107}$$

The above conditions hold if both fluid phases are continuous in the pore space at each side of the interface. A special case arises if the one of the materials, say material II, is characterized by a distinct air entry pressure, higher than the entry pressure of the other material. As the value of p_{e}^{II} is reached, the air (or non-wetting fluid in general) is no longer continuous, and the macroscopic capillary pressure remains at its minimum value. At the other side of the interface, the capillary pressure can assume smaller values, or even reach zero if $p_{\mathrm{e}}^{I} = 0$. The state of the system can be meaningfully defined by the capillary pressure p_{c}^{I} or the corresponding water saturation S_{w}^{I}. On the other hand, the state of the material (I) cannot be uniquely determined by the saturation or the capillary pressure in material (II). In such a situation, the extended capillary pressure condition can be formulated as [15]:

$$\begin{cases} p_{\mathrm{c}}^{I}(S_{\mathrm{w}}^{I}) = p_{\mathrm{c}}^{II}(S_{\mathrm{w}}^{II}) & \text{if} \quad S_{\mathrm{w}}^{I} < S_{\mathrm{cw}}^{I} \\ S_{\mathrm{w}}^{II} = 1 - S_{\mathrm{ra}}^{II} & \text{if} \quad S_{w}^{I} \geq S_{\mathrm{cw}}^{I} \end{cases} \tag{2.108}$$

where the threshold saturation at the left side of the interface S_{cw}^{I} corresponds to the entry pressure of the material at the right-hand side, $S_{\mathrm{cw}}^{I} = S_{\mathrm{w}}^{I}(p_{\mathrm{e}}^{II})$. At the same time, the pressure continuity condition for the water phase (2.104) holds, as the water phase is continuous at both sides of the interface.

In the case of the Richards equation, only conditions for the water phase have to be formulated at the interface. They include the continuity of the normal flux and continuity of the water pressure. The water saturation, now uniquely defined by the water pressure, is in general discontinuous at the interfaces. The interface conditions must be properly taken into account in the development of spatial discretization schemes for both two-phase model and the Richards equation, as it will be shown in the following chapter.

Application of the pressure and flux continuity conditions for the case of single-phase flow leads to the well known formula for the equivalent permeability of a layered medium in the direction perpendicular to the layers. Assuming that the values of the water pressure at points i, j and k are known, one can write:

$$-k_{\mathrm{s}}^{I}\,\frac{p^{I(j)} - p^{(i)}}{\Delta x^{I}} = -k_{\mathrm{s}}^{II}\,\frac{p^{(k)} - p^{II(j)}}{\Delta x^{II}} = -k_{\mathrm{s}}^{\mathrm{eq}}\,\frac{p^{(k)} - p^{(i)}}{\Delta x^{I} + \Delta x^{II}} \tag{2.109}$$

where $k_{\mathrm{s}}^{\mathrm{eq}}$ is the equivalent intrinsic permeability and by virtue of the pressure continuity $p^{I(j)} = p^{II(j)}$. Solving the above double equation, one can express the equivalent permeability as a weighted harmonic average of the permeabilities of the two materials:

$$k_{\mathrm{s}}^{\mathrm{eq}} = \frac{(\Delta x^{I} + \Delta x^{II})\,k_{\mathrm{s}}^{I}\,k_{\mathrm{s}}^{II}}{\Delta x^{I}\,k_{\mathrm{s}}^{II} + \Delta x^{II}\,k_{\mathrm{s}}^{I}} \tag{2.110}$$

This formula will be used in the subsequent chapters to develop spatial discretization schemes for both homogeneous and heterogeneous porous media.

References

1. Auriault JL (1987) Nonsaturated deformable porous media: Quasistatics. Transport in Porous Media 2(1):45–64,10.1007/BF00208536
2. Auriault JL, Boutin C, Geindreau C (2009) Homogenization of coupled phenomena in heterogeneous media. Wiley, Hoboken
3. Baker D (1995) Darcian weighted interblock conductivity means for vertical unsaturated flow. Ground Water 33(3):385–390,10.1111/j.1745-6584.1995.tb00294.x
4. Bear J (1972) Dynamics of fluids in porous media. Elsevier, Amsterdam
5. Berninger H, Kornhuber R, Sander O (2011) Fast and robust numerical solution of the Richards' equation in homogeneous soil. SIAM Journal on Numerical Analysis 49(6):2576–2597,10.1137/100782887
6. Binning P, Celia M (1999) Practical implementation of the fractional flow approach to multi-phase flow simulation. Advances in Water Resources 22(5):461–478,10.1016/S0309-1708(98)00022--0
7. Brooks R, Corey A (1964) Hydraulic properties of porous media. Tech. rep., Hydrology Paper 3, Colorado State University, Fort Collins, Colorado, USA
8. Buckingham E (1907) Studies on the movement of soil moisture. Tech. rep., Bulletin 38 U.S. Department of Agriculture Bureau of Soils
9. Burdine N (1953) Relative permeability calculations from pore size distribution data. Transactions of the American Institute of Mining, Metallurgical and Petroleum Engineers 198:71–77
10. Carsel R, Parrish R (1988) Developing of joint probability distributions of soil water retention characteristics. Water Resources Research 24(5):755–769,10.1029/WR024i005p00755
11. Celia M, Binning P (1992) A mass conservative numerical solution for two-phase flow in porous media with application to unsaturated flow. Water Resources Research 28(10):2819–2828,10.1029/92WR01488
12. Celia M, Bouloutas E, Zarba R (1990) A general mass-conservative numerical solution for the unsaturated flow equation. Water Resources Research 26(7):1483–1496,10.1029/WR026i007p01483
13. Chen Z, Huan G, Ma Y (2006) Computational methods for multiphase flows in porous media. SIAM, Philadelphia
14. Darcy H (1856) Les fontaines publiques de la ville de Dijon. Dalmont, Paris
15. de Neef M, Molenaar J (1997) Analysis of DNAPL infiltration in a medium with a low permeable lens. Computational Geosciences 1(2):191–214,10.1023/A:1011569329088
16. Domenico P, Schwartz F (1998) Physical and chemical hydrogeology. Wiley, New York
17. Feddes R, de Rooij G, van Dam J (eds) (2004) Unsaturated-zone modeling: progress, challenges and applications. Kluwer, Dordrecht
18. Fletcher C (1991) Computational techniques for fluid dynamics 1. Fundamental and general techniques, Springer, Berlin
19. Forsyth P (1988) Comparison of the single-phase and two-phase numerical model formulation for saturated-unsaturated groundwater flow. Computer Methods in Applied Mechanics and Engineering 69(2):243–259
20. Fredlund D, Rahardjo H (1993) Soil mechanics for unsaturated soils. Wiley, New York
21. Fredlund D, Xing A (1994) Equations for the soil-water characteristic curve.Canadian Geotechnical Journal 31(4):521–532,10.1139/t94-061
22. Furman A (2008) Modeling coupled surface-subsurface flow processes: A review. Vadose Zone Journal 7(2):741–756,10.2136/vzj2007.0065
23. Gardner W (1958) Some steady-state solutions of the unsaturated moisture flow equation with the application to evaporation from a water table. Soil Science 85(4):228–232
24. Gawin D, Baggio P, Schrefler B (1995) Coupled heat, water and gas flow in deformable porous media. International Journal for Numerical Methods in Fluids 20:969–987
25. Gray W, Hassanizadeh S (1991) Paradoxes and realities in unsaturated flow theory. Water Resources Research 27(8):1847–1854,10.1029/91WR01259

26. Guo H, Jiao J, Weeks E (2008) Rain-induced subsurface airflow and Lisse effect. Water Resources Research 44:W07409,10.1029/2007WR006294
27. Hammecker C, Antonino A, Maeght J, Boivin P (2003) Experimental and numerical study of water flow in soil under irrigation in northern senegal: evidence of air entrapment. European Journal of Soil Science 54:491–503
28. Hassanizadeh M, Gray W (1980) General conservation equations for multi-phase systems: 3. Constitutive theory for porous media flow. Advances in Water Resources 3(1):25–40,10.1016/0309-1708(80)90016--0
29. Hassanizadeh M, Gray W (1993) Toward an improved description of the physics of two-phase flow. Advances in Water Resources 16(1):53–67,10.1016/0309-1708(93)90029-F
30. Hassanizadeh S, Gray W (1989) Boundary and interface conditions in porous media. Water Resources Research 25(7):1705–1715,10.1029/WR025i007p01705
31. Helmig R (1997) Multiphase flow and transport processes in the subsurface: a contribution to the modeling of the hydrosystems. Springer, Berlin
32. Hilfer R (2006) Capillary pressure, hysteresis and residual saturation in porous media. Physica A 359:119–128
33. Hillel D (1998) Environmental soil physics. Academic Press, San Diego, California
34. Ippisch O, Vogel HJ, Bastian P (2006) Validity limits for the van Genuchten—Mualem model and implications for parameter estimation and numerical simulation. Advances in Water Resources 29(12):17801789,10.1016/j.advwatres.2005.12.011
35. Ishihara K, Tsukamoto Y, Nakazawa H, Kamada K, Huang Y (2002) Resistance of partly saturated sand to liquefaction with reference to longitudinal and shear wave velocities. Journal of Soils and Foundations, JGS 42:6
36. Ji SH, Park YJ, Sudicky E, Sykes J (2008) A generalized transformation approach for simulating steady-state variably-saturated subsurface flow. Advances in Water Resources 31(2):313–323,10.1016/j.advwatres.2007.08.010
37. Khlosi M, Cornelis W, Douaik A, van Genuchten M, Gabriels D (2008) Performance evaluation of models that describe the soil water retention curve between saturation and oven dryness. Vadose Zone Journal 7(1):87–96,10.2136/vzj2007.0099
38. Kosugi K, Hopmans J, Dane J (2002) Parametric models. In: JH D, GC T (eds) Methods of soil analysis. Part 4: Physical methods, Soil Science Society of America, Inc., Madison, Wisconsin, pp 739–757
39. Kovács G (1981) Seepage hydraulics. Elsevier, Amsterdam
40. Kuang X, Jiao J, Wan L, Wang X, Mao D (2011) Air and water flows in a vertical sand column. Water Resources Research 47:W04506,10.1029/2009WR009030
41. Kutílek M, Nielsen D (1994) Soil hydrology. Catena , Cremlingen
42. Lassabatere L, Angulo-Jaramillo R, Soria Ugalde J, Cuenca R, Braud I, Haverkamp R (2006) Beerkan estimation of soil transfer parameters through infiltration experiments - BEST. Soil Science Society of America Journal 70(2):521–532,10.2136/sssaj2005.0026
43. Leij F, Russel W, Lesch S (1997) Closed-form expressions for water retention and conductivity data. Ground Water 35(5):848–858,10.1111/j.1745-6584.1997.tb00153.x
44. Lenhard R, Parker J, Mishra S (1989) On the correspondence between Brooks-Corey and van Genuchten models. Journal of Irrigation and Drainage Engineering ASCE 115:744–751
45. Leong EC, Rahardjo H (1997) Review of soil-water characteristic curve equations. Journal of Geotechnical and Geoenvironmental Engineering 123(12):1106–1117
46. Lesniewska D, Zaradny H, Bogacz P, Kaczmarek J (2008) Study of flood embankment behaviour induced by air entrapment. In: Samuels P, Huntington S, Allsop W, Harrop J (eds) Flood risk management: research and practice. Taylor & Francis, London, pp 655–665
47. Lewis R, Schrefler B (1998) The finite element method in the static and dynamic deformation and consolidation of porous media. Wiley, Chichester
48. Lu N, Likos W (2004) Unsaturated soil mechanics. Wiley, Hoboken
49. Luckner L, van Genuchten M, Nielsen D (1989) A consistent set of parametric models for the two-phase flow of immiscible fluids in the subsurface. Water Resources Research 25(10):2113–2124,10.1029/WR025i010p02187

50. Morel-Seytoux H, Billica J (1985a) A two-phase numerical model for prediction of infiltration: applications to a semi-infinite soil column. Water Resources Research 21(4):607–615,10.1029/WR021i004p00607
51. Morel-Seytoux H, Billica J (1985b) A two-phase numerical model for prediction of infiltration: case of an impervious bottom. Water Resources Research 21(9):1389–1396,10.1029/WR021i009p01389
52. Mosthaf K, Baber K, Flemisch B, Helmig R, Leijnse T, Rybak I, Wohlmuth B (2011) A coupling concept for two-phase compositional porous-medium and single-phase compositional free flow. Water Resources Research 47:W10522,10.1029/2011WR010685
53. Mualem Y (1976) A new model for predicting the hydraulic conductivity of unsaturated porous media. Water Resources Research 12(3):513–522,10.1029/WR012i003p00513
54. Mualem Y (1978) Hydraulic conductivity of unsaturated porous media: Generalized macroscopic approach. Water Resources Research 14(2):325–334,10.1029/WR014i002p00325
55. Narasimhan T (2007) Central ideas of Buckingham (1907): A century later. Vadose Zone Journal 6(4):687–693,10.2136/vzj2007.0080
56. Niessner J, Hassanizadeh S (2008) A model for two-phase flow in porous media including fluid-fluid interfacial area. Water Resources Research 44:W08439,10.1029/2007WR006721
57. Oettl G, Stark R, Hofstetter G (2004) Numerical simulation of geotechnical problems based on a multi-phase finite element approach. Computers and Geotechnics 31(8):643–664,10.1016/j.compgeo.2004.10.002
58. Or D, Wraith J (2002) Soil water content and water potential relationships. Warrick A (ed) Soil physics companion, CRC Press, In, pp 49–84
59. Ossowski R, Sikora Z (2004) Numeryczne modelowanie sondowania statycznego CPTU (Numerical modeling of static CPTU tests). Politechnika Gdańska, Gdańsk
60. Parlange JY, Hill D (1979) Air and water movement in porous media: compressibility effects. Soil Science 127(5):257–263
61. Philip J (1969) Theory of infiltration. Advances in Hydroscience 5:215–296
62. Pinder G, Celia M (2006) Subsurface hydrology. Wiley, Hoboken
63. Pinder G, Gray W (2008) Essentials of multiphase flow and transport in porous media. Wiley, Hoboken
64. Radcliffe D, Šimunek J (2010) Soil physics with Hydrus. CRC Press, Boca Raton, Florida, Modeling and applications
65. Richards L (1931) Capillary conduction of liquids through porous medium. Physics 1:318–333
66. Rose W (2000) Myths about later-day extensions of Darcy's law. Journal of Petroleum Science and Engineering 26:187–198
67. Ross P (2003) Modeling soil water and solute transport—fast simplified numerical solutions. Agronomy Journal 95(6):1352–1361,10.2134/agronj2003.1352
68. Rucker D, Warrick A, Ferré T (2005) Parameter equivalence for the Gardner and van Genuchten soil hydraulic conductivity functions for steady vertical flow with inclusions. Advances in Water Resources 28(7):689–699,10.1016/j.advwatres.2005.01.004
69. Schaap M, Leij F (2000) Improved prediction of unsaturated hydraulic conductivity with the Mualem - van Geuchten model. Soil Science Society of America Journal 64(3):843–851,10.2136/sssaj2000.643843x
70. Sheng D, Sloan S, Gens A, Smith D (2003) Finite element formulation and algorithms for unsaturated soils. Part I: Theory. International Journal for Numerical and Analytical Methods in Geomechanics 27(9):745–765
71. Sikora Z (1992) Hypoplastic flow of granular materials - A numerical approach, vol 123. Veröffentlichungen des Institutes für Bodenmechanik und Felsmechanik der Universität Fridericiana in Karlsruhe, Karlsruhe
72. Šimunek J, Šejna M, Saito H, Sakai M, van Genuchten M (2008) The HYDRUS-1D software package for simulating the one-dimensional movement of water, heat and multiple solutes in variably-saturated media. Version 4.0. Department of Environmental Sciences, University of California Riverside, Riverside, California

73. Tegnander C (2001) Models for groundwater flow: A numerical comparison between Richards model and fractional flow model. Transport in Porous Media 43(2):213–224,10.1023/A:1010749708294
74. Touma J, Vauclin M (1986) Experimental and numerical analysis of two-phase infiltration in a partially saturated soil. Transport in Porous Media 1(1):27–55,10.1007/BF01036524
75. Touma J, Vachaud G, Parlange JY (1984) Air and water flow in a sealed, ponded vertical soil column: experiment and model. Soil Science 137(3):181–187
76. Vachaud G, Vauclin M, Khanji D, Wakil M (1973) Effects of air pressure on water flow in an unsaturated stratified vertical column of sand. Water Resources Research 9(1):160–173,10.1029/WR009i001p00160
77. Valdes-Parada F, Ochoa-Tapia J, Alvarez-Ramirez J (2009) Validity of the permeability Carman-Kozeny equation: A volume averaging approach. Physica A 388(6):789–798
78. van Dijke M, van der Zee S (1998) Modeling of air sparging in a layered soil: Numerical and analytical approximations. Water Resources Research 34(3):341–353,10.1029/97WR03069
79. van Genuchten M (1980) A closed form equation for predicting the hydraulic conductivity of unsaturated soils. Soil Science Society of America Journal 44(5):892–898,10.2136/sssaj1980.03615995004400050002x
80. Vauclin M (1989) Flow of water and air in soils: theoretical and environmental aspects. In: Morel-Seytoux H (ed) Unsaturated flow in hydrologic modeling: theory and practice. Kluwer, Dordrecht
81. Vogel T, Císlerová M (1988) On the reliability of unsaturated hydraulic conductivity calculated from the moisture retention curve. Transport in Porous Media 3(1):1–15,10.1007/BF00222683
82. Vuković M, Soro A (1992) Determination of Hydraulic Conductivity of Porous Media from Grain-Size Composition. Water Resources Publications, Litleton, Colorado
83. Wang Z, Feyen J, Nielsen D, van Genuchten M (1997) Two-phase flow infiltration equations accounting for air entrapment effects. Water Resources Research 33(12):2759–2767,10.1029/97WR01708
84. Wang Z, Feyen J, van Genuchten M, Nielsen D (1998) Air entrapment effects on infiltration rate and flow instability. Water Resources Research 34(2):213–222,10.1029/97WR02804
85. Warrick A (2003) Soil water dynamics. Oxford University Press, New York
86. Whitaker S (1986) Flow in porous media I: A theoretical derivation of Darcy's law. Transport in Porous Media 1(1):3–25,10.1007/BF01036523
87. Wu Y, Forsyth P, Jiang H (1996) A consistent approach for applying numerical boundary conditions for multiphase subsurface flow. Journal of Contaminant Hydrology 23(3):157–184,10.1016/0169-7722(95)00099--2
88. Yazzan S, Bentsen R, Trivedi J (2011) Theoretical development of a novel equation for dynamic spontaneous imbibition with variable inlet saturation and interfacial coupling effects. Transport in Porous Media 86(3):705–717,10.1007/s11242-010-9647-z

Chapter 3
Numerical Solution of Flow Equations

The governing equations for fluid flow in porous media presented in Chap. 2 can be written in a general form of the following partial differential equation of parabolic type:

$$\frac{\partial M_\alpha}{\partial t} + \nabla \left(\rho_\alpha \, \mathbf{v}_\alpha \right) = 0 \tag{3.1}$$

where $M_\alpha = \rho_\alpha \, \phi \, S_\alpha$ denotes the mass of the fluid in a unit volume of porous medium and $\mathbf{v}_\alpha$ is the volumetric fluid flux, given by the extended Darcy formula:

$$\mathbf{v}_\alpha = -\frac{\mathsf{k}_\alpha}{\mu_\alpha} \left(\nabla p_\alpha - \rho_\alpha \, \mathbf{g} \right) \tag{3.2}$$

The two-phase model consists of two coupled equations (3.1), which are nonlinear with respect to the chosen pair of primary unknowns, e.g. p_w–S_w or p_w–p_a. The Richards model is given by a single equation, nonlinear with respect to the chosen primary unknown p_w, h_w or S_w. Finally, the single-phase water flow model is defined by a single equation, linear with respect to the primary unknown p_w (or h_w). While other formulations of the governing equations are possible (e.g. the fractional flow formulation for the two-phase flow, or a variety of variable transformation approaches for the Richards equation), in this work the formulation given by Eq. (3.1) is used, due to its clear physical interpretation and consistent representation of the two-phase, unsaturated and saturated flow cases.

Analytical solution of the governing equations is possible only for a few simple cases, and numerical methods are typically employed to obtain approximate solutions. Numerical solution of a nonlinear partial differential equations describing transient phenomena in a time-space domain involves several tasks or stages. For each task, a number of alternative techniques exist, and the choice of one or other approach may significantly influence the accuracy and efficiency of the computations. For an overview of various numerical approaches available for flow in porous media, see e.g. [14, 33]. The main steps of the solution algorithm are as follows:

A. Szymkiewicz, *Modelling Water Flow in Unsaturated Porous Media*,
GeoPlanet: Earth and Planetary Sciences, DOI: 10.1007/978-3-642-23559-7_3,

1. Discretization in space. It is typically performed with the finite difference, finite element or finite volume methods, and requires defining a number of points (nodes) in the considered spatial domain, at which the values of the unknown function are sought. Spatial discretization leads to a system of ordinary differential equations (or algebraic differential equations), containing the unknown nodal values and their derivatives with respect to time.
2. Discretization in time. The resulting system of ordinary differential equations has to be integrated in the specified time interval, which is divided into several time steps. The solution at the next time level can be obtained using a variety of explicit or implicit methods. For the reasons of stability, implicit schemes are preferred. Application of an implicit scheme results in a system of nonlinear algebraic equations for each time step, where the unknowns represent the nodal values of the primary variables from the new time level.
3. Linearization. As the system of discrete equations arising for each time level is nonlinear, it must be solved using an iterative method. First, an initial guess of the unknown values is provided, and then a number of successive corrections are calculated. To this order one can apply either different versions of the Newton method, or a simpler approach, known as the modified Picard method.
4. Solution of the linear systems. For each nonlinear iteration, a system of linear equations has to be solved, to compute the corrections to the unknown values. The system is characterized by a sparse and banded coefficient matrix. Depending on the problem under consideration, either direct or iterative methods can be employed to solve the linear system.

In the following sections an overview of the basic discretization methods is presented, with the focus on the control-volume finite-element approach, which is used in the numerical examples presented in the following part of the book. The solution algorithm is discussed in general terms, which allows for its application to one-dimensional and multi-dimensional problems, and for alternative choices with respect to the primary unknowns.

3.1 Basic Properties of Numerical Discretization Schemes

In the process of numerical discretization, the differential terms of the governing equations are replaced by algebraic terms. The numerical scheme should satisfy several requirements, in order to ensure that the solution of the system of discrete equations approximates the solution of the original differential equation with sufficient accuracy for the range of practically applicable discretization parameters (node spacings and time steps). The basic property of the discretization scheme is convergence. The numerical scheme is convergent if the resulting approximate solutions tend to the exact solution of the original differential equation for decreasing spatial and temporal discretization steps, e.g. [25, 33]. For nonlinear equations the convergence is difficult to prove. It can be investigated empirically, by performing

subsequent numerical solutions of the same initial-boundary problem with decreasing spatial and temporal discretization steps, and comparing them with known analytical solution. Moreover, some insights into the numerical properties of the nonlinear flow equations can be obtained by considering the linear advection–diffusion equation of the following form:

$$\frac{\partial u}{\partial t} + v_u \frac{\partial u}{\partial x} - D_u \frac{\partial^2 u}{\partial x^2} = 0 \tag{3.3}$$

where u is a physical quantity subjected to the advective and diffusive transport and v_u and D_u are constant parameters. Equation (3.3) can be regarded as a simplified version of the saturation equation in the fractional flow model, Eq. (2.63), or the Richards equation, e.g. Eq. (2.75). For linear differential equations the Lax theorem holds, which states that the properties of consistency and stability are necessary and sufficient conditions for a numerical scheme to be convergent [25, 33]. Analysis of these properties is well-established for linear advection–diffusion equation. While the results of the analysis of a linear equation cannot be directly applied to its nonlinear counterparts, they offer some hints about the expected behaviour of the discretization scheme.

The consistency of the discrete equation with the original differential equation means that the local truncation errors tend to zero as the node spacings and time steps decrease. The consistency analysis is performed by inserting the Taylor series expansions of the unknown functions around the computational nodes into the algebraic approximations of the derivatives in the discrete scheme. The resulting equation contains the differential terms of the original equation and the truncation error, i.e. additional higher order terms from the Taylor expansions, which were neglected in the discretization, e.g. [31]:

$$\frac{\partial u}{\partial t} + v_u \frac{\partial u}{\partial x} - D_u \frac{\partial^2 u}{\partial x^2} = \sum_{p,q} \alpha_{p,q} \Delta t^{\beta_{p,q}} \Delta x^{\gamma_{p,q}} \frac{\partial^{p+q} u}{\partial t^p \, \partial x^q} \tag{3.4}$$

where $p, q = 0, 1, 2, \ldots$ and the coefficients $\alpha_{p,q}$ and the exponents $\beta_{p,q}$ and $\chi_{p,q}$ depend on the considered numerical scheme. The order of accuracy of the approximation with respect to time and space corresponds to the value of the exponent $\beta_{p,q}$ or $\gamma_{p,q}$, respectively, in the leading term of the truncation error. Furthermore, according to the modified equation approach, the mixed time-space derivatives can be eliminated from the expression for the truncation error by differentiation of the original differential equation, so that only spatial derivatives remain [30]. If the leading term contains an even-order spatial derivative, then numerical dissipation effects can be expected. The dissipation caused by the lowest (i.e. second) order term is called numerical diffusion. Numerical diffusion (and dissipation in general) acts in a manner analogous to the physical diffusion, smoothing sharp gradients present in the solution. If the leading term contains an odd-order derivative, the solution is influenced by numerical dispersion. Numerical dispersion leads to oscillations in the solution, while keeping the initial steep gradients. The effects of numerical

diffusion and dispersion are particularly important for advection dominated problems. If a significant physical diffusive mechanism is included in the governing equation, the additional numerical diffusion becomes relatively less pronounced. On the other hand, physical diffusion smoothes the oscillations caused by a dispersive numerical scheme. In advection-dominated problems the appearance of diffusion and dispersion errors is related to the method of approximation of the advective flux. Strong numerical diffusion is typical for upwind (or upstream) schemes, where the algebraic approximation of the advective flux at a specific node of the grid involves values of the unknown function only from the nodes located upstream with respect to the direction of transport. Numerical dispersion occurs for centred approximations of the advective flux, which involve nodes located both upstream and downstream of the considered grid point [25].

In the two-phase flow model, the diffusion is related to capillary forces, while the advection to gravity and viscous forces. Due to the large value of viscosity ratio between water and air, the viscous terms are relatively less important in the unsaturated zone, as compared for example to the water–oil system. In the Richards equation only capillarity and gravity forces are present. For gravity-dominated flow numerical errors typically associated with the advection equation occur. Generally, numerical diffusion errors are considered more acceptable than the numerical dispersion errors. This is due to the fact that dispersion leads to non-monotonous, oscillatory profiles of the pressures and/or saturations, which are not admissible from the physical point of view. Numerical diffusion smears the saturation gradients, but the results are physically admissible, because similar profiles could be obtained from an accurate solution of the same initial-boundary problem for a medium characterized by different constitutive relationships with increased role of the capillary forces. For a discussion of the monotonicity issues in relation to the relative importance of diffusive and advective terms in the governing equation, see e.g. [26, 33]. Monotonicity is usually achieved by applying upstream averaging of the relative permeability. Nevertheless, the lack of oscillations does not guarantee that the solution is accurate and excessive numerical diffusion may cause large errors, for instance by speeding up the arrival time of the saturation front at a specific point. Thus, some authors argue that the use of numerical diffusion to ensure monotonous solutions should be avoided [29].

Another important property of a numerical scheme is the stability. A scheme is stable if small perturbations in the solution are not amplified. In the context of numerical solution of the advection–diffusion equation, stability is related to the method of discretization in time. The time-discretization schemes can be categorized into explicit and implicit. In the explicit schemes, values of primary unknown for any given point at the next time level can be obtained from the previous time levels, independently of the values at other nodes. In the implicit schemes the algebraic formulae approximating the spatial derivatives are written using nodal values from the new time level, which usually results in a system of algebraic equations that must be solved for each time step. Explicit schemes are only conditionally stable, which means that the length of time step must be smaller than a specific limit value. In contrast, some implicit schemes are unconditionally stable, which means that the solution is stable for any choice of the time step. However, the presence of

nonlinear terms in the governing differential equation may give rise to numerical instabilities, even if the discretization scheme is unconditionally stable for linear equations [2]. Moreover, for nonlinear equations the length of the time step is limited by the convergence of the iterative solution of the nonlinear equations.

As the governing equations for the two-phase flow represent the mass conservation principle, it is advantageous if the discrete scheme is also mass-conservative. It means that the change of the fluid mass in the considered domain between two time steps should be equal to the integral of the mass flux over the domain boundary. If this principle holds for the whole solution domain, the method is said to be globally conservative. If the principle holds for any of the sub-domains resulting from the spatial discretization of the solution domain, the method is said to be locally conservative. Mass conservation is affected by the choice of the form of the governing equation, as well as by the choice of the actual discretization technique. The discrete equations should satisfy the integral (divergence) form of the mass conservation principle, as given by Eq. (2.65) [30]. With respect to the spatial discretization, it is important to use a unique value of the numerical flux for each internal boundary between two adjacent subdomains in the solution domain, so that the same quantity which leaves one subdomain enters the neighbouring one. Such a property is satisfied by the finite volume discretization. Also, the mass balance in the numerical solution can be negatively affected if the time derivative in the storage term is expanded using the chain differentiation rule, in order to obtain the time derivative of the primary unknown, as shown in Chap. 2, Eq. (2.67).

3.2 Spatial Discretization

In the following, an approach to the discretization in the time-space domain known as the method of lines is adopted. The partial differential equations are first discretized in space, resulting in a semi-discrete form represented by a system of ordinary differential equations (or differential algebraic equations) with respect to time. The semi-discrete formulation allows for a direct comparison of various spatial discretization techniques. The semi-discrete system is then integrated in the prescribed time interval, as described in Sect. 3.3.

A fixed-grid spatial discretization is assumed, where the number of nodes and their position in the solution domain remain constant during the simulation. For a description of spatially adaptive algorithms, which coarsen or refine the mesh according to the solution behavior see e.g. [46, 48].

3.2.1 Finite Difference Method

The finite difference method is applied to the strong (differential) form of the flow equation, as given by Eq. (3.1). It is particularly useful for one-dimensional problems,

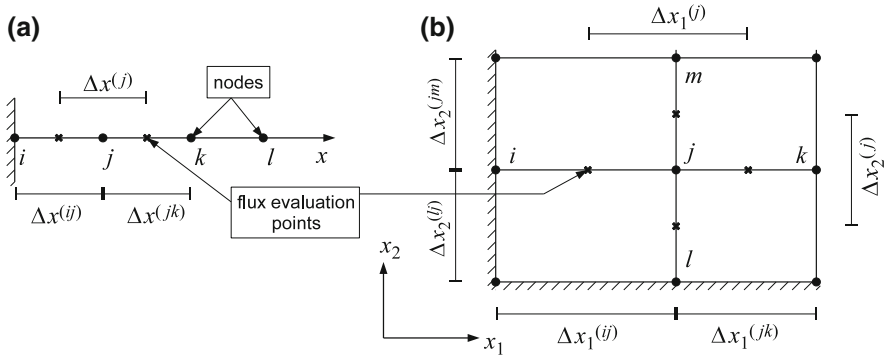

Fig. 3.1 Numerical grid for the finite difference method in one (**a**) and two (**b**) dimensions

e.g. [13, 32] or multidimensional problems in rectangular domains, e.g. [15, 28, 41, 60]. The numerical grid is defined by a number of lines which are parallel to the axes of the spatial coordinate system with computational nodes placed at their intersections, Fig. 3.1.

The finite difference method consists in replacing the derivatives of the unknown functions by differential quotients involving the values of the unknown function from the neighbouring nodes, according to the definition of the derivative. In the one-dimensional case shown in Fig. 3.1a the mass fluxes between nodes ij and jk can be approximated at mid-distance between nodes in the following way:

$$v_\alpha^{(ij)} = -\frac{k_s\, k_{r\alpha}^{(ij)}}{\mu_\alpha}\left(\frac{p_\alpha^{(j)} - p_\alpha^{(i)}}{\Delta x^{(ij)}} - \rho_\alpha^{(ij)}\, g\, \zeta\right), \tag{3.5}$$

$$v_\alpha^{(jk)} = -\frac{k_s\, k_{r\alpha}^{(jk)}}{\mu_\alpha}\left(\frac{p_\alpha^{(k)} - p_\alpha^{(j)}}{\Delta x^{(jk)}} - \rho_\alpha^{(jk)}\, g\, \zeta\right), \tag{3.6}$$

where $p_\alpha^{(i)}$, $p_\alpha^{(j)}$ and $p_\alpha^{(k)}$ denote the pressure values at the computational nodes, $\Delta x^{(ij)}$ and $\Delta x^{(jk)}$ are the distances between the respective nodes, $k_{r\alpha}^{(ij)}$ and $k_{r\alpha}^{(jk)}$ are the average inter-nodal values of the relative permeability, $\rho_\alpha^{(ij)}$ and $\rho_\alpha^{(jk)}$ are the average inter-nodal values of the fluid density, g is the magnitude of gravitational acceleration and ζ is the cosine of the angle between the x axis and the vector of the gravity force. For horizontal flow $\zeta = 0$, for vertical flow $\zeta = 1$ if the x axis is oriented downward and $\zeta = -1$ if the x axis is oriented upward.

Typically, the variations in density between the two nodes are small and $\rho_\alpha^{(ij)}$ can be approximated as the arithmetic average of the nodal values [33]:

$$\rho_\alpha^{(ij)} = \frac{1}{2}\left(\rho_\alpha^{(i)} + \rho_\alpha^{(j)}\right). \tag{3.7}$$

The inter-nodal relative permeability is often approximated either as an arithmetic average:

$$k_{\mathrm{r}\alpha}^{(ij)} = \frac{1}{2}\left(k_{\mathrm{r}\alpha}^{(i)} + k_{\mathrm{r}\alpha}^{(j)}\right), \tag{3.8}$$

or as an upstream (upwind) average. In the latter case, $k_{\mathrm{r}\alpha}^{(ij)}$ is equal to the permeability of the node which is positioned upstream with respect to the direction of the flow:

$$k_{\mathrm{r}\alpha}^{(ij)} = \begin{cases} k_{\mathrm{r}\alpha}^{(i)} & \text{if} \quad \frac{p_\alpha^{(j)} - p_\alpha^{(i)}}{\Delta x^{(ij)}} - \rho_\alpha^{(ij)}\, g\, \zeta \leq 0, \\ \\ k_{\mathrm{r}\alpha}^{(j)} & \text{if} \quad \frac{p_\alpha^{(k)} - p_\alpha^{(j)}}{\Delta x^{(jk)}} - \rho_\alpha^{(jk)}\, g\, \zeta > 0. \end{cases} \tag{3.9}$$

Several other permeability averaging schemes were proposed, particularly for the case of incompressible Richards equation, e.g. [6, 10, 28, 70]. As the permeabilities at the neighbouring nodes may differ by several orders of magnitude, the choice of the averaging method significantly influences the accuracy of the results. This problem is discussed in detail in Chap. 4.

The flux divergence operator at node j can be approximated as:

$$\nabla\left(\rho_\alpha\, \mathbf{v}_\alpha\right) = \frac{1}{\Delta x^{(j)}}\left(\rho_\alpha^{(jk)}\, v_\alpha^{(jk)} - \rho_\alpha^{(ij)}\, v_\alpha^{(ij)}\right), \tag{3.10}$$

where

$$\Delta x^{(j)} = \frac{\Delta x^{(ij)} + \Delta x^{(jk)}}{2}. \tag{3.11}$$

The resulting semi-discrete flow equation for fluid phase α at node j can be written in the following general form:

$$\Delta x^{(j)} \frac{\mathrm{d}M_\alpha^{(j)}}{\mathrm{d}t} + A_\alpha^{(ij)} p_\alpha^{(i)} + A_\alpha^{(jj)} p_\alpha^{(j)} + A_\alpha^{(jk)} p_\alpha^{(k)} + G_\alpha^{(j)} = 0, \tag{3.12}$$

where the partial derivative with respect to time was replaced by an ordinary derivative, because $M_\alpha^{(j)}$ is defined point-wise and is no longer a function of space. The flow coefficients A_α are defined as follows:

$$A_\alpha^{(ij)} = -\frac{1}{\Delta x^{(ij)}} \frac{\rho_\alpha^{(ij)}}{\mu_\alpha}\, k_{\mathrm{s}}\, k_{\mathrm{r}\alpha}^{(ij)}, \tag{3.13}$$

$$A_\alpha^{(jk)} = -\frac{1}{\Delta x^{(jk)}} \frac{\rho_\alpha^{(jk)}}{\mu_\alpha}\, k_{\mathrm{s}}\, k_{\mathrm{r}\alpha}^{(jk)}, \tag{3.14}$$

$$A_\alpha^{(jj)} = -\left(A_\alpha^{(ij)} + A_\alpha^{(jk)}\right) \tag{3.15}$$

and the gravity term $G_\alpha^{(j)}$ is equal to:

$$G_\alpha^{(j)} = -\frac{k_\mathrm{s}\, k_{\mathrm{r}\alpha}^{(ij)}}{\mu_\alpha} \left(\rho_\alpha^{(ij)}\right)^2 g\,\zeta + \frac{k_\mathrm{s}\, k_{\mathrm{r}\alpha}^{(jk)}}{\mu_\alpha} \left(\rho_\alpha^{(jk)}\right)^2 g\,\zeta. \tag{3.16}$$

The finite difference scheme for two-dimensional flow in a diagonally anisotropic medium, Fig. 3.1b, can be developed in a similar manner. As a result one obtains a five-point stencil of the following form:

$$\begin{aligned}\Delta x_1^{(j)}\,\Delta x_2^{(j)}\frac{\mathrm{d}M_\alpha^{(j)}}{\mathrm{d}t} + A_\alpha^{(jj)} p_\alpha^{(j)} \\ + A_\alpha^{(ij)} p_\alpha^{(i)} + A_\alpha^{(lj)} p_\alpha^{(l)} + A_\alpha^{(jk)} p_\alpha^{(k)} + A_\alpha^{(jm)} p_\alpha^{(m)} + G_\alpha^{(j)} = 0\end{aligned} \tag{3.17}$$

where

$$\Delta x_1^{(j)} = \frac{\Delta x^{(ij)} + \Delta x^{(jk)}}{2}, \qquad \Delta x_2^{(j)} = \frac{\Delta x^{(lj)} + \Delta x^{(jm)}}{2}, \tag{3.18}$$

and the flow coefficients are defined as:

$$\begin{aligned} A_\alpha^{(ij)} &= -\frac{\Delta x_2^{(j)}}{\Delta x_1^{(ij)}}\frac{\rho_\alpha^{(ij)}}{\mu_\alpha}\, k_{\mathrm{s}1}\, k_{\mathrm{r}1\alpha}^{(ij)}, \qquad A_\alpha^{(jk)} = -\frac{\Delta x_2^{(j)}}{\Delta x_1^{(jk)}}\frac{\rho_\alpha^{(jk)}}{\mu_\alpha}\, k_{\mathrm{s}1}\, k_{\mathrm{r}1\alpha}^{(jk)}, \\ A_\alpha^{(lj)} &= -\frac{\Delta x_1^{(j)}}{\Delta x_2^{(lj)}}\frac{\rho_\alpha^{(lj)}}{\mu_\alpha}\, k_{\mathrm{s}2}\, k_{\mathrm{r}2\alpha}^{(lj)}, \qquad A_\alpha^{(jm)} = -\frac{\Delta x_1^{(j)}}{\Delta x_2^{(jm)}}\frac{\rho_\alpha^{(jm)}}{\mu_\alpha}\, k_{\mathrm{s}2}\, k_{\mathrm{r}2\alpha}^{(jm)}, \\ A_\alpha^{(jj)} &= -\left(A_\alpha^{(ij)} + A_\alpha^{(jk)} + A_\alpha^{(lj)} + A_\alpha^{(jm)}\right). \end{aligned} \tag{3.19}$$

where $k_{\mathrm{s}1}$, $k_{\mathrm{s}2}$, $k_{\mathrm{r}1\alpha}$ and $k_{\mathrm{r}2\alpha}$ represent the intrinsic and relative permeabilities in the direction of x_1 and x_2, respectively (in a general case the relative permeability can be also direction-dependent). Assuming that the gravity force acts in the direction opposite to x_2 axis, the gravity term $G_\alpha^{(j)}$ represents the balance of the gravitational fluxes between pairs of nodes l–j and j–m, for which the coefficient $\zeta = 1$. This term can be written as:

$$G_\alpha^{(j)} = -\Delta x_1^{(j)}\frac{k_\mathrm{s}\, k_{\mathrm{r}\alpha}^{(lj)}}{\mu_\alpha} \left(\rho_\alpha^{(lj)}\right)^2 g + \Delta x_1^{(j)}\frac{k_\mathrm{s}\, k_{\mathrm{r}\alpha}^{(jm)}}{\mu_\alpha} \left(\rho_\alpha^{(jm)}\right)^2 g. \tag{3.20}$$

An analogous scheme in three dimensions involves values of the fluid pressure from node j and its six closest neighbours. Implementation of a fully anisotropic permeability and material heterogeneity is more naturally performed in the framework of the finite volume schemes, of which Eqs. (3.12) and (3.17) can be considered as special cases. These schemes are discussed in Sects. 3.2.3 and 3.2.4.

3.2.2 Finite Element Method

The finite element method is widely used in many fields of engineering. A general description of the method is provided by a number of textbooks, e.g. [30, 73]. Examples of its application to the subsurface flow modelling can be found in [33, 57–59, 71]. In the finite element method the spatial domain is divided into a number of sub-domains called finite elements, Fig. 3.2. Each element can be characterized by a different set of material properties. The values of the unknown functions are sought in a number of points (nodes). The global set of nodes typically consists of the grid vertices and, if a higher order of approximation is required, of additional points located at the grid edges and inside elements. An unknown function $u(\mathbf{x}, t)$ is approximated as:

$$u(\mathbf{x}, t) = \sum_{i=1}^{N_n} u^{(i)}(t)\, \Psi^{(i)}(\mathbf{x}), \tag{3.21}$$

where N_n is the number of nodes in the domain, $u^{(i)}(t)$ represent the nodal values of the unknown function (in general time-dependent) and $\Psi^{(i)}$ is the set of shape functions (trial functions). The shape functions are defined in such a way that the value of each function equals unity at node i and zero at all other nodes. Each function $\Psi^{(i)}$ can be split into a number of components, corresponding to the elements sharing node i. These components are called element shape functions, $\Psi_e^{(i)}$. Using the element shape functions, the approximation of the unknown function inside a single element can be written as:

$$u_{\mathrm{e}}(\mathbf{x}, t) = \sum_{i \in \mathscr{N}_{\mathrm{elem}}} u^{(i)}(t)\, \Psi_{\mathrm{e}}^{(i)}(\mathbf{x}), \tag{3.22}$$

where $\mathscr{N}_{\mathrm{elem}}$ denotes the set of nodes of the considered finite element. The basic types of elements and shape functions are listed below. They are used not only in the standard finite element method, but also in the finite volume schemes described in the following sections.

In the simplest case of one-dimensional linear element E_1 spanned over nodes i and j, Fig. 3.2a, the element shape functions are defined as:

$$\Psi_{\mathrm{e}}^{(i)}(x) = \frac{x^{(j)} - x}{\Delta x^{(ij)}}, \tag{3.23}$$

$$\Psi_{\mathrm{e}}^{(j)}(x) = \frac{x - x^{(i)}}{\Delta x^{(ij)}} \tag{3.24}$$

and their derivatives with respect to x are constant in the element:

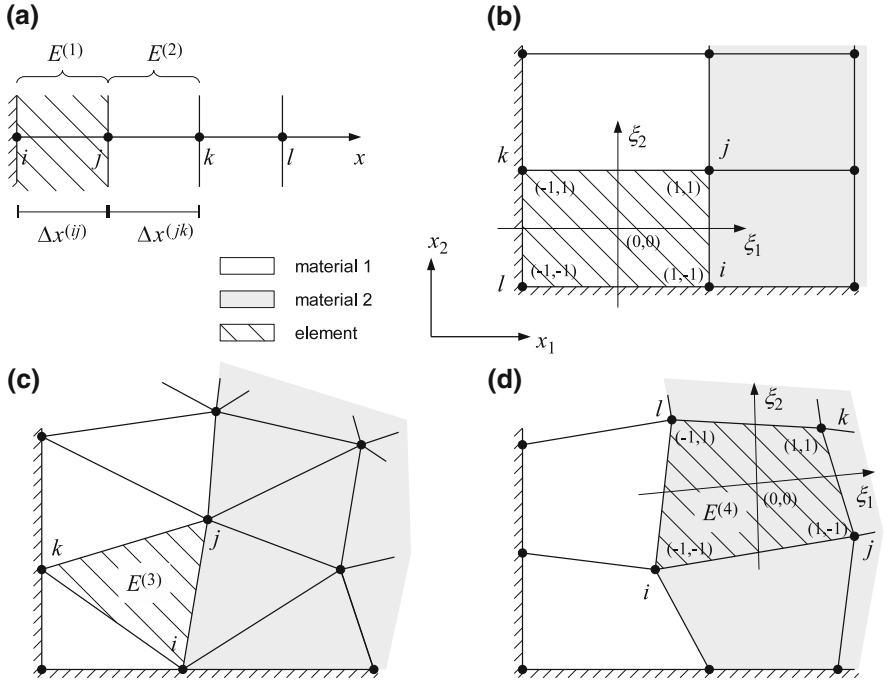

Fig. 3.2 Numerical grids for the finite element method: **a** one-dimensional linear elements, **b** two-dimensional rectangular elements, **c** two-dimensional triangular elements, **d** two-dimensional quadrilateral elements

$$\frac{\mathrm{d}\Psi_{\mathrm{e}}^{(i)}(x)}{\mathrm{d}x} = -\frac{1}{\Delta x^{(ij)}}, \tag{3.25}$$

$$\frac{\mathrm{d}\Psi_{\mathrm{e}}^{(j)}(x)}{\mathrm{d}x} = \frac{1}{\Delta x^{(ij)}}. \tag{3.26}$$

For a triangular element $E^{(3)}$ built on nodes i, j, and k, Fig. 3.2c, the linear shape functions are as follows:

$$\Psi_{\mathrm{e}}^{(i)}(x) = \frac{1}{2\,|E^{(3)}|}\left[\left(x_1^{(j)}\,x_2^{(k)} - x_1^{(k)}\,x_2^{(j)}\right) + \left(x_2^{(j)} - x_2^{(k)}\right)\,x_1 + \left(x_1^{(k)} - x_1^{(j)}\right)\,x_2\right], \tag{3.27}$$

$$\Psi_{\mathrm{e}}^{(j)}(x) = \frac{1}{2\,|E^{(3)}|}\left[\left(x_1^{(k)}\,x_2^{(i)} - x_1^{(i)}\,x_2^{(k)}\right) + \left(x_2^{(k)} - x_2^{(i)}\right)\,x_1 + \left(x_1^{(i)} - x_1^{(k)}\right)\,x_2\right], \tag{3.28}$$

$$\Psi_{\mathrm{e}}^{(k)}(x) = \frac{1}{2\,|E^{(3)}|}\left[\left(x_1^{(i)}\,x_2^{(j)} - x_1^{(j)}\,x_2^{(i)}\right) + \left(x_2^{(i)} - x_2^{(j)}\right)\,x_1 + \left(x_1^{(j)} - x_1^{(i)}\right)\,x_2\right], \tag{3.29}$$

where $|E^{(3)}|$ is the area of the element. The derivatives of the shape functions with respect to x_1 and x_2 are constant within the element:

$$\frac{\partial \Psi_{\mathrm{e}}^{(i)}}{\partial x_1} = \frac{1}{2\,|E^{(3)}|}(x_2^{(j)} - x_2^{(k)}), \qquad \frac{\partial \Psi_{\mathrm{e}}^{(i)}}{\partial x_2} = \frac{1}{2\,|E^{(3)}|}(x_1^{(k)} - x_1^{(j)}), \tag{3.30}$$

$$\frac{\partial \Psi_{\mathrm{e}}^{(j)}}{\partial x_1} = \frac{1}{2\,|E^{(3)}|}(x_2^{(k)} - x_2^{(i)}), \qquad \frac{\partial \Psi_{\mathrm{e}}^{(j)}}{\partial x_2} = \frac{1}{2\,|E^{(3)}|}(x_1^{(i)} - x_1^{(k)}), \tag{3.31}$$

$$\frac{\partial \Psi_{\mathrm{e}}^{(k)}}{\partial x_1} = \frac{1}{2\,|E^{(3)}|}(x_2^{(i)} - x_2^{(j)}), \qquad \frac{\partial \Psi_{\mathrm{e}}^{(k)}}{\partial x_2} = \frac{1}{2\,|E^{(3)}|}(x_1^{(j)} - x_1^{(i)}). \tag{3.32}$$

For an arbitrary quadrilateral element $E^{(4)}$, shown in Fig. 3.2d, the unknown functions can be conveniently approximated using shape functions defined in terms of local coordinates ξ_1 and ξ_2 :

$$u_{\mathrm{e}}(\mathbf{x}, t) = \sum_{i \in \mathcal{N}_{\mathrm{elem}}} u^{(i)}(t)\,\Psi_{\mathrm{e}}^{(i)}(\xi_1, \xi_2). \tag{3.33}$$

At the lowest approximation order, bilinear shape functions can be used, which have the following form:

$$\Psi_{\mathrm{e}}^{(i)} = \frac{1}{4}\,(1 - \xi_1)\,(1 - \xi_2)\,, \tag{3.34}$$

$$\Psi_{\mathrm{e}}^{(j)} = \frac{1}{4}\,(1 + \xi_1)\,(1 - \xi_2)\,, \tag{3.35}$$

$$\Psi_{\mathrm{e}}^{(k)} = \frac{1}{4}\,(1 + \xi_1)\,(1 + \xi_2)\,, \tag{3.36}$$

$$\Psi_{\mathrm{e}}^{(l)} = \frac{1}{4}\,(1 - \xi_1)\,(1 + \xi_2)\,, \tag{3.37}$$

where the nodes i, j, k and l are positioned with respect to the local coordinate axes ξ_1 and ξ_2, as shown in Fig. 3.2d. In contrast to the case of linear triangular elements, in the bilinear quadrilateral elements the gradients of the shape functions vary linearly in the element:

$$\frac{\partial \Psi_{\mathrm{e}}^{(i)}}{\partial \xi_1} = -\frac{1}{4}\,(1 - \xi_2)\,, \qquad \frac{\partial \Psi_{\mathrm{e}}^{(i)}}{\partial \xi_2} = -\frac{1}{4}\,(1 - \xi_1)\,, \tag{3.38}$$

$$\frac{\partial \Psi_{\mathrm{e}}^{(j)}}{\partial \xi_1} = \frac{1}{4}(1-\xi_2), \qquad \frac{\partial \Psi_{\mathrm{e}}^{(j)}}{\partial \xi_2} = -\frac{1}{4}(1+\xi_1), \tag{3.39}$$

$$\frac{\partial \Psi_{\mathrm{e}}^{(k)}}{\partial \xi_1} = \frac{1}{4}(1+\xi_2), \qquad \frac{\partial \Psi_{\mathrm{e}}^{(k)}}{\partial \xi_2} = \frac{1}{4}(1+\xi_1), \tag{3.40}$$

$$\frac{\partial \Psi_{\mathrm{e}}^{(l)}}{\partial \xi_1} = -\frac{1}{4}(1+\xi_2), \qquad \frac{\partial \Psi_{\mathrm{e}}^{(l)}}{\partial \xi_2} = \frac{1}{4}(1-\xi_1). \tag{3.41}$$

The relationship between the local coordinates and the global coordinates $\mathbf{x}$ is often obtained using the isoparametric approach, e.g. [30]. It is assumed that the global coordinate at an arbitrary point within the element can be expressed using the same shape functions as the unknown function:

$$x_1^{(\mathrm{e})}(\xi_1,\xi_2) = \sum_{i \in \mathcal{N}_{\mathrm{elem}}} x_1^{(i)}\, \Psi_{\mathrm{e}}^{(i)}(\xi_1,\xi_2), \tag{3.42}$$

$$x_2^{(\mathrm{e})}(\xi_1,\xi_2) = \sum_{i \in \mathcal{N}_{\mathrm{elem}}} x_2^{(i)}\, \Psi_{\mathrm{e}}^{(i)}(\xi_1,\xi_2). \tag{3.43}$$

The relations between the gradients of the shape functions with respect to the local and global coordinates can be written as:

$$\begin{bmatrix} \dfrac{\partial \Psi_{\mathrm{e}}^{(i)}}{\partial \xi_1} \\ \dfrac{\partial \Psi_{\mathrm{e}}^{(i)}}{\partial \xi_2} \end{bmatrix} = \mathbf{J}_{\mathrm{e}} \begin{bmatrix} \dfrac{\partial \Psi_{\mathrm{e}}^{(i)}}{\partial x_1} \\ \dfrac{\partial \Psi_{\mathrm{e}}^{(i)}}{\partial x_2} \end{bmatrix}, \tag{3.44}$$

$$\begin{bmatrix} \dfrac{\partial \Psi_{\mathrm{e}}^{(i)}}{\partial x_1} \\ \dfrac{\partial \Psi_{\mathrm{e}}^{(i)}}{\partial x_2} \end{bmatrix} = \mathbf{J}_{\mathrm{e}}^{-1} \begin{bmatrix} \dfrac{\partial \Psi_{\mathrm{e}}^{(i)}}{\partial \xi_1} \\ \dfrac{\partial \Psi_{\mathrm{e}}^{(i)}}{\partial \xi_2} \end{bmatrix}, \tag{3.45}$$

where $\mathbf{J}_{\mathrm{e}}$ and $\mathbf{J}_{\mathrm{e}}^{-1}$ denote the transformation jacobian for the element and its inverse, respectively:

$$\mathbf{J}_{\mathrm{e}} = \begin{bmatrix} \dfrac{\partial x_1}{\partial \xi_1} & \dfrac{\partial x_2}{\partial \xi_1} \\ \dfrac{\partial x_1}{\partial \xi_2} & \dfrac{\partial x_2}{\partial \xi_2} \end{bmatrix}, \tag{3.46}$$

$$\mathbf{J}_{\mathrm{e}}^{-1} = \frac{1}{|\mathbf{J}_{\mathrm{e}}|} \begin{bmatrix} \dfrac{\partial x_2}{\partial \xi_2} & -\dfrac{\partial x_2}{\partial \xi_1} \\ -\dfrac{\partial x_1}{\partial \xi_2} & \dfrac{\partial x_1}{\partial \xi_1} \end{bmatrix}, \tag{3.47}$$

The approximations described above are applied to the unknown functions in the governing equations (3.1). As the approximate functions do not satisfy exactly the governing equation, the differential operator at the left-hand side of equation yields a non-zero residual. The finite element method belongs to the group of weighted residual methods, which postulate that the integral of the residual of Eq. (3.1) multiplied by a weighting function $\Upsilon(\mathbf{x})$ (also called test function) be equal to zero:

$$\int_W \left(\frac{\partial M_\alpha}{\partial t} + \nabla \left(\rho_\alpha \, \mathbf{v}_\alpha \right) \right) \Upsilon(\mathbf{x}) \, \mathrm{d}W = 0, \tag{3.48}$$

where W denotes the solution domain. Applying the Gauss–Ostrogradski theorem to the divergence operator, one obtains the following weak formulation of the flow equation, which is the basis for the finite element solution:

$$\int_W \frac{\partial M_\alpha}{\partial t} \Upsilon(\mathbf{x}) \, \mathrm{d}W - \int_W \rho_\alpha \mathbf{v}_\alpha \nabla \Upsilon(\mathbf{x}) \, \mathrm{d}W + \int_{\partial W} \rho_\alpha \mathbf{v}_\alpha \, \mathbf{n}_\mathrm{W} \, \Upsilon(\mathbf{x}) \, \mathrm{d}\partial W = 0, \tag{3.49}$$

where ∂W is the boundary of the domain W and $\mathbf{n}_W$ is a unit vector normal to ∂W and directed outward. In the standard Galerkin approach, the weighting functions correspond to the shape functions, $\Upsilon^{(i)} = \Psi^{(i)}$. Equation (3.49) represents a set of equations written for each node i and the corresponding function $\Psi^{(i)}$. Each integral over the solution domain W can be expressed as a sum of the integrals taken over those elements E for which the weighting function assumes non-zero values:

$$\sum_{E \in \mathscr{E}^{(i)}} \int_E \frac{\partial M_\alpha}{\partial t} \Psi_\mathrm{e}^{(i)}(x) \, \mathrm{d}E - \sum_{E \in \mathscr{E}^{(i)}} \int_E \rho_\alpha \mathbf{v}_\alpha \nabla \Psi_\mathrm{e}^{(i)} \, \mathrm{d}E + \sum_{E \in \mathscr{E}^{(i)}} \int_{\partial E} \rho_\alpha \mathbf{v}_\alpha \, \mathbf{n}_W \, \Psi_\mathrm{e}^{(i)} \, \mathrm{d}\partial E = 0, \tag{3.50}$$

where $\mathscr{E}^{(i)}$ is the set of elements sharing node i and ∂E is the part of the external boundary of the domain coinciding with the boundary of element E. The third term on the left-hand side of Eq. (3.50) exists only for those elements which are adjacent to the external boundary of the domain, where a non-zero flux is specified as the boundary condition.

As an example, consider the solution of one dimensional Richards equation in a homogeneous medium:

$$\frac{\partial M_\mathrm{w}}{\partial t} + \frac{\partial}{\partial x}(\rho_\mathrm{w} \, v_\mathrm{w}) = 0, \tag{3.51}$$

$$v_\mathrm{w} = -\frac{k_\mathrm{s} \, k_\mathrm{rw}}{\mu_\mathrm{w}} \left(\frac{\partial p_\mathrm{w}}{\partial x} - \rho_\mathrm{w} \, g \, \zeta \right), \tag{3.52}$$

where M_w, ρ_w and k_rw are functions of p_w. In order to obtain the semi-discrete formulation, the approximation (3.21) can be applied to both M_w and p_w functions [13, 33]:

$$M_\mathrm{w}(x,t) = \sum_{i=1}^{N_n} M_\mathrm{w}^{(i)}(t)\,\Psi^{(i)}(x), \tag{3.53}$$

$$p_\mathrm{w}(x,t) = \sum_{i=1}^{N_n} p_\mathrm{w}^{(i)}(t)\,\Psi^{(i)}(x). \tag{3.54}$$

The semi-discrete equation for node j is assembled from the integrals for the elements $E^{(1)}$ and $E^{(2)}$, Fig. 3.2a. Integration of the storage term yields:

$$\begin{aligned}\int_{E^{(1)}} \frac{\partial M_\mathrm{w}}{\partial t}\Psi_\mathrm{e}^{(j)}\,\mathrm{d}E &= \frac{\partial M_\mathrm{w}^{(i)}}{\partial t}\int_{E^{(1)}} \Psi_\mathrm{e}^{(i)}\Psi_e^{(j)}\mathrm{d}E + \frac{\partial M_\mathrm{w}^{(j)}}{\partial t}\int_{E^{(1)}} \Psi_\mathrm{e}^{(j)}\Psi_\mathrm{e}^{(j)}\mathrm{d}E \\ &= \frac{\Delta x^{(ij)}}{6}\frac{\partial M_\mathrm{w}^{(i)}}{\partial t} + \frac{\Delta x^{(ij)}}{3}\frac{\partial M_\mathrm{w}^{(j)}}{\partial t}, \end{aligned}\tag{3.55}$$

$$\begin{aligned}\int_{E^{(2)}} \frac{\partial M_\mathrm{w}}{\partial t}\Psi_\mathrm{e}^{(j)}\,\mathrm{d}E &= \frac{\partial M_\mathrm{w}^{(j)}}{\partial t}\int_{E^{(2)}} \Psi_\mathrm{e}^{(j)}\Psi_\mathrm{e}^{(j)}\mathrm{d}E + \frac{\partial M_\mathrm{w}^{(k)}}{\partial t}\int_{E^{(2)}} \Psi_\mathrm{e}^{(k)}\Psi_\mathrm{e}^{(j)}\mathrm{d}E \\ &= \frac{\Delta x^{(jk)}}{3}\frac{\partial M_\mathrm{w}^{(j)}}{\partial t} + \frac{\Delta x^{(jk)}}{6}\frac{\partial M_\mathrm{w}^{(k)}}{\partial t}. \end{aligned}\tag{3.56}$$

The integral of the flux term over element $E^{(1)}$ can be expressed as:

$$\begin{aligned}&\int_{E^{(1)}} (\rho_\mathrm{w}\, v_\mathrm{w})\,\nabla\Psi_\mathrm{e}^{(j)}\,\mathrm{d}E \\ &\quad= -\left[\int_{E^{(1)}} \rho_\mathrm{w}\frac{k_\mathrm{s}\,k_\mathrm{rw}}{\mu_\mathrm{w}}\nabla p_\mathrm{w}\,\nabla\Psi_e^{(j)}\,\mathrm{d}E - \int_{E^{(1)}} \rho_\mathrm{w}^2\frac{k_\mathrm{s}\,k_\mathrm{rw}}{\mu_\mathrm{w}}\,g\zeta\,\nabla\,\Psi_\mathrm{e}^{(j)}\,\mathrm{d}E\right], \end{aligned}\tag{3.57}$$

where k_s and μ_w do not vary within the element. For linear shape functions both the pressure gradient and the shape function gradient are also uniform:

$$\frac{\partial p_\mathrm{w}}{\partial x} = \frac{p_\mathrm{w}^{(j)} - p_\mathrm{w}^{(j)}}{\Delta x^{(ij)}}, \tag{3.58}$$

$$\frac{\partial \Psi_\mathrm{e}^{(j)}}{\partial x} = \frac{1}{\Delta x^{(ij)}}. \tag{3.59}$$

While both ρ_w and k_rw depend on x locally in the element, the variability of the fluid density is usually small and a constant average value $\rho_\mathrm{w}^{(\mathrm{e})}$ can be assumed:

$$\rho_\mathrm{w}^{(\mathrm{e})} = \frac{1}{2}\left(\rho_\mathrm{w}^{(i)} + \rho_\mathrm{w}^{(j)}\right), \tag{3.60}$$

which allows to transform Eq. (3.57), so that only the relative permeability remains within the integral:

$$\begin{aligned}&\int_{E^{(1)}} (\rho_\mathrm{w}\, v_\mathrm{w})\, \nabla\, \Psi_\mathrm{e}^{(j)}\, \mathrm{d}E \\ &\quad = -\frac{\rho_\mathrm{w}^{(\mathrm{e})}\, k_\mathrm{s}}{\mu_w}\left[\frac{p_\mathrm{w}^{(j)}}{\Delta x^{(ij)}} - \frac{p_\mathrm{w}^{(i)}}{\Delta x^{(ij)}} - \rho^{(\mathrm{e})} g\zeta\right]\int_{E^{(1)}} k_\mathrm{rw}\, \mathrm{d}E.\end{aligned} \tag{3.61}$$

The relative permeability coefficient is in general highly variable, even within a single element. The corresponding integral can be written as:

$$\int_{E^{(1)}} k_\mathrm{rw}\, \mathrm{d}E = k_\mathrm{rw}^{(\mathrm{e})}\, \Delta x^{(ij)}, \tag{3.62}$$

where $k_\mathrm{rw}^{(\mathrm{e})}$ is the average relative permeability in the element, which can be variously defined, depending on the method used to approximate the integral. For example, one can assume that the relative permeability coefficient varies linearly between the nodes, which leads to a formula equivalent to the arithmetic mean:

$$k_\mathrm{rw}^{(\mathrm{e})} = \frac{1}{2}\left(k_\mathrm{rw}^{(i)} + k_\mathrm{rw}^{(j)}\right). \tag{3.63}$$

Alternatively, one can evaluate k_rw as a function of the water pressure at a specific number of points within the element and use a quadrature rule to approximate the integral. In the simplest case of a single quadrature point, positioned in the centre of the element, one obtains:

$$k_\mathrm{rw}^{(\mathrm{e})} = k_\mathrm{rw}\left(\frac{p_\mathrm{w}^{(i)} + p_\mathrm{w}^{(j)}}{2}\right). \tag{3.64}$$

It is interesting to note that in the one-dimensional case with the water pressure varying linearly between the nodes, by increasing the number of the quadrature points one approaches the following result:

$$\int_{E^{(1)}} k_{\mathrm{rw}}\,\mathrm{d}E = \frac{\Delta x^{(ij)}}{p_{\mathrm{w}}^{(j)} - p_{\mathrm{w}}^{(i)}} \int_{p_{\mathrm{w}}^{(i)}}^{p_{\mathrm{w}}^{(j)}} k_{\mathrm{rw}}(\hat{p})\mathrm{d}\hat{p} = \Delta x^{(ij)} \frac{\Phi_{\mathrm{p}}\left(p_{\mathrm{w}}^{j}\right) - \Phi_{\mathrm{p}}\left(p_{\mathrm{w}}^{(i)}\right)}{p_{\mathrm{w}}^{(j)} - p_{\mathrm{w}}^{(i)}}, \quad (3.65)$$

where $\hat{p}$ is a dummy integration variable and Φ_{p} is the flux potential, as defined by Eq. (2.84). The corresponding value of the average permeability in the element is referred to as the integrated mean $k_{\mathrm{int}}^{(ij)}$:

$$k_{\mathrm{rw}}^{(\mathrm{e})} = k_{\mathrm{int}}^{(ij)} = \frac{1}{p_{\mathrm{w}}^{(j)} - p_{\mathrm{w}}^{(i)}} \int_{p_{\mathrm{w}}^{(i)}}^{p_{\mathrm{w}}^{(j)}} k_{\mathrm{rw}}(\hat{p})\mathrm{d}\hat{p} = \frac{\Phi_{\mathrm{p}}\left(p_{\mathrm{w}}^{(j)}\right) - \Phi_{\mathrm{p}}\left(p_{\mathrm{w}}^{(i)}\right)}{p_{\mathrm{w}}^{(j)} - p_{\mathrm{w}}^{(i)}}. \quad (3.66)$$

The final form of the integral of the flux term can be written as:

$$\int_{E^{(1)}} (\rho_{\mathrm{w}}\, v_{\mathrm{w}})\, \nabla \Psi_{\mathrm{e}}^{(j)}\,\mathrm{d}E = -\frac{\rho_{\mathrm{w}}^{(\mathrm{e})}\, k_{\mathrm{s}}\, k_{\mathrm{rw}}^{(\mathrm{e})}}{\mu_\alpha} \left(\frac{p_{\mathrm{w}}^{(j)}}{\Delta x^{(ij)}} - \frac{p_{\mathrm{w}}^{(i)}}{\Delta x^{(ij)}} + \rho_{\mathrm{w}}^{(\mathrm{e})} g \zeta \right). \quad (3.67)$$

An analogous formula arises from the integration in element $E^{(2)}$. Assembling the contributions from both elements one obtains the following semi-discrete equation for the node j:

$$\frac{\Delta x^{(ij)}}{6} \frac{\mathrm{d}M_{\mathrm{w}}^{(i)}}{\mathrm{d}t} + \frac{\Delta x^{(ij)} + \Delta x^{(jk)}}{3} \frac{\mathrm{d}M_{\mathrm{w}}^{(j)}}{\mathrm{d}t} + \frac{\Delta x^{(jk)}}{6} \frac{\mathrm{d}M_{\mathrm{w}}^{(j)}}{\mathrm{d}t} + A_\alpha^{(ji)} p_\alpha^{(i)} + A_\alpha^{(jj)} p_\alpha^{(j)} + A_\alpha^{(jk)} p_\alpha^{(k)} + G_\alpha^{(j)} = 0, \quad (3.68)$$

where the flow coefficients $A_\alpha^{(ij)}$ and the gravity term $G_\alpha^{(j)}$ are the same as in Eqs. (3.13)–(3.16), if the element permeability $k_{\mathrm{rw}}^{(\mathrm{e})}$ is evaluated by the same formula as the internodal permeability $k_{\mathrm{rw}}^{(ij)}$.

The approximation of the storage term includes contributions from node j and neighbouring nodes i and k. It was shown that such an approximation of the time derivative leads to oscillations in the water pressure profiles. This problem was investigated in detail in [13, 36, 51]. The technique commonly applied in multiphase and unsaturated flow simulations in order to avoid oscillations is known as the mass-lumping (diagonalization of the storage term). The integral of the storage term evaluated consistently with the finite element approach, which for an element $E^{(n)}$ can be written as:

$$\int_{E^{(n)}} \frac{\partial M_\alpha}{\partial t}\, \Psi_{\mathrm{e}}^{(j)}\,\mathrm{d}E = \sum_{i \in \mathscr{N}_{\mathrm{elem}}^{(n)}} \left(\frac{\partial M_\alpha^{(i)}}{\partial t} \int_{E^{(n)}} \Psi_{\mathrm{e}}^{(i)}\, \Psi_{\mathrm{e}}^{(j)} \mathrm{d}E \right), \quad (3.69)$$

is replaced by the mass-lumped approximation:

$$\int_{E^{(n)}} \frac{\partial M_\alpha}{\partial t} \Psi_{\mathrm{e}}^{(j)} \, \mathrm{d}E = \frac{\partial M_\alpha^{(j)}}{\partial t} \sum_{i \in \mathcal{N}_{\mathrm{elem}}^{(n)}} \left(\int_{E^{(n)}} \Psi_{\mathrm{e}}^{(i)} \, \Psi_{\mathrm{e}}^{(j)} \mathrm{d}E \right). \tag{3.70}$$

As a result, the semi-discrete equation for node j contains only the spatial derivative of the conserved quantity at node j, i.e. the storage properties are restricted to grid nodes. For one-dimensional flow in a homogeneous medium, the application of mass lumping leads to a semi-discrete finite element scheme that is identical to the finite difference scheme, provided that the average relative permeability in the element and the inter-nodal permeability in the finite difference scheme are approximated in the same way (e.g. as arithmetic means of nodal permeabilities).

If two-dimensional Richards equation is solved on a mesh composed of linear triangular elements, the gradients of shape functions are constant in each element and the average values of the density and relative permeability in the element can be approximated in a manner analogous to the one-dimensional case. For instance, arithmetic average of the nodal values is often used, e.g. [59, 71]:

$$k_{\mathrm{rw}}^{(\mathrm{e})} = \frac{1}{3} \left(k_{\mathrm{rw}}^{(i)} + k_{\mathrm{rw}}^{(j)} + k_{\mathrm{rw}}^{(k)} \right). \tag{3.71}$$

Alternatively, numerical integration can be employed. For a single quadrature point one obtains:

$$k_{\mathrm{rw}}^{(\mathrm{e})} = k_{\mathrm{rw}} \left(\frac{p_{\mathrm{w}}^{(i)} + p_{\mathrm{w}}^{(j)} + p_{\mathrm{w}}^{(k)}}{3} \right), \tag{3.72}$$

while for three quadrature points the formula is [66]:

$$k_{\mathrm{rw}}^{(\mathrm{e})} = \frac{1}{3} \left(k_{\mathrm{rw}} \left(p_{\mathrm{w}}^{A} \right) + k_{\mathrm{rw}} \left(p_{\mathrm{w}}^{B} \right) + k_{\mathrm{rw}} \left(p_{\mathrm{w}}^{C} \right) \right), \tag{3.73}$$

where the values of the pressure at the quadrature points can be interpolated from the nodal values:

$$\begin{bmatrix} p_{\mathrm{w}}^{A} \\ p_{\mathrm{w}}^{B} \\ p_{\mathrm{w}}^{C} \end{bmatrix} = \frac{1}{6} \begin{bmatrix} 4 & 1 & 1 \\ 1 & 4 & 1 \\ 1 & 1 & 4 \end{bmatrix} \begin{bmatrix} p_{\mathrm{w}}^{(i)} \\ p_{\mathrm{w}}^{(j)} \\ p_{\mathrm{w}}^{(k)} \end{bmatrix}. \tag{3.74}$$

In contrast to the one-dimensional case, for two-dimensional elements the integral of the relative permeability cannot be easily expressed in terms of the flux potential. In the case of quadrilateral elements, the gradients of the shape functions vary within the element and the flux term has to be integrated numerically.

Material heterogeneity is naturally accounted for in the finite element scheme, because the integral for each element is evaluated using element-specific capillary

and relative permeability functions. For the Richards equation the water saturation (and consequently the unit mass of water M_w) at node j in both elements is uniquely defined by the primary variable $p_w^{(j)}$. Additional considerations are required for the two-phase flow, since the water saturation is discontinuous at the material interface. However, the two values of saturation are related to each other by the extended capillary continuity condition, Eq. (2.108). A more detailed discussion of this issue is presented in Sect. 3.2.4.

Besides the standard Galerkin finite element method described above, other finite element schemes are also used to solve the two-phase flow model and the Richards equation. They include mixed-hybrid finite element, e.g. [9, 10, 22, 23] and the locally discontinuous Galerkin finite element [21, 44, 45]. In the mixed-hybrid finite elements the set of unknowns includes the values of the pressure in the centres of the elements and the values of the flow velocities at the centres of element edges, each type of unknown being approximated by different shape functions. This method provides more accurate description of the velocity field, which is crucial in many applications, for example when simulating the transport of dissolved contaminants. However, there is additional numerical cost due to the larger number of unknowns. The locally discontinuous Galerkin finite element method is based on the approximation of the unknown functions using shape functions that are defined only in a single element (in contrast to the standard Galerkin approach, where each shape function is defined over a number of neighbouring elements, sharing the same node). The local approximations are then coupled by appropriate conditions defined for the fluxes at element edges.

3.2.3 Cell-Centred Finite Volume Method

Due to their inherent conservative properties, the finite volume methods are widely used to solve partial differential equations representing principles of conservation of various physical quantities. In this group of methods, several discretization schemes are available. Some of them can be regarded as a development of the finite difference method, while others as special cases of the finite element approach. A general discussion is provided in e.g. [7, 20, 43]. Applications to subsurface flow are numerous, and include among others [16, 18, 19, 27, 55].

In the finite volume method, the solution domain is divided into a number of cells (finite volumes or control volumes), each containing a single computational node. The discretization schemes are based on the integral form of the mass conservation equation, applied to a control volume $V^{(j)}$, which can be written as follows:

$$\frac{\partial}{\partial t}\int\limits_{V^{(j)}} M_\alpha \,\mathrm{d}V^{(j)} + \int\limits_{\partial V^{(j)}} (\rho_\alpha \,\mathbf{v}_\alpha \mathbf{n}_V^{(j)})\,\mathrm{d}\partial V^{(j)} = 0, \tag{3.75}$$

where $\partial V^{(j)}$ denotes the boundary of cell $V^{(j)}$ and $\mathbf{n}_V^{(j)}$ is a unit vector normal to $\partial V^{(j)}$ and directed outwards. The semi-discrete analogue of Eq. (3.75) is then written for each cell. Assuming that the average value of the unit mass of fluid phase M_α in the control volume corresponds to the nodal value $M_\alpha^{(j)}$, the integral of the storage term can be expressed as:

$$\frac{\partial}{\partial t} \int\limits_{V^{(j)}} M_\alpha \, \mathrm{d}V = |V^{(j)}| \frac{\mathrm{d}M_\alpha^{(j)}}{\mathrm{d}t}, \tag{3.76}$$

The integral of the mass flux over the cell boundary is expressed as the sum of integrals over cell faces:

$$\int\limits_{\partial V^{(j)}} (\rho_\alpha \, \mathbf{v}_\alpha \, \mathbf{n}_V^{(j)}) \, \mathrm{d}\partial V^{(j)} = \sum_{F \in \partial V^{(j)}} \int\limits_F \left(\rho_\alpha \, \mathbf{v}_\alpha \, \mathbf{n}_V^{(j)} \right) \mathrm{d}\partial V^{(j)}, \tag{3.77}$$

where $|V^{(j)}|$ is the volume, area or length of the cell, depending on the dimensionality of the problem and F denotes those control volume faces which belong to the boundary of the cell $V^{(j)}$. The flux at each face is approximated by an algebraic formula involving the values of the fluid potential from the control volume $V^{(j)}$ and one or more adjacent control volumes. The resulting value is used with the opposite sign in the flux balance of both control volumes sharing the considered face. Thus, finite volume schemes ensure local mass conservation. Within this framework a variety of finite volume schemes can be developed, which differ in the methods of defining the control volumes, representing the material heterogeneities and approximating the fluxes at control volume faces.

A general division can be drawn between the cell-centred and vertex-centred schemes. In both approaches, the finite volume grid is constructed on a primary grid of the same type as used for the finite difference or finite element solution. In the cell-centred schemes, each element of the primary grid becomes a control volume, with the corresponding computational node placed in its geometric center, Fig. 3.3. Each control volume is assumed to be materially homogeneous and the boundaries between distinct material regions coincide with the control volume boundaries. This approach is particularly appealing for one-dimensional problems or two-dimensional problems involving diagonally anisotropic media and rectangular grids. In such cases, the flux integral at an arbitrary face $F^{(ij)}$ between the control volumes $V^{(j)}$ and $V^{(i)}$ in Fig. 3.3a, can be approximated by a simple differential formula:

$$\int\limits_{F^{(ji)}} (\rho_\alpha \mathbf{v}_\alpha \, \mathbf{n}_V^{(j)}) \, \mathrm{d}F = -|F^{(ji)}| \frac{\rho_\alpha \, k_\mathrm{s} \, k_{\mathrm{r}\alpha}}{\mu_\alpha} \left(\frac{p_\alpha^{(j)} - p_\alpha^{(i)}}{\Delta x^{(ij)}} - \rho_\alpha \, g \, \zeta \right), \tag{3.78}$$

where $|F^{(ij)}|$ is the length or area of the face, depending on the dimension of the problem. This approach is sometimes called the control volume finite difference

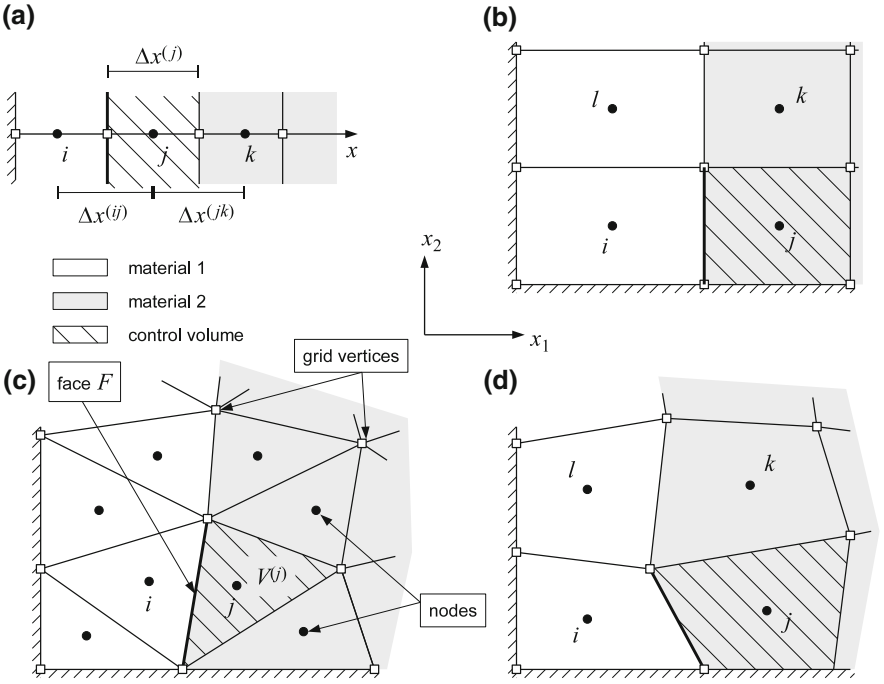

Fig. 3.3 Numerical grids for the cell-centred finite volume method: **a** one-dimensional grid, **b** two-dimensional rectangular grid, **c** two-dimensional triangular grid, **d** two-dimensional quadrilateral grid

method [68], because it can be viewed as a natural extension of the finite difference method. For instance, for one-dimensional problem, assuming unit dimensions of the domain in the directions perpendicular to the flow, the resulting semi-discrete equation for node j can be written in the same form as Eq. (3.12):

$$\Delta x^{(j)} \frac{\mathrm{d}M_\alpha^{(j)}}{\mathrm{d}t} + A_\alpha^{(ji)} p_\alpha^{(i)} + A_\alpha^{(jj)} p_\alpha^{(j)} + A_\alpha^{jk} p_\alpha^{(k)} + G_\alpha^{(j)} = 0, \tag{3.79}$$

with the coefficients $A_\alpha^{(ji)}$ and the gravity term $G_\alpha^{(j)}$ defined by Eqs. (3.13)–(3.15) and (3.16), respectively. However, the two schemes differ in the definition of $\Delta x^{(j)}$. In the finite difference method, the distance $\Delta x^{(j)}$ results from the assumed node spacing $\Delta x^{(ij)}$ and $\Delta x^{(jk)}$. In the cell-centred finite volume scheme the cell dimensions $\Delta x^{(j)}$ are assumed first, and the inter-nodal distances are then computed as:

$$\Delta x^{(ij)} = \frac{1}{2}\left(\Delta x^{(i)} + \Delta x^{(j)}\right). \tag{3.80}$$

In a general case of non-uniform cell sizes, the position of cell faces does not correspond to mid-distance between the cell centres. Therefore, in contrast to Eq. (3.5), Eq. (3.78) is only first-order accurate.

Another difference between the standard finite difference scheme and the cell-centred finite volume scheme is related to the implementation of the boundary conditions. In the cell-centred scheme, Neumann boundary conditions can be introduced in a natural way, by specifying the fluxes through the boundary faces of the corresponding cells. If the boundary condition is of Dirichlet type, the flux through the boundary face is approximated by a finite difference formula using the values of the pressure at the boundary and in the cell centre. The issue becomes more complicated for two phase flow, when the boundary condition for one phase is of Neumann type, while for the other of Dirichlet type. Consider, for example, a typical situation at the soil surface, when a specific infiltration flux is given for the wetting phase and the non-wetting phase pressure is equal to the atmospheric pressure (see Sect. 3.5). The non-wetting phase boundary flux can be computed from the pressure difference between the boundary and cell centre, but the permeability depends on the capillary pressure, which is a priori unknown at the surface, because the wetting phase pressure is unknown. The wetting phase pressure can be obtained from the flux condition, but this requires solution of a nonlinear equation.

Similarly to the finite element method, the cell-centred finite volume method allows for a natural representation of the material heterogeneities, by assigning a different set of constitutive properties to each cell. If the neighbouring cells belong to different material regions, the intrinsic permeabilities k_s are different at each node, which means that instead of averaging only the relative permeability, one has to average the total permeability $k_\alpha = k_s k_{r\alpha}$. A physically consistent averaging scheme should satisfy the conditions for the continuity of the fluid pressure and normal flux across the material interface, introduced in Sect. 2.3.3. The estimation of the inter-nodal permeability across a material interface for one-dimensional problems is discussed in more detail in the next chapter.

For non-rectangular grids, a two-point flux approximation based only on the values of the fluid pressures from the two control volumes adjacent to the considered face is generally inaccurate, as the lines connecting cell centres are not orthogonal to the cell faces [18]. The accuracy can be improved if the values of the fluid pressure from other neighbouring cells are taken into account in the approximation of the pressure gradient, which leads to multi-point flux approximations. For instance, in the case of triangular grids the diamond scheme can be used. This scheme requires the pressure values from the cells i and j and from the two vertices of primary grid, which coincide with the endpoints of the considered face. However, the values at the vertices are not explicitly computed in the solution to the discrete equation, and a reconstruction (interpolation) procedure is required to express each vertex value as a weighted average of the values at the centres of the control volumes sharing the vertex. Several reconstruction schemes are available, including weighting by inverse distance and least squares interpolation [47, 63]. While the diamond scheme can be considered as a simple case of multi-point stencil, the term multi-point flux approximations is generally applied to the schemes, which makes explicit use of the

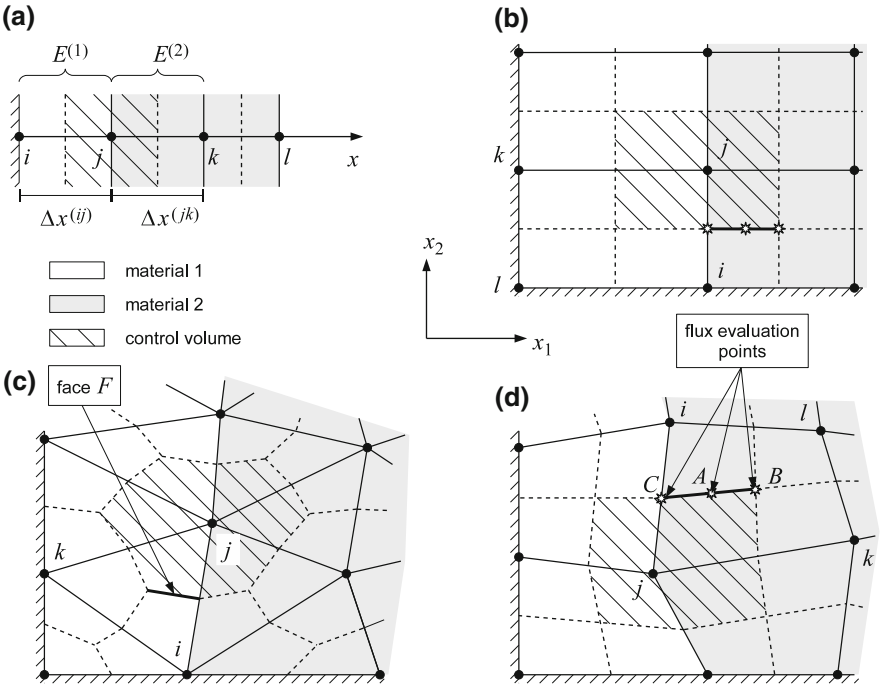

Fig. 3.4 Numerical grids for the vertex-centred finite volume method: **a** one-dimensional grid, **b** two-dimensional rectangular grid, **c** two-dimensional triangular grid, **d** two-dimensional quadrilateral grid

pressure and flux continuity conditions to reconstruct pressure values at the control volume faces. For a more detailed discussion of such schemes, see e.g. [1, 18].

3.2.4 Vertex-Centred Finite Volume Method

The second branch of the finite volume discretization approaches is represented by the vertex-centred schemes. In this case the control volumes are created around each vertex of the primary grid, forming a dual grid, as shown in Fig. 3.4. For one-dimensional problems the dual grid is created in a straightforward manner by assigning to the control volume around vertex j one half of each of the two elements sharing this vertex, i.e. $E^{(1)}$ and $E^{(2)}$. At the boundary, the control volume contains only a half of the adjacent element. Note that if the size of the elements is not uniform, the computational nodes (vertices) are not at the geometric centres of the corresponding control volumes.

For two-dimensional primary grids consisting of triangular elements, the dual grid can be defined using a number of alternative approaches, as shown in Fig. 3.5, e.g. [7].

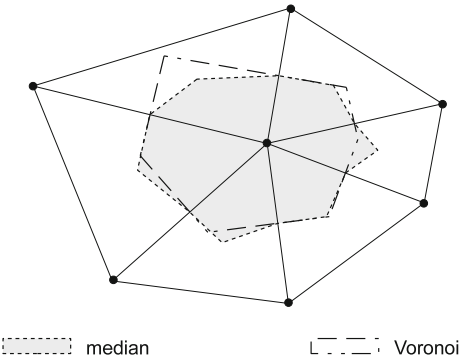

Fig. 3.5 Various methods of defining the dual grid for a triangular primary grid

In the median-dual method, the barycenter of each element is connected by line segments to the mid-points of the element sides (primary grid edges). Another possibility is to use the Voronoi diagram. In this approach the dual mesh consists of lines joining the circumcentres of adjacent elements. The circumcentre of a triangle (the centre of circumscribed circle) is located at the point of intersection of the perpendicular bisectors of its sides. Therefore, the control volume faces are perpendicular to the edges of the primary mesh. This is a useful property in the case of isotropic medium, because the gradient and flux normal to the faces can be easily computed from the values at the two endpoints of the corresponding edge. The third option is the centroid-dual grid, obtained by joining the barycenters of adjacent elements with straight segments. The median-dual method is the most flexible approach, as it does not require any limitations on the shape of the triangles. It can be easily extended to quadrilateral elements (Fig. 3.4 b, d) and to other element shapes in two and three dimensions.

Several important features distinguish the vertex-centred schemes from the cell-centred schemes. The computational nodes coincide with the vertices of the primary grid. Therefore, one has a direct access to the values of unknowns at the external boundaries of the domain, and at the internal boundaries separating different material regions. The control volumes located at the internal boundaries are heterogeneous, containing two or more materials. Thus, the saturations of the fluid phases are discontinuous within the control volumes, which must be properly accounted for in the discretization of the storage term. On the other hand, the faces separating control volumes are located in materially homogeneous elements of the primary grid, which simplifies the evaluation of the flux term. Even more importantly, the gradients of the fluid pressures at a given point of the control volume face can be evaluated using the finite element approach, where the pressure within an element is represented via the nodal values and element shape functions. The resulting scheme is often called control volume finite element method [33, 68]. It is described in more detail below.

Consider the control volume around node j, composed of two materials, (I) and (II), as shown in Fig. 3.4. In evaluating the storage term, one has to refer to the conditions at material interfaces, as described in Sect. 2.3.3. The continuity of the water pressure implies that a unique primary unknown $p_{\mathrm{w}}^{(j)}$ can be defined for node j.

Consequently, the water density is also uniquely defined. However, the porosities and water saturations are discontinuous at the interface. In the case of the Richards equation, the values of the saturations in both materials can be computed from the respective capillary functions, for the value of the capillary pressure $p_{\mathrm{c}}^{(j)} = -p_{\mathrm{w}}^{(j)}$:

$$\frac{\partial}{\partial t} \int\limits_{V^{(j)}} M_{\mathrm{w}}^{(j)} \, \mathrm{d}V^{(j)} = |V^{I(j)}| \frac{\partial}{\partial t} \left(\phi^I \, S_{\mathrm{w}}^I \left(p_{\mathrm{w}}^{(j)} \right) \rho_{\mathrm{w}}^{(j)} \right) + |V^{II(j)}| \frac{\partial}{\partial t} \left(\phi^{II} S_{\mathrm{w}}^{II} \left(p_{\mathrm{w}}^{(j)} \right) \rho_{\mathrm{w}}^{(j)} \right), \tag{3.81}$$

where $|V^{I(j)}|$ and $|V^{II(j)}|$ denote the volumes of the parts of the cell occupied by materials I and II, respectively.

In the case of two phase flow, the water saturation is the second independent variable, and a question arises, which of the two saturations should be taken as the primary variable at the given node. In view of the considerations presented in Sect. 2.3.3, the primary variable should represent the saturation in the material which has the lowest air-entry pressure [34], because in this case the second saturation can be uniquely defined as a function of the primary saturation, via the extended capillary pressure continuity condition, Eq. (2.108). Assuming that material I has a lower air entry pressure than material II, the primary variable $S_{\mathrm{w}}^{(j)}$ represents the saturation in material I, S_{w}^I. The corresponding capillary pressure is $p_{\mathrm{c}}^I(S_{\mathrm{w}}^{(j)})$ and the saturation in the second material is defined as $S_{\mathrm{w}}^{II} \left(p_{\mathrm{c}}^I \left(S_{\mathrm{w}}^{(j)} \right) \right)$, leading to the following approximation of the storage term:

$$\frac{\partial}{\partial t} \int\limits_{V^{(j)}} M_{\mathrm{w}}^{(j)} \, \mathrm{d}V^{(j)} = |V^{I(j)}| \frac{\partial}{\partial t} \left(\phi^I \, S_{\mathrm{w}}^{(j)} \, \rho_{\mathrm{w}}^{(j)} \right) + |V^{II(j)}| \frac{\partial}{\partial t} \left(\phi^{II} \, S_{\mathrm{w}}^{II} \left(p_{\mathrm{c}}^I \left(S_{\mathrm{w}}^{(j)} \right) \right) \rho_{\mathrm{w}}^{(j)} \right). \tag{3.82}$$

Similarly to the cell-centred scheme, in order to approximate the integral of the mass flux over a specific control volume face, the value of the flux is evaluated at a chosen point of the face and multiplied by the face length or area, depending on the dimensionality of the problem. In turn, the computation of the flux at a specific point requires the values of the pressure gradient, average density and average relative permeability:

$$\int\limits_F \left(\rho_\alpha \, \mathbf{v}_\alpha \, \mathbf{n}_V^{(j)} \right) \mathrm{d}F = Q_\alpha^{(\mathrm{fc})} = -|F| \frac{\rho_\alpha^{(\mathrm{fc})}}{\mu_\alpha} \mathsf{k}_\alpha^{(\mathrm{fc})} \left((\nabla p_\alpha)^{(\mathrm{fc})} - \rho_\alpha^{(\mathrm{fc})} \mathbf{g} \right) \mathbf{n}_V^{(j)}, \tag{3.83}$$

where the superscripts (fc) denote the average values of the specific quantities at the considered control volume face. In the control volume finite element approach, the

pressure gradient at face F is approximated using the shape functions for the respective element of the primary grid, which contains the control volume face. For one-dimensional or triangular elements and linear shape functions, the resulting values of the gradient are uniform within each element. For quadrilateral elements and bilinear shape functions, the gradient is non-uniform and a specific point on the face has to be chosen for evaluation. A usual choice is the midpoint of the face, denoted by A in Fig. 3.4d. The resulting algebraic formula involves values from all four vertices of the element. Alternatively one of the endpoints of the face can be used, i.e. either the geometric center of the element, B or the midpoint of the adjacent primary grid edge, C. In the former case, the same value of the gradient can be used for all faces in the element. The latter option can be advantageous for rectangular elements because the resulting formula for the normal gradient involves only two nodes (endpoints of the edge), instead of all four. For an isotropic or diagonally anisotropic medium, the five point finite difference stencil is recovered.

While the intrinsic permeability is uniform within the element, the relative permeability, which in general can be given by a tensor, depends on the position. It can be evaluated using several approaches. For instance, a single average value can be assumed for all faces in the element. This value can be obtained using one of the formulas presented in Sect. 3.2.2. Alternatively, the value of the permeability can be computed at the mid-point of the considered face, assuming a linear (or bilinear) distribution of either the permeability itself, or the argument to the permeability function, i.e. the water saturation or capillary pressure. In each of these cases the permeability depends on the primary unknowns from all vertices of the element. Another, widely used option is to evaluate the permeability for the considered face based only on the two nodes located at the opposite sides of the face, which are the endpoints of the adjacent edge of the primary grid (nodes i and j for the face F shown in Fig. 3.4b, c and d). This approach allows to apply the upstreaming of the relative permeability:

$$k_{\mathrm{r}\alpha}^{(\mathrm{fc})} = \begin{cases} k_{\mathrm{r}\alpha}^{(j)} & \text{if} \quad (\nabla p_\alpha - \rho_\alpha^{(\mathrm{fc})} \mathbf{g})\, \mathbf{n}_V^{(j)} \quad \leq 0, \\ k_{\mathrm{r}\alpha}^{(i)} & \text{if} \quad (\nabla p_\alpha - \rho_\alpha^{(\mathrm{fc})} \mathbf{g})\, \mathbf{n}_V^{(j)} \quad > 0. \end{cases} \tag{3.84}$$

As it has been already mentioned, permeability upstreaming ensures monotonous solution in case of advection-dominated flow, at the cost of increased numerical diffusion. However, in the case of the Richards equation with scalar relative permeability, a number of more accurate schemes are available to estimate the average permeability for one dimensional flow between two nodes. As shown in the following chapter, they can be also used in a multidimensional setting.

The density at the control volume face can be approximated using various methods, e.g. it can be equal to the arithmetic mean of the values from the opposite nodes, to the value from the upstream node, or to the value at face mid-point, interpolated from all nodes of the grid element containing the face. In the following numerical simulations, the density is approximated as an arithmetic average.

Assembling the flux integrals from all faces of the control volume $V^{(j)}$ results in the following equation:

$$|V^{(j)}|\frac{\mathrm{d}M_\alpha^{(j)}}{\mathrm{d}t} + \sum_{F\in\partial V^{(j)}} Q_\alpha^{(\mathrm{fc})} = 0, \tag{3.85}$$

where each flux term $Q_\alpha^{(\mathrm{fc})}$ depends on the nodal values of the phase pressure:

$$Q_\alpha^{(\mathrm{fc})} = \sum_{i\in\mathscr{N}_{\mathrm{elem}}} (A_\alpha^{\mathrm{fc(i)}} p_\alpha^{(i)}) + G_\alpha^{(\mathrm{fc})}, \tag{3.86}$$

where $\mathscr{N}_{\mathrm{elem}}$ denotes the set of vertices of the element containing the considered control volume face and the coefficients $A_\alpha^{\mathrm{fc(i)}}$ depend on the geometry, permeability and fluid properties. The above equation can be rewritten in an expanded form:

$$|V^{(j)}|\frac{\mathrm{d}M_\alpha^{(j)}}{\mathrm{d}t} + \sum_{k\in\mathscr{N}_{\mathrm{node}}^{(j)}} \left(A_\alpha^{(jk)} p_\alpha^{(k)}\right) + G_\alpha^{(j)} = 0, \tag{3.87}$$

where the set $\mathscr{N}_{\mathrm{node}}^{(j)}$ includes the nodes of all elements contributing to the control volume $V^{(j)}$. The coefficients $A_\alpha^{(jk)}$ and the gravity term $G_\alpha^{(j)}$ are obtained by assembling the contributions from all control volume faces.

A number of particular cases of this general control volume finite element scheme can be distinguished. For instance, in one dimensional flow one obtains the finite difference scheme given by Eq. (3.12), which is also identical with the lumped finite element scheme, if the same formula is used for the average permeability in the element and for the permeability at the control volume face. For a rectangular grid in a homogeneous and diagonally anisotropic domain, Eq. (3.87) reduces to the five point finite difference scheme given by Eq. (3.17), if the flux for each control volume face is evaluated at the midpoint of the adjacent edge, instead of the midpoint of the face. Another special case arises for a triangular grid in an isotropic domain, if the dual grid is constructed as the Voronoi diagram, Fig. 3.5. In such a case, the pressure gradient in the direction normal to the face can be accurately approximated using only the values from the two nodes at the opposite sides of the face.

The control volume finite element spatial discretization described above can be easily extended to the case of axisymmetric flow in coordinate system r–z. In such a case, it is only necessary to replace two-dimensional area $|V^{(j)}|$ with the volume of three-dimensional figure obtained by rotation with respect to the z axis. In a similar manner the lengths of the faces $|F|$ should be replaced by the areas of the corresponding surfaces of revolution. The scheme can be also extended to three dimensions.

It should be noted that another variant of the vertex-centred method exists, where the material properties are assigned to the control volumes of the dual grid and not

to the elements of the primary grid. The resulting scheme becomes similar to the cell-centred scheme. As each control volume is homogeneous, the evaluation of the storage term is simpler than in the case of element-oriented material distribution. On the other hand, the material interfaces run across the elements of primary grid, implying a discontinuity of the pressure gradient within the corresponding element. Therefore, special discretization techniques, similar to the ones developed for the cell-centred schemes, are required to obtain physically consistent flux approximations, which satisfy the continuity conditions at the material interfaces [17]. Moreover, the position of the material interfaces in the solution domain typically corresponds to the primary grid edges, since the primary grid is constructed from the geometric data characterizing the solution domain. If uniform material properties are assigned to the control volumes located at the interface, it means that the position of the interface on the numerical grid is shifted with respect to its real position [49]. For this reasons vertex-centred schemes with control volume-oriented material distribution are not used in this book.

3.3 Solution of Semi-Discrete Equations

3.3.1 Discretization in Time

Spatial discretization of the flow equations by the control volume finite element method results in a system of semi-discrete equations, which for the two-phase model can be written in the following form:

$$|V^{(j)}|\frac{\mathrm{d}\,M_{\mathrm{w}}^{(j)}}{\mathrm{d}\,t} + \sum_{k\in\mathscr{N}_{\mathrm{node}}^{(j)}} \left(A_{\mathrm{w}}^{(jk)} p_{\mathrm{w}}^{(j)}\right) + G_{\mathrm{w}}^{(j)} = 0, \tag{3.88}$$

$$|V^{(j)}|\frac{\mathrm{d}\,M_{\mathrm{a}}^{(j)}}{\mathrm{d}\,t} + \sum_{k\in\mathscr{N}_{\mathrm{node}}^{(j)}} \left(A_{\mathrm{a}}^{(jk)} p_{\mathrm{w}}^{(j)}\right) + \sum_{k\in\mathscr{N}_{\mathrm{node}}^{(j)}} \left(A_{\mathrm{a}}^{(jk)} p_{\mathrm{c}}\left(S_{\mathrm{w}}^{(j)}\right)\right) + G_{\mathrm{a}}^{(j)} = 0. \tag{3.89}$$

If the p_{w}–S_{w} formulation is chosen, the bulk fluid density $M_{\alpha}^{(j)}$ at node j depends on the water pressure and saturation at this node. The flow coefficients $A_{\alpha}^{(jk)}$ and the gravity terms $G_{\alpha}^{(j)}$ depend in general on the water pressures and saturations at node i and the surrounding nodes from the set $\mathscr{N}_{\mathrm{node}}^{(j)}$. For the Richards model there is only one equation per node:

$$|V^{(j)}|\frac{\mathrm{d}\,M_{\mathrm{w}}^{(j)}}{\mathrm{d}\,t} + \sum_{k\in\mathscr{N}_{\mathrm{node}}^{(j)}} \left(A_{\mathrm{w}}^{(jk)}\, p_{\mathrm{w}}^{(j)}\right) + G_{w}^{(j)} = 0, \tag{3.90}$$

in which the bulk fluid density $M_{\mathrm{w}}^{(j)}$ depends solely on the nodal water pressure, while the coefficients $A_{\mathrm{w}}^{(jk)}$ and the term $G_{\mathrm{w}}^{(j)}$ are functions of the nodal water pressures from node j and the set of surrounding nodes. Similar formulations result from the application of the methods of finite differences, cell-centred finite volumes and mass-lumped finite elements.

Since $M_{\alpha}^{(j)}$ is an algebraic function of the primary variables p_{w} and S_{w}, Eqs. (3.88)–(3.89) represent a system of differential algebraic equations, e.g. [39]. It is possible to convert it to a system of ordinary differential equations, where the derivatives of the primary variables with respect to time appear explicitly. This can be done by applying the chain differentiation rule to the storage term, as shown in Eq. (2.66). Such an approach is typically used in the single-phase groundwater flow simulations, where $M_{\mathrm{w}}^{(j)}$ depends linearly on p_{w} [54, 74]. A shortcoming of this technique is that the conserved quantity (the mass of water M_{w}) no longer appears explicitly in the discrete equation. Moreover, in the case of multiphase flow the storage coefficients depend nonlinearly on the primary variables, and additional error is introduced when their value is averaged between the subsequent discrete time levels [3]. This is particularly important in the case of the Richards equation, for which conversion to the ordinary differential equations (i.e. to the pressure-based form, given by Eq. (2.69)), may lead to significant mass balance errors [13], because the specific storage capacity C_{ch} strongly depends of p_{w}. For this reason a mass-conserving approach is adopted here, following [12, 13]. The time-discretization scheme is applied directly to the mass storage term $\mathrm{d}M_{\alpha}^{(j)}/\mathrm{d}t$.

Equations (3.88)–(3.89) and (3.90) can be written more concisely as:

$$\frac{\mathrm{d}M_{\alpha}^{(j)}}{\mathrm{d}t} = \mathscr{D}_{\alpha}^{(j)} \tag{3.91}$$

where $\mathscr{D}_{\alpha}^{(j)}$ is the spatial discretization operator. The semi-discrete system has to be solved in the considered time domain $\langle 0, t_{max} \rangle$. The values of the primary variables p_{w} and S_{w} at $t = 0$ and the corresponding values of $M_{\alpha}^{(j)}$ and $\mathscr{D}_{\alpha}^{(j)}$ are defined by the initial condition. Thus, the solution of the semi-discrete system is equivalent to the solution of an initial value problem for a system of differential algebraic equations. This can be achieved using a number of methods, as described for example in [4]. A general distinction can be made between explicit and implicit discretization schemes. In the explicit schemes, the value of the time derivative for the specific time step is approximated using the spatial discretization operator $\mathscr{D}_{\alpha}^{(j)}$ evaluated at a number of preceding time levels, for which the solution is known. In such a case, the values of unknowns for each node at the new time level can be computed independently of the other nodes. In the implicit schemes, the time derivative is approximated using the spatial discretization operator evaluated at the new time level. Consequently, one obtains a system of algebraic equations describing the dependencies between the nodal values of primary variables at the new time level, which must be solved for each time step. Depending on the number of previous time levels used to approximate

the new solution, the methods can be divided into single-step (only values from the last level) and multi-step (based on values from several earlier time levels).

Some commonly used single-step time-discretization schemes can be written in the following generalized form, e.g. [33]:

$$M_\alpha^{(j,\tau+1)} = M_\alpha^{(j,\tau)} + \Delta t \left(\Theta \mathscr{D}_\alpha^{(j,\tau+1)} + (1-\Theta) \mathscr{D}_\alpha^{(j,\tau)} \right), \tag{3.92}$$

where τ is the time level index, Δt is the time step and the weighting coefficient Θ ranges from 0 to 1. For $\Theta = 0$ one obtains the explicit Euler scheme, for $\Theta = 1$ the implicit Euler (or fully implicit) scheme and for $\Theta = 0.5$ the trapezoid scheme (also known as mid-point or Crank–Nicholson scheme). The latter one has the accuracy of the second order, while the two former—of the first order. Stability analysis carried out for the linear advection–diffusion equation shows that for $\Theta \geq 0.5$ the scheme is unconditionally stable, while for $\Theta < 0.5$ it is only conditionally stable, i.e. the time step Δt must be limited. For nonlinear equations the choice of $\Theta = 0.5$ may lead to oscillations in the solution between subsequent time steps [62, 71]. Due to its simplicity and stability, the implicit Euler scheme ($\Theta = 1$) is chosen for time discretization in the simulations presented in the following chapters.

While the use of low-order schemes is well-established in subsurface flow modelling, more recently a trend towards application of higher order time-discretization methods can be observed. Efficient implementation of such methods requires that the time step size and the order of approximation are continuously adjusted in response to the solution behaviour. A number of ready-made numerical packages for the integration of differential algebraic systems were successfully applied to model two-phase, unsaturated and saturated flow, including DASPK [64, 65], IDA [16] or DLSODIS [22]. It was shown that higher-order methods are more efficient than low-order methods, especially if very high solution accuracy is required. Their potential benefits notwithstanding, such approaches are not considered in this work, which focuses on the spatial discretization of the flux terms.

3.3.2 Linearization

Application of the implicit Euler time discretization scheme to the semi-discrete system given by Eqs. (3.88)–(3.89) or (3.90) yields a system of nonlinear algebraic equations for the time level $\tau + 1$, which can be written in the following general form:

$$\mathbf{F}(\mathbf{u}^{(\tau+1)}) = \begin{bmatrix} P^{(1)}(\mathbf{u}^{(\tau+1)}) \\ \vdots \\ P^{(N_u)}(\mathbf{u}^{(\tau+1)}) \end{bmatrix} = 0 \tag{3.93}$$

where N_u is the number of unknowns, $\mathbf{u}$ is the vector of the unknown nodal values at the new time level and $P^{(i)}$ are nonlinear algebraic functions. For the

two-phase flow model, the number of unknowns is twice the number of nodes, $N_u = 2N_n$:

$$\mathbf{P} = \begin{bmatrix} P_{\mathrm{w}}^{(1)} \\ P_{\mathrm{a}}^{(1)} \\ \vdots \\ P_{\mathrm{w}}^{(N_n)} \\ P_{\mathrm{a}}^{(N_n)} \end{bmatrix} \quad \text{and} \quad \mathbf{u} = \begin{bmatrix} p_{\mathrm{w}}^{(1)} \\ S_{\mathrm{w}}^{(1)} \\ \vdots \\ p_{\mathrm{w}}^{(N_n)} \\ S_{\mathrm{w}}^{(N_n)} \end{bmatrix} \tag{3.94}$$

and the nonlinear operators are defined as:

$$\begin{aligned} P_{\mathrm{w}}^{(j)} &= |V^{(j)}|\, M_{\mathrm{w}}^{(j,\tau+1)} - |V^{(j)}|\, M_{\mathrm{w}}^{(j,\tau)} \\ &\quad + \Delta t^{(\tau+1)} \sum_{k \in \mathcal{N}_{\mathrm{node}}^{(j)}} \left(A_{\mathrm{w}}^{(jk,\tau+1)}\, p_{\mathrm{w}}^{(k,\tau+1)} \right) + \Delta t^{(p+1)}\, G_{\mathrm{w}}^{(j,\tau+1)}, \end{aligned} \tag{3.95}$$

$$\begin{aligned} P_{\mathrm{a}}^{(j)} &= |V^{(j)}|\, M_{\mathrm{a}}^{(j,\tau+1)} - |V^{(j)}|\, M_{\mathrm{a}}^{(j,\tau)} + \Delta t^{(\tau+1)} \sum_{k \in \mathcal{N}_{\mathrm{node}}^{(j)}} \left[A_{\mathrm{a}}^{(jk,\tau+1)}\, p_{\mathrm{w}}^{(j,\tau+1)} \right] \\ &\quad + \Delta t^{(\tau+1)} \sum_{k \in \mathcal{N}_{\mathrm{node}}^{(j)}} \left[A_{\mathrm{a}}^{(jk,\tau+1)}\, p_{\mathrm{c}}^{(j,\tau+1)} \right) + \Delta t^{(\tau+1)}\, G_{\mathrm{a}}^{(j,\tau+1)} = 0. \end{aligned} \tag{3.96}$$

For the Richards equation the number of unknowns is equal to the number of nodes:

$$\mathbf{P} = \begin{bmatrix} P_R^{(1)} \\ \vdots \\ P_R^{(N_n)} \end{bmatrix} \quad \text{and} \quad \mathbf{u} = \begin{bmatrix} p_{\mathrm{w}}^{(1)} \\ \vdots \\ p_{\mathrm{w}}^{(N_n)} \end{bmatrix} \tag{3.97}$$

and the nonlinear operator for node j is:

$$\begin{aligned} P_R^{(j)} &= |V^{(j)}|\, M_{\mathrm{w}}^{(j,\tau+1)} - |V^{(j)}|\, M_{\mathrm{w}}^{(j,\tau)} \\ &\quad + \Delta t^{(\tau+1)} \sum_{k \in \mathcal{N}_{\mathrm{node}}^{(j)}} \left(A_{\mathrm{w}}^{(jk,\tau+1)}\, p_{\mathrm{w}}^{(j,\tau+1)} \right) + \Delta t^{(\tau+1)}\, G_{\mathrm{w}}^{(j,\tau+1)}. \end{aligned} \tag{3.98}$$

The algebraic system has to be solved iteratively. To this end, the Newton and or Picard methods are often employed. The Newton method is based on the Taylor expansion of a function of multiple variables around a specific point. Suppose that the value of $\mathbf{P}$ is known for an approximation of the solution $\mathbf{u}^{(\tau+1,\nu)}$, and one searches for the correction $\delta\mathbf{u}^{(\nu+1)}$, such that

$$\mathbf{P}(\mathbf{u}^{(\tau+1,\nu+1)}) = 0, \tag{3.99}$$

where:

$$\mathbf{u}^{(\tau+1,\nu+1)} = \mathbf{u}^{(\tau+1,\nu)} + \delta\mathbf{u}^{(\nu+1)}. \tag{3.100}$$

Making use of the Taylor expansion one can write:

$$\mathbf{P}\left(\mathbf{u}^{(\tau+1),\nu} + \mathbf{u}^{(\nu)}\right) \approx \mathbf{P}\left(\mathbf{u}^{(\tau+1,\nu)}\right) + \mathbf{J}^{(\nu)}\,\delta\mathbf{u}^{(\nu+1)} \tag{3.101}$$

where $\mathbf{J}^{(\nu)}$ denotes the jacobian matrix, containing the derivatives of the functions P with respect to the unknowns:

$$J_{mn}^{(\nu)} = \frac{\partial P^{(m,\tau+1,\nu)}}{\partial u^{(n,\tau+1,\nu)}}. \tag{3.102}$$

Requiring that Eq. (3.99) is satisfied, one obtains the following system of linear equations for the corrections of the primary unknowns:

$$\mathbf{J}^{(\nu)}\,\delta\mathbf{u}^{(\nu+1)} = -\mathbf{P}\left(\mathbf{u}^{(\tau+1,\nu)}\right). \tag{3.103}$$

Since Eq. (3.101) is only an approximation, the system of nonlinear equations is not exactly satisfied by $\mathbf{u}^{(\tau+1,\nu+1)}$ and the procedure must be repeated. The iterations are continued until a specific convergence criterion is met, as discussed below.

Consider a simple case of one-dimensional incompressible two-phase flow. The discretization operators for each node j can be written as:

$$\begin{aligned} P_{\mathrm{w}}^{(j,\tau+1,\nu)} = \Delta x^{(j)} &\left(M_{\mathrm{w}}^{(j,\tau+1,\nu)} - M_{\mathrm{w}}^{(j,\tau)}\right) + A_{\mathrm{w}}^{(ji,\tau+1,\nu)} p_{\mathrm{w}}^{(i,\tau+1,\nu)} \\ &+ A_{\mathrm{w}}^{(jj,\tau+1,\nu)} p_{\mathrm{w}}^{(j,\tau+1,\nu)} + A_{\mathrm{w}}^{jk,\tau+1,\nu} p_{\mathrm{w}}^{(k,\tau+1,\nu)} + G_{\mathrm{w}}^{(j,\tau+1,\nu)}. \end{aligned} \tag{3.104}$$

$$\begin{aligned} P_{\mathrm{a}}^{(j,\tau+1,\nu)} = \Delta x^{(j)} &\left(M_{\mathrm{a}}^{(j,\tau+1,\nu)} - M_{\mathrm{a}}^{(j,\tau)}\right) + A_{\mathrm{w}}^{(ji,\tau+1,\nu)} p_{\mathrm{w}}^{(i,\tau+1,\nu)} \\ &+ A_{\mathrm{a}}^{(jj,\tau+1,\nu)} p_{\mathrm{w}}^{(j,\tau+1,\nu)} + A_{\mathrm{a}}^{(jk,\tau+1,\nu)} p_{\mathrm{w}}^{(k,\tau+1,\nu)} \\ &+ A_{\mathrm{a}}^{(ji,\tau+1,\nu)} p_{\mathrm{c}}^{(i,\tau+1,\nu)} + A_{\mathrm{a}}^{(jj,\tau+1,\nu)} p_{\mathrm{c}}^{(j,\tau+1,\nu)} \\ &+ A_{\mathrm{a}}^{(jk,\tau+1,\nu)} p_{\mathrm{c}}^{(k,\tau+1,\nu)} + G_{\mathrm{a}}^{(j,\tau+1,\nu)}. \end{aligned} \tag{3.105}$$

The derivatives of the algebraic functions $P_{\mathrm{w}}^{(j,\tau+1,\nu)}$ and $P_{\mathrm{a}}^{(j,\tau+1,\nu)}$ with respect to the primary nodal unknowns $p_{\mathrm{w}}^{(j,\tau+1,\nu)}$ and $S_{\mathrm{w}}^{(j,\tau+1,\nu)}$ can be written as follows (superscripts $(\tau+1,\nu)$ are omitted for brevity):

$$\frac{\partial P_{\mathrm{w}}^{(j)}}{\partial p_{\mathrm{w}}^{(j)}} = \Delta t\, A_{\mathrm{w}}^{(jj)}, \tag{3.106}$$

$$\frac{\partial P_{\mathrm{w}}^{(j)}}{\partial S_{\mathrm{w}}^{(j)}} = \Delta x^{(j)} \frac{\partial M_{\mathrm{w}}^{(j)}}{\partial S_{\mathrm{w}}^{(j)}} + \Delta t \left(\frac{\partial A_{\mathrm{w}}^{(ji)}}{\partial S_{\mathrm{w}}^{(j)}} p_{\mathrm{w}}^{(i)} + \frac{\partial A_{\mathrm{w}}^{(jj)}}{\partial S_{\mathrm{w}}^{(j)}} p_{\mathrm{w}}^{(j)} + \frac{\partial A_{\mathrm{w}}^{(jk)}}{\partial S_{\mathrm{w}}^{(j)}} p_{\mathrm{w}}^{(k)} + \frac{\partial G_{\mathrm{w}}^{(j)}}{\partial S_{\mathrm{w}}^{(j)}} \right), \tag{3.107}$$

$$\frac{\partial P_{\mathrm{a}}^{(j)}}{\partial p_{\mathrm{w}}} = \Delta t \, A_{\mathrm{a}}^{(jj)}, \tag{3.108}$$

$$\frac{\partial P_{\mathrm{a}}^{(j)}}{\partial S_{\mathrm{w}}^{(j)}} = \Delta x^{(j)} \frac{\partial M_{\mathrm{a}}^{(j)}}{\partial S_{\mathrm{w}}^{(j)}} + \Delta t \left(\frac{\partial A_{\mathrm{a}}^{(ji)}}{\partial S_{\mathrm{w}}^{(j)}} p_{\mathrm{w}}^{(i)} + \frac{\partial A_{\mathrm{a}}^{(jj)}}{\partial S_{\mathrm{w}}^{(j)}} p_{\mathrm{w}}^{(j)} + \frac{\partial A_{\mathrm{a}}^{(jk)}}{\partial S_{\mathrm{w}}^{(j)}} p_{\mathrm{w}}^{(k)} + \frac{\partial A_{\mathrm{a}}^{(ji)}}{\partial S_{\mathrm{w}}^{(j)}} p_{\mathrm{c}}^{(i)} + \frac{\partial A_{\mathrm{a}}^{(jj)}}{\partial S_{\mathrm{w}}^{(j)}} p_{\mathrm{c}}^{(j)} + \frac{\partial A_{\mathrm{a}}^{(jk)}}{\partial S_{\mathrm{w}}^{(j)}} p_{\mathrm{c}}^{(k)} + A_{\mathrm{a}}^{(jj)} \frac{\partial p_{\mathrm{c}}^{(j)}}{\partial S_{\mathrm{w}}^{(j)}} + \frac{\partial G_{\mathrm{a}}^{(j)}}{\partial S_{\mathrm{w}}^{(j)}} \right), \tag{3.109}$$

where the derivatives of the subsequent terms are:

$$\frac{\partial M_{\mathrm{w}}^{(j)}}{\partial S_{\mathrm{w}}^{(j)}} = \phi \rho_{\mathrm{w}}, \tag{3.110}$$

$$\frac{\partial M_{\mathrm{a}}^{(j)}}{\partial S_{\mathrm{w}}^{(j)}} = -\phi \rho_{\mathrm{a}}, \tag{3.111}$$

$$\frac{\partial A_{\alpha}^{(ji)}}{\partial S_{\mathrm{w}}^{(j)}} = -\frac{1}{\Delta x^{(ij)}} \frac{\rho_{\alpha} k_{\mathrm{s}}}{\mu_{\alpha}} \frac{\partial k_{\mathrm{r}\alpha}^{(ij)}}{\partial S_{\mathrm{w}}^{(j)}}, \tag{3.112}$$

$$\frac{\partial A_{\alpha}^{(jk)}}{\partial S_{\mathrm{w}}^{(j)}} = -\frac{1}{\Delta x^{(jk)}} \frac{\rho_{\alpha} k_{\mathrm{s}}}{\mu_{\alpha}} \frac{\partial k_{\mathrm{r}\alpha}^{(jk)}}{\partial S_{\mathrm{w}}^{(j)}}, \tag{3.113}$$

$$\frac{\partial A_{\alpha}^{(jj)}}{\partial S_{\mathrm{w}}^{(j)}} = \frac{\rho_{\alpha} k_{\mathrm{s}}}{\mu_{\alpha}} \left(\frac{1}{\Delta x^{(ij)}} \frac{\partial k_{\mathrm{r}\alpha}^{(ij)}}{\partial S_{\mathrm{w}}^{(j)}} + \frac{1}{\Delta x^{(jk)}} \frac{\rho_{\alpha} k_{\mathrm{s}}}{\mu_{\alpha}} \frac{\partial k_{\mathrm{r}\alpha}^{(jk)}}{\partial S_{\mathrm{w}}^{(j)}} \right), \tag{3.114}$$

$$\frac{\partial G_{\alpha}^{(j)}}{\partial S_{\mathrm{w}}^{(j)}} = \frac{\rho_{\alpha}^2 k_{\mathrm{s}} g \zeta}{\mu_{\alpha}} \left(\frac{\partial k_{\mathrm{r}\alpha}^{(jk)}}{\partial S_{\mathrm{w}}^{(j)}} - \frac{\partial k_{\mathrm{r}\alpha}^{(jk)}}{\partial S_{\mathrm{w}}^{(j)}} \right). \tag{3.115}$$

For one-dimensional Richards equation (also without compressibility), the diagonal jacobian entry is:

$$\frac{\partial P_{\mathrm{w}}}{\partial p_{\mathrm{w}}} = \Delta x^{(j)} \frac{\partial M_{\mathrm{w}}^{(j)}}{\partial p_{\mathrm{w}}^{(j)}} + \Delta t \, A_{\mathrm{w}}^{(jj)} + \Delta t \left(\frac{\partial A_{\mathrm{w}}^{(ji)}}{\partial p_{\mathrm{w}}^{(j)}} p_{\mathrm{w}}^{(i)} + \frac{\partial A_{\mathrm{w}}^{(jj)}}{\partial p_{\mathrm{w}}^{(j)}} p_{\mathrm{w}}^{(j)} + \frac{\partial A_{\mathrm{w}}^{(jk)}}{\partial p_{\mathrm{w}}^{(j)}} p_{\mathrm{w}}^{(k)} + \frac{\partial G_{\mathrm{w}}^{(j)}}{\partial p_{\mathrm{w}}^{(j)}} \right), \tag{3.116}$$

where

$$\frac{\partial M_{\mathrm{w}}^{(j)}}{\partial p_{\mathrm{w}}^{(j)}} = -\phi \rho_{\mathrm{w}} \frac{\partial S_{\mathrm{w}}^{(j)}}{\partial p_{\mathrm{c}}^{(j)}}, \tag{3.117}$$

$$\frac{\partial A_{\mathrm{w}}^{(ji)}}{\partial p_{\mathrm{w}}^{(j)}} = \frac{1}{\Delta x^{(ij)}} \frac{\rho_{\mathrm{w}} k_{\mathrm{s}}}{\mu_{\mathrm{w}}} \frac{\partial k_{\mathrm{rw}}^{(ij)}}{\partial S_{\mathrm{w}}^{(j)}} \frac{\partial S_{\mathrm{w}}^{(j)}}{\partial p_{\mathrm{c}}^{(j)}}, \tag{3.118}$$

$$\frac{\partial A_{\mathrm{w}}^{(jk)}}{\partial p_{\mathrm{w}}^{(j)}} = \frac{1}{\Delta x^{(jk)}} \frac{\rho_{\mathrm{w}} k_{\mathrm{s}}}{\mu_{\mathrm{w}}} \frac{\partial k_{\mathrm{rw}}^{(jk)}}{\partial S_{\mathrm{w}}^{(j)}} \frac{\partial S_{\mathrm{w}}^{(j)}}{\partial p_{\mathrm{c}}^{(j)}}, \tag{3.119}$$

$$\frac{\partial A_{\mathrm{w}}^{(jj)}}{\partial p_{\mathrm{w}}^{(j)}} = -\frac{\rho_{\alpha} k_{\mathrm{s}}}{\mu_{\mathrm{w}}} \left(\frac{1}{\Delta x^{(ij)}} \frac{\partial k_{\mathrm{rw}}^{(ij)}}{\partial S_{\mathrm{w}}^{(j)}} + \frac{1}{\Delta x^{(jk)}} \frac{\rho_{w} k_{\mathrm{s}}}{\mu_{\mathrm{w}}} \frac{\partial k_{\mathrm{rw}}^{(jk)}}{\partial S_{\mathrm{w}}^{(j)}} \right) \frac{\partial S_{\mathrm{w}}^{(j)}}{\partial p_{\mathrm{c}}^{(j)}}, \tag{3.120}$$

$$\frac{\partial G_{\mathrm{w}}^{(j)}}{\partial p_{\mathrm{w}}^{(j)}} = -\frac{\rho_{\mathrm{w}}^2 k_{\mathrm{s}} g \zeta}{\mu_{\mathrm{w}}} \left(\frac{\partial k_{\mathrm{rw}}^{(jk)}}{\partial S_{\mathrm{w}}^{(j)}} - \frac{\partial k_{\mathrm{rw}}^{(jk)}}{\partial S_{\mathrm{w}}^{(j)}} \right) \frac{\partial S_{\mathrm{w}}^{(j)}}{\partial p_{\mathrm{c}}^{(j)}}. \tag{3.121}$$

The derivatives of $P_{\mathrm{w}}^{(j)}$ and $P_{\mathrm{a}}^{(j)}$ with respect to the primary variables from neighbouring nodes are calculated in a manner similar to the one shown above for the diagonal entries. While the evaluation can be done analytically, if all constitutive relationships are given by closed analytical expressions, the resulting formulas become cumbersome, especially if the compressibility effects are included. Numerical differentiation is often more convenient. The derivatives can be approximated using a forward differential formula, e.g. [26]:

$$J_{mn} = \frac{\partial F^{(m)}}{\partial u^{(n)}} = \frac{F^{(m)}(u^{(n)} + \upsilon, \dots) - F^{(m)}(u^{(n)}, \dots)}{\upsilon} \tag{3.122}$$

where υ is a small number. The choice of the parameter υ requires some consideration. The values cannot be too small, due to roundoff errors in the digital number representation. On the other hand, they must be small enough to ensure accurate approximation of the derivative. For the examples shown in the following chapters, satisfactory results were obtained with υ from the range 10^{-6} to 10^{-4} for both the water pressure and the water saturation ($\upsilon = 10^{-6}$ was recommended in [26]). The perturbed value of the primary unknown should be physically meaningful. For instance, if u represents the water saturation and the node is fully saturated, the derivative of the respective equation with respect to S_w must be approximated with backward formula, i.e. $\upsilon < 0$, because the functions $p_c(S_w)$ and $k_{r\alpha}(S)$ are defined for $S_w \leq 1$.

The Picard method can be considered as a simplification of the Newton method, obtained by neglecting some terms of the nonlinear equation in the evaluation of the derivatives. In the standard Picard approach only the terms of the form $A(u^{(j)})\, u^{(j)}$ are taken into account, with the derivative approximated as:

$$\frac{\partial \left(A(u^{(j)})\, u^{(j)} \right)}{\partial u^{(j)}} \approx A(u^{(j)}) \tag{3.123}$$

The standard Picard method is not used for subsurface flow equations. Instead, modified schemes are employed, where the dependency of p_c on S_w (or vice versa) is additionally taken into account. For the one-dimensional incompressible two-phase flow model, the diagonal entries of the jacobian are computed as:

$$\frac{\partial F_w^{(j)}}{\partial p_w^{(j)}} = \Delta t \; A_w^{(jj)} \tag{3.124}$$

$$\frac{\partial F_w^{(j)}}{\partial S_w^{(j)}} = \Delta x^{(j)} \frac{\partial M_w^{(j)}}{\partial S_w^{(j)}} \tag{3.125}$$

$$\frac{\partial F_a^{(j)}}{\partial p_w^{(j)}} = \Delta t \; A_a^{(jj)} \tag{3.126}$$

$$\frac{\partial F_a^{(j)}}{\partial S_w^{(j)}} = \Delta x^{(j)} \frac{\partial M_a^{(j)}}{\partial S_w^{(j)}} + \Delta t \; A_a^{(jj)} \frac{\partial p_c^{(j)}}{\partial S_w^{(j)}} \tag{3.127}$$

For the Richards equation without fluid compressibility, the diagonal entries are computed as follows:

$$\frac{\partial F_w^{(j)}}{\partial p_w^{(j)}} = \Delta x^{(j)} \frac{\partial M_w^{(j)}}{\partial p_w^{(j)}} + \Delta t \; A_w^{(jj)} \tag{3.128}$$

The above scheme, introduced by Celia et al. [13], is commonly used to solve the Richards equation, e.g. [10, 47, 59, 67]. In this context, it is often referred to as the modified Picard method. It can be further extended by taking into account the derivative of the gravity term, evaluated numerically [72]. Such modification was shown to be beneficial for gravity-dominated flow.

Both Newton and Picard schemes require appropriate specification of the first guess to the solution and the convergence criterion to terminate the iterations. The iterative procedure is usually started using the value from the last time step as the initial guess of the solution:

$$\mathbf{u}^{(\tau+1,\nu=0)} = \mathbf{u}^{(\tau)} \tag{3.129}$$

An alternative approach is to use value extrapolated from previous time steps, e.g. using the following formula [38]:

$$\mathbf{u}^{(\tau+1,\nu=0)} = \mathbf{u}^{(\tau)} + \frac{\partial \mathbf{u}}{\partial t} \Delta t^{(\tau+1)} + \frac{\partial^2 \mathbf{u}}{\partial t^2} \left(\Delta t^{(\tau+1)} \right)^2 \tag{3.130}$$

where the values of the derivatives can be approximated by finite difference formulas from the results at the previous time levels:

$$\frac{\partial \mathbf{u}}{\partial t} = \frac{\mathbf{u}^{(\tau)} - \mathbf{u}^{(\tau-1)}}{\Delta t^{(\tau)}} \tag{3.131}$$

$$\frac{\partial^2 \mathbf{u}}{\partial t^2} = \frac{2}{\Delta t^{(\tau)} + \Delta t^{(\tau-1)}} \left[\frac{\mathbf{u}^{(\tau)} - \mathbf{u}^{(\tau-1)}}{\Delta t^{(\tau)}} - \frac{\mathbf{u}^{(\tau-1)} - \mathbf{u}^{(\tau-2)}}{\Delta t^{(\tau-1)}} \right] \tag{3.132}$$

It should be noted that this formula may not be efficient if abrupt changes in the boundary conditions occur. Thus, if the time step is rejected due to the lack of convergence of the iterative solver, in the next attempt the more conservative initial guess given by Eq. (3.129) is recommended.

The iterative process ends when some specific termination criterion is satisfied. A common approach is to specify the termination criterion in terms of the absolute and relative change in the values of the primary variable, i.e. iterations are stopped when:

$$\delta u^{(j,\nu+1)} \leq s_{\text{abs}} + s_{\text{rel}} \left| u^{(j,\tau+1,\nu)} \right| \tag{3.133}$$

for all nodes j, where s_{abs} is the absolute error tolerance and s_{rel} is the relative error tolerance. In the case of two-phase flow, different tolerances should be specified for the saturation and water pressure. Most of the numerical simulations described in the following part of the book were performed using $s_{\text{abs}} = 1\,\text{Pa}$ and $s_{\text{abs}} = 10^{-5}$ for p_w, while for the water saturation only absolute tolerance was used, $s_{\text{abs}} = 10^{-4}$. For the Richards equation the termination criterion can be specified in terms of the water pressure, or a mixed criterion can be used [35, 59]. In the latter case, the allowable error is specified in terms of the absolute error in the water content (or saturation) in the unsaturated conditions and absolute error in the water pressure in the saturated conditions. It was shown that such criterion allows for faster termination of the iterative process without negatively affecting the accuracy.

Another possibility is to use a criterion related to the mass balance error. The value of the discrete operator $P_\alpha^{(j,\tau+1,\nu)}$ corresponds to the local error in the mass balance for node j, and ideally should be equal to zero. The iterations are stopped if the value is sufficiently close to zero:

$$P_\alpha^{(j,\tau+1,\nu)} \leq s_{\text{abs}}^{\text{mb}} + s_{\text{rel}}^{\text{mb}} \, M_\alpha^{(j,\tau+1,\nu)} \, |V^{(j)}| \tag{3.134}$$

where the absolute and relative tolerance $s_{\text{abs}}^{\text{mb}}$ and $s_{\text{rel}}^{\text{mb}}$ is provided by the user. For a discussion of other possible termination criteria, see e.g. [71].

The Newton and Picard iterative schemes for flow in porous media were compared by several authors, e.g. [5, 42, 52, 72]. Theoretically, the standard Newton method has quadratic convergence rate, compared to the linear convergence rate of the Picard method. Therefore, if the first guess is sufficiently close to the solution the Newton method converges faster than the Picard method. If this is not the case, the Newton scheme may fail to converge. The Picard scheme converges slower, but is less sensitive to the first guess. Some authors proposed a mixed iterative approach, where the first few iterations are performed with the Picard scheme, and the remaining ones with the Newton scheme. However, it is difficult to estimate a priori the number of Picard iterations required to reach the vicinity of the solution. For instance,

Lehmann and Ackerer [42] obtained good results using Picard scheme only for the first iteration, while in the simulations of Tracy [66] up to 20 Picard iterations were needed. Another option is to switch the schemes when the magnitude of corrections $\delta u^{(j,\nu+1)}$ falls below a specific threshold, which depends on the parameters of the numerical grid [11]. It is also important to note that the Newton method requires more computational effort than the Picard one, due to the necessity to evaluate the full jacobian. Other iterative approaches, which were proposed to solve the subsurface flow equations, include the quasi-Newton methods, where the value of the jacobian from the first iteration is reused in subsequent iterations e.g. [11], Broyden and Anderson acceleration applied to either Newton or Picard scheme, e.g. [11, 24, 69], relaxation, e.g. [71] and line search techniques, e.g. [53]. In the solution of coupled flow and deformation problems, the arc-length iterative method is often used, e.g. [50].

In the numerical examples from the following chapters the Newton method was used in conjunction with line search algorithm, which increases the chance of finding the solution if the first approximation is not in its neighbourhood [40, 53]. It is based on the assumption that the vector $\delta\mathbf{u}^{(\nu+1)}$ shows the correct direction of the decreasing residual value for the nonlinear system, but its magnitude may be too large, resulting in an overshooting of the solution. In each iteration the vector $\delta\mathbf{u}^{(\nu+1)}$ is first computed using the standard Newton approach, Eq. (3.103). The new approximation is accepted only if the corresponding residuum of the discretization operator is smaller than the residuum computed for the previous approximation:

$$\left\|\mathbf{P}\left(\mathbf{u}^{(\tau+1,\nu)}+\delta\mathbf{u}^{(\nu+1)}\right)\right\| < \left\|\mathbf{P}\left(\mathbf{u}^{(\tau+1,\nu)}\right)\right\| \tag{3.135}$$

where $\|\cdot\|$ denotes the Euclidean norm. If this condition is not satisfied, the Newton step is successively reduced by half: $\delta\mathbf{u}' = \delta\mathbf{u}^{(\nu+1)}/2,\ \delta\mathbf{u}^{(\nu+1)}/4, \ldots$ until a decrease in the residuum norm is obtained for $\mathbf{u}^{(\tau+1,\nu)} + \delta\mathbf{u}'$. For the range of examples considered in this book, the Newton approach with line search performed better than Picard, standard Newton, mixed Picard–Newton or quasi-Newton schemes. However, the efficiency of various iteration schemes is problem-dependent and this conclusion cannot be generalized.

3.3.3 Selection of Time Step Size

The use of constant time step is in most cases inefficient. The time step size should be adjusted during the simulation, so that small steps are taken when the solution varies strongly in time, for instance due to an abrupt change in the boundary conditions, while large steps are applied for the periods of smooth behaviour. In general, there are two strategies for the control of time step size. The first one is based on the

performance of the iterative method, e.g. [33, 59], while the other one on the estimation of the accuracy of approximation of the time discretization scheme, e.g. [37, 48, 64]. In the first case, it is required that the number of iterations necessary to reach convergence for each time step remains within a specified interval $\langle N_{\mathrm{it}}^{\min}, N_{\mathrm{it}}^{\max} \rangle$. If the number of iterations for a given time step was $N_{\mathrm{it}} > N_{\mathrm{it}}^{\max}$ then the next time step is reduced by a factor $C_{\mathrm{it}}^{\mathrm{dec}} < 1$. Conversely, if the number of iterations was $N_{\mathrm{it}} < N_{\mathrm{it}}^{\min}$, the time step is increased by a factor $C_{\mathrm{it}}^{\mathrm{inc}} > 1$. Since rapid changes in the time step size are not desirable, both factors are relatively close to 1. Usually, the minimum and maximum allowable values of Δt are also specified, in order to keep the time step size within reasonable limits. Numerical simulations showed in this book were performed using this approach, with $N_{\mathrm{it}}^{\min} = 3$, $N_{\mathrm{it}}^{\max} = 7$, $C_{\mathrm{it}}^{\mathrm{dec}} = 0.6$ and $C_{\mathrm{it}}^{\mathrm{inc}} = 1.1$.

An alternative method of time step control is based on the estimation of the truncation error of the time discretization scheme, which is proportional to $(\Delta t^p)^n$, where n is the order of accuracy of the scheme. The obtained values are compared to the error tolerance required for the specific problem, and the time step size is adjusted in such a way that the tolerance criterion is met. Such schemes are typically used in conjunction with high-order time integration methods, e.g. [22, 39, 48, 64], but they can be applied also in the framework of simpler low-order schemes, e.g. implicit Euler or trapezoid [37, 38].

3.3.4 Solution of Linear Systems

For each iteration performed in the framework of the Newton or Picard method, the system of linear equations (3.103) must be solved to obtain the corrections to the unknown nodal values $\delta \mathbf{u}^{(\nu+1)}$. The linear system is characterized by a sparse and banded coefficient matrix $\mathbf{J}^{(\nu)}$.

Systems of linear algebraic equations can be solved using either direct or iterative method. Direct methods allow to obtain an exact solution to the system in a finite number of arithmetic operations, with the accuracy limited only by the numerical roundoff error. These methods are usually based on Gaussian elimination or lower-upper decomposition. They are very efficient for sparse systems characterized by very narrow bandwidth, which arise from the discretization of one-dimensional flow equations. For multi-dimensional problems, the direct methods are generally considered inefficient, because the execution of the algorithm requires large amount of memory to store temporary values and large number of arithmetic operations.

The iterative methods provide a series of approximate solutions to the system, starting from the first guess, which is successively updated. If the series is convergent, its limit is the solution of the system. The major advantage of the iterative methods is that one can fully exploit the sparse structure of the coefficient matrix and each iteration requires much less computer memory and time than the solution by a direct

method. Thus, if sufficiently accurate approximation can be obtained in a limited number of iterations, the iterative methods largely outperform the direct methods for problems with large number of unknowns. However, similarly to the case of iterative schemes for nonlinear equations, the convergence is not warranted. Subsequent linear iterations may be divergent or the convergence may be very slow. The convergence of linear iterative methods depends heavily on the properties of the coefficient matrix, which should preferably be diagonally dominant, i.e. the largest coefficient (in terms of the absolute value) in each row should be located at the main diagonal. Such matrices arise from the discretization of the Richards equation. However, for the two phase flow the largest coefficients are usually positioned off-diagonally. The properties of the matrix can be improved by preconditioning, i.e. multiplication of both sides of the system of equations by a specially selected matrix, so that the resulting system is more amenable to the iterative solution. For a general discussion of iterative methods and preconditioning techniques, see [56]. Iterative methods used to solve the linear systems resulting from the discretization of subsurface flow equations include, among other, the generalized minimal residual (GMRES) [23, 65], conjugate gradient (CG) [41], conjugates gradient stabilized (CGSTAB) [26], bi-conjugate gradient stabilized (BiCGSTAB) [65], and multigrid methods [9]. Preconditioning techniques include incomplete lower-upper factorization (ILU) [26] and algebraic multigrid [8].

Since in this work relatively small discrete systems are considered (up to about 5000 unknowns), all numerical solutions were obtained using direct methods. They include versions of lower-upper decomposition for matrices with bandwidth equal to three and seven [25], used for the one-dimensional Richards equation and the one-dimensional two-phase model, respectively. Two-dimensional discrete systems were solved using a variant of Gaussian elimination for sparse matrices, as described in [61].

References

1. Aavatsmark I (2002) An introduction to multipoint flux approximations for quadrilateral grids. Comput Geosci 6(3–4):405–432. doi:10.1023/A:1021291114475
2. Abbot M, Basco D (1989) Computational fluid dynamics. An introduction for engineers. Longman, Harlow
3. Abriola L, Rathfelder K (1993) Mass balance errors in modeling two-phase immiscible flows: causes and remedies. Adv Water Resour 16(4):223–239. doi:10.1016/0309-1708(93)90040-M
4. Asher U, Petzold L (1998) Computer methods for ordinary differential equations and differential-algebraic equations. SIAM, Philadelphia
5. Ataie-Ashtiani B, Raeesi-Ardekani D (2010) Comparison of numerical formulations for two-phase flow in porous media. Geotech Geol Eng 28:373–389
6. Baker D (2000) A Darcian integral approximation to interblock hydraulic conductivity means in vertical infiltration. Comput Geosci 26(5):581–590. doi:10.1016/S0098-3004(99)00129-6

7. Barth T, Ohlberger M (2004) Finite volume methods: foundation and analysis. In: Stein E et al (eds) Encyclopedia of Computational Mechanics, vol 1: fundamentals. Wiley, New York
8. Bastian P, Helmig R (1999) Efficient fully-coupled solution techniques for two-phase flow in porous media: parallel multigrid solution and large scale computations. Adv Water Resour 23(3):199–216. doi:10.1016/S0309-1708(99)00014-7
9. Bause M, Knabner P (2004) Computation of variably saturated subsurface flow by adaptive mixed hybrid finite element methods. Adv Water Resour 27(6):565–581. doi:10.1016/j.advwatres.2004.03.005
10. Belfort B, Lehmann F (2005) Comparison of equivalent conductivities for numerical simulation of one-dimensional unsaturated flow. Vadose Zone J 4(4):1191–1200. doi:10.2136/vzj2005.0007
11. Bevilacqua I, Canone D, Ferraris S (2011) Acceleration techniques for the iterative resolution of the Richards equation by the finite volume method. Int J Numer Methods Biomed Eng 27(8):13091320. doi:10.1002/cnm.1364
12. Celia M, Binning P (1992) A mass conservative numerical solution for two-phase flow in porous media with application to unsaturated flow. Water Resour Res 28(10):2819–2828. doi:10.1029/92WR01488
13. Celia M, Bouloutas E, Zarba R (1990) A general mass-conservative numerical solution for the unsaturated flow equation. Water Resour Res 26(7):1483–1496. doi:10.1029/WR026i007p01483
14. Chen Z, Huan G, Ma Y (2006) Computational methods for multiphase flows in porous media. SIAM, Philadelphia
15. Clement T, Wise W, Molz F (1994) A physically based, two-dimensional, finite-difference algorithm for modeling variably saturated flow. J Hydrol 161(1–4):71–90. doi:10.1016/0022-1694(94)90121-X
16. Cumming B, Moroney T, Turner I (2011) A mass-conservative control volume-finite element method for solving Richards equation in heterogeneous porous media. BIT Numer Math 51(4):845–864. doi:10.1007/s10543-011-0335-3
17. Edwards M (2002) Unstructured, control-volume distributed, full-tensor finite-volume schemes with flow based grids. Comput Geosci 6(3–4):433–452. doi:10.1023/A:1021243231313
18. Edwards M, Rogers C (1998) Finite volume discretization with imposed flux continuity for the general tensor pressure equation. Comput Geosci 2(4):259–290. doi:10.1023/A:1011510505406
19. Eymard R, Gutnic M, Hilhorst D (1999) The finite volume method for Richards equation. Comput Geosci 3(3–4):259–294. doi:10.1023/A:1011547513583
20. Eymard R, Gallouët T, Herbin R (2000) Finite volume methods. In: Ciarlet P, Lions J (eds) Handbook of numerical analysis, vol 7. North-Holland, Amsterdam, pp 713–1020
21. Fagherazzi S, Furbish D, Rasetarinera P, Hussaini M (2004) Application of the discontinuous spectral Galerkin method to groundwater flow. Adv Water Resour 27(2):129–140. doi:10.1016/j.advwatres.2003.11.001
22. Fahs M, Younes A, Lehmann F (2009) An easy and efficient combination of the mixed finite element method and the method of lines for the resolution of Richards equation. Environ Model Softw 24(9):1122–1126
23. Farthing M, Kees C, Miller C (2003) Mixed finite element methods and higher-order temporal approximations for variably saturated groundwater flow. Adv Water Resour 26(4):373–394. doi:10.1016/S0309-1708(02)00187-2
24. Fassino C, Manzini G (1998) Fast-secant algorithms for the non-linear Richards equation. Commun Numer Methods Eng 14:921–930
25. Fletcher C (1991) Computational techniques for fluid dynamics 1. Fundamental and general techniques. Springer, Berlin
26. Forsyth P, Wu Y, Pruess K (1995) Robust numerical methods for saturated unsaturated flow in heterogeneous media. Adv Water Resour 18(1):25–38. doi:10.1016/0309-1708(95)00020-J

27. Fuhrmann J, Langmach H (2001) Stability and existence of solutions of time-implicit finite volume schemes for viscous nonlinear conservation laws. Appl Numer Math 37(1–2):201–230
28. Gastó J, Grifoll J, Cohen Y (2002) Estimation of internodal permeabilities for numerical simulations of unsaturated flows. Water Resour Res 38(12):1326. doi:10.1029/2002WR001529
29. Gresho P, Lee R (1981) Don't suppress the wiggles—they're telling you something!. Comput Fluids 9(2):223–253
30. Gresho P, Sani R (1998) Incompressible flow and the finite element method. Wiley, Chichester
31. Guinot V (2008) Wave propagation in fluids: models and numerical techniques. Wiley, Hoboken
32. Haverkamp R, Vauclin M, Touma J, Wierenga P, Vachaud G (1977) A comparison of numerical simulation models for one-dimensional infiltration. Soil Sci Soc Am J 41(2):285–294. doi:10.2136/sssaj1977.03615995004100020024x
33. Helmig R (1997) Multiphase flow and transport processes in the subsurface: a contribution to the modeling of the hydrosystems. Springer, Berlin
34. Helmig R, Weiss A, Wohlmuth B (2009) Variational inequalities for modeling flow in heterogeneous porous media with entry pressure. Comput Geosci 13(3):373–389. doi:10.1007/s10596-008-9125-7
35. Huang K, Mohanty B, van Genuchten M (1996) A new convergence criterion for the modified picard iteration method to solve the variably saturated flow equation. J Hydrol 178(1–4):69–91. doi:10.1016/0022-1694(95)02799-8
36. Ju SH, Kung KJS (1997) Mass types, element orders and solution schemes for the Richards' equation. Comput Geosci 23(2):175–187. doi:10.1016/S0098-3004(97)85440-4
37. Kavetski D, Binning P, Sloan S (2001) Adaptive time stepping and error control in a mass conservative numerical solution of the mixed form of Richards equation. Adv Water Resour 24(6):595–605. doi:10.1016/S0309-1708(00)00076-2
38. Kavetski D, Binning P, Sloan S (2002) Noniterative time stepping schemes with adaptive truncation error control for the solution of Richards equation. Water Resour Res 38(10):1211–1220. doi:10.1029/2001WR000720
39. Kees C, Miller C (2002) Higher order time integration methods for two-phase flow. Adv Water Resour 25(2):159–177. doi:10.1016/S0309-1708(01)00054-9
40. Kelley C (1995) Iterative methods for linear and nonlinear equations. SIAM, Philadelphia
41. Kirkland M, Hills R, Wierenga P (1992) Algorithms for solving Richards equation for variably saturated soil. Water Resour Res 28(8):2049–2058. doi:10.1029/92WR00802
42. Lehmann F, Ackerer P (1998) Comparison of iterative methods for improved solutions of the fluid flow equation in partially saturated porous media. Transp Porous Media 31(3):275–292. doi:10.1023/A:1006555107450
43. LeVeque R (2002) Finite volume methods for hyperbolic problems. Cambridge University Press, Cambridge
44. Li H, Farthing M, Dawson C, Miller C (2007) Local discontinuous Galerkin approximations to Richards equation. Adv Water Resour 30(3):555–575. doi:10.1016/j.advwatres.2006.04.011
45. Li H, Farthing M, Miller C (2007) Adaptive local discontinuous Galerkin approximation to Richards equation. Adv Water Resour 30(9):1883–1901. doi:10.1016/j.advwatres.2007.02.007
46. Mansell R, Ma L, Ahuja L, Bloom S (2002) Adaptive grid refinement in numerical models for water flow and chemical transport in soil. Vadose Zone J 1(2):222–238. doi:10.2136/vzj2002.2220
47. Manzini G, Ferraris S (2004) Mass-conservative finite volume methods on 2-d unstructured grids for the Richards' equation. Adv Water Resour 27(12):1199–1215. doi:10.1016/j.advwatres.2004.08.008
48. Miller C, Abhishek C, Farthing M (2006) A spatially and temporally adaptive solution of Richards' equation. Adv Water Resour 29(4):525–545. doi:10.1016/j.advwatres.2005.06.008
49. Niessner J, Helmig R, Jakobs H, Roberts J (2005) Interface conditions and linearization schemes in the Newton iterations for two-phase flow in heterogeneous porous media. Adv Water Resour 28(7):671–687. doi:10.1016/j.advwatres.2005.01.006
50. Ossowski R, Sikora Z (2004) Numeryczne modelowanie sondowania statycznego CPTU (Numerical modeling of static CPTU tests). Politechnika Gdańska, Gdańsk

51. Pan L, Warrick A, Wierenga P (1996) Finite element methods for modeling water flow in variably saturated porous media: numerical oscillation and mass-distribution schemes. Water Resour Res 32(6):1883–1889. doi:10.1029/96WR00753
52. Paniconi C, Putti M (1994) A comparison of Picard and Newton iteration in the numerical solution of multidimensional variably saturated flow problems. Water Resour Res 30(12):3357–3374. doi:10.1029/94WR02046
53. Paniconi C, Putti M (1995) Modeling variably saturated flow problems using newton-type linearization methods. In: Verri G, Gambolati G (eds) Advanced methods for groundwater pollution control. Springer, Berlin
54. Pinder G, Gray W (2008) Essentials of multiphase flow and transport in porous media. Wiley, Hoboken
55. Rees I, Masters I, Malan A, Lewis R (2004) An edge-based finite volume scheme for saturated unsaturated groundwater flow. Comput Methods Appl Mech Eng 193(42–44):4741–4759
56. Saad Y (2003) Iterative methods for sparse linear systems. SIAM, Philadelphia
57. Šimůnek J, Vogel T, van Genuchten M (1994) The SWMS-2D code for simulating water flow and solute transport in two-dimensional variably saturated media. Version 1.21. Research report number 132. U.S. Salinity Laboratory, Agricultural Research Service, U.S. Department of Agriculture, Riverside, CA
58. Šimůnek J, Huang K, van Genuchten M (1995) The SWMS-3D code for simulating water flow and solute transport in three-dimensional variably-saturated media. Version 1.0. Research report number 139. U.S. Salinity Laboratory, Agricultural Research Service, U.S. Department of Agriculture, Riverside, CA
59. Šimůnek J, Šejna M, Saito H, Sakai M, van Genuchten M (2008) The HYDRUS-1D software package for simulating the one-dimensional movement of water, heat and multiple solutes in variably-saturated media. Version 4.0. Department of Environmental Sciences, University of California Riverside, Riverside, CA
60. Simpson M, Clement T (2003) Comparison of finite difference and finite element solutions to the variably saturated flow equation. J Hydrol 270(1–2):49–64. doi:10.1016/S0022-1694(02)00294-9
61. Szmelter T (1980) Metody komputerowe w mechanice (computer methods in mechanics). PWN, Warszawa
62. Szymkiewicz A (2007) Numerical simulation of one-dimensional two-phase flow in porous media. Arch Hydro-Eng Environ Mech 54(2):117–136
63. Szymkiewicz A, Burzyński K (2007) Simulation of water flow in double-porosity soils with finite-volume method on unstructured grids. TASK Q 11(4):397–410
64. Tocci M, Kelley C, Miller C (1997) Accurate and economical solution of the pressure-head form of Richards equation by the method of lines. Adv Water Resour 20(1):1–14. doi:10.1016/S0309-1708(96)00008-5
65. Tocci M, Kelley C, Miller C, Kees C (1998) Inexact Newton methods and the method of lines for solving Richards' equation in two space dimensions. Comput Geosci 2(4):291–309. doi:10.1023/A:1011562522244
66. Tracy F (2010) Testing computational algorithms for unsaturated flow. Open Hydrol J 4:227–235
67. van Dam J, Feddes R (2000) Numerical simulation of infiltration, evaporation and shallow groundwater levels with the Richards equation. J Hydrol 233(1):72–85. doi:10.106/S0022-1694(00)00227-4
68. Voller V (2009) Basic control volume finite element methods for fluids and solids. World Scientific, Singapore
69. Walker H, Woodward C, Yang U (2010) An accelaration fixed-point iteration for solution of variably saturated flow. In: Carrera J (ed) Proceedings of XVIII International Conference on Water Resources, Barcelona
70. Warrick A (1991) Numerical approximation of Darcian flow through unsaturatedsoil. Water Resour Res 27(6):1215–1222. doi:10.1029/91WR00093

71. Zaradny H (1993) Groundwater flow in saturated and unsaturated soil. Balkema, Rotterdam
72. Zhang X, Ewen J (2000) Efficient method for simulating gravity-dominated water flow in unsaturated soils. Water Resour Res 36(9):2777–2780. doi:10.1029/2000WR900182
73. Zienkiewicz O, Taylor R, Zhu J (2005) Finite element method—its basis and fundamentals. Elsevier, Oxford
74. Zijl W, Nawalany M (1993) Natural groundwater flow. Lewis, Boca Raton

Chapter 4
Computation of Inter-Nodal Permeabilities for Richards Equation

As shown in Chap. 3, an important problem in the spatial discretization of the unsaturated and two-phase flow equations is related to the averaging of the fluid permeabilities. Various averaging techniques are presented in this chapter, with particular focus on the case of one-dimensional unsaturated flow in a homogeneous medium, for which accurate inter-nodal permeability estimations based on the steady flow analysis are available. It is shown that the relation between capillary and gravity forces at the scale of a single grid cell has key importance for the choice of the averaging scheme. The method proposed by the author is presented in detail, and its extensions to heterogeneous materials and multidimensional problems are discussed. Finally, implications for two-phase flow modelling are considered.

4.1 Overview of Averaging Approaches for One-Dimensional Flow

The averaging methods described below can be used for one-dimensional incompressible unsaturated flow in a homogeneous medium. The water pressure head h_{w} is chosen as the primary variable, in order to facilitate the presentation of the averaging methods based on the analysis of the steady state pressure distribution between nodes. The semi-discrete equation for node j obtained using the finite difference method, Eq. (3.12), can be rewritten as follows:

$$\Delta x^{(\mathrm{ij})} \frac{\mathrm{d}\theta_{\mathrm{w}}^{(j)}}{\mathrm{d}\,t} + v_{\mathrm{w}}^{(\mathrm{jk})} - v_{\mathrm{w}}^{(ij)} = 0 \,, \tag{4.1}$$

where the volumetric fluxes (Darcian velocities) are defined as:

$$v_{\mathrm{w}}^{(ij)} = -K_{\mathrm{sw}}\, k_{\mathrm{rw}}^{(ij)} \left(\frac{h_{\mathrm{w}}^{(j)} - h_{\mathrm{w}}^{(i)}}{\Delta x^{(ij)}} - \zeta \right) , \tag{4.2}$$

A. Szymkiewicz, *Modelling Water Flow in Unsaturated Porous Media*,
GeoPlanet: Earth and Planetary Sciences, DOI: 10.1007/978-3-642-23559-7_4,

$$v_{\mathrm{w}}^{(jk)} = -K_{\mathrm{sw}}\, k_{\mathrm{rw}}^{(jk)} \left(\frac{h_{\mathrm{w}}^{(k)} - h_{\mathrm{w}}^{(j)}}{\Delta x^{(jk)}} - \zeta \right) . \tag{4.3}$$

In the above equations K_{sw} is the saturated conductivity of the water phase and ζ is the cosine of the angle between the x axis and the gravity vector, introduced in Eqs. (3.5) and (3.6). The average relative permeabilities $k_{\mathrm{rw}}^{(ij)}$ and $k_{\mathrm{rw}}^{(jk)}$ can be computed using a number of methods as discussed below.

4.1.1 Simple Averaging Methods

In the simplest approach, if the nodal relative permeabilities are known, the average value can be calculated as one of the well-known algebraic means:

- arithmetic mean:

$$k_{\mathrm{rw}}^{(ij)} = \frac{1}{2} \left(k_{\mathrm{rw}}^{(i)} + k_{\mathrm{rw}}^{(j)} \right) , \tag{4.4}$$

- geometric mean:

$$k_{\mathrm{rw}}^{(ij)} = \sqrt{k_{\mathrm{rw}}^{(i)}\, k_{\mathrm{rw}}^{(j)}} , \tag{4.5}$$

- harmonic mean:

$$k_{\mathrm{rw}}^{(ij)} = \frac{2\, k_{\mathrm{rw}}^{(i)}\, k_{\mathrm{rw}}^{(j)}}{k_{\mathrm{rw}}^{(i)} + k_{\mathrm{rw}}^{(j)}} . \tag{4.6}$$

For the same pair of numbers, the arithmetic averaging yields the largest value of the three methods listed above, while the harmonic averaging—the smallest one. The use of arithmetic mean is well-established in the numerical solution of the unsaturated flow equation, e.g. [11, 23, 25, 35, 43]. It provides relatively accurate results for many typical flow problems, but also has some deficiencies. It tends to overestimate the infiltration rate for capillary-dominated flow, e.g. [19, 21], while for gravity-dominated flow on coarse grids it may lead to unphysical oscillations in the resulting water pressure profile, e.g. [5, 39]. This effect can be considered as equivalent to the oscillations appearing in the solution of linear advection equation using centred in space approximation of fluxes, i.e. it is related to the numerical dispersion.

Geometric averaging yields values of the inter-nodal permeability smaller than the arithmetic averaging. Therefore, it offers some improvement when the arithmetic mean overestimates the flow rate, i.e. during capillary-driven infiltration, e.g. [8, 21, 32]. However, for precisely the same reason, the geometric mean, as compared to the arithmetic mean, leads to larger oscillations and more severe convergence problems in the case of gravity-dominated flow, e.g. [3, 40].

The harmonic mean yields accurate values of the average permeability for steady-state saturated flow in a layered medium in the direction perpendicular to the layers

(see Sect. 2.3.3). While some authors recommended its use also for unsaturated flow in a homogeneous medium [7, 29], in such a case it could be accurate only if the distribution of the relative permeability between nodes were piecewise-constant, i.e. the whole half of the grid cell adjacent to node i had a constant permeability $k_{\mathrm{rw}}^{(i)}$, while the other half, adjacent to node j had a constant permeability $k_{\mathrm{rw}}^{(j)}$. This is not true, since in unsaturated flow the permeability varies continuously between nodes, following the variation of the saturation in a nonlinear manner. Thus, the harmonic mean tends to underestimate the inter-nodal permeability, particularly for downward water infiltration into a dry porous medium. Note that in the limit case of the initial water saturation equal to the residual saturation and the initial relative permeability equal to zero, both geometric and harmonic averaging predict $k_{rw}^{(ij)} = 0$, i.e. no flow at all, which is inconsistent from the physical point of view.

Some schemes are based on the averaging of the argument to the relative permeability function, rather than the relative permeability itself. For example, the inter-nodal permeability can be calculated for the arithmetic average of the nodal saturations:

$$k_{\mathrm{rw}}^{(ij)} = k_{\mathrm{rw}}\left(\frac{S_{\mathrm{w}}^{(i)} + S_{\mathrm{w}}^{(j)}}{2}\right). \tag{4.7}$$

It was shown [28, 30, 46] that this method provides somewhat better results than the averaging of the nodal permeabilities given by Eq. (4.4).

Since in the unsaturated flow the relative permeability is uniquely defined by the water pressure head, the inter-nodal permeability can be calculated using the average of the nodal values of the pressure head:

$$k_{\mathrm{rw}}^{(ij)} = k_{\mathrm{rw}}\left(\frac{h_{\mathrm{w}}^{(i)} + h_{\mathrm{w}}^{(j)}}{2}\right). \tag{4.8}$$

While Eq. (4.8) is rather seldom used, one can note that it is consistent with the finite element approximation of the flux term if linear shape functions and a single-point quadrature rule are used, as discussed in Sect. 3.2.2. Geometric and harmonic averaging of the nodal water pressure heads in the argument of the permeability function in Eq. (4.8) was also tested, but these approaches do not seem to offer any particular advantage [21].

Another averaging method, which was already mentioned in Sect. 3.2.2, is the integrated mean:

$$k_{\mathrm{rw}}^{(ij)} = k_{\mathrm{int}}^{(ij)} = \frac{1}{h_{\mathrm{w}}^{(j)} - h_{\mathrm{w}}^{(i)}} \int_{h_{\mathrm{w}}^{(i)}}^{h_{\mathrm{w}}^{(j)}} k_{\mathrm{rw}}(\hat{h})\,\mathrm{d}\hat{h} = \frac{\Phi_{\mathrm{h}}(h_{\mathrm{w}}^{(j)}) - \Phi_{\mathrm{h}}(h_{\mathrm{w}}^{(i)})}{h_{\mathrm{w}}^{(j)} - h_{\mathrm{w}}^{(j)}}, \tag{4.9}$$

where Φ_h is the flux potential defined with respect to the water pressure head. Following Eq. (2.83) the volumetric water flux can be written in terms of the flux potential as:

$$v_w = -K_{sw}\left(\frac{\partial \Phi_h}{\partial x} - \zeta\, k_{rw}\right), \tag{4.10}$$

or in a discrete form as:

$$v_w^{(ij)} = -K_{sw}\frac{\Phi_h^{(j)} - \Phi_h^{(i)}}{\Delta x^{(ij)}} - \zeta\, K_{sw}\, k_{rw}^{(ij)}. \tag{4.11}$$

For $\zeta = 0$, comparing Eq. (4.11) with the discrete form of the Darcy equation given by Eq. (4.2) results in a formula for $k_{rw}^{(ij)}$ identical with Eq. (4.9). Thus, the integrated mean is an accurate approximation of the inter-nodal conductivity for horizontal unsaturated flow. It was also reported to give accurate results for vertical flow if the node spacing was sufficiently fine, i.e. when the capillary gradient was much larger than the gravity gradient at the scale of a single grid cell [30, 34]. On the other hand, as mentioned in Sect. 3.2.2, the integrated mean results from the exact integration of the flux term in one-dimensional finite element method with linear shape functions used to represent the distribution of p_w or h_w.

Comparative studies available in the literature [6, 21, 30, 34, 36] show that the performance of the simple averaging methods listed above is highly problem-dependent. For example, Haverkamp and Vauclin [21] obtained accurate solutions using geometric averaging, while the simulations presented by Belfort and Lelmann [6] indicated that the geometric mean severely underestimates the flow rate. It is clear that the performance of simple averaging schemes varies according to the following factors: form of the relative permeability function, direction of the flow, initial and boundary conditions and distance between nodes. This observation motivated the development of more accurate averaging methods, in which these factors are at least partially represented. Such methods are described in the following sections.

4.1.2 Direction Dependent Methods

The second group of methods takes into account the direction of the flow. The two most basic approaches are the upstream mean and the downstream mean:

- upstream mean:

$$k_{rw}^{(ij)} = \begin{cases} k_{rw}^{(i)} & \text{if} \quad \dfrac{h_w^{(j)} - h_w^{(i)}}{\Delta x^{(ij)}} - \zeta \le 0 \\ k_{rw}^{(j)} & \text{if} \quad \dfrac{h_w^{(j)} - h_w^{(i)}}{\Delta x^{(ij)}} - \zeta > 0 \end{cases} \tag{4.12}$$

- downstream mean:

$$k_{\mathrm{rw}}^{(ij)} = \begin{cases} k_{\mathrm{rw}}^{(i)} & \text{if} \quad \dfrac{h_{\mathrm{w}}^{(j)} - h_{\mathrm{w}}^{(i)}}{\Delta x^{(ij)}} - \zeta > 0 \\ k_{\mathrm{rw}}^{(j)} & \text{if} \quad \dfrac{h_{\mathrm{w}}^{(j)} - h_{\mathrm{w}}^{(i)}}{\Delta x^{(ij)}} - \zeta \leq 0 \end{cases} \tag{4.13}$$

As mentioned in Chap. 3, in the case of linear advection equation, the upstreaming of the advective flux introduces numerical diffusion, and thus ensures oscillation-free solution at the cost of additional smoothing. Therefore, the upstream mean is the preferred choice for two-phase flow with important contribution of advective (viscous or gravity) terms [16, 22]. It is also recommended for the simulation of gravity-driven unsaturated flow [16]. On the other hand, upstream averaging introduces large errors for capillary-dominated (diffusive) flow, for example in the case of upward flow driven by capillary forces [5, 39, 40].

The downstream mean is practically not used, since it may lead to severe underestimation of the average permeability and, similarly to the geometric and harmonic average, it cannot reproduce infiltration into very dry medium [6]. Moreover, in the case of pure advection equation the use of downstream approximation of the advective fluxes causes instability of solution [14].

The unsaturated water flux consists of two parts. The first one is related to the capillary forces, and has diffusive character, while the other one is related to the gravity forces, and has advective character. In view of this fact, some authors propose to split the flux and use a different permeability averaging scheme for each component:

$$v_{\mathrm{w}}^{(ij)} = -K_{\mathrm{sw}} \left(k_{\mathrm{ca}}^{(ij)} \frac{h_{\mathrm{w}}^{(j)} - h_{\mathrm{w}}^{(i)}}{\Delta x^{(ij)}} - \zeta \, k_{\mathrm{gr}}^{(ij)} \right), \tag{4.14}$$

where $k_{\mathrm{ca}}^{(ij)}$ and $k_{\mathrm{gr}}^{(ij)}$ denote the average relative permeabilities for the capillary and gravity term, respectively. The principal difficulty related to the application of such methods is that if different averaging schemes are used for the capillary and gravity term, the expression:

$$k_{\mathrm{ca}}^{(ij)} \frac{h_{\mathrm{w}}^{(j)} - h_{\mathrm{w}}^{(i)}}{\Delta x^{(ij)}} - \zeta \, k_{\mathrm{gr}}^{(ij)}$$

does not necessarily has the same sign as the water potential gradient:

$$\frac{h_{\mathrm{w}}^{(j)} - h_{\mathrm{w}}^{(i)}}{\Delta x^{(ij)}} - \zeta \ .$$

If this is the case, the flux becomes wrongly oriented leading to physically inadmissible solutions. In particular, depending on the choice of the two permeabilities, this method may predict a non-zero flux for hydrostatic case, when the total potential gradient is equal to zero. Nevertheless, such an approach offers some advantages

over the simple averaging methods, like the arithmetic mean, especially for the case of downward infiltration, when both capillary and gravity gradients are oriented in the same direction.

Taking into account the considerations presented above, a natural choice for $k_{\mathrm{ca}}^{(ij)}$ is the integrated mean $k_{\mathrm{int}}^{(ij)}$, while for the gravity term the upstream mean should be used. Note that in this case the choice of the upstream direction should be based on the gravitational potential, not the total potential, which means that $k_{\mathrm{gr}}^{(ij)}$ is equal to the permeability of the node which is placed higher with regard to the reference level:

$$k_{\mathrm{gr}}^{(ij)} = \begin{cases} k_{\mathrm{rw}}^{(i)} & \text{if} \quad \zeta \geq 0 \,, \\ k_{\mathrm{rw}}^{(j)} & \text{if} \quad \zeta < 0 \,. \end{cases} \tag{4.15}$$

The combination of integrated average for $k_{\mathrm{ca}}^{(ij)}$ and upstream average for $k_{\mathrm{gr}}^{(ij)}$ was used by Zhang and Ewen [47], while Fuhrmann and Langmach [17] applied arithmetic average for $k_{\mathrm{ca}}^{(ij)}$ and the upstream average for $k_{\mathrm{gr}}^{(ij)}$. On the other hand, Zaidel and Russo [46] used the standard arithmetic mean for $k_{\mathrm{gr}}^{(ij)}$, while for $k_{\mathrm{ca}}^{(ij)}$ they developed a simplified formula which approximates $k_{\mathrm{int}}^{(ij)}$ for the relative permeability function of the van Genuchten–Mualem type. Ross [33] also applied the arithmetic average for gravity term in his scheme based on the Kirchhoff transform, but recognized that it should be replaced by a weighted average, with weighting parameters giving more importance to the upper node. In general, if $k_{\mathrm{gr}}^{(ij)}$ is approximated with other schemes than the upstream mean, the monotonicity of the solution is not guaranteed [17].

Equation (4.14) can be transformed to the form of Eq. (4.2):

$$v_{\mathrm{w}}^{(ij)} = -K_{\mathrm{sw}}\, k_{\mathrm{rw}}^{(ij)} \left(\frac{h_{\mathrm{w}}^{(j)} - h_{\mathrm{w}}^{(i)}}{\Delta x^{(ij)}} - \zeta \right) , \tag{4.16}$$

if the inter-nodal permeability for the whole flux term is defined as:

$$k_{\mathrm{rw}}^{(ij)} = \left[k_{\mathrm{ca}}^{(ij)} \frac{h_{\mathrm{w}}^{(j)} - h_{\mathrm{w}}^{(i)}}{\Delta x^{(ij)}} - \zeta\, k_{\mathrm{gr}}^{(ij)} \right] \Bigg/ \left[\frac{h_{\mathrm{w}}^{(j)} - h_{\mathrm{w}}^{(i)}}{\Delta x^{(ij)}} - \zeta \right] . \tag{4.17}$$

4.1.3 Darcian Means

A physically consistent framework for computing inter-nodal permeabilities in the discretized unsaturated flow equation was introduced by Warrick [44]. It is called the Darcian mean approach, because it postulates equivalence between the discrete and differential (continuous) forms of the Darcy equation for steady unsaturated water

flow between nodes $x^{(i)}$ and $x^{(j)}$. Assuming (without the loss of generality) that the saturated conductivity K_{sw} is equal to unity, one can write the following relation:

$$v_{\mathrm{st}}^{(ij)} = -k_{\mathrm{rw}}^{(ij)} \left(\frac{\Delta h_{\mathrm{w}}^{(ij)}}{\Delta x^{(ij)}} - \zeta \right) = -k_{\mathrm{rw}}(h_{\mathrm{w}}) \left(\frac{\mathrm{d}h_{\mathrm{w}}}{\mathrm{d}x} - \zeta \right) , \tag{4.18}$$

where $v_{\mathrm{st}}^{(ij)}$ is the uniform steady flux between nodes and $\Delta h_{\mathrm{w}}^{(ij)} = h_{\mathrm{w}}^{(j)} - h_{\mathrm{w}}^{(i)}$. The differential form of the Darcy equation can be integrated as follows:

$$\int_{x^{(i)}}^{x^{(j)}} \mathrm{d}x = -\int_{h_{\mathrm{w}}^{(i)}}^{h_{\mathrm{w}}^{(j)}} \frac{k_{\mathrm{rw}}(h_{\mathrm{w}})\, \mathrm{d}h_{\mathrm{w}}}{v_{\mathrm{st}}^{(ij)} - \zeta k_{\mathrm{rw}}(h_{\mathrm{w}})} . \tag{4.19}$$

For horizontal flow with $\zeta = 0$ one obtains:

$$\Delta x^{(ij)} = -\frac{1}{v_{\mathrm{st}}^{(ij)}} \int_{h_{\mathrm{w}}^{(i)}}^{h_{\mathrm{w}}^{(j)}} k_{\mathrm{rw}}(h_{\mathrm{w}}) \mathrm{d}h_{\mathrm{w}} . \tag{4.20}$$

Comparing this result with the discrete form of the Darcy equation appearing in Eq. (4.18) gives:

$$k_{\mathrm{rw}}^{(ij)} = \frac{1}{\Delta h_{w}^{(ij)}} \int_{h_{w}^{(i)}}^{h_{w}^{(j)}} k_{\mathrm{rw}}(\hat{h}) \mathrm{d}\hat{h} = k_{\mathrm{int}}^{(ij)} . \tag{4.21}$$

Thus, the integrated mean corresponds to the Darcian mean for horizontal flow.

For $\zeta \neq 0$ the Darcian mean depends on $\Delta x^{(ij)}$ and is different from any of the simple averages listed in the previous section. Analytical solution can be obtained if the relative permeability is an exponential function of h_{w} as defined by Eq. (2.44):

$$k_{\mathrm{rw}}(h_{\mathrm{w}}) = \exp\left(h_{\mathrm{w}}/h_{\mathrm{g}}\right) , \tag{4.22}$$

where $h_{\mathrm{g}} > 0$ is a scaling parameter expressed in terms of the water pressure head. For such a constitutive relationship, the integration of Eq. (4.19) yields [2, 12]:

$$v_{\mathrm{st}}^{(ij)} = \frac{\zeta' \left(k_{\mathrm{rw}}^{(j)} - \exp(\zeta')\, k_{\mathrm{rw}}^{(i)} \right)}{1 - \exp(\zeta')} , \tag{4.23}$$

where:

$$\zeta' = \Delta x^{(ij)}\, \zeta / h_{\mathrm{g}} . \tag{4.24}$$

Making use of the following relationship:

$$\Delta h_{\mathrm{w}} = h_{\mathrm{w}}^{(j)} - h_{\mathrm{w}}^{(i)} = h_{\mathrm{g}}\, \mathscr{L}_k \ , \tag{4.25}$$

where $\mathscr{L}_k = \ln(k_{\mathrm{rw}}^{(j)}/k_{\mathrm{rw}}^{(i)})$, one can define the inter-nodal permeability as:

$$k_{\mathrm{rw}}^{(ij)} = \frac{-v_{\mathrm{st}}^{(ij)}\, \Delta x^{(ij)}/h_{\mathrm{g}}}{\Delta h_{\mathrm{w}}^{(ij)} - \zeta\, \Delta x^{(ij)}} = \frac{\zeta' \left(\exp(\zeta')\, k_{\mathrm{rw}}^{(i)} - k_{\mathrm{rw}}^{(j)}\right)}{(1 - \exp(\zeta'))\ (\mathscr{L}_k - \zeta')} \ . \tag{4.26}$$

The above formula was developed by Baker [2] for the case of $\zeta = 1$, while an equivalent result was obtained by Desbarats [12] for a more general case of arbitrary ζ. Moreover, Baker [2] and Baker et al. [5] showed that the Darcian average varies in the range between the integrated mean ($k_{\mathrm{int}}^{(ij)}$) and the permeability at the upper node ($k_{\mathrm{rw}}^{(i)}$, assuming that the gravity force acts in the direction of x axis). Baker et al. [5] proposed to compute the inter-nodal permeability as a weighted arithmetic average of those two values:

$$k_{\mathrm{rw}}^{(ij)} = \omega_{\mathrm{v}}\, k_{\mathrm{rw}}^{(i)} + (1 - \omega_{\mathrm{v}})\, k_{\mathrm{int}}^{(ij)} \ , \tag{4.27}$$

where ω_{v} is a weighting parameter ranging from 0 to 1. In this work the original formula for ω_{v} [3, 5] is extended for the case of arbitrary ζ:

$$\omega_{\mathrm{v}} = \frac{\left(k_{\mathrm{rw}}^{(i)}\, \exp(\zeta') - k_{\mathrm{rw}}^{(j)}\right) \mathscr{L}_k\, \zeta' - \left(1 - \exp(\zeta')\right)\, \Delta k\, \left(\mathscr{L}_k - \zeta'\right)}{(1 - \exp(\zeta'))\ (\mathscr{L}_k - \zeta') \left(k_{\mathrm{rw}}^{(i)}\, \mathscr{L}_k - \Delta k\right)} \tag{4.28}$$

where $\Delta k = k_{\mathrm{rw}}^{(j)} - k_{\mathrm{rw}}^{(i)}$, and

$$\zeta' = \frac{\Delta x^{(ij)}\, \zeta}{\sqrt{k_{\mathrm{rw}}^{(i)}\, k_{\mathrm{rw}}^{(j)}}} \left.\frac{\partial k_{\mathrm{rw}}}{\partial h_{\mathrm{w}}}\right|_{k_{\mathrm{rw}} = \sqrt{k_{\mathrm{rw}}^{(i)}\, k_{\mathrm{rw}}^{(j)}}} \ . \tag{4.29}$$

It means that the modified gravity coefficient ζ' depends on the derivative of the relative permeability function computed for the geometric mean of the nodal permeabilities. The above formula is exact for the exponential relative permeability function, for which Eqs. (4.27)–(4.28) reduce to Eq. (4.26). As shown by Baker et al. [5] and Baker [3], it is a relatively accurate approximation of the true Darcian mean also for other types of the relative permeability functions. An advantage of such approach is that the inter-nodal permeability always remains in the physically consistent range between $k_{\mathrm{int}}^{(ij)}$, which is the limit value for capillary dominated flow and $k_{\mathrm{rw}}^{(i)}$ which is the limit value for gravity-dominated flow. On the other hand, the relative permeability function must be inverted to obtain $h_{\mathrm{w}}\left(\sqrt{k_{\mathrm{rw}}^{(i)}\, k_{\mathrm{rw}}^{(j)}}\right)$,

which may be impossible to carry out analytically for more complicated functions (e.g. van Genuchten–Mualem model).

In principle, the Darcian means can be computed for an arbitrary relative permeability function by integrating numerically Eq. (4.18) or by solving (also numerically) the steady-state flow equation:

$$-\frac{\partial}{\partial x}k_{\mathrm{rw}}(h_{\mathrm{w}})\left(\frac{\partial h_{\mathrm{w}}}{\partial x}-\zeta\right)=0 \tag{4.30}$$

in the domain $\langle x^{(i)}, x^{(j)}\rangle$ with the boundary conditions $h_{\mathrm{w}}=h_{\mathrm{w}}^{(i)}$ for $x=x^{(i)}$ and $h_{\mathrm{w}}=h_{\mathrm{w}}^{(j)}$ for $x=x^{(j)}$. The resulting value of the steady-state flux can be subsequently used to calculate the inter-nodal permeability. Unfortunately, the numerical solution of steady-state Richards equation is a non-trivial problem in itself, and the amount of work necessary to compute the permeabilities for each pair of nodes at each time step of a transient simulation is prohibitive. Warrick [44] suggested to express the inter-nodal permeability as a weighted arithmetic average of the permeability values at the upper and lower node:

$$k_{\mathrm{rw}}^{(ij)}=\omega_{\mathrm{w}}\,k_{\mathrm{rw}}^{(i)}+(1-\omega_{\mathrm{w}})\,k_{\mathrm{rw}}^{(j)} \tag{4.31}$$

where ω_{w} is a weighting parameter ranging from 0 to 1. For a known grid spacing and relative permeability function it is possible to perform multiple solutions of the steady problem at the preprocessing stage in order to obtain the values of the parameter ω_{w} as a function of the two nodal permeability values. During transient flow simulation, ω_{w} can be interpolated from the table for the considered pair of permeabilities $k_{\mathrm{rw}}^{(i)}$ and $k_{\mathrm{rw}}^{(j)}$. However, if the relative permeability function or the grid spacing change, a new interpolation table must be generated, which requires additional numerical effort.

The method based on Eq. (4.31) was further developed by Gasto et al. [19]. They showed that for Brooks–Corey–Burdine and van Genuchten–Mualem permeability functions, the weighting parameter ω_{w} can be expressed as a function of four variables: $k_{\mathrm{rw}}^{(i)}$, $k_{\mathrm{rw}}^{(j)}$, $\Delta x'$ and n'. For Brooks–Corey model $\Delta x'=\Delta x^{(ij)}/h_{\mathrm{e}}$, where h_{e} is the air entry pressure head, and $n'=1+n_{\mathrm{b}}$, while for van Genuchten–Mualem model $\Delta x'=\Delta x^{(ij)}/h_{\mathrm{g}}$, where h_{g} is the pressure scaling parameter expressed in terms of the pressure head, and $n'=n_{\mathrm{g}}$. Gasto et al. [19] fitted a closed form analytical function, which allows to compute ω_{w} directly if the four variables are known. The calculation is performed according to the following formula:

$$\omega_{\mathrm{w}}=\left[1+\frac{a'\left(k_{\mathrm{rw}}^{(i)}\right)^{b'}\Big/\left(k_{\mathrm{rw}}^{(j)}\right)^{c'}}{1+\beta' n'\left(k_{\mathrm{rw}}^{(i)}\right)^{b'}\Big/\left(k_{\mathrm{rw}}^{(j)}\right)^{c'}}\right]^{-1}, \tag{4.32}$$

with the parameters a', b' and c' defined as follows:

Table 4.1 Fitting parameters used in the formula of [19] for Brooks–Corey (BC) and van Genuchten–Mualem (VG) relative permeability functions

	a'_{10}	a'_{11}	a'_2	b'_{01}	b'_{02}	b'_1	c'_0	β'
BC	0.208	0.634	0.191	0.690	2.294	0.049	0.020	0.008
VG	0.465	0.052	0.112	0.551	1.939	0.057	0.009	0.011

$$a' = \frac{1 - \left(a'_{10} + a'_{11}\,\log n'\right)\,\Delta x'}{1 + a'_2\,(n')^2\,\Delta x'}\,, \tag{4.33}$$

$$b' = \frac{b'_{01}\,n'}{b'_{02}\,n' - 1} - b'_1\,\Delta x'\,, \tag{4.34}$$

$$c' = \frac{b'_{01}\,n'}{b'_{02}\,n' - 1} + c'_0\,\left(n' - 1\right)\,\Delta x'\,. \tag{4.35}$$

Thus, the approximating formula contains altogether eight fitting parameters. Two sets of parameters were provided—one for Brooks–Corey–Burdine and the other one for van Genuchten–Mualem functions. Their values are listed in Table 4.1. This approach is relatively simple to implement, but has some limitations. First, the fitted analytical formula is valid only for $1.05 \le n' \le 5$ and the values of the normalized node spacing $\Delta x' < 1$, which is satisfied when:

$$\Delta x^{(ij)} \le h_\mathrm{e} \quad \text{or} \quad \Delta x^{(ij)} \le h_\mathrm{g}\,. \tag{4.36}$$

The above condition limits the applicability of this approach for coarse textured soils, where the pressure scaling parameter is of the order of a few centimetres. Moreover, adaptation of the method to other types of hydraulic functions would require a new parameter fitting procedure.

4.2 Improved Approximation Scheme

In this section, the averaging method proposed by the author, which also belongs to the Darcian averaging framework, is presented in more detail. The presentation closely follows the original paper [39]. The method is based on the analysis of the approximate shape of steady-state water pressure head profiles. The form of the pressure profile depends on the type of flow and three major cases can be distinguished, as shown in Fig. 4.1. In the following discussion it is assumed (without the loss of generality) that x axis is inclined downward, so that the values of ζ range from 0 to 1. The three basic flow regimes are as follows:

- *Infiltration in dry soil*:

$$-\infty < \Delta h_\mathrm{w}^{(ij)} / \Delta x^{(ij)} < 0\,.$$

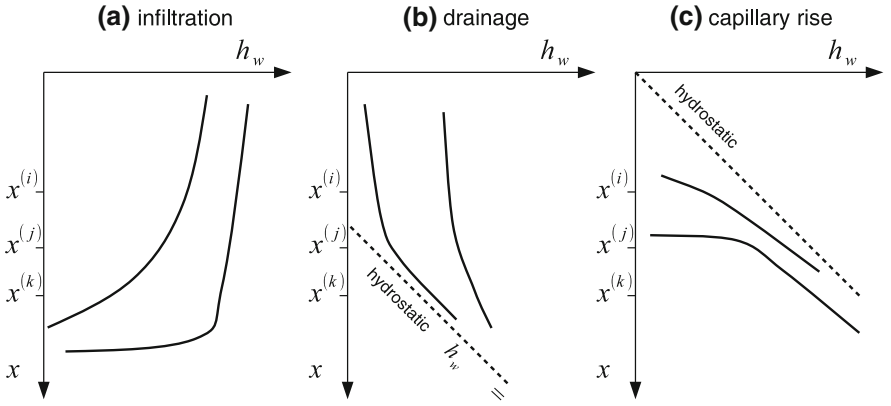

Fig. 4.1 Steady-state profiles of the water potential head for different types of flow (after [45])

In this case, both capillary and gravity forces act in the direction of x axis. In the upper part of the profile the water saturation and relative permeability are larger. Consequently, the gradient in the water pressure is smaller than in the lower part of the domain, in order to ensure uniform flux in both parts. For

$$\Delta h_{\mathrm{w}}^{(ij)} / \Delta x^{(ij)} \to 0$$

the pressure profile tends to a vertical line.

- *Drainage or infiltration close to the water table*:

$$0 < \Delta h_{\mathrm{w}}^{(ij)} / \Delta x^{(ij)} < \zeta \ .$$

In this case, the saturation in the lower part of the domain is larger than in the upper part, but the flow direction is downward, because the capillary potential gradient is smaller than the gravity potential gradient. The pressure profile varies from uniform ($\Delta h_{\mathrm{w}}^{(ij)} / \Delta x^{(ij)} \to 0$) to hydrostatic ($\Delta h_{\mathrm{w}}^{(ij)} / \Delta x^{(ij)} \to \zeta$).

- *Capillary rise or evaporation*:

$$\zeta < \Delta h_{w}^{(ij)} / \Delta x^{(ij)} < \infty \ .$$

The gradients of the capillary and gravity potentials act in the opposite directions. Since the capillary gradient in larger, the flow is in upward direction.

Note that for each flow regime the profiles are monotonous. The differences in profile shapes suggest that for each case a separate averaging formula should be considered. Moreover, three special limit cases can be distinguished:

- *Horizontal flow*: $\zeta = 0$. As shown above, in this case the Darcian mean corresponds to the integrated mean.
- *Uniform pressure distribution*:

$$\Delta h_{\mathrm{w}}^{(ij)} / \Delta x^{(ij)} = 0 \, .$$

  In this case, the average permeability is trivially $k_{\mathrm{rw}}^{(ij)} = k_{\mathrm{rw}}^{(i)} = k_{\mathrm{rw}}^{(j)}$.
- *Hydrostatic pressure distribution*:

$$\Delta h_{\mathrm{w}}^{(ij)} / \Delta x^{(ij)} - \zeta = 0 \, .$$

  In this case, the Darcian averaging principle cannot be used, because both flux and gradient are equal to zero. However, the limit value of the inter-nodal permeability for

$$(\Delta \, h_{\mathrm{w}}^{(ij)} / \Delta x^{(ij)} - \zeta) \to 0$$

  is given by the upstream value $k_{\mathrm{rw}}^{(i)}$ [5].

4.2.1 Infiltration

For infiltration in a dry soil inaccurate approximations of the inter-nodal permeability may lead to two types of errors. For capillary-dominated flow, the correct limit value is given by the integrated mean. Many other averaging methods (in particular the arithmetic or upstream average) overestimate the inter-nodal permeability and consequently predict too large infiltration rates. On the other hand, for gravity-dominated flow all simple averaging methods except the upstream average underestimate $k_{\mathrm{rw}}^{(ij)}$, which leads to oscillatory profile of the water pressure head. The deficiencies of the commonly used averaging methods were shown by Baker [4] on the example of a simple numerical grid consisting of three nodes. Here a similar analysis is performed in order to derive an improved formula for the inter-nodal permeability. It is based on the observation that for steady state unsaturated flow in a homogeneous porous medium the pressure profile resulting form the solution of the Richards equation is monotonous. On coarser numerical grid, the monotonicity can be violated by inaccurate approximation of the inter-nodal permeability, leading to unphysical oscillations (wiggles).

Consider a numerical approximation of steady flow equation on a grid consisting of three nodes, as shown in Fig. 4.2. The flux continuity condition at node j can be written as:

$$-k_{\mathrm{rw}}^{(ij)} \left(\frac{h_{\mathrm{w}}^{(j)} - h_{\mathrm{w}}^{(i)}}{\Delta x^{(ij)}} - \zeta \right) = -k_{\mathrm{rw}}^{(jk)} \left(\frac{h_{\mathrm{w}}^{(k)} - h_{\mathrm{w}}^{(j)}}{\Delta x^{(jk)}} - \zeta \right) . \tag{4.37}$$

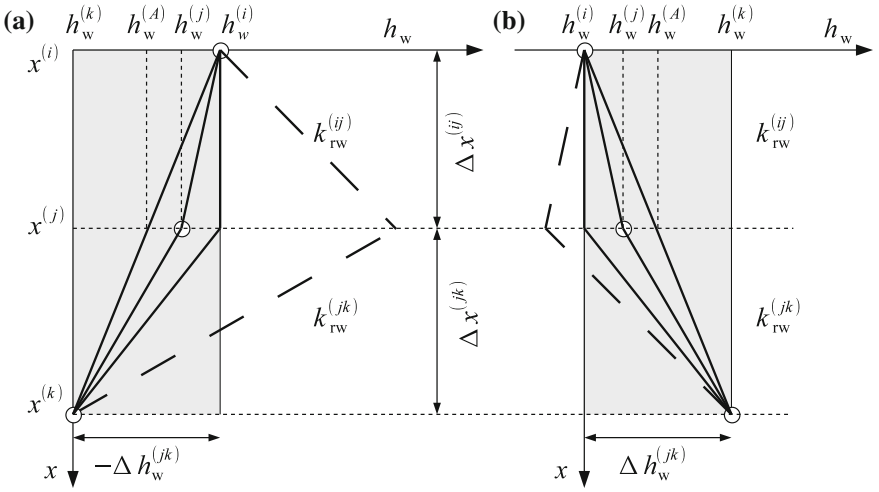

Fig. 4.2 Approximate water pressure head profiles for infiltration (**a**) and drainage (**b**). Modified with permission from [39]

Physically admissible profiles for steady flow are represented by solid lines in Fig. 4.2. The values of the water potential head at the central node $h_w^{(j)}$ should be in the range between $h_w^{(A)}$ and $h_w^{(i)}$, where $h_w^{(A)}$ corresponds to a linear profile and is defined as:

$$h_w^{(A)} = \frac{\Delta x^{(jk)}\, h_w^{(i)} + \Delta x^{(ij)}\, h_w^{(k)}}{\Delta x^{(ij)} + \Delta x^{(jk)}} \,. \tag{4.38}$$

Assuming $h_w^{(j)} = h_w^{(A)}$, the continuity condition given by Eq. (4.37) can be satisfied only if the relative permeability is constant, $k_{rw}^{(ij)} = k_{rw}^{(ik)}$, which is the case for saturated flow. In unsaturated conditions, $k_{rw}^{(ij)} > k_{rw}^{(jk)}$, because the upper part of the medium is more saturated with water. Consequently, if $h_w^{(j)} = h_w^{(A)}$ then $v_w^{(ij)} > v_w^{(jk)}$ and the flux continuity condition is not satisfied. In order to equilibrate the fluxes, the value at the central node j must be larger than $h_w^{(A)}$.

In the second limit case, when $h_w^{(j)} = h_w^{(i)}$ the relative permeabilities at nodes i and j are equal, $k_{rw}^{(i)} = k_{rw}^{(j)}$, and the capillary pressure gradient is zero. The flux in the upper part of the column can be written as:

$$v_w^{(ij)} = \zeta\, k_{rw}^{(i)} = \zeta\, k_{rw}^{(j)} \,, \tag{4.39}$$

while the flux between the nodes j and k can be written as:

$$v_w^{(jk)} = -k_{rw}^{(jk)} \left(\frac{\Delta h_w^{(jk)}}{\Delta x^{(jk)}} - \zeta \right) . \tag{4.40}$$

If the following condition holds:

$$v_{\mathrm{w}}^{(ij)} \leq v_{\mathrm{w}}^{(jk)} \,, \tag{4.41}$$

then one can be sure that there exists a value of the pressure head $h_{\mathrm{w}}^{(j)}$ between $h_{\mathrm{w}}^{(A)}$ and $h_{\mathrm{w}}^{(i)}$, for which $v_{\mathrm{w}}^{(ij)} = v_{\mathrm{w}}^{(jk)}$. Inequality (4.41) together with Eqs. (4.39) and (4.40) imply the following condition for the inter-nodal permeability $k_{\mathrm{rw}}^{(jk)}$:

$$k_{\mathrm{rw}}^{(jk)} \geq \frac{\zeta \; k_{\mathrm{rw}}^{(j)}}{\zeta - \Delta h_{\mathrm{w}}^{(jk)} / \Delta x^{(jk)}} \,. \tag{4.42}$$

If the applied averaging method underestimates the permeability $k_{\mathrm{rw}}^{(jk)}$, the fluxes are not in equilibrium even for $h_{\mathrm{w}}^{(j)} = h_{\mathrm{w}}^{(i)}$ and the profile becomes non-monotonous, as shown by the dashed line in Fig. 4.2. The maximum amplitude of the wiggle cannot exceed $\Delta x^{(ij)}$, since for $h_{\mathrm{w}}^{(j)} = h_{\mathrm{w}}^{(i)} + \Delta x^{(ij)}$ one obtains a hydrostatic potential distribution between $x^{(i)}$ and $x^{(j)}$, and thus $v_{\mathrm{w}}^{(ij)} = 0 < v_{\mathrm{w}}^{(jk)}$ for any value of $k_{\mathrm{rw}}^{(jk)}$. Equation (4.42) represents a sufficient condition, although not a necessary one, for a non-oscillating solution. In some situations physically admissible profiles can be obtained for smaller values of $k_{\mathrm{rw}}^{(jk)}$, but the use of the presented approximation guarantees a monotonous solution for all cases. Note that as $\Delta h_{\mathrm{w}}^{(jk)}$ tends to zero, the limit permeability value from Eq. (4.42) tends to the upstream mean $k_{\mathrm{rw}}^{(jk)} = k_{\mathrm{rw}}^{(j)}$, while, on the other hand, the upstream mean always satisfies the condition given by Eq. (4.42). This is consistent with the findings of other authors who recommended the use of upstream mean to ensure monotonous solution of the Richards equation [15, 16].

In the case of capillary dominated flow, $(\Delta h_{\mathrm{w}}^{(jk)} / \Delta x^{(jk)}) \to -\infty$ and consequently the lower limit for $k_{\mathrm{rw}}^{(jk)}$ given by Eq. (4.42) tends to zero. On the other hand, it is known that for capillary dominated flow the appropriate averaging method is the integrated mean $k_{\mathrm{int}}^{(jk)}$. Therefore, one can use the integrated mean as long as it satisfies the condition Eq. (4.42) and then switch to the limit value given by Eq. (4.42). To summarize, the inter-nodal relative permeability between any two adjacent nodes j (upper) and k (lower) can be computed according to the following formula:

$$k_{\mathrm{rw}}^{(jk)} = \max\left(k_{\mathrm{int}}^{(jk)}, \frac{\zeta \; k_{\mathrm{rw}}^{(j)}}{\zeta - \Delta h_{\mathrm{w}}^{(jk)} / \Delta x^{(jk)}} \right) . \tag{4.43}$$

This method requires only slightly more computational effort than the integrated mean approach.

4.2.2 Drainage

A similar reasoning can be applied to derive the limit value of the average permeability for drainage as $(\Delta h_{\mathrm{w}}^{(jk)}/\Delta x^{(jk)}) \to 0$. This case is shown in Fig. 4.2b. Physically admissible profiles are obtained for values of $h_{\mathrm{w}}^{(j)}$ in the range between $h_{\mathrm{w}}^{(i)}$ and $h_{\mathrm{w}}^{(A)}$, the latter one being interpolated linearly according to Eq. (4.38). In unsaturated conditions, $k_{\mathrm{rw}}^{(ij)}$ is smaller than $k_{\mathrm{rw}}^{(jk)}$ and consequently the total water potential gradient in the lower part of the domain should be smaller than in the upper part. In the limit case when $h_{\mathrm{w}}^{(j)} = h_{\mathrm{w}}^{(i)}$ the average permeability $k_{\mathrm{rw}}^{(jk)}$ should satisfy the following condition:

$$\zeta k_{\mathrm{rw}}^{(j)} \geq -k_{\mathrm{rw}}^{(jk)} \left(\frac{h_{\mathrm{w}}^{(k)} - h_{\mathrm{w}}^{(j)}}{\Delta x^{(jk)}} - \zeta \right) . \tag{4.44}$$

Inequality (4.44) can be transformed to the following form:

$$k_{\mathrm{rw}}^{(jk)} \leq \frac{\zeta k_{\mathrm{rw}}^{(j)}}{\zeta - \Delta h_{\mathrm{w}}^{(jk)}/\Delta x^{(jk)}} . \tag{4.45}$$

If $k_{\mathrm{rw}}^{(jk)}$ is overestimated and does not satisfy Eq. (4.45), the water fluxes $v_{\mathrm{w}}^{(ij)}$ and $v_{\mathrm{w}}^{(jk)}$ equilibrate for a value of the water pressure head $h_{\mathrm{w}}^{(j)} < h_{\mathrm{w}}^{(i)}$, producing a wiggle in the pressure head profile, shown with the dashed line in Fig. 4.2b. The value of $h_{\mathrm{w}}^{(j)}$ will not exceed $h_{\mathrm{w}}^{(k)} - \Delta x^{(jk)}$, for which a zero gradient of the total water potential in the lower part of the domain is obtained. As in the previous case, Eq. (4.45) gives a sufficient, although not a necessary condition to obtain a monotonous solution.

The limit value of $k_{\mathrm{rw}}^{(jk)}$ defined by Eq. (4.45) tends to infinity as the value of the capillary gradient $\Delta h_{\mathrm{w}}^{(jk)}/\Delta x^{(jk)}$ approaches ζ. In such a case, another formula is necessary. It can be obtained from an analysis of the approximate potential head profile within a singe grid cell between nodes j and k, as shown in Fig. 4.3. Let us assume that $\Delta x^{(jk)}$ is larger than $\Delta h_{\mathrm{w}}^{(jk)}$ only by a small value $\Delta x^{(jD)}$, i.e. the hydrostatic distribution of the water pressure is approached. An intermediate point $x^{(D)}$ is introduced in such a way that it divides the grid cell in two unequal segments $\langle x^{(j)}, x^{(D)} \rangle$ and $\langle x^{(D)}, x^{(k)} \rangle$. For a linear potential distribution, the value of $h_{\mathrm{w}}^{(D)}$ would be equal to $h_{\mathrm{w}}^{(B)}$ defined as:

$$h_{\mathrm{w}}^{(B)} = h_{\mathrm{w}}^{(k)} - \frac{\left(\Delta h_{\mathrm{w}}^{(jk)}\right)^2}{\zeta \, \Delta x^{(jk)}} . \tag{4.46}$$

In unsaturated conditions, the value of the potential head $h_{\mathrm{w}}^{(D)}$ should fall between $h_{\mathrm{w}}^{(j)}$ and $h_{\mathrm{w}}^{(B)}$. On the basis of Fig. 4.3 one can assume that the total hydraulic gradient within the segment $\langle x^{(D)}, x^{(j)} \rangle$ is approximately the same as the hydraulic gradient between $x^{(j)}$ and $x^{(k)}$, and both of them are close to zero:

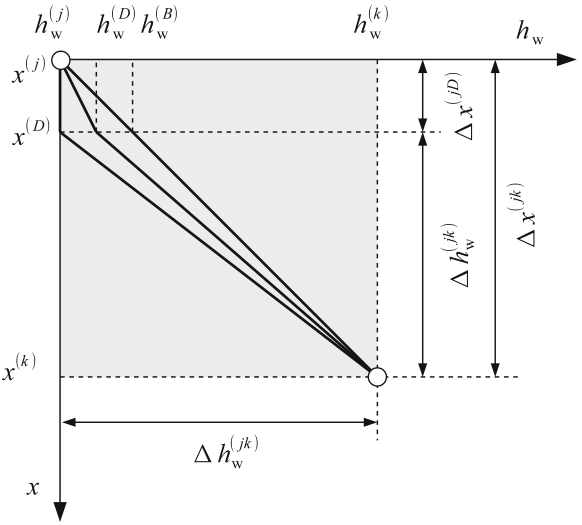

Fig. 4.3 Water potential head profile during drainage close to the hydrostatic state. Modified with permission from [39]

$$\frac{h_w^{(k)} - h_w^{(D)}}{x^{(k)} - x^{(D)}} - \zeta \approx \frac{h_w^{(k)} - h_w^{(j)}}{x^{(k)} - x^{(j)}} - \zeta \to 0 \,. \tag{4.47}$$

On the other hand, for the conditions close to the hydrostatic state the value of the inter-nodal permeability approaches the permeability of the upper node. Thus, the average permeability in the segment $\langle x^{(D)}, x^{(k)} \rangle$ is approximately $k_{rw}^{(Dk)} \approx k_{rw}^{(D)}$. The value of $k_{rw}^{(D)}$ is not known—it is between $k_{rw}^{(j)}$ and $k_{rw}^{(B)}$. Let us assume $k_{rw}^{(D)} \approx k_{rw}^{(B)}$—if one assumes $k_{rw}^{(D)} = k_{rw}^{(j)}$, then the conductivity for the whole grid block would be equal to $k_{rw}^{(j)}$, which is correct only for the limit case when $\Delta h_w^{(jk)} / \Delta x^{(jk)} = \zeta$. Consequently, the water flux between $x^{(D)}$ and $x^{(k)}$ is estimated as:

$$v_w^{(Dk)} \approx -k_{rw}^{(Dk)} \left(\frac{h_w^{(k)} - h_w^{(D)}}{\Delta x^{(jk)} - \Delta x^{(jD)}} - \zeta \right) \approx -k_{rw}^{(B)} \left(\frac{h_w^{(k)} - h_w^{(j)}}{\Delta x^{(jk)}} - \zeta \right) . \tag{4.48}$$

For steady flow, the flux $v_w^{(Dk)}$ should be equal to the average flux between the nodes j and k:

$$v_w^{(Dk)} = v_w^{(jk)} = -k_{rw}^{(jk)} \left(\frac{h_w^{(k)} - h_w^{(j)}}{\Delta x^{(jk)}} - \zeta \right) . \tag{4.49}$$

Therefore, the following approximation can be developed:

$$k_{rw}^{(jk)} \approx k_{rw}^{(B)} \,, \tag{4.50}$$

where:

$$k_{\mathrm{rw}}^{(B)} = k_{\mathrm{rw}}\left(h_{\mathrm{w}}^{(B)}\right) = k_{\mathrm{rw}}\left(h_{\mathrm{w}}^{(k)} - \frac{\left(\Delta h_{\mathrm{w}}^{(jk)}\right)^2}{\zeta\ \Delta x^{(jk)}}\right) \tag{4.51}$$

For $\Delta h_{\mathrm{w}}^{(jk)} \to \Delta x^{(jk)}$, Eq. (4.50) yields the expected limit value $k_{\mathrm{rw}}^{(jk)} \to k_{\mathrm{rw}}^{(j)}$, while for $\Delta h_{\mathrm{w}}^{(jk)} \ll \Delta x^{(jk)}$ the value of the inter-nodal conductivity tends to $k_{\mathrm{rw}}^{(k)}$, which is an overestimation and does not satisfy Eq. (4.45). The suggested approach is to use the minimum of the two values of $k_{\mathrm{rw}}^{(jk)}$ given by Eqs. (4.45) and (4.50):

$$k_{\mathrm{rw}}^{(jk)} = \min\left(k_{\mathrm{rw}}^{(B)}, \frac{\zeta\ k_{\mathrm{rw}}^{(j)}}{\zeta - \Delta h_{\mathrm{w}}^{(jk)}/\Delta x^{(jk)}}\right). \tag{4.52}$$

The obtained averaging formula is very simple to implement, as it does not involve the integrated average.

4.2.3 Capillary Rise

In contrast to the previous cases, for capillary rise the over- or underestimation of the inter-nodal permeability does not lead to oscillations in the numerical solution. While the permeability in the upper part of the domain is smaller than in the lower part, this can be always compensated for by an arbitrarily small potential gradient in the lower part, i.e. the water pressure profile close to hydrostatic, see Fig. 4.4. Therefore, any value of the inter-nodal permeability from the range $k_{\mathrm{rw}}^{(j)}$ to $k_{\mathrm{rw}}^{(k)}$ will lead to physically admissible monotonous solution. Nevertheless, depending on $\Delta x^{(jk)}$, the actual steady-state relative permeability varies from the permeability of the upper node $k_{\mathrm{rw}}^{(j)}$ to the integrated mean $k_{\mathrm{int}}^{(jk)}$, which in the case of initially dry soil may represent a range of several orders of magnitude. A more accurate approximation of $k_{\mathrm{rw}}^{(j)}$ can be obtained if the grid cell is divided in two parts, as shown in Fig. 4.4. The length of the upper sub-cell is denoted by $\Delta x^{(jE)}$, while the length of the lower sub-cell is $\Delta x^{(Ek)}$. The position of point $x^{(E)}$ is chosen in such a way that the corresponding value of the water pressure head is:

$$h_{\mathrm{w}}^{(E)} = h_{\mathrm{w}}^{(k)} - \zeta\ \Delta x^{(jk)}\ . \tag{4.53}$$

In the lower sub-cell, the water pressure distribution is close to the hydrostatic one, which means that the average permeability between the points $x^{(E)}$ and $x^{(k)}$ can be estimated as:

$$k_{\mathrm{rw}}^{(Ek)} \approx k_{\mathrm{rw}}^{(E)} = k_{\mathrm{rw}}\left(h_{\mathrm{w}}^{(E)}\right)\ . \tag{4.54}$$

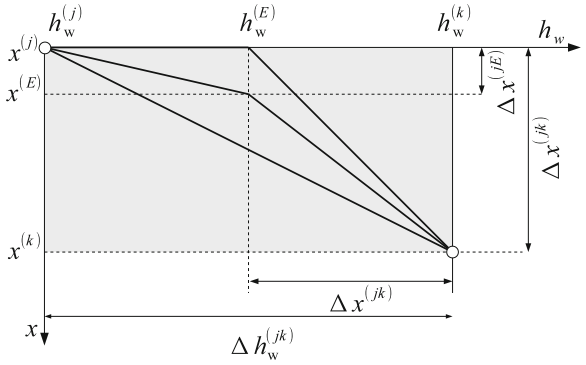

Fig. 4.4 Water pressure head profile for capillary rise. Modified with permission from [39]

In the upper sub-cell, the flow is dominated by capillary forces and the average permeability can be approximated by the integrated mean:

$$k_{\text{int}}^{(jE)} = \frac{1}{h_{\text{w}}^{(E)} - h_{\text{w}}^{(j)}} \int_{h_{\text{w}}^{(j)}}^{h_{\text{w}}^{(E)}} k_{\text{rw}}(\hat{h})\, \mathrm{d}\hat{h} \,. \tag{4.55}$$

For steady-state flow, the water flux should be the same in each part of the cell. Moreover, it should be equal to the flux between nodes j and k estimated using the average inter-nodal permeability $k_{\text{rw}}^{(jk)}$. This conditions can be written as follows:

$$v_{\text{w}}^{(jk)} = v_{\text{w}}^{(jE)} = v_{\text{w}}^{(Ek)} \,, \tag{4.56}$$

where:

$$v_{\text{w}}^{(jk)} = -k_{\text{rw}}^{(jk)} \left(\frac{\Delta h_{\text{w}}^{(jk)}}{\Delta x^{(jk)}} - \zeta \right) , \tag{4.57}$$

$$v_{\text{w}}^{(jE)} = -k_{\text{int}}^{(jE)} \left(\frac{\Delta h_{\text{w}}^{(jk)} - \zeta\, \Delta x^{(jk)}}{\Delta x^{(jE)}} - \zeta \right) , \tag{4.58}$$

$$v_{\text{w}}^{(Ek)} = -k_{\text{rw}}^{(E)} \left(\frac{\zeta\, \Delta x^{(jk)}}{\Delta x^{(jk)} - \Delta x^{(jE)}} - \zeta \right) . \tag{4.59}$$

The double equality (4.56) can be transformed to a system of two equations with two unknowns, $k_{\text{rw}}^{(jk)}$ and $\Delta x^{(jE)}$. By requiring $v_{\text{w}}^{(jE)} = v_{\text{w}}^{(Ek)}$ one arrives at a quadratic equation with respect to $\Delta x^{(jE)}$. This equation has one positive and one negative root. The positive root is given by the following formula:

$$\Delta x^{(jE)} = \frac{-\Delta h_{\mathrm{w}}^{(jk)} + Z_{\mathrm{k}}}{2\,\zeta\,(k_{\mathrm{rw}}^{(E)}/k_{\mathrm{int}}^{(jE)} - 1)}\,, \tag{4.60}$$

where:

$$Z_{\mathrm{k}} = \sqrt{\left(\Delta h_{\mathrm{w}}^{(jk)}\right)^2 + 4\,\zeta\,\Delta x^{(jk)}\,\left(k_{\mathrm{rw}}^{(E)}/k_{\mathrm{int}}^{(jE)} - 1\right)\,\left(\Delta h_{\mathrm{w}}^{(jk)} - \zeta\,\Delta x^{(jk)}\right)}\,. \tag{4.61}$$

The average permeability $k_{\mathrm{rw}}^{(jk)}$ is equal to the weighted harmonic average of the permeabilities of the two sub-cells:

$$k_{\mathrm{rw}}^{(jk)} = \frac{\Delta x^{(jk)}\,k_{\mathrm{int}}^{(jE)}\,k_{\mathrm{rw}}^{(E)}}{(\Delta x^{(jk)} - \Delta x^{(jE)})\,k_{\mathrm{int}}^{(jE)} + \Delta x^{(jE)}\,k_{\mathrm{rw}}^{(E)}}\,. \tag{4.62}$$

Note that the harmonic averaging is applied to the values of $k_{\mathrm{int}}^{(jE)}$ and $k_{\mathrm{rw}}^{(E)}$ which themselves represent average permeabilities and can be considered uniform in the respective parts of the cell. Such an approach is physically justified, in contrast to the harmonic averaging of nodal relative permeabilities $k_{\mathrm{rw}}^{(j)}$ and $k_{\mathrm{rw}}^{(k)}$ as described in Sect. 4.1.1. While the final formula for capillary rise is somewhat more complex than the formulas for infiltration and drainage, the arithmetic operations are straightforward to perform once the value of the integrated mean $k_{\mathrm{int}}^{(jE)}$ is known.

4.2.4 Implementation Issues

The application of the method described above requires that for any pair of nodal values of the pressure head, $h_{\mathrm{w}}^{(j)}$ and $h_{\mathrm{w}}^{(k)}$, first the value of the capillary gradient $\Delta h_{\mathrm{w}}^{(jk)}/\Delta x^{(jk)}$ needs to be computed and compared to the gravity coefficient ζ. Based on this comparison, one of the three available formulae must be chosen. It means that for more complex flow scenarios the averaging formula may change with time and/or spatial position.

While the method was developed for the pressure head as the primary variable in the Richards equation, it can be easily adapted to the case of primary variable p_{w}. To this order the values of pressure head should be replaced by the values of the pressure, while the gravity coefficient ζ should be replaced by $\zeta\,\rho_{\mathrm{w}}\,g$, where g is the magnitude of the gravitational acceleration. In the numerical examples presented below both forms of the governing equations are used.

The proposed approach, similarly to the integrated mean and the method of Baker [3], requires an integration of the relative permeability defined as a function of the water pressure (or pressure head). For several models of the relative permeability functions, including the exponential, Brooks–Corey–Burdine and Brooks–Corey–Mualem models, this can be done analytically. However, for the widely used van Genuchten–Mualem model (and many other), analytical integration

is not possible. The use of numerical integration significantly increases the computational effort and the time of the simulation. An efficient approach is to create at the preprocessing stage a look-up table containing the values of the flux potential Φ_p or Φ_h defined as a function of the water pressure (or head). These values are calculated using numerical integration with a large number of quadrature points, in order to obtain an accurate approximation. During the simulation of unsteady flow, the integrated mean is computed as the difference in flux potentials divided by the difference in the pressures (or heads), with the values of the flux potential interpolated from the look-up table. In the examples presented below, linear interpolation was used, although more sophisticated techniques are also available [30]. Interpolation from a look-up table can be also used to evaluate the water saturation and the relative permeability as functions of the water pressure. Such an approach offers a significant speedup of the computations, even if simple permeability averaging schemes are employed. In order to minimize the error introduced by interpolation, the points should be spaced non-uniformly, with higher density in the regions where the values of hydraulic functions change more rapidly. Numerical experiments presented in [39] and [40] showed that if the interpolation is used, the proposed averaging method requires simulation time comparable to the standard averaging approaches like arithmetic or geometric means.

4.2.5 Evaluation for Steady Flow

The accuracy of the formulae presented in the previous sections can be evaluated by comparing the resulting values of the inter-nodal permeability with the ones obtained from the solution of equation describing steady state incompressible unsaturated flow between two nodes. First, let us consider exponential relative permeability function given by Eq. (4.22). In this case the exact value of the steady-state inter-nodal permeability is given by the formula of Baker et al. [5], Eq. (4.26), which results from the analytical solution of the steady flow equation. In Tables 4.2 and 4.3 these exact permeability values (K-EXACT) are compared with the approximations obtained using the formulae of Szymkiewicz [39] (K-SZYM), described in Sects. 4.2.1–4.2.3, as well as other commonly used averaging schemes. They include the arithmetic (K-ARIT), geometric (K-GEOM), harmonic (K-HARM) and integrated (K-INT) averages, as well as upstream weighting (K-UPS) and the method based of flux splitting (K-SPLIT), as given by Eqs. (4.14) and (4.17). In the latter case, it was assumed that the relative permeability for the capillary flux is equal to the integrated mean approach and the relative permeability for the gravitational flux is equal to the permeability of the upper node. The calculations were carried out for two values of the pressure scaling parameter: $h_g = 1\,\mathrm{m}$ and $h_g = 0.05\,\mathrm{m}$, which correspond respectively to a moderate and a strong nonlinearity in the $k_{rw}(h_w)$ relationship. Two values of the gravity coefficient were used: $\zeta = 1$ (vertical flow) and $\zeta = 0.707$ (flow direction inclined by 45° to the horizontal plane). The inter-nodal distance was assumed constant, $\Delta x = 0.2\,\mathrm{m}$. A number of boundary value problems were

Table 4.2 Exact and approximate steady-state inter-nodal permeability values for exponential relative permeability function with $h_g = 1$ m, $\Delta x = 0.2$ m

Test case	1	2	3	4	5	6
Flow type	Infiltration	Capillary rise	Drainage	Infiltration	Capillary rise	Drainage
$h_w^{(j)}$ (m)	−1.00E−03	−5.00E+00	−1.50E−01	−1.00E−03	−5.00E+00	−1.00E−01
$k_{rw}^{(j)}$ (–)	9.99E−01	6.74E−03	8.61E−01	9.99E−01	6.74E−03	9.05E−01
$h_w^{(k)}$ (m)	−5.00E+00	−1.00E−03	−1.00E−03	−5.00E+00	−1.00E−03	−1.00E−03
$k_{rw}^{(k)}$ (–)	6.74E−03	9.99E−01	9.99E−01	6.74E−03	9.99E−01	9.99E−01
ζ (–)	1.00E+00	1.00E+00	1.00E+00	7.07E−01	7.07E−01	7.07E−01
K-EXACT	2.11E−01	1.86E−01	9.26E−01	2.07E−01	1.90E−01	9.50E−01
K-SZYM	1.98E−01	1.92E−01	8.94E−01	1.98E−01	2.00E−01	9.32E−01
K-ARIT	5.03E−01	5.03E−01	9.30E−01	5.03E−01	5.03E−01	9.52E−01
K-GEOM	8.20E−02	8.20E−02	9.27E−01	8.20E−02	8.20E−02	9.51E−01
K-HARM	1.34E−02	1.34E−02	9.25E−01	1.34E−02	1.34E−02	9.50E−01
K-INT	1.98E−01	1.98E−01	9.28E−01	1.98E−01	1.98E−01	9.51E−01
K-UPS	9.99E−01	9.99E−01	8.61E−01	9.99E−01	9.99E−01	9.05E−01
K-SPLIT	2.29E−01	2.06E−01	6.64E−01	2.21E−01	2.04E−01	7.97E−01

Table 4.3 Exact and approximate steady-state inter-nodal permeability values for exponential relative permeability function with $h_g = 0.05$ m, $\Delta x = 0.2$ m

Test case	7	8	9	10	11	12
Flow type	Infiltration	Capillary rise	Drainage	Infiltration	Capillary rise	Drainage
$h_w^{(j)}$ (m)	−1.00E−03	−5.00E+00	−1.50E−01	−1.00E−03	−5.00E+00	−1.00E−01
$k_{rw}^{(j)}$ (–)	9.80E−01	3.72E−44	4.98E−02	9.80E−01	3.72E−44	1.35E−01
$h_w^{(k)}$ (m)	−5.00E+00	−1.00E−03	−1.00E−03	−5.00E+00	−1.00E−03	−1.00E−03
$k_{rw}^{(k)}$ (–)	3.72E−44	9.80E−01	9.80E−01	3.72E−44	9.80E−01	9.80E−01
ζ (–)	1.00E+00	1.00E+00	1.00E+00	7.07E−01	7.07E−01	7.07E−01
K-EXACT	3.84E−02	7.62E−04	1.27E−01	2.87E−02	1.79E−03	2.74E−01
K-SZYM	3.77E−02	4.74E−04	1.06E−01	2.70E−02	1.51E−03	2.45E−01
K-ARIT	4.90E−01	4.90E−01	5.15E−01	4.90E−01	4.90E−01	5.58E−01
K-GEOM	1.91E−22	1.91E−22	2.21E−01	1.91E−22	1.91E−22	3.64E−01
K-HARM	7.44E−44	7.44E−44	9.38E−02	7.44E−44	7.44E−44	2.38E−01
K-INT	9.80E−03	9.80E−03	3.12E−01	9.80E−03	9.80E−03	4.27E−01
K-UPS	9.80E−01	9.80E−01	4.98E−02	9.80E−01	9.80E−01	1.35E−01
K-SPLIT	4.71E−02	1.02E−02	−7.17E−01	3.65E−02	1.01E−02	−5.45E−01

examined, which represent all three types of flow, i.e. infiltration, drainage and capillary rise in either vertical or inclined direction.

It can be seen that the approximation method proposed by the author (K-SZYM) is in most cases more accurate than any other method. The exceptions are represented by test cases 3 and 6, corresponding to drainage where the permeabilities at the upper and lower node are very similar, and consequently most of the averaging methods give similar results. It should be noted that for the same two cases the method based on flux splitting predicts average permeability which is outside the range of values defined

by the two nodal permeabilities, and thus physically inadmissible. It means that such an averaging scheme should be used with care. The advantages of the new method can be seen even more clearly in Table 4.3, where the results for highly nonlinear relative permeability function are reported. Here the maximum relative error of the new method does not exceed 40 %, while other methods often lead to errors of more than one order of magnitude. For drainage (test cases 9 and 12) the method based on flux splitting predicts negative values of the permeability coefficient, which means that the flux direction is opposite to the direction resulting from the water potential gradient.

Further results for steady-state flow can be found in [39]. In that paper various averaging schemes were verified against numerical solutions of steady flow equation for fifteen relative permeability functions, corresponding to a range of soils from sands to clays. Included were four Brooks–Corey–Burdine functions, four van Genuchten–Mualem functions, two exponential functions, one Gardner function, two van Genuchten–Mualem functions with negative connectivity parameter κ (see Sect. 2.1.6), and two combinations of van Genuchten capillary function with power-type relative permeability functions, as proposed in [27]. For each function a large number of steady flow problems was solved, with the internodal distances varying between 1 mm and 100 m and the nodal values of the water pressure head ranging from -1 mm to -100 m. For any specific test case, the error of the considered averaging scheme was defined as follows:

$$\text{ERR-K} = \log_{10} \frac{k_{\text{rw}}^{(jk)}}{k_{\text{ref}}^{(jk)}} \tag{4.63}$$

where $k_{\text{rw}}^{(jk)}$ was computed with the considered averaging scheme, and $k_{\text{ref}}^{(jk)}$ is the reference value obtained from the numerical solution of steady state flow equation between nodes. Such a formulation was chosen in order to give equal weight to over- and underestimation of the average permeability, and to facilitate comparison of the relative errors, which often differ by several orders of magnitude. In view of the large number of results, representative error measures were defined to quantify the accuracy of each method of inter-nodal permeability approximation:

- root-mean square error, RMS-ERR-K

$$\text{RMS-ERR-K} = \sqrt{\frac{1}{N} \sum_{1}^{N} (\text{ERR-K})^2} \tag{4.64}$$

  where N is the number of test cases in the considered set,
- maximum error value (largest overestimation), max(ERR-K),
- minimum error value (largest underestimation), min(ERR-K).

The values of these error measures are reported in Table 4.4 for some of the averaging methods used in the previous example: K-ARIT, K-GEOM, K-INT, K-UPS

Table 4.4 Root-mean-square errors obtained with various permeability averaging schemes for steady flow test cases. Data from [39]

	K-SZYM	K-BAKER	K-GASTO	K-ARIT	K-GEOM	K-INT	K-UPS
Average	0.12	0.36	0.29	1.61	1.14	1.01	1.30
Small Δx	0.04	0.07	0.33	1.13	0.84	0.09	1.34
Medium Δx	0.13	0.38	0.22	1.33	0.89	0.62	1.44
Large Δx	0.17	0.49	0.19	2.17	1.55	1.68	1.10
Infiltration	0.04	0.11	0.33	0.86	1.26	0.57	1.04
Drainage	0.22	0.51	0.09	2.57	1.29	1.90	0.27
Capillary rise	0.11	0.49	0.26	1.74	0.77	0.64	1.96

and K-SZYM. Moreover, computations were performed with the method of [19] (K-GASTO), for Brooks–Corey and van Genuchten–Mualem functions and node spacing satisfying condition given by Eq. (4.36), and with the method of Baker [3] (K-BAKER), for those relative permeability functions, which can be inverted analytically to obtain $h_{\mathrm{w}}(k_{\mathrm{rw}})$.

Table 4.4 provides the average value of RMS-ERR-K for all test cases, as well as separate results obtained for three ranges of inter-nodal distances Δx: small (1 mm, 1 cm, 2 cm), medium (10, 20, 50 cm) and large (1, 10, 100 m), and three types of flow (infiltration, drainage, capillary rise). It should be noted that due to its definition RMS-ERR-K is always positive and provides information only on the magnitude of error, without indicating whether the specific method under- or overestimates the internodal permeability. As the errors are defined in terms of decimal logarithm, a value of RMS-ERR-K $= 1.0$ corresponds to an error of one order of magnitude (i.e. 1000 %), while a value of 0.17—to an error of about 50 %.

Overall, it can be seen that the methods based on Darcian means are significantly more accurate than the simple averaging schemes, especially on medium or coarse grids. On fine grids, accurate results were obtained also with the integrated mean approach. As far as the type of flow is considered, the author's method gave the best results of all methods for infiltration and capillary rise, while for drainage it was second best, after the method of Gasto et al. [19]. The performance of the simple methods differ significantly, depending on the type of flow. For infiltration, the arithmetic and integrated averages provided average errors below one order of magnitude, while the average errors of the geometric average and the upstream weighting exceeded this value. In contrast, for drainage the upstream weighting largely outperformed the other simple methods, allowing to obtain very high accuracy. For the capillary rise, the geometric and integrated means proved more accurate than the arithmetic and upstream means.

Finally, the methods can be also compared in terms of the largest error obtained for the ensemble of test problems. The maximum and minimum error values are reported in Table 4.5. The most extreme case corresponds to the overestimation of the inter-nodal permeability by 10.5 orders of magnitude using the arithmetic mean approach, which occurred for drainage with large Δx in a soil characterized by a very rapid decrease of the relative permeability within a small range of the negative

Table 4.5 Root-mean-square errors obtained with various permeability averaging schemes for steady flow test cases. Data from [39]

	K-SZYM	K-BAKER	K-GASTO	K-ARIT	K-GEOM	K-INT	K-UPS
min(ERR-K)	−1.50	−4.30	−1.24	−2.89	−5.38	−3.23	−6.05
max(ERR-K)	0.11	4.47	1.60	10.50	5.40	8.55	8.18

values of the water pressure head. Other simple averaging methods may also lead to over- or underestimation of the permeability by several orders of magnitude in particular conditions. Significant errors were generated also by the method of Baker [3], despite the fact that the average errors obtained with this method are rather small. This indicates that the latter method may be relatively inaccurate for some specific types of the relative permeability functions. In contrast, the largest errors generated by the method of Szymkiewicz [39] did not exceed 1.5 order of magnitude. The method of Gasto et al. [19] was similarly accurate, but due to its limitations it could be applied to a substantially smaller number of test cases.

4.2.6 Evaluation for Unsteady Flow

In this section, four one-dimensional unsteady flow test cases are discussed, in order to show the performance of the proposed method in comparison with other averaging schemes. The first two examples are similar to the ones presented in [39], but differ in the values of soil parameters and in accounting for the compressibility of water. The soil is characterized by Brooks–Corey–Burdine hydraulic functions with the following parameters: porosity $\phi = 0.4$, residual saturations $S_{rw} = S_{ra} = 0$, intrinsic permeability $k_s = 8.5 \times 10^{-12}\,\mathrm{m}^2$, entry pressure $p_e = 440\,\mathrm{Pa}$, exponent $n_b = 1.124$. The parameters correspond to sand with a relatively uniform grain size distribution.

The first example is vertical downward infiltration in a 2-m thick soil layer with initially uniform distribution of the water pressure $p_w = -49050\,\mathrm{Pa}$, corresponding to the water saturation of 0.005. At the soil surface a constant value of the water pressure is imposed, $p_w = -500\,\mathrm{Pa}$ ($S_w = 0.866$), while at the bottom of the layer the free drainage condition is applied. Numerical simulations were performed for two values of node spacing, $\Delta x = 20\,\mathrm{cm}$ and $\Delta x = 1\,\mathrm{cm}$, respectively. Figure 4.5 shows the water saturation profiles after 3 h of infiltration obtained on the coarser grid for various permeability averaging schemes. They are compared to the reference solution obtained on a fine grid with $\Delta x = 1\,\mathrm{mm}$. For such a fine discretization, essentially the same results were obtained using K-INT and K-UPS schemes. As discussed above, these two averaging schemes represent the limit values of the inter-nodal conductivity for downward infiltration. Thus, the corresponding solution is assumed to be a close approximation of the exact solution. The reference solution predicts a very sharp wetting front, which cannot be exactly reproduced on the coarse grid. However, K-UPS, K-ARIT, K-BAKER and K-SZYM approximate the position of the wetting front with reasonable accuracy. The latter two methods give very similar

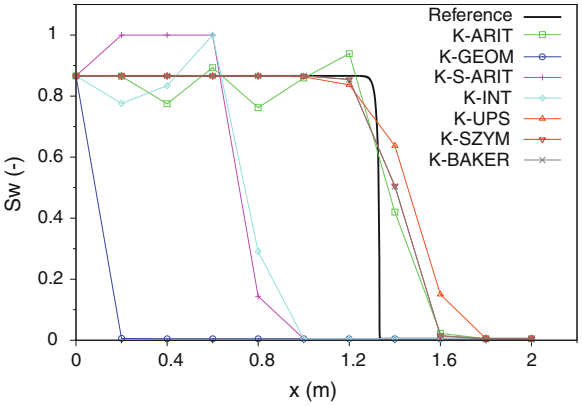

Fig. 4.5 Example 1: water saturation profiles obtained with various permeability averaging methods, coarse grid

results, which are somewhat more accurate than the upstream weighting and on the other hand do not produce oscillations, which occur in the solution obtained with K-ARIT. The integrated mean (K-INT) and the method based on arithmetic averaging of the water saturation (K-S-ARIT) not only lead to oscillations but also considerably underestimate the position of the wetting front. The least accurate solution is given by the geometric mean, which severely underestimates the inter-nodal permeability and consequently predicts virtually no flow. The latter three methods are clearly not adequate to simulate gravity-dominated infiltration on coarse grids.

In contrast, if a finer node spacing of 1 cm is used, the differences between various methods are much smaller. The only exception is the geometric mean, which still underestimates the position of the wetting front and produces saturation values larger than the boundary saturation in the wet zone (not shown here). In order to better show the differences between the other methods, only a small part of the solution domain near the wetting front is presented in Fig. 4.6. For the considered node spacing, K-SZYM gives the same values as K-INT (the latter one is not shown in the figure). This approach underestimates the position of the wetting front, albeit only slightly. Even better results are obtained with K-BAKER, K-GASTO and K-S-ARIT. In contrast, both K-ARIT and K-UPS give more diffuse solutions, which overestimate the position of the wetting front, K-UPS being less accurate than K-ARIT. Note also that the geometric averaging predicts the position of the wetting front at the value of $x \approx 0.5$ m, well outside the range shown in the figure.

The second example concerns drainage in the same domain as in Example 1. The initial condition is $p_w = 0$ in the whole soil layer and this value is maintained at the bottom as the boundary condition. At the soil surface a zero-flux condition is imposed. Water drains from the layer under the influence of gravity. The same values of Δx as in Example 1 were used. The water saturation profiles for coarse grid after 4 h of drainage are shown in Fig. 4.7. It can be seen that all simple permeability averaging

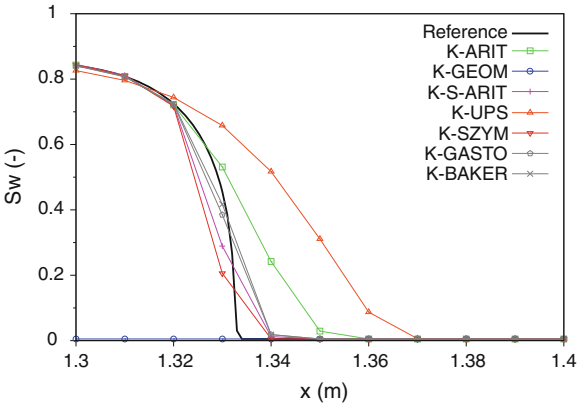

Fig. 4.6 Example 1: water saturation profiles obtained with various permeability averaging methods, fine grid

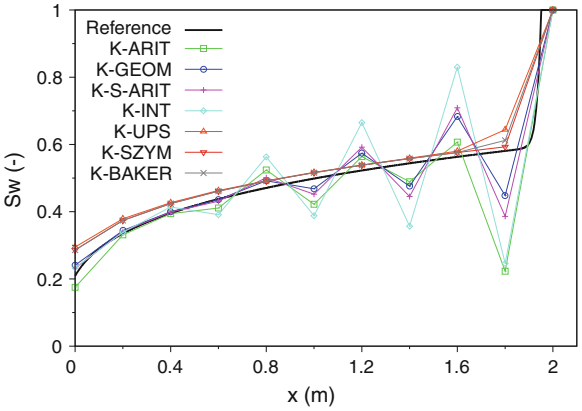

Fig. 4.7 Example 2: water saturation profiles obtained with various permeability averaging methods, coarse grid

schemes lead to oscillatory solutions. In contrast, monotonous saturation profiles are obtained with K-UPS, K-BAKER and K-SZYM, the latter one being closest to the reference solution. For the finer grid, $\Delta x = 1$ cm, all averaging schemes produce very accurate solutions, thus the results are not shown here.

The test cases presented above may suggest that the node spacing of about 1 cm is fine enough to obtain sufficiently accurate results with the arithmetic averaging scheme, which is widely used in unsaturated flow modelling. Such a conclusion was drawn by van Dam and Feddes [43] on the basis of several numerical simulations performed by those authors. However, a re-examination of two of their test cases presented by Szymkiewicz [39] showed that the results obtained with $\Delta x = 1$ cm significantly differ from those obtained for a finer grid if arithmetic averaging is

applied. The two cases (Examples 3 and 4 in the numeration of this chapter) are briefly described here, following [39]. Both problems concern vertical flow in a 40 cm column of soil characterized by the van Genuchten capillary function and Mualem relative permeability function with the following parameters: $\theta_{sw} = 0.43$, $\theta_{rw} = 0.01$, $p_g = 3940\,\text{Pa}$, $n_g = 1.507$, $m_g = 1 - 1/n_g$, $k_s = 2.065 \times 10^{-13}\,\text{m}^2$ ($K_{sw} = 17.5\,\text{cm}\,\text{d}^{-1}$) and the connectivity parameter $\kappa = -0.14$. Note that for the non-standard Mualem permeability function neither K-GASTO nor K-BAKER can be applied.

The boundary conditions correspond to the soil–atmosphere interface, as described in Sect. 2.3.2. In Example 3 the soil is initially dry, with a uniform water content $\theta_w^{init} = 0.1$, corresponding to the water pressure head $h_w^{init} = -832.5\,\text{cm}$. At the top of the column a constant infiltration flux of $v_w^{top} = 100\,\text{cm}\,\text{d}^{-1}$ is imposed, until the soil surface reaches saturation. Afterwards, the boundary condition is switched to a constant pressure head, $h_w^{top} = 0$. The infiltration continues, but the value of the flux decreases in time. At the bottom, the initial value of the water content is maintained. The solutions are compared in terms of the cumulative infiltration q_{inf}, defined as the integral of the infiltration flux over time. The reference solution obtained on a fine grid with $\Delta x = 0.05\,\text{cm}$ predicted the cumulative infiltration of $q_{inf} = 3.69\,\text{cm}$ at $t = 0.1\,\text{d}$, while the ponding occured (the surface became saturated) at $t_{pond} = 0.006\,\text{day}$. On such a fine grid, virtually the same results were obtained using the arithmetic and integrated permability averaging and they were cross-checked with the Hydrus-1D code [35]. On a coarser grid of $\Delta x = 1\,\text{cm}$, the arithmetic averaging yielded the cumulative infiltration $q_{inf} = 3.88\,\text{cm}$ and $t_{pond} = 0.009\,\text{d}$, the geometric averaging: $q_{inf} = 3.66\,\text{cm}$ and $t_{pond} = 0.002\,\text{d}$, respectively, while the author's method: $q_{inf} = 3.68\,\text{cm}$ and $t_{pond} = 0.006$ d. In this case the new method offers a considerable improvement over the arithmetic averaging.

In Example 4 the soil is initially moderately wet ($\theta_w^{init} = 0.1$, $h_w^{init} = -200\,\text{cm}$) and a constant evaporation flux of $v_w^{top} = -0.5\,\text{cm}\,\text{d}^{-1}$ is applied at the surface, until the water pressure head at the surface reaches the value of $h_{dry} = -1377\,\text{m}$, which is then maintained as a Dirichlet boundary condition. The evaporation continues, but the flux diminishes with time. At the bottom, the initial value of the water pressure head is kept. Similarly to the previous case, the solutions are compared in terms of the cumulative flux at the surface. According to the reference solution ($\Delta x = 0.05\,\text{cm}$), the cumulative evaporation flux after 5 days is $q_{ev} = 0.89\,\text{cm}$ and the water pressure head at the soil surface reaches its limit value after $t_{dry} = 0.51$ day. For $\Delta x = 1\,\text{cm}$ the differences between averaging schemes are even larger than in the previous case, with the arithmetic averaging predicting $q_{ev} = 1.12\,\text{cm}$ and $t_{dry} = 1.14\,\text{d}$, the upstream averaging: $q_{ev} = 1.26\,\text{cm}$ and $t_{dry} = 1.41\,\text{d}$, and the author's method: $q_{ev} = 0.90\,\text{cm}$ and $t_{dry} = 0.63\,\text{d}$. Again, the new method proved more accurate than the arithmetic mean.

4.3 Saturated–Unsaturated Transition

A special case for permeability averaging arises when one of the nodes is fully water-saturated, with the water pressure larger than the entry pressure for the given soil, while the other node is unsaturated. If the value of the water pressure at the saturated node increases, the inter-nodal relative permeability obtained from the steady-state solution will also increase, tending in the limit to the value $k_{\mathrm{rw}}^{(\mathrm{jk})} = 1$. Among the simple averaging methods presented in Sect. 4.1, only the integrated mean, Eq. (4.9), and the formula based on the arithmetic average of nodal pressures, Eq. (4.8), are able to reproduce this behaviour. Other methods, based on the averaging of the nodal permeabilities or saturations, do not predict any change in the inter-nodal permeability, because both permeability and saturation are independent of the water pressure in the saturated range. For a more detailed discussion of the errors arising at the saturated–unsaturated interface, see [31].

As far as the methods based on the Darcian averaging approach are considered, one should note that the formulae presented in Sect. 4.2 are applicable without any modifications to the case of saturated–unsaturated transition. They are based on the integrated mean permeability and on the values of permeability calculated for some intermediate values of the pressure head. Thus, a change of the pressure head at the saturated node will influence the resulting inter-nodal permeability, even if both nodal permeabilities remain constant. The same is true for the formulae of Baker [2], Baker et al. [5] and Baker [3]. In contrast, the formula of Gasto et al. [19] was developed for strictly unsaturated conditions, but the authors proposed a modification to account for the saturated–unsaturated transition, which can be also used with any other scheme for unsaturated permeability averaging. The grid cell is explicitly divided in two parts, one fully saturated and the other one unsaturated, with the interface located at $x^{(S)}$, as shown in Fig. 4.8. Assuming that node j is saturated, one can write the flux continuity condition at the saturated–unsaturated interface as follows:

$$-k_{\mathrm{rw}}^{(jS)}\left(\frac{h_{\mathrm{w}}^{(S)}-h_{\mathrm{w}}^{(j)}}{\Delta x^{(jS)}}-\zeta\right)=-k_{\mathrm{rw}}^{(Sk)}\left(\frac{h_{\mathrm{w}}^{(k)}-h_{\mathrm{w}}^{(S)}}{\Delta x^{(Sk)}}-\zeta\right), \tag{4.65}$$

where $h_{\mathrm{w}}^{(S)}$ is the water pressure head corresponding to the transition from unsaturated to saturated state (equal to zero or the air entry pressure, depending on the assumed constitutive relationship). The relative permeability in the saturated zone is $k_{\mathrm{rw}}^{(jS)} = 1$, while the permeability in the unsaturated zone $k_{\mathrm{rw}}^{(Sk)}$ can be computed with the formula of Gasto et al. [19], or any other formula suitable for unsaturated flow. If $k_{\mathrm{rw}}^{(Sk)}$ depends on $\Delta x^{(Sk)}$, Eq. (4.65) is nonlinear with respect to $\Delta x^{(Sk)}$ and has to be solved iteratively. A further simplification can be introduced if one considers that the pressure distribution between nodes j and k is linear. This leads to the following expression for the inter-nodal permeability $k_{\mathrm{rw}}^{(jk)}$ [19]:

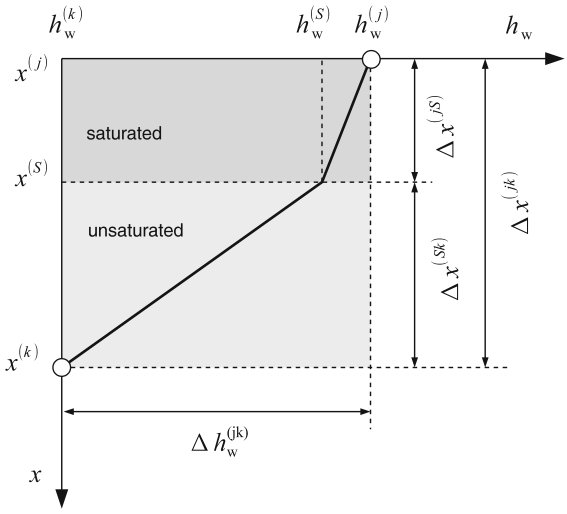

Fig. 4.8 Water pressure head profile near the saturated–unsaturated interface

$$k_{rw}^{(jk)} = \frac{k_{rw}^{(Sk)}\,\Delta h_w^{(jk)}}{\left(h_w^{(k)} - h_w^{(S)}\right) + k_{rw}^{(Sk)}\,\left(h_w^{(S)} - h_w^{(j)}\right)}\,, \tag{4.66}$$

where the unsaturated permeability $k_{rw}^{(Sk)}$ is computed assuming the position of the interface:

$$x^{(S)} = x^{(k)} - \Delta x^{(jk)}\,\frac{h_w^{(k)} - h_w^{(S)}}{\Delta h_w^{(jk)}}\,. \tag{4.67}$$

An analogous formula can be easily obtained for the opposite case, i.e. when the lower node is saturated.

As an example, let us consider steady-state vertical downward flow ($\zeta = 1$) in a porous medium characterized by Brooks–Corey–Burdine relative permeability function with the air-entry pressure head $h_e = 0.25\,\text{m}$ and the shape parameter $n_b = 2.0$. The distance between nodes is $\Delta x = 0.20\,\text{m}$ and the water pressure head at the lower node is $h^{(k)} = -5.0\,\text{m}$, with the corresponding relative permeability $k_{rw}^{(k)} = 3.91 \times 10^{-11}$. At the upper node, the water pressure head assumes four different values, such that $h_w^{(j)} \geq -h_e$ and $k_{rw}^{(j)} = 1$, as shown in Table 4.6. For each case, the inter-nodal relative permeability obtained from a numerical solution of the steady-state problem is compared with four approximations. The approximate methods include those proposed by Szymkiewicz [39] (K-SZYM), Baker et al. [5] (K-BAKER) and Gasto et al. [19] (K-GASTO), as well as the integrated mean (K-INT) and the method based on the arithmetic average of the water pressure head (K-H-ARIT). The results in Table 4.6 shows that the most accurate approximation in this case is obtained with the formula of Baker et al. [5]. Good results are also obtained with K-SZYM, which predicts values equal to the integrated mean, except for the first

Table 4.6 Inter-nodal permeability values for saturated–unsaturated transition obtained from the numerical solution of steady flow equation and various approximating formulae

Test case	1	2	3	4
$h_{\mathrm{w}}^{(j)}$ (m)	−0.25	0.00	1.00	5.00
K-NUM	4.04E−02	9.24E−02	2.42E−01	5.44E−01
K-SZYM	4.04E−02	5.71E−02	2.14E−01	5.29E−01
K-BAKER	4.10E−02	8.89E−02	2.41E−01	5.44E−01
K-GASTO	8.82E−02	9.24E−02	1.09E−01	1.61E−01
K-INT	7.52E−03	5.71E−02	2.14E−01	5.29E−01
K-H-ARIT	6.77E−09	1.00E−08	5.96E−08	1.00E+00

case, where it is close to the reference value, while K-INT underestimates the steady-state permeability by a factor of about 5. K-GASTO is the most accurate method for $h_{\mathrm{w}} = 0$, while in other cases it is less accurate than K-BAKER and K-SZYM, but still correctly reproduces the order of magnitude of the inter-nodal permeability. Finally, the arithmetic averaging of the water pressure head, K-H-ARIT, while showing the expected increase of the inter-nodal permeability with the increase of the pressure at the upper node, leads to very inaccurate results for all cases except the last one, where at least the correct order of magnitude is reproduced.

4.4 Heterogeneous Medium

The permeability averaging methods described in the previous sections were based on the assumption that the porous medium between the two adjacent nodes is homogeneous. Nevertheless, they can be directly applied also for heterogeneous media if the material properties are associated with grid cells (elements) and the nodes are placed at material interfaces (vertex-centred scheme with element-oriented material properties, discussed in Sect. 3.2.4). In such a case, the porous medium between two adjacent nodes is always homogeneous, and any of the averaging methods described above can be applied.

On the other hand, additional considerations are necessary if the adjacent nodes belong to different material regions, as shown in Fig. 4.9. In such a case, physically consistent approximation of the inter-nodal permeability can be obtained if one makes use of the interface conditions discussed in Sect. 2.3.3. The following discussion focuses again on the case of one-dimensional incompressible unsaturated flow. The interface separating materials *I* and *II* is located at $x^{(F)}$, between nodes $x^{(j)}$ and $x^{(k)}$, as shown in Fig. 4.9. The materials are characterized by the saturated hydraulic conductivities K_{sw}^{I} and K_{sw}^{II} and the relative permeability functions $k_{\mathrm{rw}}^{I}(h_{\mathrm{w}})$ and $k_{\mathrm{rw}}^{II}(h_{\mathrm{w}})$, respectively. The flux continuity condition for the interface can be written as follows:

$$v_{\mathrm{w}}^{(jF)} = v_{\mathrm{w}}^{(Fk)} \,, \tag{4.68}$$

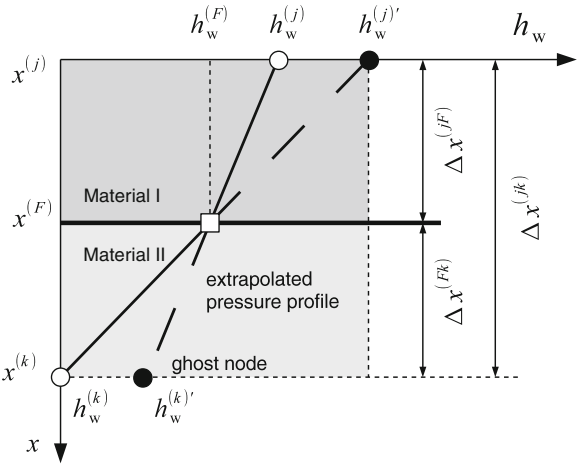

Fig. 4.9 Water pressure head profile in a layered medium. Modified with permission from [40]

where:

$$v_w^{(jF)} = -K_{sw}^{I} \, k_{rw}^{I(jF)} \left[\frac{h_w^{(F)} - h_w^{(j)}}{\Delta x^{(jF)}} - \zeta \right], \tag{4.69}$$

$$v_w^{(Fk)} = -K_{sw}^{II} \, k_{rw}^{II(Fk)} \left[\frac{h_w^{(k)} - h_w^{(F)}}{\Delta x^{(Fk)}} - \zeta \right]. \tag{4.70}$$

In the above equations, $k_{rw}^{I(jF)}$ denotes the average relative permeability in material *I* between node *j* and the interface, while $k_{rw}^{II(Fk)}$ is the average relative permeability in material *II* between the interface and node *k*. Equations (4.68)–(4.70) account for the continuity of the water pressure across the interface since the same value of $h_w^{(F)}$ is used for both sides. The average relative permeabilities for the two layers above and below the interface can be computed with any suitable method, leading to a nonlinear equation with respect to $h_w^{(F)}$. The equation can be solved iteratively, yielding the value of $h_w^{(F)}$ and the corresponding permeabilities in each of the two the sub-cells. The resulting value of the inter-nodal conductivity $K_w^{(jk)}$ must satisfy the following relationship:

$$- K_w^{(jk)} \left[\frac{h_w^{(k)} - h_w^{(j)}}{\Delta x^{(jk)}} - \zeta \right] = v_w^{(jF)} = v_w^{(Fk)} . \tag{4.71}$$

In contrast to the case of homogeneous medium with constant saturated conductivity, here the averaging is applied to the total conductivity $K_w = K_{sw} \, k_{rw}$, not only to the relative permeability k_{rw}. In view of the flux continuity condition given by Eqs. (4.68)–(4.70), the average inter-nodal conductivity $K_w^{(jk)}$ can be subsequently computed the as weighted harmonic mean of the two sub-cell conductivities:

$$K_{\mathrm{w}}^{(jk)} = \left[\Delta x^{(jF)} + \Delta x^{(Fk)}\right] \left[\frac{\Delta x^{(jF)}}{K_{\mathrm{sw}}^{I}\, k_{\mathrm{rw}}^{I(jF)}} + \frac{\Delta x^{(Fk)}}{K_{\mathrm{sw}}^{II}\, k_{\mathrm{rw}}^{II(Fk)}}\right]^{-1} . \tag{4.72}$$

It is clear that the choice of the method used to compute the average relative permeability in each of the homogeneous sub-cells will have significant influence on the final result. Therefore, the use of improved methods based on the Darcian averaging principle is recommended. Note also that for saturated flow, when the relative permeabilities are equal to unity at both sides of the interface, one recovers from Eq. (4.72) a formula for the average saturated conductivity analogous to Eq. (2.110):

$$K_{\mathrm{sw}}^{(jk)} = \left[\Delta x^{(jF)} + \Delta x^{(Fk)}\right] \left[\frac{\Delta x^{(jF)}}{K_{\mathrm{sw}}^{I}} + \frac{\Delta x^{(Fk)}}{K_{\mathrm{sw}}^{II}}\right]^{-1} . \tag{4.73}$$

A number of other methods to calculate inter-nodal permeability at a material interface can be found in the literature. Possibly the most straightforward option is to apply one of the simple averages defined by Eqs. (4.4)–(4.6) to the total conductivity K_{w} or permeability k_{w}, instead of the relative permeability k_{rw}. For the case of arithmetic averaging, the resulting formula can be written as follows:

$$K_{\mathrm{w}}^{(jk)} = \frac{1}{2}\left(K_{\mathrm{sw}}^{I}\, k_{\mathrm{rw}}^{I(j)} + K_{\mathrm{sw}}^{II}\, k_{\mathrm{rw}}^{II(k)}\right) . \tag{4.74}$$

This formula is used, for example, in the well known HYDRUS-1D numerical code [35]. Its drawback is that it does not lead to physically consistent inter-nodal permeability for steady-state saturated flow. In the latter case, as it was mentioned above, accurate results are obtained using the harmonic mean. Therefore, an often used approach, e.g. [1, 13, 26], is to compute the average intrinsic permeability (or saturated conductivity) as the harmonic mean of the intrinsic permeabilities (or saturated conductivities) of the two materials, while the relative permeability is computed by the upstream weighting:

$$K_{\mathrm{w}}^{(jk)} = K_{\mathrm{sw}}^{(jk)}\, k_{\mathrm{rw}}^{(jk)} , \tag{4.75}$$

$$k_{\mathrm{rw}}^{(jk)} = \begin{cases} k_{\mathrm{rw}}^{(j)} & \text{if} \quad \dfrac{h_{\mathrm{w}}^{(k)} - h_{\mathrm{w}}^{(j)}}{\Delta x^{(jk)}} - \zeta \le 0 , \\ k_{\mathrm{rw}}^{(k)} & \text{if} \quad \dfrac{h_{\mathrm{w}}^{(k)} - h_{\mathrm{w}}^{(j)}}{\Delta x^{(jk)}} - \zeta > 0 , \end{cases} \tag{4.76}$$

where $K_{\mathrm{sw}}^{(jk)}$ is given by Eq. (4.73) This method leads to physically consistent result for saturated flow. On the other hand, the use of upstream averaging ensures a monotonous solution.

The scheme proposed by Romano et al. [32] is based on Eq. (4.68) but introduces two additional ghost points in the vicinity of the interface, Fig. 4.9. One of them is located above the interface and extrapolates the pressure profile from the lower layer.

The other one is positioned below the interface and extrapolates the pressure profile from the upper layer. It is assumed that the interface is located mid-way between the nodes j and k and the extrapolation is linear, so the following relation holds:

$$\frac{1}{2}\left(h_{\mathrm{w}}^{(j)} + h_{\mathrm{w}}^{(k)'}\right) = \frac{1}{2}\left(h_{\mathrm{w}}^{(j)'} + h_{\mathrm{w}}^{(k)}\right) , \tag{4.77}$$

where $h_{\mathrm{w}}^{(j)'}$ and $h_{\mathrm{w}}^{(k)'}$ denote the water pressure head values at the ghost nodes. The flux continuity condition is written as:

$$-K_{\mathrm{sw}}^{I}\, k_{\mathrm{rw}}^{I(jk)} \left[\frac{h_{\mathrm{w}}^{(k)'} - h_{\mathrm{w}}^{(j)}}{\Delta x^{(jk)}} - \zeta\right] = -K_{\mathrm{sw}}^{II}\, k_{\mathrm{rw}}^{II(jk)} \left[\frac{h_{\mathrm{w}}^{(k)} - h_{\mathrm{w}}^{(j)'}}{\Delta x^{(jk)}} - \zeta\right] , \tag{4.78}$$

where the average relative permeability for each of the materials is equal to the geometric mean of the values at the real and ghost node:

$$k_{\mathrm{rw}}^{I(jk)} = \sqrt{k_{\mathrm{rw}}^{I}\left(h_{\mathrm{w}}^{(j)}\right) \times k_{\mathrm{rw}}^{I}\left(h_{\mathrm{w}}^{(k)'}\right)} , \tag{4.79}$$

$$k_{\mathrm{rw}}^{II(jk)} = \sqrt{k_{\mathrm{rw}}^{II}\left(h_{\mathrm{w}}^{(j)'}\right) \times k_{\mathrm{rw}}^{II}\left(h_{\mathrm{w}}^{(k)}\right)} . \tag{4.80}$$

The nonlinear system of equations (4.77)–(4.78) has to be solved iteratively for each material interface. The inter-nodal conductivity is then computed as the harmonic average of the conductivities in two sub-layers:

$$K_{\mathrm{w}}^{(jk)} = \frac{2\, K_{\mathrm{sw}}^{I}\, k_{\mathrm{rw}}^{I(jk)}\, K_{\mathrm{sw}}^{II}\, k_{\mathrm{rw}}^{II(jk)}}{K_{\mathrm{sw}}^{I}\, k_{\mathrm{rw}}^{I(jk)} + K_{\mathrm{sw}}^{II}\, k_{\mathrm{rw}}^{II(jk)}} \tag{4.81}$$

While this method was shown to be more accurate than the standard arithmetic and geometric weighting of the nodal conductivities in the test cases considered by Romano et al. [32] and Brunone et al. [8], it raises two questions. First, it is not clear, why the pressure values at ghost nodes, which do not have any physical interpretation, should be used instead of the value of the pressure at the interface, as in Eq. (4.68). Second, geometric averaging of the relative permeabilities was shown to be very inaccurate in some problems involving homogeneous media, and one can expect similar type of errors in the heterogeneous case.

Szymkiewicz and Helmig [40] compared the performance of various permeability averaging schemes for one-dimensional incompressible flow in layered soils. Principal results of their investigation are presented here. Four approximation methods were used to compute the average permeability across a material interface separating sand and clay layers. They include Eqs. (4.68)–(4.72) combined with the method of Szymkiewicz [39] to evaluate the permeability at each side of the interface (referred to as CC-SZYM), the simple arithmetic averaging, Eq. (4.74)

Table 4.7 Parameters of soils used in the numerical simulations of steady-state flow in a heterogeneous medium. Modified with permission from [40]

Soil	θ_{rw} (–)	θ_{sw} (–)	p_e or p_g (Pa)	n_b or n_g (–)	K_{sw} ($m\,s^{-1}$)
BC-sand	0.020	0.417	711	0.592	5.83×10^{-5}
BC-clay	0.056	0.423	3360	0.127	2.50×10^{-7}
VGM-sand	0.043	0.430	677	2.68	8.25×10^{-5}
VGM-clay	0.007	0.360	19620	1.09	5.56×10^{-8}

(CC-ARIT), the combination of harmonic averaging of the intrinsic permeability and upstream weighting of the relative permeability, Eqs. (4.73), (4.75) and (4.76) (CC-UPS), and the method of Romano et al. [32] (CC-ROM). The results were compared to the values of the inter-nodal permeability obtained from the numerical solution of steady-state flow equation between the two points, using very fine spatial discretization. The two soils were characterized by either Brooks–Corey–Burdine or van Genuchten–Mualem functions. Their parameters are listed in Table 4.7. For each set of hydraulic functions, a large number of simulations was performed, with varying sequence of the layers (sand over clay, clay over sand), distance between nodes, $\Delta x = \{1, 2, 5, 10, 20, 50, 100, 200, 500\}$ cm, and potential head values at the nodes, $h_w = \{10, 0, -1, -10, -100, -1000\}$ cm (for Brooks–Corey model the potential values were modified by adding negative value corresponding to h_e, as listed in Table 4.7 for respective soils).

The error of each averaging scheme was defined similarly to Eq. (4.63). However, the values of total conductivity were used instead of the relative permeability:

$$\text{ERR-K} = \log_{10} \frac{K_w^{(jk)}}{K_{ref}^{(jk)}} \tag{4.82}$$

where $K_w^{(jk)}$ and $K_{ref}^{(jk)}$ denote, respectively, the approximate inter-nodal conductivity and the reference conductivity obtained from the steady-state solution. For each averaging method the root mean square, maximum and minimum error values were defined in the way described in Sect. 4.2.5. The values of these parameters are listed in Table 4.8 for soils characterized by Brooks-Corey functions and in Table 4.9 for the van Genuchten–Mualem functions. Additionally, for the schemes CC-ROM and CC-SZYM the values of the potential head at the interface $h_w^{(F)}$ can be compared with the values obtained from the numerical steady flow solution. The corresponding root mean square errors, denoted as RMS-ERR-H, are also reported.

The results shown in the tables indicate that the averaging scheme CC-SZYM, based on the approximation of the Darcian means, is much more accurate in predicting the value of steady-state average conductivity than the other three methods. CC-ROM is second best, but still can lead to over- or underestimation of the conductivity by several orders of magnitude. It can be also noted that all methods are less accurate for the van Genuchten–Mualem model than for the Brooks–Corey–Burdine model.

Table 4.8 Errors of permeability approximation schemes for steady-state flow in a heterogeneous medium, Brooks–Corey–Burdine functions. Reproduced with permission from [40]

Scheme	RMS-ERR-K (–)	max(ERR-K) (–)	min(ERR-K) (–)	RMS-ERR-H (m)
CC-ARIT	1.91	6.18	−0.24	–
CC-ROM	0.66	2.32	−2.77	0.1815
CC-UPS	1.56	5.46	−2.55	–
CC-SZYM	0.08	1.34	−0.32	0.0041

Table 4.9 Errors of permeability approximation schemes for steady-state flow in a heterogeneous medium, van Genuchten–Mualem functions. Reproduced with permission from [40]

Scheme	RMS-ERR-K (–)	max(ERR-K) (–)	min(ERR-K) (–)	RMS-ERR-H (m)
CC-ARIT	3.21	10.37	−0.28	–
CC-ROM	1.78	5.58	−7.30	23.42
CC-UPS	1.94	7.88	−3.71	–
CC-SZYM	0.10	0.07	−0.51	1.31

Moreover, Szymkiewicz and Helmig [40] carried out comparisons of various permeability averaging schemes for several unsteady flow problems, using both cell-centred and vertex-centred spatial discretizations. In cell-centred scheme they used the same four methods for approximating permeability at material interface, as in the steady state analysis described above. In the framework of vertex-centred approach, where the porous material between the nodes is always homogeneous, the inter-nodal permeabilities were computed as arithmetic averages, Eq. (4.4) (VC-ARIT), geometric average, Eq. (4.5) (VC-GEOM), upstream weighting, Eq. (4.12) (VC-UPS) and the method of Szymkiewicz [39] (VC-SZYM). Two examples from [40] are presented below.

The first example concerns vertical downward infiltration with prescribed water flux at the surface, see Fig. 4.10a for the details of the geometry and the initial and boundary conditions. The sand and clay layer are characterized by Brooks–Corey–Burdine hydraulic functions with the parameters listed in Table 4.7. Since the hydraulic conductivity of clay is much smaller than the conductivity of sand, after some time a saturated zone develops at the material interface. Figure 4.11 shows the distribution of the volumetric water content in the soil profile after 32 h of infiltration. The thick solid line denotes the reference solution obtained on a dense grid with $\Delta x = 1$ mm. One can note the presence of a fully saturated zone in the vicinity of the interface with the maximum values of $\theta_w = 0.417$ for sand and $\theta_w = 0.423$ for clay. Below the interface a relatively sharp wetting front can be observed in the clay layer, while above the interface the water content in sand also decreases rapidly. The simulations performed on a coarse grid with $\Delta x = 20$ cm show significant influence of the method used for computing inter-nodal

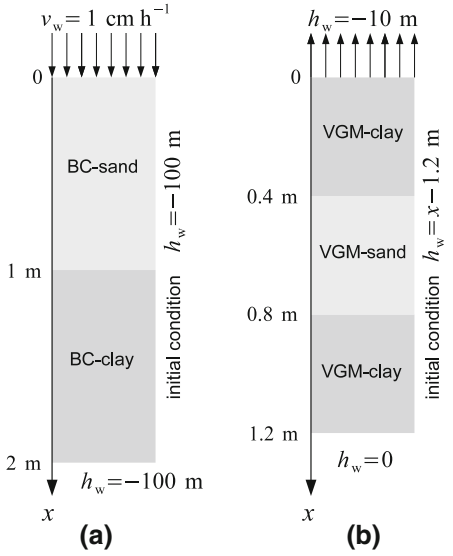

Fig. 4.10 Initial and boundary conditions used in simulations of flow in layered media. Modified with permission from [40]

permeabilities, for either vertex-centred (Fig. 4.11a) or cell-centred (Fig. 4.11b) discretization approaches. The results obtained with VC-SZYM and CC-SZYM schemes are relatively close to the reference solution. Similarly accurate results (not shown here) can be obtained with the method of Baker et al. [5]. In contrast, the schemes based on geometric averaging lead to very inaccurate profiles, with large saturated zone in the sand layer. The arithmetic and upstream weighting lead to moderately accurate solutions, which reproduce the general shape of the reference profile, but with more shifting and smoothing than the methods based on Darcian averaging.

In the second test case, evaporation from a three-layer soil profile was simulated. Evaporation was enforced by imposing a very large negative value of the pressure head at the soil surface. The details of the problem formulation are presented in Fig. 4.10b. The soil materials are characterized by van Genuchten–Mualem functions, with parameters listed in Table 4.7. A very long process was considered, with the final time equal to 5×10^4 h, and the cumulative amount of evaporated water equal to 7.26 cm, as predicted by the reference solution on fine grid ($\Delta x = 1$ mm). The coarse grid simulations with $\Delta x = 10$ cm predicted very different amounts of cumulative evaporation, depending on the applied method of permeability averaging. The relative error can be defined as:

$$\text{ERR-EV} = \frac{q_{\text{ev}} - q_{\text{ev}}^{\text{ref}}}{q_{\text{ev}}^{\text{ref}}} \times 100\,\% \tag{4.83}$$

where q_{ev} and $q_{\text{ev}}^{\text{ref}}$ denote the value of cumulative evaporation obtained in a given solution and the reference value, respectively. The relative errors are listed in

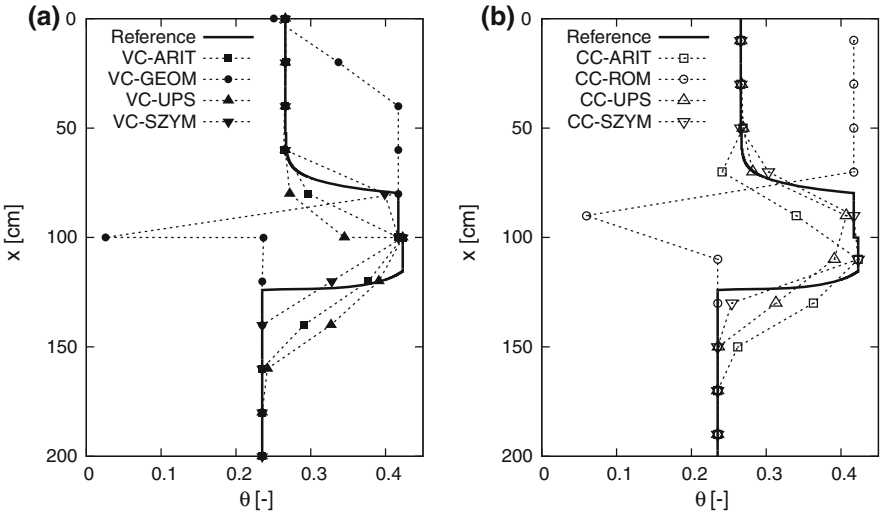

Fig. 4.11 Infiltration in layered medium: water content profiles obtained with vertex-centred (**a**) and cell-centred (**b**) schemes ($t = 32$ h, $\Delta x = 20$ cm). Reproduced with permission from [40]

Table 4.10. It can be seen that the smallest errors were obtained with the schemes based on the method of Szymkiewicz [39] and with the CC-UPS scheme. Arithmetic averaging and VC-UPS led to very large overestimation of the cumulative evaporation. In contrast, the schemes based on geometric mean significantly underestimated the evaporation. The profiles of the water pressure head at the end of simulation obtained using the same spatial discretization are shown in Fig. 4.12. They confirm high accuracy of the improved method of permeability averaging discussed in this work. The results obtained with VC-SZYM and CC-SZYM schemes are very close to the reference solution. In particular, these methods correctly predict the large gradient of the pressure head in the upper part of the central sand layer. Such a large gradient is necessary to sustain the upward flow in sand, as the relative permeability in the dry upper part of the sand layer is very small. Obviously, the accuracy in the the pressure gradient is strongly influenced by the accuracy in the inter-nodal permeability, as the product of these two values gives the volumetric water flux. The schemes VC-UPS, VC-ARIT and CC-ARIT overestimate the inter-nodal permeability. Therefore, the resulting gradients are smaller than in the reference solution. On the other hand, CC-ROM and VC-GEOM underestimate the inter-nodal permeability, leading to gradients much larger than in the reference profile.

For a finer discretization, $\Delta x = 1$ cm, the errors caused by arithmetic and upstream averaging significantly diminish, but they are still much larger than for the K-SZYM approach, with the exception of CC-UPS, which provides the most accurate results. The difference in performance between the two schemes based on upstream weighting, i.e. CC-UPS and VC-UPS, may be due to the fact that in VC

Table 4.10 Evaporation in a layered medium: relative errors in the cumulative amount of evaporated water for various permeability averaging schemes. Data from [40]

$\Delta x = 10$ cm				$\Delta x = 1$ cm			
Scheme	ERR-EV (%)	Scheme	ERR-EV (%)	Scheme	ERR-EV (%)	Scheme	ERR-EV (%)
CC-ARIT	400	VC-ARIT	237	CC-ARIT	19.7	VC-ARIT	16.4
CC-ROM	−59.1	VC-GEOM	−63.9	CC-ROM	−58.9	VC-GEOM	−59.3
CC-UPS	−9.63	VC-UPS	469	CC-UPS	2.11	VC-UPS	29.1
CC-SZYM	−2.33	VC-SZYM	−5.25	CC-SZYM	3.09	VC-SZYM	3.07

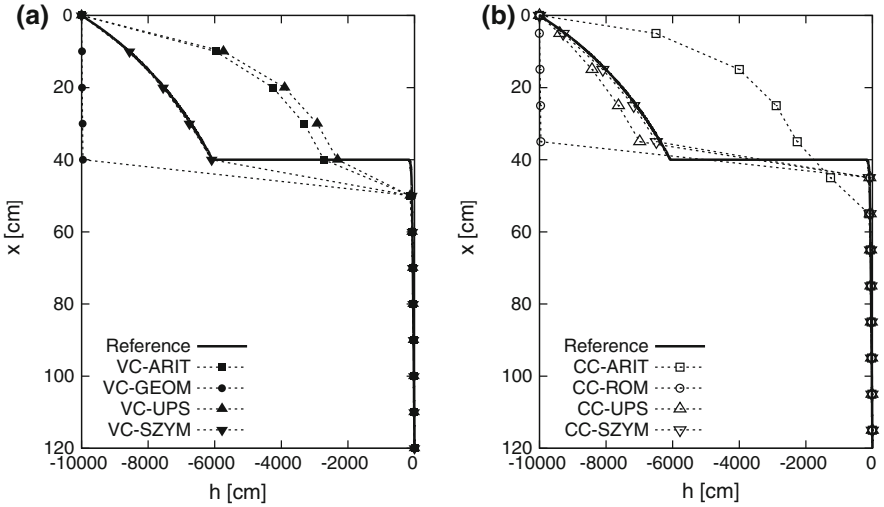

Fig. 4.12 Evaporation in a layered medium: pressure head profiles obtained with vertex-centred (**a**) and cell-centred (**b**) schemes ($t = 50000$ h, $\Delta x = 10$ cm). Reproduced with permission from [40]

scheme the change in water content at highly permeable side of the interface results in an immediate change in the part of the control volume located at the weakly permeable part of the interface. This is caused by the assumption of the continuity of the water pressure across the interface. If the control volumes at the interface are large, considerable amounts of water can move instantaneously across the interface. In the CC-UPS scheme, the interface coincides with the boundary between control volumes and harmonic averaging of the saturated conductivity (which gives more weight to the weakly permeable medium) partly compensates for the acceleration caused by upstream weighting of the relative conductivity [40]. Finally, it should be noted that in this numerical example the performance of the schemes based on geometric averaging (CC-ROM and VC-GEOM) does not improve as the grid is refined.

4.5 Multidimensional Problems

As shown in Chap. 3, permeability averaging in multidimensional problems can be carried out either using a finite-element like approach or a finite-difference like approach (used either in the finite difference or finite volume framework). In the first case, the permeability value at a specific point in the element is interpolated from the nodal values at all vertices of the element, or is evaluated as a function of the capillary pressure or water saturation at the considered point, which in turn is interpolated from the nodal pressures or saturations. In the second case, the permeability is evaluated at the midpoint of a primary grid edge, connecting two nodes. To this order many averaging schemes developed for one-dimensional flow can be used. However, their applicability depends on the properties of the numerical grid and the degree of anisotropy of the porous medium. Assuming that the spatial discretization is performed with the control volume finite element approach, several specific cases can be distinguished, as discussed below:

- *Isotropic permeability, rectangular grid*. In this case, all methods developed for one-dimensional flow can be used. The methods based on flux splitting and Darcian averaging can be expected to yield more accurate results, as they provide different relative permeabilities for horizontal and vertical fluxes.
- *Isotropic permeability, unstructured grid*. All simple averaging methods can be used, as well as the flux splitting methods, if one takes into account that the value of the gravitational coefficient ζ varies from one edge to the other, depending on their orientation with respect to the gravity vector. In the group of Darcian means, the variability of gravitational coefficient is included in the method of Szymkiewicz [39], and can be easily introduced in the methods of Baker [2] and Baker et al. [5], as shown in Sect. 4.1.3.
- *Diagonally anisotropic permeability, rectangular grid*. If the main anisotropy axes are aligned with the axes of spatial coordinate system and with the grid lines, the permeability in each direction can be computed with the one-dimensional approach. The relative permeability functions can be different in the horizontal and vertical direction.
- *Anisotropic intrinsic permeability, isotropic relative permeability, arbitrary grid*. For anisotropic media, the flux along specific edge depends on the components of the water potential gradient in both parallel and perpendicular directions. It means that the one-dimensional steady-state analysis, which is the basis of the Darcian averaging schemes, does not hold strictly. However, such methods can still be used to approximate the scalar relative permeability, which is then multiplied by the intrinsic permeability tensor.
- *Anisotropic intrinsic and relative permeability, arbitrary grid*. In this case, it is impossible to define the relative permeability function for an arbitrary direction. Therefore, methods based on the integration of the relative permeability function, including the integrated mean and Darcian mean approaches, cannot be used. In contrast, methods based on averaging of the nodal permeability values can be still applied, for example by averaging each component of the permeability tensor

separately. Upstreaming can be easily implemented assuming that the permeability tensor is positively definite, which in the context of groundwater flow means that the flux is directed from the node with larger potential to the node with lower potential.

In all the above cases, the permeability averaging is performed within a materially homogeneous grid element, according to the vertex-centred discretization scheme. In a heterogeneous medium, the inter-nodal permeabilities are calculated separately for the elements at each side of the edge, using the same pair of nodal pressures and different relative permeability functions. In some cases, the methods based on Darcian mean concept can be applied for multidimensional problems also in the framework of the cell-centred discretization, which implies the existence of material interfaces between nodes. This is possible if the medium is diagonally anisotropic and the grid is rectangular. In such a case, the interface condition given by Eq. (4.68) can be easily formulated for each spatial direction and the relative permeabilities at each side of the interface can be computed using more accurate formulae. However, in a more general case of unstructured cell-centred grids, one-dimensional Darcian approximations cannot be easily implemented.

In order to show the applicability of the improved averaging scheme [39] to two-dimensional flow in an isotropic medium, a comparison of the numerical results with the analytical solution of Tracy [42] is performed. The flow domain is a square $L_1 = 1\,\mathrm{m}$ by $L_2 = 1\,\mathrm{m}$, with x_1 axis horizontal and x_2 axis oriented vertically upward. The capillary and relative permeability functions are formulated with respect to the water pressure head h_w and have the exponential form:

$$\theta_\mathrm{w} = \theta_\mathrm{rw} + (\theta_\mathrm{sw} - \theta_\mathrm{rw}) \exp(h_\mathrm{w}/h_\mathrm{g}) \,, \tag{4.84}$$

$$K_\mathrm{w} = K_\mathrm{sw} \exp(h_\mathrm{w}/h_\mathrm{g}) \,, \tag{4.85}$$

with the parameters $\theta_\mathrm{sw} = 0.45$, $\theta_\mathrm{rw} = 0.15$, $h_\mathrm{g} = 2\,\mathrm{m}$ and $K_\mathrm{sw} = 10^{-5}\,\mathrm{m\,s^{-1}}$. The compressibility of soil and water is neglected. As the initial condition, a uniform distribution of the water pressure $h_\mathrm{w}^\mathrm{init} = -10\,\mathrm{m}$ is assumed. Along the bottom and the vertical sides of the domain this value is maintained as the boundary condition. At the top boundary a sinusoidal distribution of the pressure head is imposed:

$$h_\mathrm{w}^\mathrm{top}(x_1) = h_\mathrm{g} \ln\left[\exp\left(\frac{h_\mathrm{w}^\mathrm{init}}{h_\mathrm{g}}\right) + \left(1 - \exp\left(\frac{h_\mathrm{w}^\mathrm{init}}{h_\mathrm{g}}\right)\right) \sin\left(\frac{\pi x_1}{L_1}\right)\right] \tag{4.86}$$

For the above assumptions the value of the water pressure for a given spatial point (x_1, x_2) and time t can be calculated analytically as [42]:

$$h_{\mathrm{w}}(x_1, x_2, t) = h_{\mathrm{g}} \ln \left\{ \exp\left(\frac{h_{\mathrm{w}}^{\mathrm{init}}}{h_{\mathrm{g}}}\right) + h'' \sin\frac{\pi x_1}{L_1} \exp\left(\frac{L_2 - x_2}{2\,h_{\mathrm{g}}}\right) \left[\frac{\sinh(\beta'' x_2)}{\sinh(\beta'' L_2)} + \frac{2}{L_2\, c''} \sum_{n=1}^{\infty} (-1)^n \frac{\lambda_n''}{\gamma''} \sin(\lambda_n'' x_2) \exp(-\gamma'' t) \right] \right\} \tag{4.87}$$

where:

$$c'' = \frac{(\theta_{\mathrm{sw}} - \theta_{\mathrm{rw}})}{h_{\mathrm{g}}\, K_{\mathrm{sw}}}, \quad \gamma'' = \frac{(\beta'')^2 + (\lambda_n'')^2}{c''}, \quad \lambda_n'' = \frac{n\,\pi}{L_2},$$

$$\beta'' = \sqrt{\frac{1}{4\,(h_{\mathrm{g}})^2} + \left(\frac{\pi}{L_1}\right)^2}, \quad h'' = 1 - \exp(h_{\mathrm{w}}^{\mathrm{init}}/h_{\mathrm{g}}).$$

Numerical simulations were performed using both rectangular and unstructured (triangular) meshes. For each mesh type, two levels of refinement were considered: a coarser one with $\Delta x = 10\,\mathrm{cm}$ and a finer one with $\Delta x = 2\,\mathrm{cm}$. In the case of unstructured grid, these values refer to the node spacing imposed along the boundaries of the domain. The unstructured mesh was generated using NetGen code, developed by Burzyński [9]. The vertex centred finite volume approach was used with two-point approximation of the average permeability at each cell face, which allowed for the use of various schemes developed for one-dimensional flow. The pressure gradient was evaluated using the finite element approach. For structured meshes the evaluation point was chosen as either the edge midpoint or the face midpoint, as shown in Chap. 3, Fig. 3.4. In the first case the scheme becomes equivalent to the finite difference scheme, and is denoted by FD. For each simulation the root mean square error of the nodal values of the water pressure at the final time $t = 720\,\mathrm{s}$ was computed:

$$RMSE_p = \sqrt{\frac{1}{N} \sum_{1}^{N} (p_{\mathrm{num}} - p_{\mathrm{ref}})^2} \tag{4.88}$$

where N is the number of internal nodes in the domain, p_{num} is the final water pressure at a specific node from the numerical solution and p_{ref} is the corresponding pressure value obtained from the analytical solution ($p_{\mathrm{w}} = h_{\mathrm{w}}\, \rho_{\mathrm{w}}\, g$). The values of RMSE for different grids and permeability averaging schemes are listed in Table 4.11.

It can be seen that the permeability averaging schemes K-SZYM and K-BAKER are significantly more accurate than the other approaches. In this test case, the flow is dominated by capillary forces and K-SZYM is equivalent to the integrated mean method. On the other hand, for exponential permeability function K-BAKER represents the exact solution of steady-state flow. Thus, one could expect K-BAKER to be the most accurate of all methods. However, the results show that it is slightly less accurate than K-SZYM. This apparent contradiction can be explained by the fact that

Table 4.11 Example 7: root mean square errors in the water pressure (Pa) for different numerical approximation schemes

Grid	K-SZYM	K-BAKER	K-GEOM	K-ARIT	K-UPS
Structured, FD					
Fine	32	35	271	388	1915
Coarse	836	911	1036	2183	6308
Structured, FE					
Fine	29	31	271	389	1914
Coarse	676	746	920	2160	6298
Unstructured, FE					
Fine	39	39	219	322	1634
Coarse	502	536	979	1754	5334

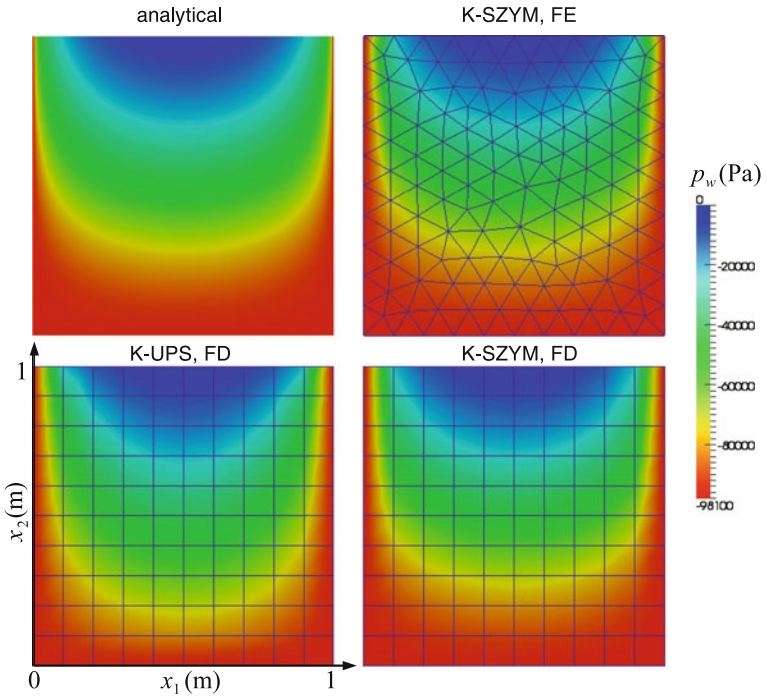

Fig. 4.13 Example 7: water pressure distribution for the final time $t = 720$ s according to the analytical solution and three numerical solutions of coarse grid

applying steady-state results to transient flow introduces additional error. It should be also noted that for this particular setting the geometric mean is more accurate than the arithmetic mean, while the upstream weighting produces considerable errors, even on finer grids.

In Fig. 4.13 the distribution of the water pressure for $t = 720$ s obtained with the K-SZYM method on structured and unstructured coarse grids is compared to

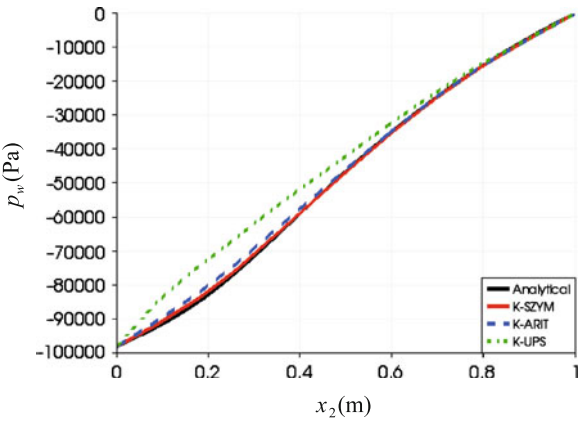

Fig. 4.14 Example 7: water pressure profile along the vertical symmetry axis according to the analytical solution and three numerical solutions of coarse grid ($t = 720$ s)

the analytical solution and to the solution on structured grid using K-UPS averaging scheme. The plots are consistent with the error measures reported in Table 4.11. The solutions obtained using K-SZYM scheme are in a very good visual agreement with the reference analytical solution, while K-UPS predicts a more diffuse wetting front. Figure 4.14 shows the water pressure profiles along the vertical symmetry axis at the end of the simulation obtained for the coarse unstructured grid using K-SZYM, K-ARIT and K-UPS. It can be seen that the result for K-SZYM is virtually the same as the analytical solution, K-ARIT gives a slight discrepancy, while K-UPS predicts significantly different profile shape.

4.6 Two-Phase Flow

The development of approximate Darcian averages, such as the ones presented in Sect. 4.2, is not possible for two-phase flow, because the relative permeability depends on the pressures in both fluid phases. In contrast, the simple averaging methods such as the arithmetic, geometric, harmonic and upstream mean can be in principle used to compute the inter-nodal permeability for each of the fluid phases. It is also possible to define an integrated mean for each fluid phase by integrating the relative permeability with respect to the capillary pressure:

$$k_{\mathrm{rw}}^{(ij)} = \frac{1}{p_{\mathrm{c}}^{(j)} - p_{c}^{(i)}} \int_{p_{\mathrm{c}}^{(i)}}^{p_{\mathrm{c}}^{(j)}} k_{\mathrm{rw}}(\hat{p})\, \mathrm{d}\hat{p} \tag{4.89}$$

$$k_{\mathrm{ra}}^{(ij)} = \frac{1}{p_{\mathrm{c}}^{(j)} - p_{\mathrm{c}}^{(i)}} \int_{p_{\mathrm{c}}^{(i)}}^{p_{\mathrm{c}}^{(j)}} k_{\mathrm{ra}}(\hat{p})\, \mathrm{d}\hat{p} \tag{4.90}$$

It should be noted that the above formula for k_{rw} is equivalent to the integrated mean developed for the Richards equation, Eq. (4.9), only if the air pressure is atmospheric ($p_{\mathrm{a}} = 0$) and both nodes are unsaturated.

The two-phase flow model includes advective terms related to viscous and gravity forces, as well as the capillary diffusion term. The Richards equation represents a limit case where the viscous forces are negligible and only capillary and gravity terms remain. Thus some insights into the problem of permeability averaging for two phase flow can be gained from the analysis of the Richards equation presented in the above sections. In particular, one can expect that if the pressure gradients in the air phase are negligible, the average permeability of the water phase will vary in the range from the integrated mean (for capillary dominated flow) to the permeability of the upper node (for gravity dominated flow), with the arithmetic mean being a reasonable approximation for intermediate conditions. This is confirmed by numerical solutions of Celia and Binning [10] and Kees and Miller [24], who employed arithmetic averaging, and Touma and Vauclin [41], who used geometric averaging on a relatively fine grid. On the other hand, if significant pressure gradients exist in the non-wetting phase, the role of advective terms related to the viscous forces increases. Consequently, arithmetic, geometric or integrated averaging will produce oscillatory solutions, which can be avoided by employing upstream average. Permeability upstreaming is commonly used for two-phase flow with non-wetting to wetting phase mobility ratio close to one or smaller than one, e.g. in liquid hydrocarbons—water system [22]. However, the application of upstreaming for capillary driven two-phase flow in air-water system may lead to overly diffusive and inaccurate solutions. An approach alternative to upstreaming is the explicit addition of artificial diffusion to the discrete equations. This method was applied in [20] for the fractional flow formulation.

The influence of the permeability averaging method on the solution of one-dimensional two phase flow equations was investigated in the framework of the finite element discretization by Helmig and Huber [22], and in the framework of the finite volume formulation by Szymkiewicz [38]. In the following two other illustrative examples are presented. In the first test case, one-dimensional, horizontal, capillary dominated flow is considered. The dimension of the solution domain is 0.5 m and the soil is characterized by Brooks–Corey–Burdine hydraulic functions with the following parameters: $\phi = 0.4$, $S_{\mathrm{rw}} = S_{\mathrm{ra}} = 0$, $k = 1.25 \times 10^{-12}\,\mathrm{m}^2$, $p_{\mathrm{e}} = 814\,\mathrm{Pa}$, $n_{\mathrm{b}} = 0.686$. The compressibility of water and soil is neglected. Initially, the pore air is at atmospheric pressure ($p_{\mathrm{a}} = 0$) and the water saturation is $S_{\mathrm{w}} = 0.1$. At the left-hand side boundary ($x = 0$), a constant value of water saturation $S_{\mathrm{w}} = 0.95$ is

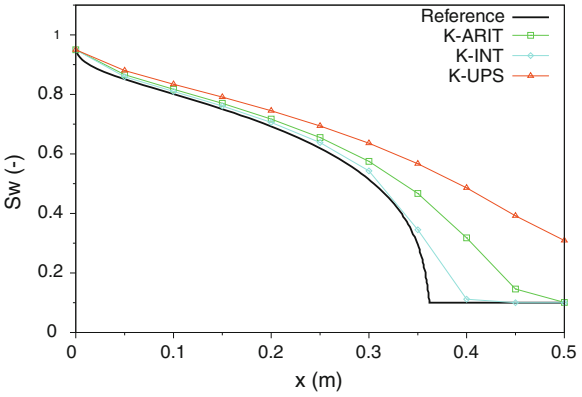

Fig. 4.15 Water saturation profiles for two-phase horizontal flow ($t = 4$ h)

imposed, while the air phase is maintained at atmospheric pressure. The right-hand side boundary is assumed to be impermeable for both fluids ($v_w = v_a = 0$). For such conditions, a semi-analytical solution of Sunada and McWhorter [37] can be applied. The semi-analytical solution is computed following the improved method by Fucik et al. [18]. It is compared to the results of the numerical simulations using three permeability averaging schemes: the upstream weighting, arithmetic averaging and integrated averaging with respect to the $k_\alpha(p_c)$ function. For a fine grid, $\Delta x = 0.5$ cm, all three approaches gave results very close to the analytical solution (results not shown here). For a coarser grid with $\Delta x = 5$ cm, significant differences occur, as shown in Fig. 4.15. The integrated mean provides results very close to the reference solution, while K-ARIT and K-UPS lead to more diffuse wetting fronts, which in the case of K-UPS reaches the boundary of the domain. Note that the same relative accuracy of the three methods is observed for the Richards equation if the flow is capillary-dominated, which is the case for horizontal flow or vertical flow with small Δx, as shown in Example 1, Fig. 4.6.

In the final example, vertical two phase flow is considered. The geometry, soil parameters and initial conditions are the same as in the previous case. The boundary conditions correspond to ponded infiltration, i.e. at the top of the soil layer $p_w = 100$ Pa and $S_w = 1$, while at the bottom the initial values of the water pressure and saturation are maintained. In this case no analytical solution can be applied and a numerical solution on dense grid $\Delta x = 0.05$ cm is considered as the reference. The coarse grid solutions ($\Delta x = 0.5$ cm) shown in Fig. 4.16 behave differently from the previous case. The integrated mean underestimates the position of the wetting front, while the upstream weighting and arithmetic averaging are more accurate with respect to the position of the front, but show more significant numerical diffusion, especially in the case of upstream weighting.

An additional issue arises when a part of the solution domain is fully saturated with water and the medium has a non-zero value of the entry pressure. In such a case, the air pressure at the water-saturated nodes is physically undefined, but in the

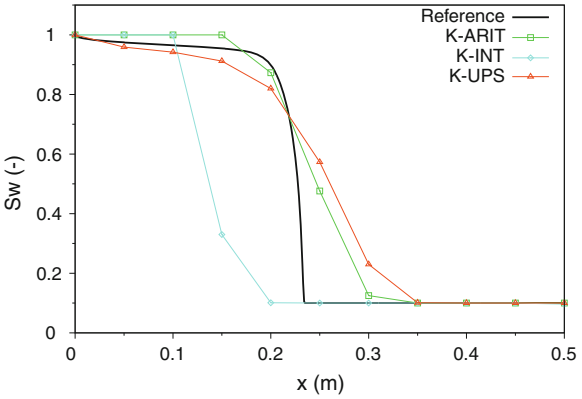

Fig. 4.16 Water saturation profiles for two-phase vertical flow ($t = 3$ h)

numerical algorithm it is computed as $p_a = p_w + p_e$, and thus can be higher than the atmospheric pressure. If air at atmospheric pressure is present at a neighboring node, a gradient in the air potential occurs between the water-saturated node and the unsaturated node, even though physically no flow is possible. The average air permeability in this case should be equal to zero, which is naturally accounted for by the use of upstream weighting and geometric averaging. For other averaging formulae, appropriate modifications have to be made to prevent non-physical fluxes.

The above examples show that there is a potential for improvement of the permeability averaging formulas for the two-phase flow, based on the relations between capillary, gravity and viscous forces at the scale of a single numerical grid cell. However, such an analysis is beyond the scope of the present work.

References

1. Aziz K, Settari A (1979) Petroleum reservoir simulation. Applied Science, Essex
2. Baker D (1995) Darcian weighted interblock conductivity means for vertical unsaturated flow. Ground Water 33(3):385–390. doi:10.1111/j.1745-6584.1995.tb00294.x
3. Baker D (2000) A Darcian integral approximation to interblock hydraulic conductivity means in vertical infiltration. Comput Geosci 26(5):581–590
4. Baker D (2006) General validity of conductivity means in unsaturated flow. J Hydrol Eng 11(6):526–538
5. Baker D, Arnold M, Scott H (1999) Some analytic and approximate Darcian means. Ground Water 37(4):532–538. doi:10.1111/j.1745-6584.1999.tb01139.x
6. Belfort B, Lehmann F (2005) Comparison of equivalent conductivities for numerical simulation of one-dimensional unsaturated flow. Vadose Zone J 4(4):1191–1200
7. Berg P (1999) Long-term simulation of water movement in soils using mass-conserving procedures. Adv Water Resour 22(5):419–430
8. Brunone B, Ferrante M, Romano N, Santini A (2003) Numerical simulations of one-dimensional infiltration into layered soils with the Richards' equation using different enstimates of the interlayer conductivity. Vadose Zone J 2(2):193–200

9. Burzyński K, Szymkiewicz A (2011) Unstructured finite-volume meshes for two-dimensional flow in variably saturated porous media. TASK Q 15(3):1001–10,014
10. Celia M, Binning P (1992) A mass conservative numerical solution for two-phase flow in porous media with application to unsaturated flow. Water Resour Res 28(10):2819–2828
11. Celia M, Bouloutas E, Zarba R (1990) A general mass-conservative numerical solution for the unsaturated flow equation. Water Resour Res 26(7):1483–1496
12. Desbarats A (1995) An interblock conductivity scheme for finite difference models of steady unsaturated flow in heterogeneous media. Water Resour Res 31(11):2883–2889
13. Fagerlund F, Niemi A, Odén M (2006) Comparison of relative permeabilityfluid saturationcapillary pressure relations in the modelling of non-aqueous phase liquid infiltration in variably saturated, layered media. Adv Water Resour 29(11):1705–1730. doi:10.1016/j.advwatres.2005.12.007
14. Fletcher C (1991) Computational techniques for fluid dynamics 1. Fundamental and general techniques. Springer, Berlin
15. Forsyth P, Kropinski M (1997) Monotonicity considerations for saturated–unsaturated subsurface flow. SIAM J Sci Comput 18(5):1328–1354
16. Forsyth P, Wu Y, Pruess K (1995) Robust numerical methods for saturated–unsaturated flow in heterogeneous media. Adv Water Resour 18(1):25–38
17. Fuhrmann J, Langmach H (2001) Stability and existence of solutions of time-implicit finite volume schemes for viscous nonlinear conservation laws. Appl Numer Math 37(1–2):201–230
18. Fučik R, Mikyška J, Beneš M, Illangasekare T (2007) An improved semi-analytical solution for verification of numerical models of two-phase flow in porous media. Vadose Zone J 6(1):93–104
19. Gastó J, Grifoll J, Cohen Y (2002) Estimation of internodal permeabilities for numerical simulations of unsaturated flows. Water Resour Res 38(12):1326
20. Guarnaccia J, Pinder G, Fishman M (1997) NAPL: simulator documentation. Environmental Protection Agency, USA
21. Haverkamp R, Vauclin M (1979) A note on estimating finite difference interblock hydraulic conductivity values for transient unsaturated flow. Water Resour Res 15(1):181–187
22. Helmig R, Huber R (1998) Comparison of Galerkin-type discretization techniques for two-phase flow in heterogenous porous media. Adv Water Resour 21(8):697–711
23. Kavetski D, Binning P, Sloan S (2001) Adaptive time stepping and error control in a mass conservative numerical solution of the mixed form of Richards equation. Adv Water Resour 24(6):595–605
24. Kees C, Miller C (2002) Higher order time integration methods for two-phase flow. Adv Water Resour 25(2):159–177
25. Kirkland M, Hills R, Wierenga P (1992) Algorithms for solving Richards equation for variably saturated soil. Water Resour Res 28(8):2049–2058
26. Kueper B, Frind E (1991) Two-phase flow in heterogeneous porous media 1. Model development. Water Resour Res 27(6):1049–1057
27. Lassabatere L, Angulo-Jaramillo R, Cuenca R, Braud I, Haverkamp R (2006) Beerkan estimation of soil transfer parameters through infiltration experiments—BEST. Soil Sci Soc Am J 70(2):521–532
28. Lima-Vivancos V, Voller V (2004) Two numerical methods for modeling variably saturated flow in layered media. Vadose Zone J 3(3):1031–1037
29. Manzini G, Ferraris S (2004) Mass-conservative finite volume methods on 2-d unstructured grids for the Richards' equation. Adv Water Resour 27(12):1199–1215
30. Miller C, Williams G, Kelley C, Tocci M (1998) Robust solution of Richards equation for nonuniform porous media. Water Resour Res 34(10):2599–2610
31. Pei Y, Wang J, Tian Z, Yu J (2006) Analysis of interfacial error in saturated–unsaturated flow models. Adv Water Resour 29(4):515–524
32. Romano N, Brunone B, Santini A (1998) Numerical analysis of one-dimensional unsaturated flow in layered soils. Adv Water Resour 21(4):315–324

33. Ross P (2003) Modeling soil water and solute transport—fast simplified numerical solutions. Agron J 95(6):1352–1361
34. Schnabel R, Richie E (1984) Calculation of internodal conductances for unsaturated flow simulations. Soil Sci Soc Am J 48(5):1006–1010
35. Šimnek J, Šejna M, Saito H, Sakai M, van Genuchten M (2008) The HYDRUS-1D software package for simulating the one-dimensional movement of water, heat and multiple solutes in variably-saturated media. Version 4.0. Department of Environmental Sciences, University of California Riverside, Riverside
36. Srivastava R, Guzman-Guzman A (1995) Analysis of hydraulic conductivity averaging schemes for one-dimensional, steady-state unsaturated flow. Ground Water 33(6):946–952. doi:10.1111/j.1745-6584
37. Sunada D, McWhorter D (1990) Exact integral solutions for two phase flow. Water Resour Res 26(3):399–413
38. Szymkiewicz A (2007) Numerical simulation of one-dimensional two-phase flow in porous media. Arch Hydro-eng Environ Mech 54(2):117–136
39. Szymkiewicz A (2009) Approximation of internodal conductivities in numerical simulation of 1D infiltration, drainage and capillary rise in unsaturated soils. Water Resour Res 45:W10403
40. Szymkiewicz A, Helmig R (2011) Comparison of conductivity averaging methods for one-dimensional unsaturated flow in layered soils. Adv Water Resour 34(8):1012–1025
41. Touma J, Vauclin M (1986) Experimental and numerical analysis of two-phase infiltration in a partially saturated soil. Transp Porous Media 1(1):27–55
42. Tracy F (2006) Clean two and three-dimensional analytical solutions of Richards' equation for testing numerical solvers. Water Resour Res 42:W08503
43. van Dam J, Feddes R (2000) Numerical simulation of infiltration, evaporation and shallow groundwater levels with the Richards equation. J Hydrol 233(1):72–85
44. Warrick A (1991) Numerical approximation of Darcian flow through unsaturated soil. Water Resour Res 27(6):1215–1222
45. Warrick A, Yeh TC (1990) One-dimensional, steady vertical flow in a layered soil profile. Adv Water Resour 13(4):207–210
46. Zaidel J, Russo D (1992) Estimation of finite difference interblock conductivities for simulation of infiltration into initially dry soils. Water Resour Res 28(9):2285–2295
47. Zhang X, Ewen J (2000) Efficient method for simulating gravity-dominated water flow in unsaturated soils. Water Resour Res 36(9):2777–2780

Chapter 5
Upscaling from Darcy Scale to Field Scale

Many porous media, either natural or human-made, show heterogeneous structure at the Darcy scale, represented by spatial variability of their characteristics such as porosity, intrinsic permeability or capillary function. If the domain under consideration consists of a limited number of well-defined locally homogeneous material regions, e.g. an earth dam with a clay core or a soil profile with few distinct layers, the flow can be modelled analytically or numerically using the Darcy-scale flow equations in each region, linked by appropriate conditions at the interfaces. However, porous media are often characterized by spatial variability of their hydraulic properties at a scale which is very small compared to the size of the domain under consideration. For example, rocks often have dense network of fractures with the spacing of the order of centimeters or decimeters, while the size of the flow domain is of the order of tens of meters to kilometers. Similarly, many soils and loose geological sediments contain large numbers of relatively small inclusions or lenses having properties different from the background material. Explicit representation of such features on a numerical grid would require excessively large number of grid cells. Even with the ever-increasing capabilities of the computers, such problems are difficult to solve within a reasonable time frame. Moreover, if the materials of the neighbouring sub-regions have contrasting hydraulic properties, e.g. permeability, the convergence of the numerical solution is usually negatively affected, because the linear systems of algebraic equations, arising from the discretization of the governing differential equations, tend to be ill-conditioned, even in the case of single phase flow. These difficulties increase for highly nonlinear unsaturated or two-phase flow phenomena. Finally, the heterogeneous structure is often not known in much detail, which means that it is difficult, and perhaps not purposeful to reconstruct the heterogeneity field. Instead, some representative pattern can be assumed.

All these factors motivate the development of upscaling approaches, which attempt to reproduce the behaviour of the system in terms of large-scale variables, defined as some kind of average values, representative for a volumetric element containing a number of small-scale material heterogeneities. In the context of flow in porous media, upscaling can be performed at various levels of the hierarchy of scales.

A. Szymkiewicz, *Modelling Water Flow in Unsaturated Porous Media*,
GeoPlanet: Earth and Planetary Sciences, DOI: 10.1007/978-3-642-23559-7_5,

For instance, the Darcy equation can be regarded as a result of upscaling pore-scale Navier-Stokes equations, while the latter ones represent an upscaled description of the molecular-scale processes. This chapter and the following ones focus on upscaling from the Darcy scale to the field scale. In the following discussion, those two scales are also denoted by more generic names: small (or local) scale and large (or macroscopic) scale. While an overview of various heterogeneity patterns is presented, the major focus of this work is on binary media containing disconnected inclusions scattered in the background material. It should be also noted that in many applications it is possible to distinguish more than one scale larger than the Darcy scale, for instance the scale of a single geological layer, which is heterogeneous due to the presence of fractures or lenses, and the scale of a reservoir composed of several layers. In this work, only the first level of upscaling above the Darcy scale is considered.

The literature on upscaling is very broad and its comprehensive review is beyond the scope of this book. General works consulted by the author include [17, 18, 99]. Other contributions are cited in the following sections.

5.1 Heterogeneity Patterns

Porous media show various types of heterogeneity at the Darcy scale. Some of them are shown in Fig. 5.1. Perhaps the most well known and widely studied pattern is that of layered medium (Fig. 5.1a), e.g. [79, 115]. Horizontal layering, in particular, is present in many geological formations of sedimentary rocks or loose sediments, due to the conditions of depositional environment in which they were formed. Such media are characterized by very high (actually the highest possible) anisotropy of the field-scale permeability. The problem of upscaling of layered media arises, for example, if a three dimensional mathematical model of flow is replaced by a two dimensional model describing flow in the horizontal plane, which is a typical situation in reservoir modeling, e.g. [116].

Another widely studied heterogeneity pattern is represented by media containing lenses or inclusions of one or more porous materials dispersed in a porous background material of different physical characteristics (Fig. 5.1b), e.g. [13, 36, 37, 46, 50, 55, 77, 78, 86, 95, 104, 105]. This pattern is also encountered in many sedimentary formations. Knudby et al. [55] lists the following examples: fluvial sediments containing paleochannels (high permeability inclusions embedded in a low permeability background), sandstone/shale sequences (low permeability inclusions embedded in a high permeability material), coastal deposits (deltaic paleochannels represent the highly permeable regions), and some glacial deposits. The limit cases are represented by stony soils (stones as impermeable inclusions, e.g. [73]) and porous media containing cavities or vugs, much larger than the pore size, e.g. [9]. The background material is often referred to as matrix, however the term matrix is also used in a different meaning for fractured media (see below). Similar structures are also encountered in human-made porous media, e.g. masonry walls consisting

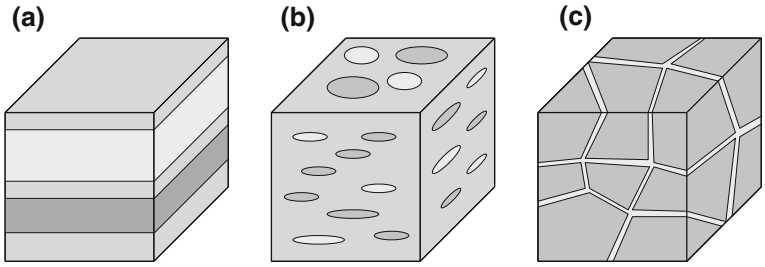

Fig. 5.1 Typical field-scale heterogeneity patterns: **a** layered medium, **b** medium with dispersed inclusions, **c** fractured medium

of bricks or porous rock slabs cemented with mortar. The inclusions can be either separated form each other, or they can overlap, forming continuous paths of the corresponding porous material in one or more spatial directions. Field-scale properties of such media are significantly influenced by the volume fraction, shape and connectivity of the inclusions, e.g. [55, 96]. Binary media with disconnected inclusions are the major focus of the following chapters.

Fractured rocks show a very distinct heterogeneous structure, resulting from the presence of multiple thin, approximately planar discontinuities, which arise mostly due to mechanical failure (Fig. 5.1c). The volume of the fractures is negligible compared to the volume of the rock mass, which is referred to as matrix, but if they are connected they form a network of preferential flowpaths, which greatly modifies the field-scale hydraulic properties of the medium. Since a large part of oil and groundwater resources resides in fractured rocks (mostly limestones and sandstones), this type of heterogeneous porous media receives considerable attention in the literature, e.g. [14, 16, 28, 58, 83]. The large-scale hydraulic behaviour of fractured media is influenced by several factors. For instance, while it is often assumed that the flow in a single fracture can be described by the Darcy formula, this is not always the case, and other models have to be used, like the Forchheimer equation, e.g. [113]. The rock matrix may be either permeable (in the case of many sedimentary rocks) or impermeable (in the case of igneous or metamorphic rocks). If the matrix is permeable, its permeability is orders of magnitude smaller than the permeability of fractures. Moreover, the matrix can be continuous and contribute to the large-scale flow or it can be divided by fractures into separate blocks, which release or absorb fluid from the fracture network. Due to the presence of two hydraulic systems with widely different characteristics, it is often impossible to reproduce the large-scale flow in fractured rocks using simple parameter averaging, because large local gradients of pressure arise between the fractures and matrix. The recognition of this fact led to the development of double porosity models. In this case the governing equations for field-scale flow are formulated separately for each pore system and they are coupled by additional terms describing fluid transfer between the systems.

Dual structure is also observed in many soils. Primary soil particles tend to coalesce into secondary structural units called peds, clods or aggregates [82, 90].

These objects have variable geometric forms, described as platy, blocky, columnar or angular, and they are separated from each other by failure zones, which can be void or filled with porous material coarser than the aggregates. Such soils are characterized by a bimodal distribution of the pore sizes, with two distinct classes corresponding to the intra-aggregate micropores and inter-aggregate macropores. The term macropores is also used to describe shrinkage cracks, wormholes, root channels and other highly permeable structural forms. Due to their relatively large size, macropores become saturated with water only when the soil water pressure is close to zero and they drain quickly. During heavy rainfall, when the soil surface reaches saturation, water enters macropores, leading to the preferential (bypass) flow. In such a case significant amount of contaminants can be rapidly transferred to deeper soil horizons. Below the uppermost saturated layer of soil, the flow is characterized by local non-equilibrium conditions, because significant local pressure gradients arise between the water-filled macropores and the surrounding dry or moderately wet matrix. In order to capture this effect, double porosity models, similar in form to the ones developed for fractured media, are often applied at the field-scale. The flow in macropores is typically described either by the Darcy formula (assuming very steep capillary and relative permeability functions), e.g. [41], or by the kinematic wave model, which neglects the capillary forces and takes into account only gravity, e.g. [51].

The term binary media is often used to describe heterogeneous porous media composed of two materials, such that the variability of hydraulic parameters within each material can be neglected, e.g. [55]. At the local scale, binary media are characterized by two distinct sets of hydraulic parameters. Binary structures include, among other, layered media composed of two materials and inclusions of single material dispersed in a homogeneous background. Assuming that the Darcy formula is valid for all pore systems, both fractured rocks and structured soils can be regarded as special cases of binary porous media, with very small fraction of the highly permeable material and large permeability contrast between the two components.

A general case of heterogeneity is represented by media which do not show any particular structure. The upscaling problem for such media often arise in large scale simulations of flow in groundwater or petroleum reservoirs, due to the discrepancy in the resolution of the geological model, providing detailed rock characteristics, and the numerical model used to simulate flow processes. Each cell of the numerical grid contains many cells of the geological model, and a question arises how to transfer the small scale variability to the large scale model in such a way that the overall behaviour of the medium is correctly represented.

5.2 Overview of Upscaling Approaches

Development of a large number of upscaling techniques for subsurface flow modeling was motivated by problems arising in petroleum engineering, hydrogeology and vadose zone hydrology, e.g. [18, 24, 25, 71, 72, 84, 101, 106, 111]. Each of these fields of application has its distinct features. In petroleum engineering, the

focus is on large scale (up to hundreds of kilometers), predominantly horizontal two phase or three phase flow, which at the reservoir scale is driven mostly by viscous forces, although capillarity and gravity can be locally important. Hydrogeological applications are related to mostly horizontal, single-phase water flow in aquifers, with the dimension of several kilometers. In contrast, water flow in vadose zone is typically driven by capillary and gravity forces, and occurs mostly in vertical direction, at a scale of several meters, although the importance of horizontal flow has been increasingly recognized [45, 101]. Nevertheless, there is a significant degree of overlap between conceptual approaches applied in these three domains and each of them can benefit from the advancement made in the other ones. For example, the double porosity models initially developed for fractured reservoirs, e.g. [11, 103] were later applied to describe flow in structured soils at considerably smaller spatial scales, e.g. [41].

Upscaling approaches can be broadly categorized in two groups, according to the way in which the large-scale mathematical model is developed. In the first group, an a priori assumption is made on the form of the mathematical model describing flow at the field scale, based on some phenomenological considerations. For instance, it is often assumed that the field-scale flow equations have the same form as the Darcy-scale flow equations presented in Chap. 2. In such a case, the upscaling problem consists in finding the large-scale constitutive properties and parameters characterizing the system. However, this type of models can be inaccurate, particularly for media with large permeability contrast between the component materials. For such cases, other phenomenological models were developed, e.g. the double-porosity models mentioned above, the relaxation models, e.g. [85], or the stream-tube approach, e.g. [101]. In these approaches the large-scale flow equations have different form than the Darcy-scale ones.

In the second group of methods, the description of the field-scale behaviour is obtained in a more rigorous way, by mathematical derivation starting from the description of flow at the Darcy scale. The form of the field-scale equations is not assumed a priori, rather it results from the assumptions on the physics of the local scale process and the local structure of the medium, which are taken into account during the derivation procedure. The transition from small scale equations to large scale equations can be performed using different mathematical techniques, for example the asymptotic homogenization for periodic media, e.g. [8, 15, 88], the volume averaging, e.g. [108] or various stochastic approaches, e.g. [26, 39, 114]. These methods offer a sound theoretical background to deal with the following important issues related to upscaling:

- Is it possible to replace a heterogeneous medium with a homogeneous equivalent characterized by intrinsic effective parameters, independent of the boundary conditions of the large-scale problem?
- What is the form of the governing equations at the large scale?
- What is the relation between the large-scale parameters and the parameters of the small-scale model?
- What is the domain of validity of the large-scale model?

Two basic prerequisites for the existence of an equivalent large-scale model with intrinsic parameters are the separation of scales and the existence of a representative elementary volume (REV) at the smaller scale. These two conditions are invoked, in slightly different forms, by both the periodic homogenization method and the volume averaging method. In the former approach the medium is assumed to be periodic, with the periodic cell being equivalent to an REV. The condition of separation of scales is specified in the following form, e.g. [8]:

$$\varepsilon = \frac{l}{L} \ll 1 \,, \tag{5.1}$$

where ε is the scale separation parameter, l is the dimension of the periodic cell and L is the dimension of the large scale domain. While this criterion is rather imprecise, it is generally considered that the large-scale model is a good approximation if $\varepsilon < 0.1$ [8] and the accuracy of approximation increases for decreasing ε. It should be noted that besides the geometric scale separation, the asymptotic homogenization method postulates the separation of scales with respect to the characteristic length of the relevant physical processes. For instance, if wave propagation is considered, it is required that the periodic cell dimension be much smaller than the length of the wave [8].

In the volume averaging method, the averaging procedure is performed in a region of dimension l_v, which satisfies the following assumption [108]:

$$l_h \ll l_v \ll L \,, \tag{5.2}$$

where l_h is the characteristic dimension of the local heterogeneities. The averaging region is equivalent to a representative elementary volume. The medium may not be periodic in the deterministic sense, but the distribution of heterogeneities is assumed to be stationary, such that the medium shows translational invariance.

If the conditions of separation of scales and existence of REV are not satisfied, it is generally not possible to obtain a large-scale model with intrinsic parameters. It means that at the large scale the parameters of the governing equations will be problem-specific, depending on the actual boundary conditions. In this context, a distinction can be made between equivalent and effective large-scale parameters, which applies particularly to the permeability or hydraulic conductivity [84]. The effective parameters represent intrinsic large scale properties of the material and they can be defined only in the particular case mentioned above. The term equivalent parameters has a more general meaning and denotes the parameters of any upscaled model for a heterogeneous medium, which can be problem-dependent. It should be also noted that the separation of scales and the presence of REV are necessary but not sufficient conditions for the existence of the large-scale model with effective parameters. In other words, even if both of them hold it may be not possible to derive a large-scale model, depending on the physics of the small-scale process.

The methods described above were developed in the deterministic framework, which assumes that full information about the spatial distribution of all parameters

of the porous medium is available at the smaller scale. However, both of them can be used in the stochastic framework, which assumes that the local heterogeneity pattern of the porous medium is uncertain and can be characterized by some specific probability distribution, e.g. [1, 69]. The assumptions of stationarity and scale separation, Eq. (5.2), are also relevant to the stochastic analysis [26]. If they are satisfied, the results obtained by stochastic upscaling are qualitatively equivalent to those obtained by the deterministic approach, i.e. the large scale models should have the same form [7, 8]. The difference is in the effective parameters, which in the stochastic case are given by random functions with specific probability distribution. Under certain additional assumptions, stochastic large-scale models can be also derived analytically when the separation of scales does not hold, with the resulting effective parameters depending on the large-scale boundary conditions of the problem.

In this work, a deterministic point of view is adopted and the upscaled models of flow in heterogeneous porous media of binary periodic structure are considered. The following part of this chapter presents an overview of the upscaling techniques applicable for such type of media, while in the subsequent chapters the results obtained with the asymptotic homogenization approach for a medium with disconnected inclusions are discussed in more detail. In particular, it will be shown how the form of the field-scale model and the definition of effective parameters are influenced by the local geometric structure and the ratio of the permeability and the entry pressure between the two materials constituting the heterogeneous medium.

5.3 Permeability Upscaling for Steady Single-Phase Flow

Steady-state incompressible single-phase flow represents possibly the simplest upscaling problem on the conceptual level, because the only parameter to be upscaled is the intrinsic permeability tensor. Nevertheless, it turns out to be a non-trivial task, given the large variety of heterogeneous structures occurring in natural porous media. Comprehensive reviews of various methods used to estimate the large-scale equivalent permeability tensor can be found in [84, 89, 106]. In this section, three groups of techniques are presented in more detail: algebraic averaging formulas, effective medium approximations and the methods based on direct solution of the steady flow equation. All of them can be easily applied to binary media, which are the primary focus of this work and they can be useful also for more complex cases of transient unsaturated or two-phase flow, as will be discussed later. The first two approaches have the advantage of simplicity, as the upscaled permeability can be calculated from an explicit analytical formula or from the solution of a simple nonlinear equation, but on the other hand they are accurate only for some particular heterogeneity patterns. In contrast, the methods from the latter group are more difficult to implement but offer much larger flexibility.

5.3.1 Algebraic Averaging

Consider a binary porous medium composed of two isotropic materials having absolute permeabilities k^I and k^{II} (the subscript s is omitted to simplify notation) and the corresponding volumetric fractions of w^I and w^{II}. Even if both constituents are isotropic, the equivalent field-scale permeability is in a general case a tensor, due to the possible anisotropic spatial distribution of the materials. Assuming that the spatial coordinate axes are parallel to the main axes of field-scale anisotropy, the permeability tensor becomes diagonal. The permeability value in each direction k_{ii}^{eq} is bounded by the weighted harmonic mean and the weighted arithmetic mean of the components' permeabilities, e.g. [8, 84, 99]:

$$k^{\text{harm}} \leqslant k_{ii}^{\text{eq}} \leqslant k^{\text{arit}} , \tag{5.3}$$

where the weighted harmonic and arithmetic averages are defined as follows:

$$k^{\text{harm}} = \left[\frac{w^I}{k^I} + \frac{w^{II}}{k^{II}} \right]^{-1} . \tag{5.4}$$

$$k^{\text{arit}} = w^I \, k^I + w^{II} \, k^{II} . \tag{5.5}$$

In a layered medium, the arithmetic average corresponds to the equivalent permeability in the two directions parallel to the layers, while the harmonic average corresponds to the equivalent permeability in the direction perpendicular to the layers. For any specific pair of the volumetric fractions, the layered medium represents the heterogeneity pattern with maximum anisotropy. For all other geometric configurations, the equivalent permeability in any direction is somewhere between these two limit values. The bounds for equivalent permeability given by (5.3) are known as Wiener bounds or Voigt–Reuss bounds [8, 84, 99, 110].

In view of the fact that the equivalent permeability in any direction is bounded by Eq. (5.3), some simple averaging formulas to estimate the equivalent permeability of a heterogeneous medium can proposed. For example, the generalized power mean has the following form [53, 84]:

$$k_{ii}^{\text{eq}} = \left[w^I \left(k^I \right)^{\pi_i} + w^{II} \left(k^{II} \right)^{\pi_i} \right]^{\frac{1}{\pi_i}} , \tag{5.6}$$

where π_i is a weighting coefficient, which in principle can be different for each spatial direction i. In order to respect the Wiener bounds, π_i should be between -1 and 1. In the former case, Eq. (5.6) represents harmonic averaging, while in the latter case—arithmetic averaging. For $\pi_i \to 0$ the limit value is given by the weighted geometric mean:

$$k_{ii}^{\text{eq}} = \left(k^I \right)^{w^I} \left(k^{II} \right)^{w^{II}} . \tag{5.7}$$

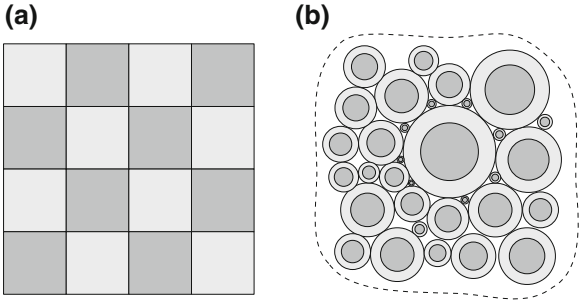

Fig. 5.2 Heterogeneity patterns of two-dimensional binary medium showing large-scale permeability isotropy: **a** checkerboard, **b** coated circles

Geometric mean represents the accurate value of the effective permeability for a two dimensional binary medium with equal volume fractions of the constituents, which are arranged in a checkerboard pattern, Fig. 5.2a [99]. In the stochastic framework, geometric mean corresponds to the effective permeability of an isotropic two-dimensional medium, for which the logarithm of permeability follows the normal probability distribution [84].

However, the principles of harmonic and arithmetic averaging can be also used to derive estimations for the equivalent permeability which take into account more detailed information on the small-scale structure of the medium, such as, for example, the Cardwell and Parsons bounds [21, 63, 84]. Consider a three dimensional heterogeneous upscaling cell, consisting of $N_1 \times N_2 \times N_3$ uniform sub-cells with known permeability values, Fig. 5.3. One possible method to estimate the permeability in x_1 direction is to replace the domain by a bundle of columns parallel to x_1 axis, Fig. 5.3a. The equivalent permeability of each column is given by the harmonic average of the permeabilities of the sub-cells constituting the column:

$$k_{11}^{h,jk} = \left(\frac{1}{N_1} \sum_{i=1}^{N_1} \frac{1}{k^{ijk}} \right)^{-1} , \tag{5.8}$$

where the superscripts i, j and k refer to the position of the sub-cell with respect to the three coordinate axes. Since the columns are parallel to each other, the permeability of the whole domain is given by the arithmetic mean of the columns' permeabilities.

$$k_{11}^{\mathrm{cpl}} = \frac{1}{N_2\, N_3} \sum_{j=1}^{N_2} \sum_{k=1}^{N_3} k^{h,jk} . \tag{5.9}$$

This result corresponds to the lower Cardwell and Parsons bound of the equivalent permeability. In a limit case, the presence of a single impermeable sub-cell in each

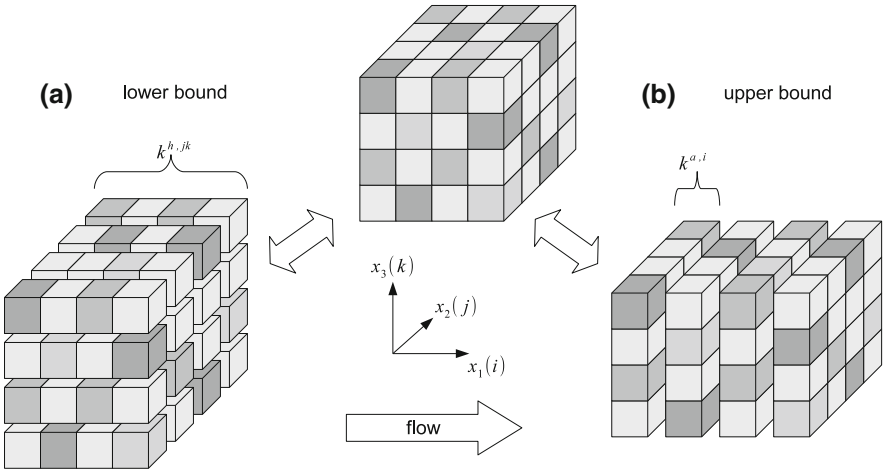

Fig. 5.3 Computation of Cardwell and Parsons bounds for the equivalent permeability in x_1 direction

column is sufficient to make the equivalent permeability zero, even if the impermeable sub-cells are widely separated from each other in the three dimensional medium.

The complementary upper bound is derived by conceptualizing the heterogeneous domain as a sequence of slices perpendicular to x_1 direction, Fig. 5.3b. The permeability of each slice in x_1 direction is given by the arithmetic mean of the permeabilities of the sub-cells constituting the slice:

$$k_{11}^{a,i} = \frac{1}{N_2 N_3} \sum_{j=1}^{N_2} \sum_{k=1}^{N_3} k^{ijk} \,. \tag{5.10}$$

The equivalent permeability of the sequence of slices is then computed as the harmonic mean of their permeabilities:

$$k_{11}^{\text{cpu}} = \left(\frac{1}{N_1} \sum_{i=1}^{N_1} \frac{1}{k_{11}^{a,i}} \right)^{-1} \,. \tag{5.11}$$

Note that in a particular case of an impermeable medium with small amount of permeable sub-cells it is sufficient that a single permeable sub-cell is present in each slice to give a non-zero equivalent permeability k_{ii}^{cpu}, even if the permeable sub-cells do not form a continuous path through the medium.

Some authors proposed averaging formulas based on a combination of the Cardwell and Parsons bounds. For example, Li et al. [63] suggested to use a weighted power average of the lower and upper bound as an appropriate estimation for permeability in the horizontal directions:

$$k_{ii}^{\mathrm{eq}} = \left(k_{ii}^{\mathrm{cpu}}\right)^{2/3} \left(k_{ii}^{\mathrm{cpl}}\right)^{1/3} \qquad i = 1, 2. \tag{5.12}$$

Vertical permeability is estimated from another formula, which takes into account possible local-scale anisotropy of the sub-cells. If the component materials are isotropic, this formula reduces to the lower Cardwell and Parsons bound for flow in the vertical direction k_{33}^{cpl}.

In the approach of Sviercoski [94], developed for two-dimensional media, the diagonal components of the equivalent permeability tensor are calculated as:

$$k_{ii}^{\mathrm{eq}} = \frac{1}{2}\left[\frac{k_{ii}^{\mathrm{cpu}} + k_{ii}^{\mathrm{cpl}}}{2} + \left(k_{ii}^{\mathrm{cpu}}\, k_{ii}^{\mathrm{cpl}}\right)^{1/2}\right] \qquad i = 1, 2, \tag{5.13}$$

which is the arithmetic mean of the arithmetic and geometric means of the lower and upper bounds for the relevant spatial direction. A method to compute the off-diagonal components of the equivalent permeability tensor is also provided in [94].

5.3.2 Effective Medium Theory

The effective medium theory allows to estimate the permeability of heterogeneous mixtures and is particularly well suited for the case of binary media composed of spherical or ellipsoidal inclusions embedded in a background material. In this case the notion of effective permeability can be used, because separation of scales and stationarity of the medium are implied. The approach is based on the analysis of the perturbation of a uniform potential field caused by a single inclusion placed in an infinite homogeneous domain. For ellipsoidal inclusions, the corresponding solution can be obtained analytically. Various effective medium schemes differ in the way of accounting for the interactions between inclusions, which leads to significant differences in the results as the volume fraction of inclusions increases. Three formulae widely used in many disciplines of engineering are known as the Maxwell formula, the self-consistent (or symmetric Bruggeman) formula and the differential or asymmetric Bruggeman formula (although a variety of other names for each of them can be found in the literature). The formulas are presented here after [99] for the case of uniformly aligned ellipsoids, with the equivalent permeability given by a diagonal tensor. In the following the background is denoted as material I and the inclusions as material II.

The Maxwell formula is based on the assumption that the total perturbation of the potential field is the sum of perturbations caused by single inclusions. The expression for the effective permeability can written as follows [99]:

$$k_{ii}^{eq} = k^{I} + \frac{w^{II}\left(k^{II} - k^{I}\right)}{1 + d_i w^{I}\left(k^{II} - k^{I}\right)/k^{I}}, \tag{5.14}$$

Table 5.1 Depolarisation coefficients for various shapes of inclusions [52, 67]

Shape		d_1	d_2	d_3
Spheroid	$a_1 \neq a_2 = a_3$	$\frac{1}{1+1.6(a_1/a_2)+0.4(a_1/a_2)^2}$	$\frac{1-d_1}{2}$	$\frac{1-d_1}{2}$
Sphere	$a_1 = a_2 = a_3$	$\frac{1}{3}$	$\frac{1}{3}$	$\frac{1}{3}$
Infinite elliptical cylinder	$a_3 = \infty$	$\frac{a_2}{a_1+a_2}$	$\frac{a_1}{a_1+a_2}$	0
Infinite circular cylinder	$a_1 = a_2,\ a_3 = \infty$	$\frac{1}{2}$	$\frac{1}{2}$	0
Infinite disk	$a_2 = a_3 = \infty$	1	0	0

where the superscripts I and II refer to the background material and inclusions, respectively, and d_i is the depolarization coefficient in ith direction, which depends on the shape of the inclusion. In a general case of triaxial ellipsoid, the depolarisation coefficients are given be the following formula [67, 99]:

$$d_i = \frac{a_1\, a_2\, a_3}{2} \int_0^{+\infty} \frac{\mathrm{d}u}{\left(u + a_i^2\right) \sqrt{\left(u + a_1^2\right)\left(u + a_2^2\right)\left(u + a_3^2\right)}}, \tag{5.15}$$

where u is the integration variable and a_i is the length of the ellipsoid axis parallel to the spatial direction x_i. The resulting coefficients, however, depend only on the ratio between the lengths of the axes, and not on their actual lengths. Several particular cases can be distinguished, for which simpler expressions are available, as shown in Table 5.1. Note that the case of discs with infinite dimensions in two directions is equivalent to a layered medium, and the Maxwell formula provides the corresponding values of the arithmetic and harmonic averages. Due to the assumed lack of interaction between inclusions, the formula is considered to be a good approximation for the so-called dilute limit with $w^{II} \ll 1$. However, it is also relatively accurate for higher inclusion contents, provided that the inclusions are well separated from each other [67].

The Maxwell formula is asymmetric, which means that for any pair of materials with specific volume fractions two values of the effective permeability k_{ii}^{eff} are possible, depending on which of the materials is assumed to form discontinuous inclusions. It can be shown that for an arbitrary binary medium which shows large-scale isotropy the effective permeability is between the two values predicted by the Maxwell formula assuming inclusions in the form of spheres (in three-dimensional media) or circles (in two-dimensional media) [47, 67, 99]. This pair of values is known as the Hashin–Shtrikman bounds [47]. The Hashin-Shtrikman bounds give exact values of permeability for a particular type of medium represented by an assemblage of coated spheres or circles, as shown in Fig. 5.2b. The larger value is obtained for low-permeability cores inside high-permeability coatings, and the smaller value—for the inverse case. For all other macroscopically isotropic binary media the effective permeability is between these bounds.

The self consistent approximation is obtained from the analysis of a single inclusion embedded in a homogeneous medium, whose permeability is assumed to be equal to the unknown effective permeability. This leads to an implicit formula of the following form [99]:

$$\frac{w^I \ \left(k^I - k_{ii}^{\text{eff}}\right)}{d_i \ k^I + (1 - d_i) \ k_{ii}^{\text{eff}}} + \frac{w^{II} \ \left(k^{II} - k_{ii}^{\text{eff}}\right)}{d_i \ k^{II} + (1 - d_i) \ k_{ii}^{\text{eff}}} = 0 \ . \tag{5.16}$$

Using the above formula, the components of the effective tensor can be computed independently of each other, because for each spatial direction it is assumed that the material surrounding the inclusion is isotropic. Other formulations take into account the anisotropy of the surrounding material, which leads to a system of 2 or 3 coupled nonlinear equations (depending on the dimension of the problem), which must be solved to obtain the components of k^{eff} [36, 77, 78]. In contrast to the Maxwell formula, in the self-consistent scheme a specific threshold value of the volume fractions of inclusions exists, above which they become connected and their properties dominate the equivalent properties of the system. The threshold value depends on the shape of inclusions and is equal to $1/2$ for circles and $1/3$ for spheres. Moreover, the self consistent approximation shows symmetry with respect to the volumetric fraction of the materials. It means that for a specific proportion of the weakly and highly permeable material there is only one value of the effective permeability, regardless of the choice of material for background and inclusions.

Finally, the differential formula is based on the consideration of the increment of the effective permeability caused by a small increment in the volume fraction of inclusions. It is assumed that the corresponding value can be obtained using the Maxwell formula. Integration of the resulting differential equation in the range of the volume fractions of inclusions from 0 to the considered value of w^{II} yields the following expression for k^{eff} [99]:

$$w^I \ \frac{k^{II} - k^I}{k^{II} - k_{ii}^{\text{eff}}} = \left(\frac{k^I}{k_{ii}^{\text{eff}}} \right)^{d_i} \ . \tag{5.17}$$

The resulting nonlinear equation has to be solved numerically. Similarly to the Maxwell formula, the differential scheme is asymmetric.

The values of the effective permeability obtained with various effective medium formulae are plotted in Figs. 5.4 and 5.5, together with the arithmetic and harmonic averages. Figure 5.4 shows the results for isotropic inclusions in two and three dimensions (i.e. circles and spheres). For each geometry two sets of results are presented, corresponding respectively to highly permeable inclusions with $k^{II}/k^I = 10^4$ and weakly permeable inclusions with $k^{II}/k^I = 10^{-4}$. In all cases, the Maxwell formula, which assumes well-separated inclusions, predicts effective permeability which is close to the background permeability even for large inclusions fraction w^{II}. Therefore, it is close to the arithmetic mean in the case of weakly permeable inclusions and to the harmonic mean in the case of highly permeable inclusions. The self-consistent

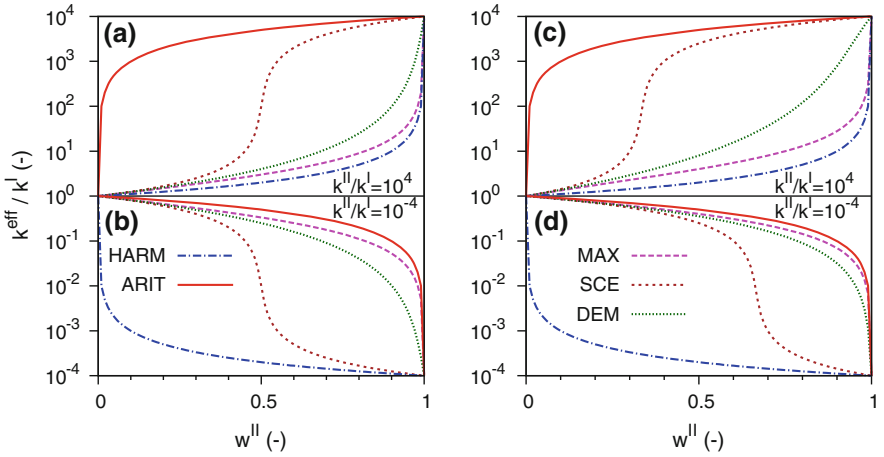

Fig. 5.4 Effective permeability as a function of inclusions fraction for an assemblage of inclusions: **a** circles, highly permeable, **b** circles, weakly permeable, **c** spheres, highly permeable, **d** spheres, weakly permeable; results are shown for the Maxwell formula (MAX), self-consistent scheme (SCE), differential scheme (DEM), arithmetic (ARIT) and harmonic (HARM) averaging

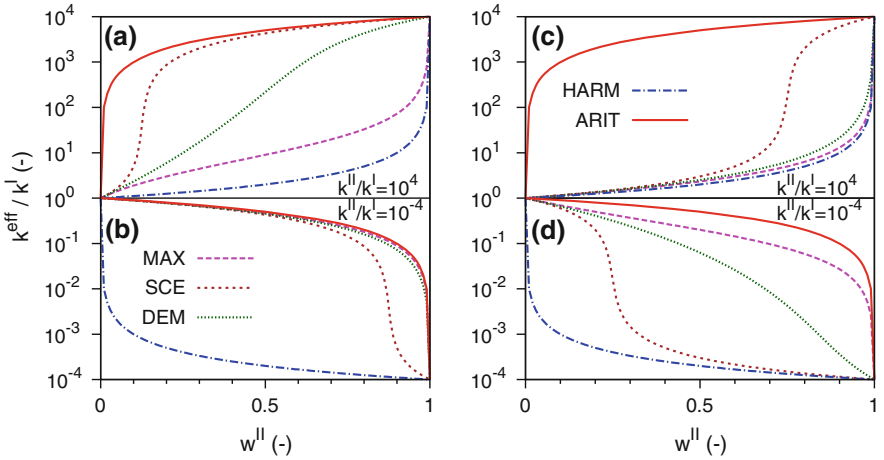

Fig. 5.5 Effective permeability as a function of inclusions fraction for ellipsoids of revolution with $a_1 = a_2 = 5\,a_3$: **a** longitudinal direction, $k_{11}^{\text{eff}} = k_{22}^{\text{eff}}$, highly permeable inclusions, **b** longitudinal direction, weakly permeable inclusions, **c** transversal direction, k_{33}^{eff}, highly permeable inclusions, **d** transversal direction, highly permeable inclusions. Abbreviations as in Fig. 5.4

approach differs significantly from the Maxwell approximation, because it predicts a rapid change of the effective permeability in the vicinity of the threshold value, while the differential scheme gives values relatively close to the Maxwell formula.

Figure 5.5 show the components of the effective permeability tensor for a medium containing oblate spheroids, with two equal axes parallel to the directions x_1 and x_2

and a shorter axis parallel to the direction x_3. The largest differences between various schemes arise for the highly permeable ellipsoids in the directions parallel to the longer axes and for the weakly permeable ellipsoids in the direction parallel to the shorter axis. In the first case, it can be intuitively understood that as the fraction of inclusions increases the connected paths will be formed principally in the directions of the longer axes and the corresponding results are highly sensitive to the assumptions on the inclusions connectivity, underlying various schemes. In the case of weakly permeable inclusions, the clusters of connected inclusions, which form parallel to the longer axes, do not have much influence on the permeability in the parallel direction, as long as the more permeable material remains connected along the same direction. However, they strongly reduce the connectivity of the background material in the perpendicular direction. Thus, the perpendicular permeability is much influenced by the connectivity of the weakly permeable ellipsoids in the direction of their longest axes.

The effective medium approximations were used by several authors to compute the field-scale permeability of heterogeneous porous media [36, 70, 77, 78, 118]. Comparisons with the results of numerical solution of steady-state flow were also made in a number of papers [36, 46, 55, 61, 96]. It was found that the Maxwell scheme provides reasonable estimates for isotropic assemblages of non-overlapping inclusions (e.g. spheres, cubes, regular octahaedra) [61, 96]. For anisotropic geometries the effective permeability is highly influenced by the shape and spatial arrangement of inclusions [46, 55]. Depending on these factors, many different values of the effective permeability are possible for the same volume fraction of inclusions. In such cases, the effective medium approximations cannot be expected to be accurate and improved formulas are required, which take into account more information on the local geometry [55]. The effective medium approximations can be extended for the case of larger number of component materials. Such extended formulas were compared by Neuweiler and Vogel [70] with the results of numerical solution of steady flow equation (see below) for media with random non-Gaussian distribution of permeability, where either weakly or highly permeable materials formed connected paths through the medium. The best agreement with the numerical solution was obtained for the differential effective medium scheme.

5.3.3 Direct Solution of Steady Flow Equation

In this group of methods, the equivalent permeability tensor for an arbitrary heterogeneous upscaling cell is calculated from the solution of the steady state flow equation. The equation can be solved in a domain which corresponds to the upscaling cell itself (local approach), in a larger domain encompassing the cell (extended local approach) or in the whole field-scale domain (global approach), e.g. [44]. In the local approach, the so-called cell problem is solved for an upscaling cell, which may correspond to an REV, if it exists, or to a cell of the numerical grid for the field-scale problem. The cell problem is given by the steady flow equation, e.g. [84, 117]:

$$-\nabla \cdot (\mathsf{k}\,\nabla p) = 0 \tag{5.18}$$

with an appropriate set of boundary conditions, as discussed below. Note that in order to simplify the presentation (and without the loss of generality) it is assumed that the density, viscosity and gravitational acceleration are all equal to one, the phase subscript is omitted, and the gravity term is not explicitly shown (p represents the excess of pressure over the hydrostatic value). The equivalent permeability tensor is computed in such a way that certain relations between the volume averages of the small-scale quantities are satisfied. These quantities include the potential gradient (driving force), the volumetric fluid flux and the energy dissipation [117]. The equivalent permeability can be defined in terms of the volumetric averages of two of those quantities. An intuitive and widely used definition is based on the correspondence between the Darcy-scale and field-scale volumetric fluxes and gradients:

$$\langle \mathbf{v} \rangle = -\langle \mathsf{k}\,\nabla p \rangle = -\mathsf{k}^{\mathrm{eq}}\,\langle \nabla p \rangle \ , \tag{5.19}$$

where the angular brackets denote the volume averaging operator:

$$\langle u \rangle = \frac{1}{|V|} \int_V u \,\mathrm{d}V \tag{5.20}$$

where V is the relevant spatial domain. Some authors suggest to use a definition based on the preservation of the energy dissipation D_e, which is motivated by thermodynamical considerations [19, 49]:

$$\langle D_\mathrm{e} \rangle = -\langle \nabla p \cdot \mathbf{v} \rangle = \langle \nabla p \rangle\, \mathsf{k}^{\mathrm{eq}}\, \langle \nabla p \rangle \ . \tag{5.21}$$

Note that the equivalent permeability is a tensor with nine components (although the number can be reduced to six if symmetry is assumed), so for a single solution of the steady flow problem Eqs. (5.19) or (5.21) represents a set of three scalar equations with nine unknowns. Therefore, three independent solution must be provided to compute all components of the large-scale tensor. It is also clear that the solution of the steady flow equation is determined by the boundary conditions, which must be carefully chosen.

A usual procedure is to perform three solutions of the cell problem with such a choice of the boundary conditions that in each case the average field-scale gradient in one of the spatial directions is equal to unity. For each considered spatial direction i it is convenient to express the Darcy-scale pressure as a sum of the average value and a spatial deviation:

$$p_i = \langle p_i \rangle + \tilde{p}_i \ . \tag{5.22}$$

Equation (5.18) can be then rewritten as:

$$-\nabla\,(\mathsf{k}\,\nabla \tilde{p}_i) = \nabla\,(\mathsf{k}\,\nabla \langle p_i \rangle) \ . \tag{5.23}$$

The above equation is solved for the spatial deviation $\tilde{p}_i$, with the gradient of the average pressure acting as a source term. The components of the average gradient $\nabla\langle p_i\rangle$ are equal to one in ith direction and zero in other directions.

Three types of boundary conditions are typically imposed for the spatial deviation of the potential, e.g. [2, 84, 113]:

1. Periodic boundary conditions imply that the values of the spatial deviations of the pressure and their derivatives at the opposite sides of the upscaling cell are equal, Fig. 5.6a. These conditions naturally arise when the large-scale flow equation is derived for a periodic medium using asymptotic homogenization procedure, e.g. [3, 59, 87]. They are also applied in the framework of the volumetric averaging method, e.g. [81]. In both these cases, the cell problem is defined for a REV of the porous medium and the resulting values of the permeability are effective (intrinsic) parameters. However, periodic conditions are also used for arbitrary upscaling cells. In order to obtain a well-posed problem, a Dirichlet boundary condition (the value of either pressure or its fluctuation) must be specified at least in a single arbitrary point of the boundary. Typically, this value is chosen as zero, although it does not influence the resulting equivalent permeability, which depends solely on the gradients of the unknown.
2. Linear (or uniform pressure drop) boundary conditions imply that the pressure varies linearly along the considered spatial direction, assuming the same values as the spatial coordinate, Fig. 5.6b. If the problem is formulated in terms of the pressure deviation, its value is uniformly equal to zero at all boundaries.
3. Confined (or permeameter) boundary conditions enforce one-dimensional flow along the considered spatial direction by specifying constant values of the pressure (corresponding to a unit gradient) at the perpendicular sides of the cell and no-flow conditions at the parallel sides, Fig. 5.6c.

For periodic or uniform boundary conditions the equivalent permeability definitions based on the preservation of flux and energy dissipation become equivalent [113]. Taking into account that the average pressure gradient for each of the three solutions is a unit vector, the components of the tensor can be calculated either according to Eq. (5.19) [100]:

$$k_{ij}^{\mathrm{eq}} = \langle \mathsf{k}\,\nabla p_j\rangle_i = \left\langle \sum_{m=1}^{3} k_{im}\,\frac{\partial p_j}{\partial x_m} \right\rangle \tag{5.24}$$

or according to Eq. (5.21) [100]:

$$k_{ij}^{\mathrm{eq}} = \langle \nabla p_i\,\mathsf{k}\,\nabla p_j\rangle_i = \left\langle \sum_{m=1}^{3}\sum_{n=1}^{3} k_{mn}\,\frac{\partial p_i}{\partial x_n}\,\frac{\partial p_j}{\partial x_m} \right\rangle . \tag{5.25}$$

If the cell problem is formulated in terms of the pressure deviation, the corresponding pressure gradients are calculated as:

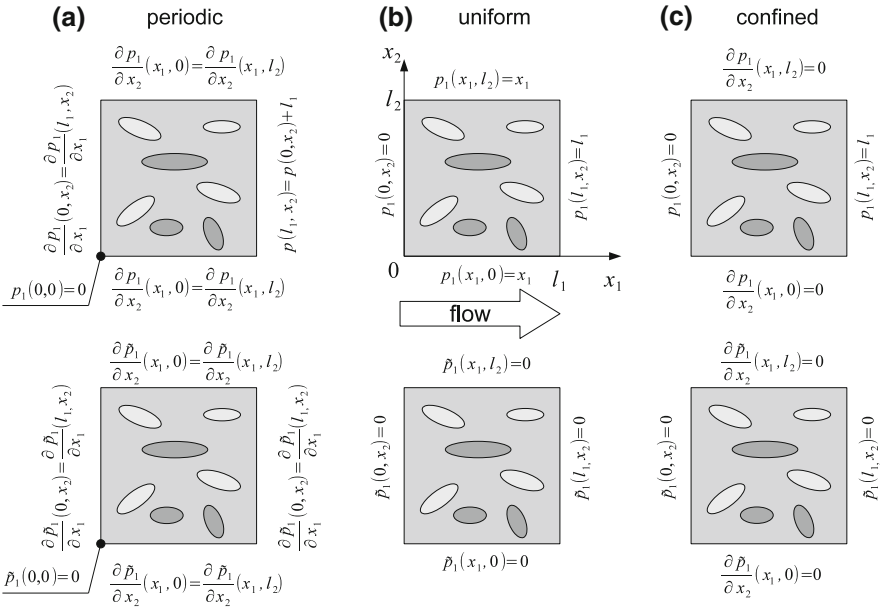

Fig. 5.6 Boundary conditions for the solution of two-dimensional cell problem formulated in terms of the pressure p (*lower row*) or the fluctuation of pressure $\tilde{p}$ (*lower row*); flow in x_1 direction

$$\frac{\partial p_m}{\partial x_n} = \frac{\partial \tilde{p}_m}{\partial x_n} + 1 \quad \text{for} \quad m = n \,, \tag{5.26}$$

$$\frac{\partial p_m}{\partial x_n} = \frac{\partial \tilde{p}_m}{\partial x_n} \quad \text{for} \quad m \neq n \,. \tag{5.27}$$

The resulting tensor is characterized by symmetry and positive-definiteness [113].

If confined boundary conditions are applied, the off-diagonal components of the equivalent tensor are often assumed to be zero, e.g. [2, 84], while the diagonal components are computed from the volume averages of the fluxes as given by Eq. (5.19) or from the surface averages evaluated at the cell boundaries perpendicular to the flow direction. However, Wu et al. [112] pointed out the inconsistency of such a formulation. For confined boundary conditions, the formulation of the cell problem in terms of the pressure p and its fluctuation $\tilde{p}$ are not equivalent, because it is not guaranteed that the volumetric average of the pressure gradient obtained from Eq. (5.18) is a unit vector in ith direction. Moreover, even if the cell boundaries parallel to the flow are considered impermeable, the volume average of the fluxes in the directions perpendicular to the main flow can be non-zero, which makes it possible to compute the off-diagonal components of the equivalent permeability tensor. Wu et al. [112] recommended to calculate the full tensor by applying Eq. (5.19) to the solutions in three spatial directions, which results in a linear system of equations with

nine unknowns. It should be noted that the confined boundary conditions become equivalent to the periodic conditions for symmetric cell geometries.

It is also possible to use other types of boundary conditions. For instance, one can solve the cell problem for multiple sets of linearly variable values of the pressure p imposed along the boundaries. If the number of solutions exceeds the geometric dimension of the cell, the corresponding set of Eq. (5.19) becomes over-determined and the components of the equivalent tensor can be obtained from the solution of an optimization problem, possibly with additional constraints imposing the symmetry of the tensor [106].

For some particular geometries, the cell problem can be solved analytically. For a layered medium with layers perpendicular to one of the coordinate axes, say the vertical axis x_3, the cell problem with either periodic or confined boundary conditions yields the well-known result of the volume-weighted harmonic average for k_{33}^{eq} and the volume-weighted arithmetic average for k_{11}^{eq} and k_{22}^{eq}. In the case of uniform boundary conditions, analytical solution is also possible, but k_{33}^{eq} depends on the dimensions of the upscaling cell. If the dimensions l_1 and l_2 are larger than l_3 by a factor of 20 or more, the result is close to the harmonic mean, while for smaller horizontal dimensions the effective permeability is larger [65]. This is due to the fact that uniform boundary conditions impose constant gradient of the potential along boundaries parallel to the flow, while according to the flux continuity condition for steady flow the gradients in the weakly permeable layers should be larger than in the highly permeable layers. The formula developed by Sviercoski [94], described in Sect. 5.3.1, represents an approximate analytical solution to the cell problem with periodic boundary conditions. Knudby et al. [55] proposed approximate analytical formulas for the effective permeability of two-dimensional medium containing rectangular inclusions, based on the numerical solution of the cell problem with confined boundary conditions.

In general, however, the cell problem must be solved numerically. The accuracy and computational efficiency of the solution of the cell problem is influenced by the number of nodes of the numerical grid, by the choice of the spatial discretization scheme applied to the steady flow equation, as well as by the choice of the method used to solve the system of linear algebraic equations resulting from spatial discretization. In the case of periodic boundary conditions, it was shown that for the same numerical grid the solution obtained with the standard Galerkin finite element method yields the upper estimate of the sum of the diagonal components of the equivalent permeability tensor, while the solution obtained with the mixed-hybrid finite element method—the lower estimate [117]. As the grid is refined, these two solutions become closer to each other and to the accurate value of the effective permeability, which is between them. If the upscaling cell contains a large number of material regions with highly contrasting permeabilities, the discontinuous Galerkin method proves particularly efficient [83].

The values of the equivalent permeability obtained from the numerical solution of cell problem for some simple geometries are listed in Tables 5.2 and 5.3. Six two-dimensional patterns were considered, as shown in Fig. 5.7. In each case the volumetric fraction of material II (inclusions) is equal to 0.25. The permeability of

Table 5.2 Equivalent permeability obtained from the solution of cell problem for geometries shown in Fig. 5.7, $k^{II}/k^{I} = 0.1$

Geometry	Periodic	Linear	Confined	k^{cpl}	k^{cpu}	Sviercoski, Eq. (5.13)	Maxwell, Eq. (5.14)
(a)	0.649	0.658	0.649	0.591	0.710	0.649	0.660
(b)	0.659	0.671	0.660	0.559	0.713	0.634	0.660
(c)	0.637	0.656	0.638	0.515	0.706	0.607	0.660
(d), k_{11}^{eq}	0.693	0.717	0.694	0.591	0.775	0.680	0.710
(d), k_{22}^{eq}	0.566	0.613	0.566	0.308	0.710	0.488	0.591
(e), k_{11}^{eq}	0.775	0.775	0.775	0.775	0.775	0.775	0.775
(e), k_{22}^{eq}	0.309	0.498	0.309	0.309	0.309	0.309	0.309
(f), k_{11}^{eq}	0.533	0.590	0.490	0.449	0.628	0.535	n/a
(f), k_{22}^{eq}	0.675	0.689	0.679	0.609	0.741	0.673	n/a
(f), k_{12}^{eq}	−0.0286	−0.0297	0.0	0.0	0.0	−0.0287	n/a

Table 5.3 Equivalent permeability obtained from the solution of cell problem for geometries shown in Fig. 5.7, $k^{II}/k^{I} = 10$

	Periodic	Linear	Confined	$k^{cp,l}$	$k^{cp,u}$	Sviercoski, Eq. (5.13)	Maxwell, Eq. (5.14)
(a)	1.54	1.68	1.54	1.41	1.69	1.55	1.51
(b)	1.52	1.65	1.51	1.40	1.79	1.59	1.51
(c)	1.56	1.69	1.56	1.42	1.94	1.67	1.51
(d), k_{11}^{eq}	1.77	2.31	1.77	1.41	3.25	2.24	1.69
(d), k_{22}^{eq}	1.44	1.74	1.45	1.69	1.29	1.48	1.41
(e), k_{11}^{eq}	3.25	3.25	3.25	3.25	3.25	3.25	3.25
(e), k_{22}^{eq}	1.29	1.62	1.29	1.29	1.29	1.29	1.29
(f), k_{11}^{eq}	1.48	1.71	1.47	1.35	1.64	1.49	n/a
(f), k_{22}^{eq}	1.88	2.33	2.05	1.59	2.23	1.90	n/a
(f), k_{12}^{eq}	−0.0796	−0.134	0.0	0.0	0.0	−0.0836	n/a

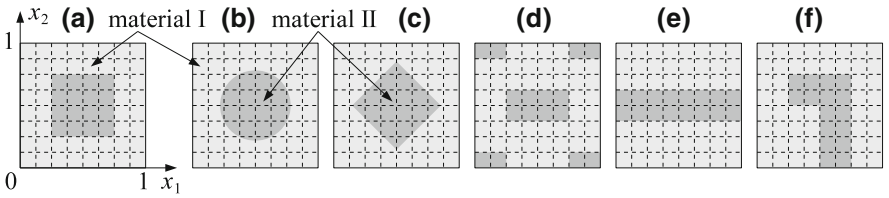

Fig. 5.7 Cell geometries used in the numerical example: **a** square inclusion, **b** round inclusion, **c** diamond-shaped inclusion, **d** rectangular inclusions, **e** layered medium, **f** L-shaped inclusion

Table 5.4 Equivalent permeability obtained with simple averaging formulas for cell geometries shown in Fig. 5.7

k^{II}/k^{I}	Arithmetic	Harmonic	Geometric
0.1	0.775	0.309	0.562
10	3.25	1.29	1.78

material 1 equals unity, while the permeability of material 2 is either 0.1 or 10. The solutions were obtained using numerical code EFFCOND, developed by the author and described in more detail in [96]. It is based on cell-centred finite volume discretization for rectangular grids. Uniform grids of 256 by 256 cells were used in each case. Periodic, uniform and confined boundary conditions were applied as described above, and the effective permeability was computed using Eq. (5.24). For confined boundary conditions, the off-diagonal components were assumed to be zero. The obtained results are close to those reported by other authors for the same geometries and permeability ratio [2, 95], with the exception of the case of uniform boundary conditions applied to geometry (a) with weakly permeable inclusions, for which the results given in [2] seem overestimated. For each case the Cardwell and Parsons bounds are provided, as well as the approximation of Sviercoski [94], Eq. (5.13), and the Maxwell approximation, Eq. (5.14), where applicable. Moreover, in Table 5.4 the values of arithmetic, geometric and harmonic averages are listed. The presented results confirm the observations from the previous paragraphs. For isotropic geometries, the numerical results obtained using periodic and confined boundary conditions are virtually the same, while uniform boundary conditions predict slightly larger permeability values. The same is true for the layered geometry, where the application of uniform boundary conditions leads to overestimation of the permeability in the direction parallel to the layers, with respect to the exact result given by the harmonic mean. For the L-shaped inclusion, each set of boundary conditions leads to a different equivalent permeability tensor. It is interesting to note that for the weakly permeable inclusion larger differences between various schemes are observed in the direction x_1, which is perpendicular to the longer dimension of the L-shaped inclusion. Conversely, if the inclusion is more permeable than the background, larger differences are observed in the direction parallel to its longer dimension. This effect is similar to the one described for the effective medium approximations. The method of Sviercoski [94] is in good agreement with the numerical solution of periodic problem, except for the case of rectangular inclusions, where the largest differences between the upper and lower Cardwell and Parsons bounds are observed. Note also that the Maxwell approximation is close to the results of periodic solution for both isotropic and rectangular inclusions.

In contrast to the local methods described above, the extended local approach assumes that the steady flow problem is defined for a larger domain which contains the considered upscaling cell, whereas the averaging of pressures and fluxes is performed only in the cell itself. It is expected that in this way the influence of boundary conditions on the equivalent permeability is reduced, while, on the other hand, the effects of larger-scale heterogeneous features (e.g. highly permeable channels

spanning several neighbouring cells) are better captured, e.g. [107]. Global upscaling methods were also proposed, e.g. [109]. These methods require that the flow problem is solved for the whole heterogeneous domain, with explicit representation of the spatial variability of the permeability tensor. The equivalent permeability is then calculated for each cell based on the detailed information on the pressures and fluxes within the cell, which is obtained from the global solution. While such approach requires considerable numerical effort and seems to contradict the very idea of upscaling, it is justified if the results are subsequently used for many coarse-grid simulations with relatively similar boundary conditions. An iterative local-global method was developed in [22]. In this method the equivalent permeabilities are first calculated for each coarse grid cell using a local or extended local approach. The obtained values are then used to solve the large-scale boundary problem on a coarse grid. The resulting values of the large-scale pressures are then interpolated to provide boundary conditions for the cell problems, which are solved in order to obtain more accurate estimates of the equivalent permeabilities. The procedure is continued until the required degree of consistency between the local and global solutions is achieved.

5.4 Upscaling of Transient Two-Phase Flow

5.4.1 Local Equilibrium and Quasi Steady-State Models

The problem of upscaling becomes significantly more complex in the case of unsteady multiphase flow, because in addition to the spatial scales, time scales must be also considered. In the phenomenological approach to upscaling, it is often considered that the field-scale governing equations have the same form as the Darcy-scale equation, while the equivalent constitutive relationships in the form of field-scale capillary and/or relative permeability functions are defined for each upscaling cell. In principle, this can be done for an arbitrary case, if one has full information on the Darcy-scale distribution of the primary variables and constitutive relationships within the cell. The averaging of additive quantities like mass or volume can be performed by taking volume integrals over the upscaling cells, which leads to the following definitions of the large-scale porosity and volumetric phase fractions:

$$\phi^{\mathrm{eq}} = \langle \phi \rangle = \frac{1}{V} \int_V \phi \, \mathrm{d}V \ , \tag{5.28}$$

$$\theta_\alpha^{\mathrm{eq}} = \langle \theta_\alpha \rangle = \frac{1}{V} \int_V \theta_\alpha \, \mathrm{d}V \ . \tag{5.29}$$

Consequently, the large scale saturation can be defined as:

$$S_\alpha^{\mathrm{eq}} = \frac{\theta_\alpha^{\mathrm{eq}}}{\phi^{\mathrm{eq}}} \ . \tag{5.30}$$

The averaging of non-additive quantities like pressure or permeability is more problematic. The average phase pressure is sometimes defined as a volumetric average weighted by the respective fluid saturation, e.g. [66]. The phase permeabilities cannot be averaged directly. Instead, they must be obtained from the average fluxes, in a manner analogous to the one described above for steady state flow. The absolute permeability can be obtained using one of the methods described in the previous section. Once the phase permeabilities and the absolute permeability are known, it is possible to introduce the large-scale relative permeabilities, which are anisotropic in a general case.

A fundamental question is how to obtain the small scale distribution of the relevant physical quantities, which would best correspond to the large-scale process under consideration. The assumption of local steady-state flow within an upscaling cell is often invoked. Intuitively, this seems justified if the time necessary to equilibrate fluid potentials at the scale of a single cell is much smaller than the time of the field-scale flow. Such an assumption simplifies the calculation of the equivalent constitutive functions, because the Darcy-scale distribution of the relevant physical quantities, which must be averaged, is uniquely determined by the conditions at the cell boundaries, which in turn can be related to the averaged field-scale variables. However, the actual steady-state distribution is significantly influenced by the local balance of viscous, gravity and capillary forces [93]. In this regard, several possibilities can be distinguished.

If the viscous forces are locally much smaller than the capillary and gravity forces, the conditions of vertical equilibrium prevail. The pressures in each fluid phase is hydrostatic and is uniquely defined by its value at a single point in the upscaling cell (e.g. at the top or bottom). The capillary pressure can be reconstructed from the difference between the two pressures and it varies linearly in the cell. The values of the saturations and relative permeabilities can be then obtained at any point from the Darcy scale constitutive functions for the respective material.

Depending on the relation between the capillary and gravity forces, two limit cases of the vertical equilibrium can be distinguished. If the capillary forces dominate locally over the gravity forces, the capillary equilibrium conditions can be assumed, e.g. [20, 24]. In this case the capillary pressure is considered constant within the whole periodic cell, since the local variations of the phase pressures due to the gravity are negligible. The average large scale phase contents and saturations can be computed in a simple manner on the basis of the volumetric fraction of the materials. The equivalent permeability can be computed by solving a cell problem described in Sect. 5.3.3 independently for each phase, using the values of the phase permeability instead of the absolute permeability. In principle, any other approach for the absolute permeability upscaling can be used. As a result, one obtains a permeability tensor for each phase, corresponding to the specified value of the capillary pressure. Note that in general this tensor cannot be related to the equivalent absolute permeability tensor by a scalar relative permeability coefficient (except for the case where all materials in the cell are characterized by the same capillary and relative permeability functions and differ only in the values of the absolute permeability). The large-scale relative permeability function has to be defined separately for each component of

the permeability tensor. Local capillary equilibrium is sometimes assumed even for structured soils, e.g. [31] or fractured rocks, e.g. [75], although it is recognized that for large local contrasts in hydraulic permeability this assumption may be invalid, as discussed below.

The other limit case of the vertical equilibrium arises when the capillary pressure is neglected, e.g. [38]. The Darcy-scale distribution of the fluid phases results from gravitational segregation. The upper part of the cell is occupied by the less dense phase with the denser fluid at residual saturation in each of the porous material, while in the lower part of the cell the denser fluid is at maximum saturation and the less dense one—at residual saturation. For an arbitrary position of the interface between the two zones one can compute the corresponding average phase saturations and permeabilities.

Another case of local steady state flow is represented by the viscous limit, obtained by neglecting both capillary and gravity forces, e.g. [24]. The flow is purely advective and the saturation distribution is determined by the saturation values at the inlet boundary of the cell. A further simplifying assumption can be introduced, which states that the fractional flow function (defined by Eq. (2.58)) is constant at the inlet, and consequently in the whole upscaling cell. The small scale saturation distribution is then obtained by inverting the fractional flow function for a specific material. Upscaling procedures based on steady-state solutions for intermediate conditions between the capillary and viscous limits were also proposed [33, 102]

The validity of the steady state approximations can be considered in the framework of more rigorous upscaling methods, like periodic homogenization or the volume averaging method. When large-scale equations are derived by such methods, it becomes clear that the relationship between the characteristic times of flow in different material regions at the smaller and larger scale plays a fundamental role. The characteristic time can be defined as the time which is necessary for an initially equilibrated system to reach a new equilibrium state after a solicitation from a change in the boundary conditions. At the Darcy scale, the characteristic times for advective and diffusive processes are (e.g. [8]):

$$t_l^{\text{adv}} \approx \frac{l}{v_l}, \qquad t_l^{\text{dif}} \approx \frac{l^2}{D_l}, \tag{5.31}$$

where l is the dimension of REV (or periodic cell), v_l the characteristic velocity, D_l is the characteristic value of the diffusion coefficient. At the large scale the corresponding times are:

$$t_L^{\text{adv}} \approx \frac{L}{v_L}, \qquad t_L^{\text{dif}} \approx \frac{L^2}{D_L}, \tag{5.32}$$

where L is the dimension of the large-scale domain and is used as a subscript to denote the relevant large-scale parameters. As mentioned earlier, two-phase flow involves both advective processes, related to gravity and viscosity forces and diffusive processes, related to the capillary forces. Moreover, the velocity and diffusion

coefficient are not constant and may vary significantly during the same flow event, which makes the estimation of appropriate time scales difficult. It is clear, however, that the ratio of the characteristic time of flow in a single upscaling cell to the characteristic time for the whole large scale domain is influenced by two factors. The first one is the ratio of the cell dimension to the dimension of the field-scale domain, given by the scale separation parameter ε, as introduced in Eq. (5.1). The second one is the ratio of the values of the large-scale advection velocities and diffusion coefficients, to their small-scale counterparts, where the latter ones can differ considerably between the porous materials constituting the upscaling cell.

$$\frac{t_l^{\mathrm{adv}}}{t_L^{\mathrm{adv}}} \approx \frac{l\ v_L}{L\ v_l}\ , \qquad \frac{t_l^{\mathrm{dif}}}{t_L^{\mathrm{dif}}} \approx \frac{l^2\ D_L}{L^2\ D_l}\ , \tag{5.33}$$

In general, the local steady state approximations are valid if the time scales for local and global flow are well separated from each other, i.e. the above ratios are much smaller than unity. However, this condition is not sufficient, because even in this case the resulting large-scale model may have form different from the Darcy-scale model. In particular, this is true for dominating viscous forces, when the flow has advective character. As shown, for instance, by Durlofsky [30] and Neuweiler [68] in such a case the field-scale model for a heterogeneous medium contains an additional diffusive term. This is analogous to the problem of hydrodynamic dispersion, where a diffusive term arises during upscaling from the pore scale to the Darcy scale, to account for the local fluctuations of advective velocity, even if there is no diffusion at the pore scale, e.g. [76, 91].

On the other hand, even for diffusive capillary flow the local steady state assumption may not hold, if the separation of spatial scales is not satisfied or if there is a large contrast in the diffusivities of the components, implying large differences in the characteristic times for local scale flow. Consider the case when the spatial scales are well separated, $l \ll L$, but the medium consists of two materials with very different diffusivities $D_l^I \gg D_l^{II}$. If the highly permeable material forms a connected path through the large-scale domain, then it is reasonable to assume that the large scale characteristic diffusivity will be of the order of the diffusivity of the more permeable material. The resulting value of the large-scale characteristic time t_L^{dif} can be much smaller than the value of characteristic time necessary to reach equilibrium at the scale of an REV in the component material with very low diffusivity t_l^{dif}. In other words, the response of the macroscopic system will be observed before the local equilibrium conditions will be established in all upscaling cells. In the following section some models developed for such media are briefly presented, while the issue is elaborated in more detail in Chap. 6 in the framework of the homogenization method.

5.4.2 Local Non-Equilibrium Models

One possibility to deal with the upscaling problems when local steady state approximations do not hold, is to use transient flow simulation to estimate the large-scale constitutive functions for each upscaling cell, which are then used as input parameters to a large-scale equation of the same form as the Darcy-scale equation. The transient simulation is performed for the whole field-scale domain, which requires considerable numerical effort, or for a part of the domain with the boundary conditions chosen to approximate the considered large-scale flow [6]. At each time step of the transient simulation, the average values of the relevant physical quantities like phase pressures, saturations and fluxes can be computed, allowing to deduce large-scale capillary and permeability functions. Such approach is applied in petroleum reservoir modeling under the name of dynamic pseudo-functions, see e.g. [12, 27] for an overview of various methods from this group. Even though the use of pseudo-functions allows in many cases to obtain very good agreement between the field-scale solution and detailed Darcy-scale solution, considerable numerical effort is necessary to solve the transient problem in a heterogeneous domain. The resulting pseudo-functions are problem-specific (not intrinsic material properties), depend heavily on the chosen initial and boundary conditions, and may be physically inconsistent [12].

While the pseudo-function approach is used mainly in oil reservoir simulations with unstructured heterogeneity patterns, many local non-equilibrium models were developed specifically for fractured media or structured soils and can be extended for other types of binary structures with connected paths of highly permeable material in a weakly permeable background material (matrix). For a review of such models, see [40, 57, 64, 92]. These models are often based on double (dual) porosity concept, which assumes that the flow phenomena in two pore systems (i.e. in the network of fractures and in the microporous matrix) are regarded as distinct, albeit coupled processes, which have to be accounted for explicitly at the field scale. The relevant models can be conveniently classified with regard to the following criteria (Fig. 5.8):

1. Degree of refinement in the representation of flow in the matrix blocks
2. Connectivity of the matrix blocks

According to the first criterion, the simplest approach is to introduce at each point of the field scale domain two sets of physical variables, characterizing the average state of the fracture and matrix systems, as originally proposed by Barenblatt et al. [11]. Consequently, the number of field-scale equations is either two (in the case of saturated flow or Richards equation) or four (in the case of two-phase flow). A further distinction of the models from this group can be made with respect to the second criterion. If the matrix blocks are connected to each other and form continuous paths for flow, the governing large-scale equations for phase α can be written as:

$$w^I \frac{\partial}{\partial t}\left(\phi^I \rho_\alpha^I S_\alpha^I\right) - \nabla\left[\rho_\alpha^I \mathsf{k}_\alpha^{\mathrm{eff},I}\left(\nabla p_\alpha^I - \rho_\alpha^I \mathbf{g}\right)\right] + T_\alpha^{\mathrm{m}} = 0\,, \quad (5.34)$$

$$w^{II} \frac{\partial}{\partial t}\left(\phi^{II} \rho_\alpha^{II} S_\alpha^{II}\right) - \nabla\left[\rho_\alpha^{II} \mathsf{k}_\alpha^{\mathrm{eff},II}\left(\nabla p_\alpha^{II} - \rho_\alpha^{II} \mathbf{g}\right)\right] - T_\alpha^{\mathrm{m}} = 0\,, \quad (5.35)$$

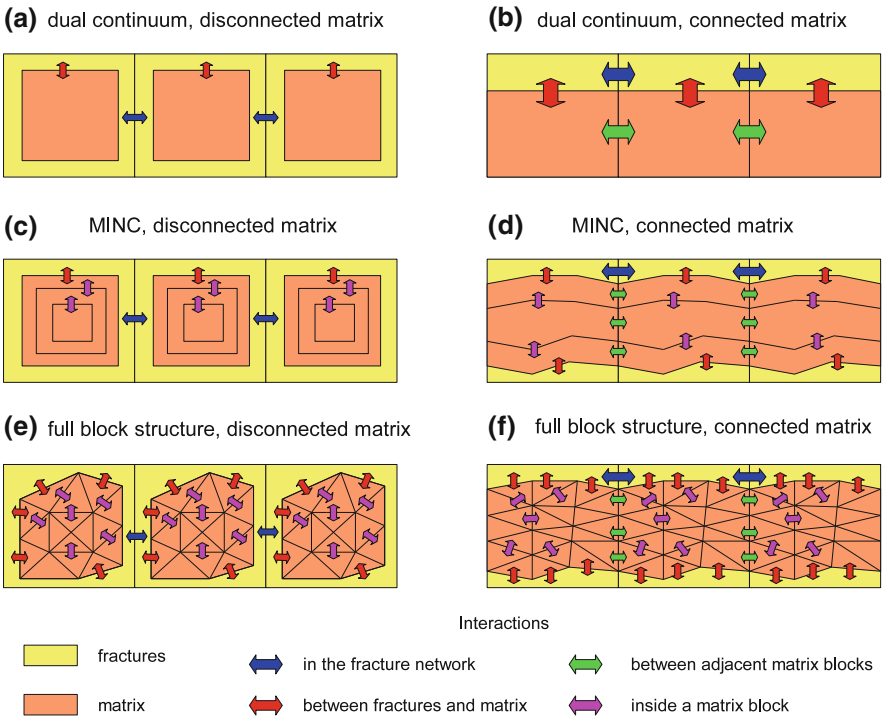

Fig. 5.8 Conceptual models of flow in dual porosity media

where the superscripts I and II refer to the fracture system and the rock matrix, respectively. Large-scale flow of fluid phase α can occur both in the fracture and matrix systems and there are two large-scale effective permeability tensors, denoted by $\mathsf{k}_\alpha^{\mathrm{eff},I}$ and $\mathsf{k}_\alpha^{\mathrm{eff},II}$. In transient conditions fluid transfer between fractures and matric may occur locally at any point of the macroscopic domain, due to the difference in the fluid potentials between the two regions. This is represented by the mass transfer term T_α^{m}, which has the dimension of mass per volume per time.

If the fracture network is dense and the rock matrix is divided into separate blocks, it can be assumed that the macroscopic flow is possible only via the fracture network, however it is affected by the fluid exchange with matrix blocks, acting as a source term. The governing equations for phase α simplify to [103]:

$$w^I \frac{\partial}{\partial t}\left(\phi^I \rho_\alpha^I S_\alpha^I\right) - \nabla\left[\rho_\alpha^I \mathsf{k}_\alpha^{\mathrm{eff},I}\left(\nabla p_\alpha^I - \rho_\alpha^I \mathbf{g}\right)\right] + T_\alpha^{\mathrm{m}} = 0\,, \tag{5.36}$$

$$w^{II} \frac{\partial}{\partial t}\left(\phi^{II} \rho_\alpha^{II} S_\alpha^{II}\right) - T_\alpha^{\mathrm{m}} = 0\,. \tag{5.37}$$

A further simplification can be introduced if one assumes that the fractures have negligible storage properties due to their very small volume fraction. Thus the flow

in fractures can be treated as stationary, which leads to the following formulation [10]:

$$-\nabla\left[\rho_\alpha^I\,\mathsf{k}_\alpha^{\mathrm{eff},I}\left(\nabla p_\alpha^I-\rho_\alpha^I\,\mathbf{g}\right)\right]+T_\alpha^{\mathrm{m}}=0\,, \tag{5.38}$$

$$w^{II}\frac{\partial}{\partial t}\left(\phi^{II}\,\rho_\alpha^{II}\,S_\alpha^{II}\right)-T_\alpha^{\mathrm{m}}=0\,. \tag{5.39}$$

Various authors use different naming conventions to distinguish between models with connected and disconnected matrix blocks. The first type (Eqs. (5.34)–(5.35)) is often termed dual (or double) permeability, while the second group (Eqs. (5.36)–(5.37))—dual (or double) porosity, e.g. [35, 92]. Since the latter name is also used to describe a broader class of models shown in Fig. 5.8, some authors use the names *dual-porosity dual-permeability* and *dual-porosity single-permeability*, e.g. [58], or *dual continuum connected matrix models* and *dual continuum disconnected matrix* [64] for the respective groups of models.

The models described above can be easily adapted to the case of incompressible unsaturated flow, described by the Richards equation. For instance, the well-known dual-permeability model proposed by Gerke and van Genuchten [41] can be written as follows:

$$w^I\frac{\partial}{\partial t}\left(\phi^I\,S_w^I\right)-\nabla\left[\mathsf{k}_w^{\mathrm{eff},I}\left(\nabla p_{\mathrm{w}}^I-\rho_{\mathrm{w}}^I\,\mathbf{g}\right)\right]+T_{\mathrm{w}}^{\mathrm{v}}=0\,, \tag{5.40}$$

$$w^{II}\frac{\partial}{\partial t}\left(\phi^{II}\,S_w^{II}\right)-\nabla\left[\mathsf{k}_w^{\mathrm{eff},II}\left(\nabla p_{\mathrm{w}}^{II}-\rho_{\mathrm{w}}^{II}\,\mathbf{g}\right)\right]-T_{\mathrm{w}}^{\mathrm{v}}=0\,, \tag{5.41}$$

where $T_{\mathrm{w}}^{\mathrm{v}}$ is the term describing volumetric water transfer between fractures and matrix (or rather, in this case, macropore and micropore domains). It has the dimension of inverse time (volume per volume per time). The above model is often applied for quasi one-dimensional field-scale flow, for which the following simplifying assumption is made [41]:

$$k_{\mathrm{w}}^{\mathrm{eff},I}=w^I\,k_{\mathrm{w}}^I(S_{\mathrm{w}}^I)\,, \tag{5.42}$$

$$k_{\mathrm{w}}^{\mathrm{eff},II}=w^{II}\,k_{\mathrm{w}}^{II}(S_{\mathrm{w}}^{II})\,. \tag{5.43}$$

However, this is strictly true only if the fractures are parallel to the field-scale flow direction.

Appropriate definition of the fracture-matrix transfer term was a subject of numerous studies, e.g. [32, 42, 43, 74, 119–121]. Difficulties associated with this task can be illustrated by considering flow in a simple periodic cell consisting of a matrix block surrounded by fractures, Fig. 5.9. In view of the discussion in the previous section, it is clear that if the fluid in the cell is subjected to an external excitation, the potential in fractures will equilibrate at much faster rate than in the matrix block and can be regarded as uniform within the cell. Due to the continuity condition, the potential in the matrix block will be equal to the potential in the fracture at the outer surface of the block, but it will vary strongly inside the block. The intensity of

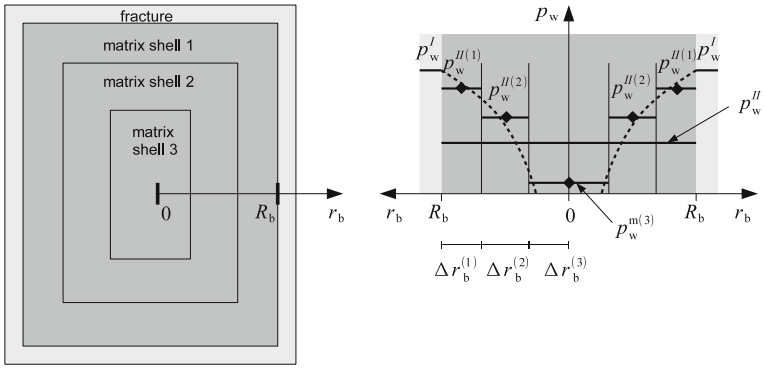

Fig. 5.9 Representation of the water pressure in a single matrix block according to different models: *dotted line*—real distribution, *solid line*—dual continuum approximation, lines with points—MINC approximation

fracture-matrix transfer is determined by the local gradient of the fluid potential in the vicinity of the surface of the block. However, it is difficult to relate the transfer intensity to the average value of the block potential. An often used approximation is the so-called first order transfer term, which relates the transfer intensity to the difference between the average fluid potentials in the two regions. For the case of incompressible unsaturated water flow, Gerke and van Genuchten [42] proposed an expression which can be rewritten as follows:

$$T_w^v = \frac{\beta^{fm}\,\gamma^{fm}}{R_b^2}\,\frac{k_w^{fm}}{\mu_w}\left(p_w^I - p_w^{II}\right)\,, \tag{5.44}$$

where β^{fm} is a dimensionless coefficient depending on the shape of the matrix block, γ^{fm} is a dimensionless scaling factor, R_b is the characteristic dimension of the block, representing the shortest distance from the centre of the block to the fracture (Fig. 5.9) and k_w^{fm} is the average permeability for fracture–matrix transfer. In the absence of mineral coating, which could potentially alter the interface permeability, the estimation of k_w^{fm} is based on the matrix block parameters:

$$k_w^{fm} = k_{sw}^{II}\,\frac{1}{2}\left[k_{rw}^{II}(p_w^I) + k_{rw}^{II}(p_w^{II})\right]\,. \tag{5.45}$$

The relative permeability function is computed for the value of the water pressure at the interface (assumed to be equal to the pressure in the fracture system, p_w^I, and for the average pressure in the matrix block, p_w^{II}, and an arithmetic average of those two values is taken. For the case of compressible liquid, an average value of the density should be defined, in addition to the average value of the relative permeability.

The first-order formula is appropriate for later stages of flow in the block, when the difference between p_w^I and p_w^{II} is relatively small. It is inaccurate during early

stages of flow, where large gradients develop close to the outer surface of the block. An improved second-order approximation was proposed by Zimmerman et al [121] and further modified by Köhne et al [56]. It can be written as follows:

$$T_{\mathrm{w}}^{\mathrm{v}} = \frac{\beta^{\mathrm{fm}}}{2\,R_{\mathrm{b}}^2}\,\frac{k_{\mathrm{w}}^{\mathrm{fm}}}{\mu_{\mathrm{w}}}\,\frac{\left(p_{\mathrm{w}}^{f} - p_{\mathrm{w}}^{II}\right)\left[\left|p_{\mathrm{w}}^{II} - p_{\mathrm{w}}^{\mathrm{init}}\right| + \left|p_{\mathrm{w}}^{I} - p_{\mathrm{w}}^{\mathrm{init}}\right|\right]}{\left(p_{\mathrm{w}}^{II} - p_{\mathrm{w}}^{\mathrm{init}}\right)}\,, \tag{5.46}$$

where $p_{\mathrm{w}}^{\mathrm{init}}$ is the initial pressure in the system (assumed to be equal in the fractures and matrix). In the original paper [121] the average permeability was equal to the matrix permeability at the interface, i.e. it was computed using the values of the water pressure and capillary pressure from the fracture system:

$$k_{\mathrm{w}}^{\mathrm{fm}} = k_{\mathrm{sw}}^{II}\,k_{\mathrm{rw}}^{II}(p_{\mathrm{w}}^{I})\,. \tag{5.47}$$

However, such approximation was shown to be inaccurate for some block shapes and porous materials [56, 62, 97]. Köhne et al. [56] obtained good results for the average permeability defined as:

$$k_{\mathrm{w}}^{\mathrm{fm}} = k_{\mathrm{sw}}^{II}\,\frac{\omega_{\mathrm{k}}\;k_{\mathrm{rw}}(p_{\mathrm{w}}^{II}) + k_{\mathrm{rw}}(p_{\mathrm{w}}^{I})}{\omega_{\mathrm{k}} + 1}\,, \tag{5.48}$$

where the value of the weighting coefficient ω_{k} depends on the texture of the porous material forming the blocks. An average value $\omega_{\mathrm{k}} = 17$ was suggested for fine textured soils [56].

A more detailed description of the local flow in the matrix blocks is offered by the second group of dual-porosity models, which include the Multiple Interacting Continua (MINC) model [80] and its subsequent modifications, e.g. [34, 54, 122]. In this approach it is assumed that the flow parameters in matrix blocks vary principally in function of the distance to the nearest fracture, as shown in Fig. 5.9. Each block is divided into several concentric shells, based on the distance to the surrounding fractures, Figs. 5.8c and 5.9. Thus, each point of the large scale domain is associated with a single set of variables characterizing the fracture system and several of sets of variables characterizing the state of each shell of the matrix block. The large scale equation for the fracture system contains a source term, describing interaction with the outermost shell of the matrix block:

$$w^{I}\,\frac{\partial}{\partial t}\left(\phi^{I}\,\rho_{\alpha}^{I}\,S_{\alpha}^{I}\right) - \nabla\left[\rho_{\alpha}^{I}\,\mathsf{k}_{\alpha}^{\mathrm{eff},I}\,\left(\nabla p_{\alpha}^{I} - \rho_{\alpha}^{I}\,\mathbf{g}\right)\right] + T_{\alpha}^{\mathrm{m}} = 0\,. \tag{5.49}$$

In this case, the mass transfer term can be written as:

$$T_{\alpha}^{\mathrm{m}} = w^{II}\,\frac{|\Lambda_{\mathrm{b}}|}{|V_{\mathrm{b}}|}\,\frac{k_{\alpha}^{\mathrm{fm}}}{\mu_{\alpha}}\,\frac{p_{\alpha}^{I} - p_{\alpha}^{II\,(1)}}{\Delta r_{\mathrm{b}}^{(1)}/2}\,, \tag{5.50}$$

where $|\Lambda_\mathrm{b}|$ and $|V_\mathrm{b}|$ denote, respectively, the area of the outer surface and the volume of a single matrix block and $\Delta r_\mathrm{b}^{(1)}$ is the thickness of the outermost shell of the matrix block, Fig. 5.9. In the standard MINC formulation the matrix blocks are separated from each other. Therefore the equation for each matrix shell i can be written as:

$$w^{II}\frac{|V^{\mathrm{b}(i)}|}{|V_\mathrm{b}|}\frac{\partial}{\partial t}\left(\phi^{II\,(i)}\,\rho_\alpha^{II\,(i)}\,S_\alpha^{II\,(i)}\right) - Q^{\mathrm{b}(i-1/2)} + Q^{\mathrm{b}(i+1/2)} = 0\,, \tag{5.51}$$

where the mass flux between adjacent matrix shells i and $i+1$ is described as:

$$Q^{\mathrm{b}(i+1/2)} = w^{II}\,\frac{|\Lambda^{(i+1/2)}|}{|V_\mathrm{b}|}\,\frac{k_{\mathrm{r}\alpha}^{II\,(i+1/2)}}{\mu_\alpha}\,\frac{p_\alpha^{II\,(i+1)} - p_\alpha^{II\,(i)}}{(\Delta r_\mathrm{b}^{(i)} + \Delta r_\mathrm{b}^{(i+1)})/2}\,. \tag{5.52}$$

In the above formulae, $|\Lambda^{(i+1/2)}|$ is the area of the interface between the neighboring shells, $|V^{\mathrm{b}(i)}|$ is the volume of ith shell and $\Delta r_\mathrm{b}^{(i)}$ is thickness of ith shell.

The MINC method is equivalent to solving one-dimensional flow equation in the representative matrix block to obtain a more accurate estimation of the fracture-matrix fluid flux. By introducing the concept of nested shells, the flow can be represented as a quasi radial process with respect to the coordinate r_b. At the outer surface of the matrix block, the fluid pressure is equal to the pressure in the fracture, while at the center of the block symmetry (i.e. no-flow) condition applies. The average permeabilities k_α^{fm} and $k_{\mathrm{r}\alpha}^{II\,(i+1/2)}$ can be computed using various approaches suitable for one dimensional flow, like the upstream weighting or arithmetic averaging. The accuracy of the MINC approximation increases with the number of shells. If only one shell is used per matrix block, MINC reduces to the dual continuum–disconnected matrix model with first order transfer term, described earlier.

In principle, it is possible to extend the MINC approach by introducing connectivity between the shells of the adjacent matrix blocks, Fig. 5.8d. Depending on the structure of the medium, the connectivity could be applied to all shells or only to the outermost of them. However, such approach is only rarely used.

The original MINC formulation did not specify the method to obtain the large-scale permeability for the fracture system. This question was addressed in an extended method developed by Karimi-Fard et al. [54]. The authors proposed to compute the effective permeability of the medium from the solution of steady state cell problem with confined boundary conditions. The approach is oriented towards irregular fracture patterns, for which it is hard to define a representative shape of the matrix block. The subdivision of the matrix domain is based on the results of the solution of another cell problem, representing single-phase flow from fractures to matrix. The boundaries between matrix shells are defined by selected isolines of the fluid pressure inside the matrix domain. This method was applied by Tatomir et al. [98] to simulate two-phase flow in a large-scale realistic fracture field from Bristol geological formation.

The third group of double porosity models represents the highest level of refinement with respect to the flow in matrix blocks. Models of this type were obtained by

several authors using the method of periodic homogenization, mostly focusing on the conceptually simpler case of disconnected matrix blocks [4, 5, 48, 60]. The resulting model consists of a single large-scale equation for the flow in the fractures, which contains an integral source term, describing the fracture-matrix transfer. The evaluation of the transfer term requires that a three-dimensional flow equation is solved for a representative matrix block at each point of the large-scale domain, Fig. 5.8e. In the next chapter a similar model obtained for unsaturated flow in a medium with disconnected inclusions [60] will be discussed in more detail. The homogenization approach has been extended to account for the possible connections between the matrix blocks for the case of single phase flow, with fluid density as the primary variable [23, 29]. The resulting model has a complex form, consisting of two large-scale equations for flow in the fracture and matrix systems, respectively, and an additional three-dimensional local-scale equation, describing time-dependent behavior of the local deviation of the density in the matrix blocks, which must be solved for each time step in each point of the macroscopic domain. The corresponding conceptual representations of the fractured medium with disconnected and connected matrix blocks are shown in Fig. 5.8f. In contrast to the standard dual continuum and MINC models, the homogenization approach provides a method to compute large-scale permeability of heterogeneous medium for an arbitrary local geometry.

References

1. Ahmadi A, Quintard M (1996) Large-scale properties for two-phase flow in random porous media. J Hydrol 183(1–2):69–99. doi:10.1016/S0022-1694(96)80035-7
2. Amaziane B, Koebbe J (2006) JHomogenizer: a computational tool for upscaling permeability for flow in heterogeneous porous media. Comput Geosci 10(4):343–359. doi:10.1007/s10596-006-9028-4
3. Amaziane B, Bourgeat A, Koebbe J (1991) Numerical simulation and homogenization of two-phase flow in heterogeneous porous media. Transp Porous Media 6(5–6):519–547. doi:10.1007/BF00137848
4. Arbogast T (1993) Gravitational forces in dual-porosity systems: I. Model derivation by homogenization. Transp Porous Media 13(2):197–203. doi:10.1007/BF00654409
5. Arbogast T, Douglas J, Hornung U (1990) Derivation of the double porosity model of single phase flow via homogenization theory. SIAM J Math Anal 21:823–836
6. Artus V, Nœtinger B (2004) Up-scaling two-phase flow in heterogeneous reservoirs: current trends. Oil Gas Sci Technol 59(2):185–195. doi:10.2516/ogst:2004014
7. Auriault JL (2011) Heterogeneous periodic and random media. Are the equivalent macroscopic descriptions similar? Int J Eng Sci 49(8):806–808. doi:10.1016/j.ijengsci.2011.01.005
8. Auriault JL, Boutin C, Geindreau C (2009) Homogenization of coupled phenomena in heterogeneous media. Wiley, Hoboken
9. Bakker M, Nieber J (2004) Analytic element modeling of cylindrical drains and cylindrical inhomogeneities in steady two-dimensional unsaturated flow. Vadose Zone J 3(3):1038–1049. doi:10.2136/vzj2004.1038
10. Barenblatt G (1963) On some boundary-value problems for the equation of filtration of fluid in fissurized rocks. J Appl Math Mech (PMM) 27(2):513–518
11. Barenblatt G, Zheltov I, Kochina I (1960) Basic concepts in the theory of seepage of homogeneous liquids in fissurized rocks. J Appl Math Mech (PMM) 24(5):1286–1303

12. Barker J, Thibeau S (1997) A critical review of the use of pseudo relative permeabilities for upscaling. SPE Reservoir Eng 12(2):138–143. doi:10.2118/35491-PA
13. Barnes R, Janković I (1999) Two-dimensional flow through large numbers of circular inhomogeneities. J Hydrol 226(3–4):204–210. doi:10.1016/S0022-1694(99)00142-0
14. Bear J, Tsang CF, de Marsily G (eds) (1993) Flow and contaminant transport in fractured rock. Academic Press, San Diego
15. Bensoussan A, Lions JL, Papanicolaou G (1978) Asymptotic analysis for periodic structures. North-Holland, Amsterdam
16. Berkowitz B (2002) Characterizing flow and transport in fractured geological media: A review. Adv Water Resour 25(8–12):861–884. doi:10.1016/S0309-1708(02)00042-8
17. Bielski W, Telega J (1997) Effective properties of geomaterials: rocks and porous media. Publ Inst Geophys Pol Acad Sci A-26(285):1–120
18. Bierkens M, Finke P, de Willigen P (eds) (2000) Upscaling and downscaling methods for environmental research. Kluwer, Dordrecht
19. Bøe Ø (1994) Analysis of an upscaling method based on conservation of dissipation. Transp Porous Media 17(1):77–86. doi:10.1007/BF00624051
20. Braun C, Helmig R, Manthey S (2005) Macro-scale effective constitutive relationships for two phase flow processes in heterogeneous porous media with emphasis on the relative permeability-saturation relationship. J Contam Hydrol 76(1–2):47–85. doi:10.1016/j.jconhyd.2004.07.009
21. Cardwell W, Parsons R (1945) Average permeabilities of heterogeneous oil sands. Trans Am Inst Mining Eng 160:34–42
22. Chen Y, Durlofsky L, Gerritsen M, Wen XH (2003) A coupled local global upscaling approach for simulating flow in highly heterogeneous formations. Ad Water Resour 26(10):1041–1060. doi:10.1016/S0309-1708(03)00101-5
23. Choquet C (2009) Homogenized model for flow in partially fractured media. Electron J Differ Equ 2009:1–27
24. Christie M (2001) Flow in porous media - scale up of multiphase flow. Curr Opin Colloid Interface Sci 6(3):236–241. doi:10.1016/S1359-0294(01)00087-5
25. Cushman J, Bennethum L, Hu B (2002) A primer on upscaling tools for porous media. Adv Water Resour 25(8–12):1043–1067. doi:10.1016/S0309-1708(02)00047-7
26. Dagan G (1989) Flow and transport in porous formations. Springer, New York
27. Darman N, Pickup G, Sorbie K (2002) A comparison of two-phase dynamic upscaling methods based on fluid potentials. Comput Geosci 6(1):5–27. doi:10.1023/A:1016572911992
28. Dietrich P, Helmig R, Sauter M, Hötzl H, Köngeter J, Teutsch G (eds) (2005) Flow and transport in fractured porous media. Springer, Berlin
29. Douglas J, Peszyńska M, Showalter R (1997) Single phase flow in partially fissured media. Transp Porous Media 28(3):285–306. doi:10.1023/A:1006562120265
30. Durlofsky L (1998) Coarse scale models of two phase flow in heterogeneous reservoirs: volume averaged equations and their relationship to existing upscaling techniques. Comput Geosci 2(2):73–92. doi:10.1023/A:1011593901771
31. Durner W (1994) Hydraulic conductivity estimation for soils with heterogeneous pore system. Water Resour Res 30(2):211–233. doi:10.1029/93WR02676
32. Dykhuizen R (1990) A new coupling term for dual-porosity models. Water Resour Res 26(2):351–356. doi:10.1029/WR026i002p00351
33. Ekrann S, Aasen J (2000) Steady-state upscaling. Transp Porous Media 41(3):245–262. doi:10.1023/A:1006765424927
34. Famy C, Bourbiaux B (2005) Accurate modeling of matrix-fracture transfers in dual-porosity models: optimal subgridding of matrix blocks. In: SPE Reservoir Simulation Symposium, 31 January-2 Feburary 2005. The Woodlands, Texas. doi:10.2118/93115-MS
35. Flint A, Flint L, Bodvarsson G, Kwicklis E, Fabryka-Martin J (2001) Evolution of the conceptual model of unsaturated zone hydrology at Yucca Mountain. Nevada. J Hydrol 247(1–2):1–30. doi:10.1016/S0022-1694(01)00358-4

36. Fokker P (2001) General anisotropic effective medium theory for the effective permeability of heterogeneous reservoirs. Transp Porous Media 44(2):205–218. doi:10.1023/A:1010770623874
37. Furman A, Warrick A (2005) Unsaturated flow through spherical inclusions with contrasting sorptive numbers. Vadose Zone J 4(2):255–263. doi:10.2136/vzj2004.0076
38. Gasda S, Nordbotten J, Celia M (2009) Vertical equilibrium with sub-scale analytical methods for geological co-2 sequestration. Comput Geosci 13(4):469–481. doi:10.1007/s10596-009-9138-x
39. Gelhar L (1993) Stochastic subsurface hydrology. Prentice Hall, Engelwood Cliffs, New Jersey
40. Gerke H (2006) Preferential flow descriptions for structured soils. J Plant Nutr Soil Sci 169:382–400
41. Gerke H, van Genuchten M (1993) A dual-porosity model for simulating the preferential movement of water and solutes in structured porous media. Water Resour Res 29(2):305–319. doi:10.1029/92WR02339
42. Gerke H, van Genuchten M (1993) Evaluation of a first-order water transfer term for variably saturated dual-porosity flow models. Water Resour Res 29(4):1225–1238. doi:10.1029/92WR02467
43. Gerke H, van Genuchten M (1996) Macroscopic representation of structural geometry for simulating water and solute movement in dual-porosity media. Adv Water Resour 19(6):343–357. doi:10.1016/0309-1708(96)00012-7
44. Guéguen Y, Le Ravalec M, Ricard L (2006) Upscaling: effective medium theory, numerical methods and the fractal dream. Pure Appl Geophys 163:1175–1192. doi:10.1007/s00024-006-0053-y
45. Harter T, Hopmans J (2004) Role of vadose-zone flow processes in regional-scale hydrology: review, opportunities and challenges. In: Unsaturated zone modelling: progress, challenges and applications, Kluwer, Dordrecht.
46. Harter T, Knudby C (2004) Effective conductivity of periodic media with cuboid inclusions. Adv Water Resour 27(10):1017–1032. doi:10.1016/j.advwatres.2004.07.004
47. Hashin Z, Shtrikman S (1962) A variational approach to the theory of effective magnetic permeability of multiphase materials. J Appl Phys 33:3125–3131
48. Hornung U (1991) Homogenization of miscible displacement in unsaturated aggregated soils. In: Dal Masse G and Dell'Antonio GF (ed) Composite media and homogenization theory, Birkhäuser, Boston, pp 143–153
49. Indelman P, Dagan G (1993) Upscaling of heterogeneous formations: General approach and application to isotropic media. Transp Porous Media 12(2):161–184. doi:10.1007/BF00616978
50. Janković I, Barnes R (1999) Three-dimensional flow through large numbers of spheroidal inhomogeneities. J Hydrol 226(3–4):224–233. doi:10.1016/S0022-1694(99)00141-9
51. Jarvis N (1994) The MACRO model (version 3.1). Technical description and sample simulation. Reports and Dissertations 19. Department of Soil Science, Swedish University of Agricultural Science, Uppsala
52. Jones S, Friedman S (2000) Particle shape effects on the effective permittivity of anisotropic or isotropic media consisting of aligned or randomly oriented ellipsoidal particles. Water Resour Res 36(10):2821–2833. doi:10.1029/2000WR900198
53. Journel A, Deutsch C, Desbarats A (1986) Power averaging for block effective permeability. In: SPE California Regional Meeting, 2–4, April 1986, Oakland, California. doi:10.2118/15128-MS
54. Karimi-Fard M, Gong B, Durlofsky L (2006) Generation of coarse-scale continuum flow models from detailed fracture characterizations. Water Resour Res 42:W10423. doi:10.1029/2006WR005015
55. Knudby C, Carrera J, Bumgardner J, Fogg G (2006) Binary upscaling - the role of connectivity and a new formula. Adv Water Resour 29(4):590–604. doi:10.1016/j.advwatres.2005.07.002

56. Köhne J, Mohanty B, Simunek J, Gerke H (2004) Numerical evaluation of a second-order water transfer term for variably saturated dual-permeability models. Water Resour Res 40:W07409. doi:10.1029/2004WR003285
57. Köhne J, Köhne S, Šimunek J (2009) A review of model applications for structured soils: (a) Water flow and tracer transport. J Contam Hydrol 104(1–4):4–35. doi:10.1016/j.jconhyd.2008.10.002
58. Lemonnier P, Bourbiaux B (2010) Simulation of naturally fractured reservoirs. State of the art. Part 1 Physical mechanisms and simulator formulation. Oil Gas Sci Technol 65(2):239–262. doi:10.2516/ogst/2009066
59. Lewandowska J, Laurent JP (2001) Homogenization modeling and parametric study of moisture transfer in an unsaturated heterogeneous porous medium. Transp Porous Media 45(3):321–345. doi:10.1023/A:1012450327408
60. Lewandowska J, Szymkiewicz A, Burzyński K, Vauclin M (2004) Modeling of unsaturated water flow in double-porosity soils by the homogenization approach. Adv Water Resour 27(3):283–296. doi:10.1016/j.advwatres.2003.12.004
61. Lewandowska J, Szymkiewicz A, Boutin C (2005) Modelling of unsaturated conductivity of double-porosity soils. In: Actes de 17ème Congrès Francais de Mécanique, Troyes
62. Lewandowska J, Szymkiewicz A, Vauclin M (2005) Study of the exchange term in the non-equilibrium water flow model for double-porosity soils. In: Abousleiman Y et al. (ed) Poro-mechanics III, Taylor and Francis, pp 365–370
63. Li D, Beckner B, Kumar A (2001) A new efficient averaging technique for scaleup of multimillion-cell geologic models. SPE Reservoir Eval Eng 4(4):297–307. doi:10.2118/72599-PA
64. Lichtner P (2000) Critique of dual continuum formulations of multicomponent reactive transport in fractured porous media. Technical Report, National Laboratory, Los Alamos
65. Lux J (2010) A non-periodic closure scheme for the determination of effective diffusivity in real porous media. Trans Porous Media 82(2):299–315. doi:10.1007/s11242-009-9423-0
66. Manthey S, Hassanizadeh M, Helmig R (2005) Macro-scale dynamic effects in homogeneous and heterogeneous porous media. Transp Porous Media 58(1–2):121–145. doi:10.1007/s11242-004-5472-6
67. Milton G (2002) The theory of composites. Cambridge University Press, Cambridge
68. Neuweiler I (2006) Scale dependence of flow and transport parameters in porous media. University of Stuttgart, Stuttgart
69. Neuweiler I, Cirpka O (2005) Homogenization of Richards equation in permeability fields with different connectivities. Water Resour Res 41:W02009. doi:10.1029/2004WR003329
70. Neuweiler I, Vogel HJ (2007) Upscaling for unsaturated flow for non-Gaussian heterogeneous porous media. Water Resour Res 43:W03443. doi:10.1029/2005WR004771
71. Nœtinger B, Zargar G (2004) Multiscale description and upscaling of fluid flow in subsurface reservoirs. Oil Gas Sci Technol 59(2):119–139. doi:10.2516/ogst:2004010
72. Nœtinger B, Artus V, Zargar G (2005) The future of stochastic and upscaling methods in hydrogeology. Hydrogeol J 13:184–201
73. Novák V, Knava K, Šimunek J (2011) Determining the influence of stones on hydraulic conductivity of saturated soils using numerical method. Geoderma 161:177–181. doi:10.1016/j.geoderma.2010.12.016
74. Penuela G, Hughes R, Civan F, Wiggins M (2002) Time-dependent shape factors for secondary recovery in naturally fractured reservoirs. In: SPE/DOE Improved Oil Recovery Symposium, 13–17, April 2002. Tulsa, Oklahoma. doi:10.2118/75234-MS
75. Peters R, Klavetter E (1988) A continuum model for water movement in an unsaturated fractured rock mass. Water Resour Res 24(3):416–430. doi:10.1029/WR024i003p00416
76. Pinder G, Gray W (2008) Essentials of multiphase flow and transport in porous media. Wiley, Hoboken
77. Poley A (1988) Effective permeability and dispersion in locally heterogeneous aquifers. Water Resour Res 24(11):1921–1926. doi:10.1029/WR024i011p01921

78. Pozdniakov S, Tsang CF (2004) A self-consistent approach for calculating the effective hydraulic conductivity of a binary, heterogeneous medium. Water Resour Res 40:W05105. doi:10.1029/2003WR002617
79. Pruess K (2004) A composite medium approximation for unsaturated flow in layered sediments. J Contam Hydrol 70(3–4):225–247. doi:10.1016/j.jconhyd.2003.09.007
80. Pruess K, Narasimhan T (1985) A practical method for modelling fluid and heat flow in fractured porous media. Soc Pet Eng J 25(1):14–26. doi:10.2118/10509-PA
81. Quintard M, Whitaker S (1988) Two-phase flow in heterogeneous porous media: The method of large scale averaging. Transp Porous Media 3(4):357–413. doi:10.1007/BF00233177
82. Radcliffe D, Šimunek J (2010) Soil physics with Hydrus. Modeling and applications. CRC Press, Boca Raton, Florida
83. Reichenberger V, Helmig R, Jakobs H, Bastian P, Niessner J (2004) Complex gas-water processes in discrete fracture-matrix system: up-scaling, mass conservative solution and efficient multilevel solution. Institut für Wasserbau, Universität Stuttgart, Stuttgart
84. Renard P, de Marsily G (1997) Calculating equivalent permeability: a review. Adv Water Resour 20(5–6):253–278. doi:10.1016/S0309-1708(96)00050-4
85. Ross P, Smettem K (2000) A simple treatment of physical nonequilibrium water flow in soils. Soil Sci Soc Am J 64(6):1926–1930. doi:10.2136/sssaj2000.6461926x
86. Rucker D, Warrick A, Ferré T (2005) Parameter equivalence for the Gardner and van Genuchten soil hydraulic conductivity functions for steady vertical flow with inclusions. Adv Water Resour 28(7):689–699. doi:10.1016/j.advwatres.2005.01.004
87. Saez A, Otero C, Rusinek I (1989) The effective homogeneous behavior of heterogeneous porous media. Transp Porous Media 4(3):213–238. doi:10.1007/BF00138037
88. Sanchez-Palencia E (1980) Non-homogeneous media and vibration theory, Lecture Notes in Physics, vol 127, Springer, Berlin
89. Sanchez-Villa X, Guadagnini A, Carrera J (2006) Representative hydraulic conductivities in saturated groundwater flow. Rev Geophys 44(3):RG3002. DOI:10.1029/2005RG000169
90. Schaetzl R, Anderson S (2005) Soils - genesis and geomorphology. Cambridge University Press, Cambridge
91. Scheidegger A (1957) The physics of flow through porous media. University of Toronto Press, Toronto
92. Šimunek J, Jarvis N, van Genuchten M, Gärdenäs A (2003) Review and comparison of models for describing non-equilibrium and preferential flow and transport in the vadose zone. J Hydrol 272(1–4):14–35. doi:10.1016/S0022-1694(02)00252-4
93. Stephen K, Pickup G, Sorbie K (2001) The local analysis of changing force balances in immiscible incompressible two-phase flow. Transp Porous Media 45(1):63–88. doi:10.1023/A:1011850618324
94. Sviercoski R (2010) An analytical effective tensor and its approximation properties for upscaling flows through generalized composites. Adv Water Resour 33(7):728–739. doi:10.1016/j.advwatres.2010.03.011
95. Sviercoski R, Warrick A, Winter C (2009) Two-scale analytical homogenization of Richards equation for flows through block inclusions. Water Resour Res 45:W05403. doi:10.1029/2006WR005598
96. Szymkiewicz A (2005) Calculating effective conductivity of heterogeneous soils by homogenization. Arch Hydro Eng Environ Mech 52(2):111–130
97. Szymkiewicz A (2008) Modelowanie przeplywu wody w utworach o podwójnej porowatosci (Modeling water flow in double porosity geological formations). Biuletyn Państwowego Instytutu Geologicznego 431:251–258
98. Tatomir A, Szymkiewicz A, Class H, Helmig R (2011) Modeling two phase flow in large scale fractured porous media with an extended multiple interacting continua method. Comput Model Eng Sci 77(2):81–112
99. Torquato S (2002) Random heterogeneous materials: microstructure and macroscopic properties. Springer, New York

100. Trykozko A, Zijl W, Bossavit A (2001) Nodal and mixed finite elements for the numerical homogenization of 3D permeability. Comput Geosci 5(1):61–84. doi:10.1023/A:1011621529611
101. Vereecken H, Kasteel R, Vanderborght J, Harter T (2007) Upscaling hydraulic properties and soil water flow processes in heterogeneous soils: a review. Vadose Zone J 6(1):1–28. doi:10.2136/vzj2006.0055
102. Virnovsky G, Friis H, Lohne A (2004) A steady-state upscaling approach for immiscible two-phase flow. Transp Porous Media 54(2):167–192. doi:10.1023/A:1026363132351
103. Warren J, Root P (1963) The behavior of naturally fractured reservoirs. Soc Pet Eng J 3(3):245–255. doi:10.2118/426-PA
104. Warrick A, Knight J (2002) Two-dimensional unsaturated flow through a circular inclusion. Water Resour Res 38(7):1113. doi:10.1029/2001WR001041
105. Warrick A, Knight J (2004) Unsaturated flow through a spherical inclusion. Water Resour Res 40:W05101. doi:10.1029/2003WR002890
106. Wen XH, Gómez-Hernández J (1996) Upscaling hydraulic conductivities in heterogeneous media: An overview. J Hydrol 183(1–2):ix–xxxii, doi:10.1016/S0022-1694(96)80030-8
107. Wen XH, Durlofsky L, Edwards M (2003) Use of border regions for improved permeability upscaling. Math Geol 35(5):521–547
108. Whitaker S (1999) The method of volume averaging. Kluwer, Dordrecht
109. White C, Horne R (1987) Computing absolute transmissibility in the presence of fine-scale heterogeneity. In: SPE Symposium on Reservoir Simulation, 1–4, February 1987. San Antonio, Texas. doi:10.2118/16011-MS
110. Wiener O (1912) Die Theorie des Mischkörpers für das Feld der Stationären Strömung: I. Die Mittelwertsatze für Kraft, Polarisation und Energie. Die Abhandlungen der Mathematisch-Physischen Klasse der Königlichen Sachsischen Gesellschaft der Wissenschaften 32:509–604
111. Wood B (2000) Review of upscaling methods for describing unsaturated flow. Technical Report, Pacific Northwest, National Laboratory
112. Wu X, Efendiev Y, Hou T (2002) Analysis of upscaling absolute permeability. Discrete Continuous Dyn Syst Ser B 2(2):185–204
113. Wu YS (2002) Numerical simulation of single-phase and multiphase non-Darcy flow in porous and fractured reservoirs. Transp Porous Media 49(2):209–240. doi:10.1023/A:1016018020180
114. Zhang D (2002) Stochastic methods for flow in porous media: coping with uncertainties. Academic Press, San Diego
115. Zhu J (2012) Effect of layered structure on anisotropy of unsaturated soils. Soil Sci 177(2):139146, DOI:10.1097/SS.0b013e31824114f6
116. Zijl W, Nawalany M (1993) Natural groundwater flow. Lewis, Boca Raton, Florida
117. Zijl W, Trykozko A (2001) Numerical homogenization of the absolute permeability using the conformal-nodal and mixed-hybrid finite element method. Transp Porous Media 44(1):33–62. doi:10.1023/A:1010776124186
118. Zimmerman R (1996) Effective conductivity of a two-dimensional medium containing elliptical inhomogeneities. Proc Royal Soc A 452:1713–1727
119. Zimmerman R, Bodvarsson G, Kwicklis E (1990) Absorption of water into porous blocks of various shapes and sizes. Water Resour Res 26(11):2797–2806. doi:10.1029/WR026i011p02797
120. Zimmerman R, Chen G, Hadgu T, Bodvarsson G (1993) A numerical dual-porosity model with semianalytical treatment of fracture/matrix flow. Water Resour Res 29(7):2127–2137. doi:10.1029/93WR00749
121. Zimmerman R, Hadgu T, Bodvarsson G (1996) A new lumped-parameter model for flow in unsaturated dual-porosity media. Adv Water Resour 19(5):317–327. doi:10.1016/0309-1708(96)00007-3
122. Zyvoloski G, Robinson B, Viswanathan H (2008) Generalized dual porosity: A numerical method for representing spatially variable sub-grid scale processes. Adv Water Resour 31(3):535–544. doi:10.1016/j.advwatres.2007.11.006

Chapter 6
Flow in Binary Media with Heterogeneous Hydraulic Diffusivity

In the previous chapter it was shown that field-scale models for unsaturated or two-phase flow may have various forms, depending on the heterogeneity pattern of the medium, hydraulic characteristics of the component materials and the interplay between various forces driving the Darcy-scale flow. In this chapter, a group of field-scale models describing capillary-dominated unsaturated flow in a medium with disconnected inclusions is examined. The models were obtained using periodic homogenization approach. The following presentation is based on papers [23–25, 42]. The focus is on the comparison of various models and the development of a generalized formulation as proposed in [42]. Numerical simulations are presented, which allow to compare the generalized upscaled model with Darcy-scale numerical solutions with explicit representation of the heterogeneous structures. Preliminary experimental validation of the generalized model is also described following [44].

6.1 Periodic Homogenization Method

The periodic homogenization method is based on asymptotic expansion of the relevant variables appearing in the governing equations. The principles of this method are described in a number of textbooks, e.g. [8, 20, 36], while the application to flow in porous media include e.g. [9, 19, 29, 32]. The models presented here were obtained using the physically-oriented approach developed by Auriault [5–7, 38]. It is assumed that the medium is periodic and shows two distinct geometric scales, as discussed in Chap. 5:

$$\varepsilon = \frac{l}{L} \ll 1. \tag{6.1}$$

The governing equations at the small scale are written in terms of dimensionless variables, with each physical (dimensional) variable u normalized with respect to its characteristic constant value:

$$u = u^* \, u^{(c)}, \tag{6.2}$$

A. Szymkiewicz, *Modelling Water Flow in Unsaturated Porous Media*,
GeoPlanet: Earth and Planetary Sciences, DOI: 10.1007/978-3-642-23559-7_6,

where u^* is a dimensionless variable and $u^{(c)}$ is a characteristic constant. The separation of scales allows to introduce a two-scale formulation with two dimensionless spatial variables, defined as:

$$\mathbf{x}^* = \mathbf{x}/L, \tag{6.3}$$
$$\mathbf{y}^* = \mathbf{x}/l, \tag{6.4}$$

where $\mathbf{x}^*$ is the large-scale spatial variable and $\mathbf{y}^*$ is the small-scale spatial variable. All dependent variables are represented as functions of the two dimensionless spatial variables and the dimensionless time variable in the form of the following asymptotic expansions:

$$u^*\left(\mathbf{x}^*, \mathbf{y}^*, t^*\right) = u^{*(0)}\left(\mathbf{x}^*, \mathbf{y}^*, t^*\right) + \varepsilon\, u^{*(1)}\left(\mathbf{x}^*, \mathbf{y}^*, t^*\right) + \varepsilon^2\, u^{*(2)}\left(\mathbf{x}^*, \mathbf{y}^*, t^*\right) + \cdots, \tag{6.5}$$

where the subsequent terms $u^{*(i)}$ are $\mathbf{y}$-periodic.

The homogenization procedure according to [6, 7] includes the following steps:

1. The governing equations describing the considered physical process at the small scale are formulated together with the conditions at the interfaces separating the material regions.
2. The equations are normalized according to Eq. (6.2). The spatial variable is normalized with respect to l, i.e. it is replaced by the dimensionless variable $\mathbf{y}^*$.
3. The order of magnitude of the arising dimensionless numbers is estimated with respect to the powers of the scale parameter ε. This is usually written as:

$$\mathscr{R} = \mathscr{O}(\varepsilon^n), \tag{6.6}$$

which means that the dimensionless number $\mathscr{R}$ satisfies the following relation:

$$\varepsilon^{n+1} \ll \mathscr{R} \ll \varepsilon^{n-1}, \tag{6.7}$$

where n is an integer number.
4. The asymptotic expansions (6.5) are introduced in the normalized small-scale equations and the spatial derivative operator is replaced by its two-scale equivalent:

$$\frac{\partial}{\partial \mathbf{y}^*} \to \frac{\partial}{\partial \mathbf{y}^*} + \varepsilon \frac{\partial}{\partial \mathbf{x}^*}. \tag{6.8}$$

The interface conditions are similarly expanded.
5. In the expanded equations the terms at the same power of ε are identified. For each power of ε, a corresponding boundary value problem is defined by a differential equation together with the interface conditions and the periodicity conditions for terms $u^{*(i)}$. These boundary problems allow to formulate the macroscopic model as the equation describing the behaviour of $u^{*(0)}$, which takes into account

the influence of higher order terms in the asymptotic expansion (6.5), up to the required order of accuracy. The higher order terms are accounted for either in the definition of the effective parameters or by additional terms arising in the governing equation. Thus, the resulting large-scale equation may have a different form than the local-scale equation.

6.2 Basic Assumptions

The considered porous medium has a binary structure and consists of isolated inclusions of porous material *II* dispersed in a continuous background material *I*, Fig. 6.1. It is assumed that the volume fractions of the two materials are of the same order of magnitude:

$$\mathcal{O}(w^I) = \mathcal{O}(w^{II}). \tag{6.9}$$

At the scale of a single periodic cell, the flow is governed by the Richards equation, Eq. (2.67):

$$C_{\mathrm{wp}} \frac{\partial p_{\mathrm{w}}}{\partial t} - \nabla \left[\frac{\mathsf{k}_{\mathrm{w}}}{\mu_w} \left(\nabla p_{\mathrm{w}} - \rho_{\mathrm{w}} \mathbf{g} \right) \right] = 0, \tag{6.10}$$

where C_{wp} is the storage coefficient defined according to Eq. (2.68):

$$C_{\mathrm{wp}} = \phi \, \beta_{\mathrm{w}} \, S_{\mathrm{w}} + \phi \, \frac{\mathrm{d}S_{\mathrm{w}}}{\mathrm{d}p_{\mathrm{w}}}. \tag{6.11}$$

Note that both the storage coefficient C_{wp} and the permeability tensor k_w are functions of the water pressure p_w. In the original papers [24, 25, 27, 42] the fluid compressibility effects were neglected. In this presentation the water compressibility is taken into account, which allows to cover the fully water-saturated case. This modification does not affect the results of homogenization. However, the porous medium is assumed to be rigid, as the development of upscaled equations describing deformation of a heterogeneous medium is outside the scope of this work.

It is assumed that Eq. (6.10) applies to both background (Ω^I) and inclusions (Ω^{II}) parts of a periodic cell Ω. The flow equations at the local scale can be thus written as follows:

$$C^I_{\mathrm{wp}} \frac{\partial p^I_{\mathrm{w}}}{\partial t} - \nabla \left[\frac{\mathsf{k}^I_{\mathrm{w}}}{\mu_{\mathrm{w}}} \left(\nabla p^I_{\mathrm{w}} - \rho^I_{\mathrm{w}} \mathbf{g} \right) \right] = 0 \quad \text{in } \Omega^I, \tag{6.12}$$

$$C^{II}_{\mathrm{wp}} \frac{\partial p^{II}_{\mathrm{w}}}{\partial t} - \nabla \left[\frac{\mathsf{k}^{II}_{\mathrm{w}}}{\mu_{\mathrm{w}}} \left(\nabla p^{II}_{\mathrm{w}} - \rho^{II}_{\mathrm{w}} \mathbf{g} \right) \right] = 0 \quad \text{in } \Omega^{II}, \tag{6.13}$$

where the subscripts *I* and *II* refer to the two porous materials. At the interface between the two materials, denoted by Γ, the water pressure and the normal

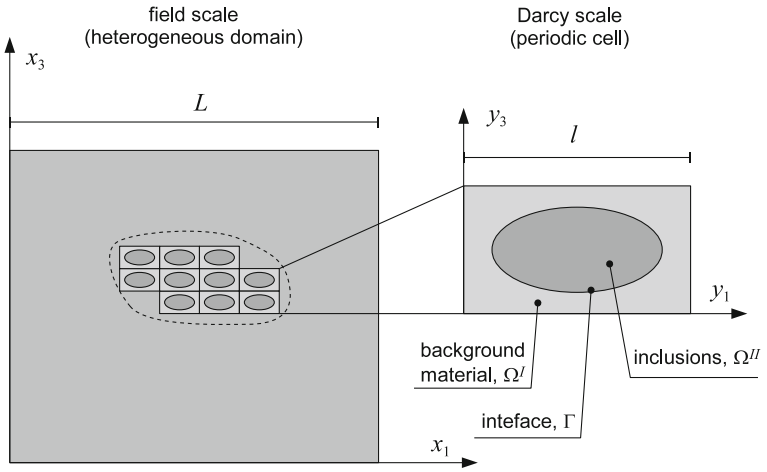

Fig. 6.1 Structure of a heterogeneous porous medium with inclusions

component of the volumetric water flux are assumed continuous. These conditions are specified as follows:

$$p_{\mathrm{w}}^{I} = p_{\mathrm{w}}^{II} \qquad \text{on } \Gamma, \tag{6.14}$$

$$\left[\frac{\mathsf{k}_{\mathrm{w}}^{I}}{\mu_{\mathrm{w}}}\left(\nabla p_{\mathrm{w}}^{I} - \rho_{\mathrm{w}}^{I}\,\mathbf{g}\right)\right]\mathbf{n}_{\Gamma} = \left[\frac{\mathsf{k}_{\mathrm{w}}^{II}}{\mu_{\mathrm{w}}}\left(\nabla p_{\mathrm{w}}^{II} - \rho_{\mathrm{w}}^{II}\,\mathbf{g}\right)\right]\mathbf{n}_{\Gamma} \quad \text{on } \Gamma, \tag{6.15}$$

where $\mathbf{n}_{\Gamma}$ is a unit vector normal to the interface Γ.

Dimensionless variables can be introduced as follows:

$$p_{\mathrm{w}}^{\iota *} = p_{\mathrm{w}}^{\iota}/p_{\mathrm{w}}^{(c)}, \tag{6.16}$$

$$\rho_{\mathrm{w}}^{\iota *} = \rho_{\mathrm{w}}^{\iota}/\rho_{\mathrm{w}}^{(c)}, \tag{6.17}$$

$$C_{\mathrm{wp}}^{\iota *} = c_{\mathrm{w}}^{\iota}/c_{\mathrm{w}}^{\iota(c)}, \tag{6.18}$$

$$\mathsf{k}_{\mathrm{w}}^{\iota *} = \mathsf{k}_{\mathrm{w}}^{\iota}/k_{\mathrm{w}}^{\iota(c)}, \tag{6.19}$$

where $\iota = I, II$ denotes the material index. Note that the characteristic pressure is the same for both materials. It represents the pressure drop resulting from initial and boundary conditions (some authors use the air entry pressure as the scaling value, which is a material-specific parameter, e.g. [30]). The characteristic values of density and viscosity are assumed the same for both materials. The local-scale equations can be recast into a normalized form:

$$\mathscr{R}_{\mathrm{t}}^{I}\, C_{\mathrm{wp}}^{I*}\,\frac{\partial p_{\mathrm{w}}^{I*}}{\partial t^*} - \frac{\partial}{\partial\, y_i^*}\left[k_{\mathrm{w},ij}^{I*}\left(\frac{\partial p_{\mathrm{w}}^{I*}}{\partial\, y_j^*} + \mathscr{R}_g\,\rho_{\mathrm{w}}^{I*}\,\frac{\partial y_3^*}{\partial\, y_j^*}\right)\right] = 0 \quad \text{in } \Omega^{I}, \tag{6.20}$$

$$\mathscr{R}_{\mathrm{t}}^{II}\, C_{\mathrm{wp}}^{II*}\, \frac{\partial p_{\mathrm{w}}^{II*}}{\partial t^*} - \frac{\partial}{\partial\, y_i^*}\left[\mathsf{k}_{\mathrm{w},ij}^{II*}\left(\frac{\partial p_{\mathrm{w}}^{II*}}{\partial\, y_j^*} + \mathscr{R}_g\, \rho_{\mathrm{w}}^{II*}\, \frac{\partial y_3^*}{\partial\, y_j^*}\right)\right] = 0 \text{ in } \Omega^{II}, \tag{6.21}$$

where y_3 is assumed to be oriented vertically upwards. The corresponding interface conditions are:

$$p_{\mathrm{w}}^{I*} = p_{\mathrm{w}}^{II*} \qquad \text{on } \Gamma, \tag{6.22}$$

$$\left[\mathsf{k}_{\mathrm{w},ij}^{I*}\left(\frac{\partial p_{\mathrm{w}}^{I*}}{\partial\, y_j^*} + \mathscr{R}_g\, \rho_{\mathrm{w}}^{I*}\, \frac{\partial y_3^*}{\partial\, y_j^*}\right)\right]\mathbf{n}_\Gamma = \left[\mathsf{k}_{\mathrm{w},ij}^{II*}\left(\frac{\partial p_{\mathrm{w}}^{II*}}{\partial\, y_j^*} + \mathscr{R}_{\mathrm{g}}\, \rho_{\mathrm{w}}^{II*}\, \frac{\partial y_3^*}{\partial\, y_j^*}\right)\right]\mathbf{n}_\Gamma \quad \text{on } \Gamma. \tag{6.23}$$

In the above equations, several dimensionless numbers appear. The numbers $\mathscr{R}_{\mathrm{t}}^{I}$ and $\mathscr{R}_{\mathrm{t}}^{II}$ represent the relations between the characteristic time of the diffusive flow at the local scale and the chosen observation time $t^{(c)}$:

$$\mathscr{R}_{\mathrm{t}}^{I} = \frac{C_{\mathrm{wp}}^{I(c)}\, \mu_{\mathrm{w}}\, l^2}{k_{\mathrm{w}}^{I(c)}\, t^{(c)}} = \frac{l^2}{D^{I(c)}\, t^{(c)}}, \tag{6.24}$$

$$\mathscr{R}_{\mathrm{t}}^{II} = \frac{C_{\mathrm{wp}}^{II(c)}\, \mu_{\mathrm{w}}\, l^2}{k_{w(2)}^{(c)}\, t^{(c)}} = \mathscr{R}_{\mathrm{t}}^{I}\, \frac{D^{I(c)}}{D^{II(c)}} = \mathscr{R}_{\mathrm{t}}^{I}/\mathscr{R}_{\mathrm{d}}, \tag{6.25}$$

where $D^{\iota(c)}$ denotes the characteristic diffusivity for a specific porous material ι:

$$D^{\iota(c)} = \frac{k_{\mathrm{w}}^{\iota(c)}}{C_{\mathrm{wp}}^{\iota(c)}\, \mu_{\mathrm{w}}} \tag{6.26}$$

and $\mathscr{R}_{\mathrm{d}}$ is the ratio of characteristic diffusivities:

$$\mathscr{R}_{\mathrm{d}} = \frac{D^{II(c)}}{D^{I(c)}}. \tag{6.27}$$

The ratio of permeabilities is:

$$\mathscr{R}_{\mathrm{k}} = \frac{k_{\mathrm{w}}^{II(c)}}{k_{\mathrm{w}}^{I(c)}}. \tag{6.28}$$

The dimensionless number representing the ratio of gravity to capillary forces (Bond number) at the local scale is:

$$\mathscr{R}_{\mathrm{g}} = \frac{\rho_{\mathrm{w}}^{(c)}\, g\, l}{p_{\mathrm{w}}^{(c)}}. \tag{6.29}$$

The order of magnitude of the dimensionless numbers has to be estimated with respect to the parameter ε. The models presented in this chapter were obtained for the following assumptions:

- The characteristic observation time corresponds to diffusive flow in the continuous background material at large spatial scale L:

$$\mathscr{O}\left(t^{(c)}\right) = \mathscr{O}\left(\frac{L^2}{D^{I(c)}}\right). \tag{6.30}$$

  Since $l/L = \varepsilon$, the following estimations hold:

$$\mathscr{O}\left(\mathscr{R}_{\mathrm{t}}^{I}\right) = \mathscr{O}\left(\varepsilon^2\right), \tag{6.31}$$

$$\mathscr{O}\left(\mathscr{R}_{\mathrm{t}}^{II}\right) = \mathscr{O}\left(\mathscr{R}_{\mathrm{t}}^{I}/\mathscr{R}_{\mathrm{d}}\right). \tag{6.32}$$

- At the local scale, the capillary forces dominate over the gravity forces:

$$\mathscr{O}\left(\mathscr{R}_{\mathrm{g}}\right) = \mathscr{O}\left(\varepsilon\right). \tag{6.33}$$

  The latter condition holds for relatively small inclusion sizes and large pressure drops. Note that this assumption does not remove gravity force from the large scale model.

It should be noted that the diffusivity depends on both permeability and storage capacity coefficients. For a specific value of the capillary pressure, the fine-textured component of a binary medium may have smaller permeability, but also smaller capacity compared the coarse-textured component. As a result, the diffusivities of both materials have the same order of magnitude, or the diffusivity of the fine-textured medium is larger. Development of the upscaled model requires assumptions on both diffusivity and permeability ratios, appearing in the normalized equations and interface conditions, respectively. The models presented below were obtained assuming that the ratio $\mathscr{R}_{\mathrm{k}}$ is of the same order as the ratio $\mathscr{R}_{\mathrm{d}}$, which implies the capacity ratio of the order of 1, i.e. similar capacity coefficients in the two components. However, the results are applicable also to the case of contrasting storage capacities, which is discussed here following [39]. In order to illustrate this problem, consider steady state flow in the neighbourhood of the material interface Γ separating two materials with the same permeability, but contrasting capacities, $C_{\mathrm{wp}}^{I} \ll C_{\mathrm{wp}}^{II}$. The water pressure is continuous at the interface and its gradient is the same at both sides, since $k_{\mathrm{w}}^{I} = k_{\mathrm{w}}^{II}$. If the pressure is increased, the increment should be the same on both sides due to the pressure continuity condition. However, the saturation will change by different values at each side, because of the contrasting capacity coefficients. The saturation increase will be much larger in the medium with larger capacity. Thus the continuity of water flux does not hold. If both flux and pressure continuity conditions are to be satisfied, one has to assume that in Ω^{II} only a small boundary layer is affected by the

process. Locally, in the boundary layer the flux is the same as in the neighbouring material. However, if the pressure gradient is evaluated with respect to the whole volume of Ω^{II}, its value will be much smaller. Thus, an additional scaling factor will appear in the normalized boundary condition and the results will be equivalent to the case with contrasting permeabilities and similar storage coefficients.

6.3 Upscaled Models for Different Diffusivity Ratios

A number of different models are obtained if the ratio of the diffusivities is varied. The models differ in the form of the governing large scale equation and in the definition of the effective parameters of the heterogeneous medium. While homogenization is performed on dimensionless equations, the resulting models are written in dimensional form, more suitable for practical purposes. The details of the derivation are omitted, as they can be found in the original papers.

6.3.1 Moderately Heterogeneous Medium

Assuming that the diffusivities of the two component materials are of the same order of magnitude, Lewandowska and Laurent [24] developed an equation for large-scale unsaturated flow, which in the notation of this work can be written as follows:

$$C_{\mathrm{wp}}^{\mathrm{eff}} \frac{\partial\, p_{\mathrm{w}}^{\mathrm{eff}}}{\partial\, t} - \nabla \left[\frac{\mathsf{k}_{\mathrm{w}}^{\mathrm{eff}}}{\mu_{\mathrm{w}}} \left(\nabla p_{\mathrm{w}}^{\mathrm{eff}} - \rho_{\mathrm{w}}^{\mathrm{eff}} \mathbf{g} \right) \right] = 0, \tag{6.34}$$

where $p_{\mathrm{w}}^{\mathrm{eff}}$ is the effective (large-scale) water pressure, $C_{\mathrm{wp}}^{\mathrm{eff}}$ is the effective storage capacity coefficient, and $\mathsf{k}_{\mathrm{w}}^{\mathrm{eff}}$ is the effective water permeability tensor. Alternatively, the storage term can be written in terms of the effective water content $\theta_{\mathrm{w}}^{\mathrm{eff}}$:

$$\frac{\partial \theta_{\mathrm{w}}^{\mathrm{eff}}}{\partial t} - \nabla \left[\frac{k_{\mathrm{w}}^{\mathrm{eff}}}{\mu_{\mathrm{w}}} \left(\nabla p_{\mathrm{w}}^{\mathrm{eff}} - \rho_{\mathrm{w}}^{\mathrm{eff}} \mathbf{g} \right) \right] = 0. \tag{6.35}$$

The main result of the homogenization is the existence of an upscaled wetting phase pressure, which can be considered as uniform within the representative elementary volume (REV, periodic cell) at the zeroth order of approximation. The dimensionless variable $p_{\mathrm{w}}^{*(0)}$ is independent of $\mathbf{y}^*$ and the same holds for the corresponding dimensional variable $p_{\mathrm{w}}^{\mathrm{eff}}$. Consequently, local capillary equilibrium conditions prevail and the upscaled parameters can be computed directly for any assumed value of the upscaled pressure $p_{\mathrm{c}}^{\mathrm{eff}} = -p_{\mathrm{w}}^{\mathrm{eff}}$. Moreover, the water density is also uniform in the cell:

$$\rho_{\mathrm{w}}^{\mathrm{eff}} = \rho_{\mathrm{w}} \left(p_{\mathrm{w}}^{\mathrm{eff}} \right). \tag{6.36}$$

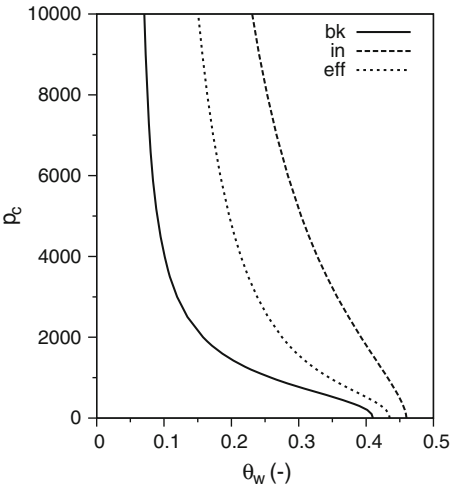

Fig. 6.2 Effective water content (eff) as an average of the water content in the background material (bk) and inclusions (in), assuming equal volume fractions of the two constituents

The local distribution of the water saturation in a periodic cell is piecewise-uniform, i.e. for each material there is a single value of the saturation:

$$S_{\mathrm{w}}^{I} = S_{\mathrm{w}}^{I}\left(p_{\mathrm{w}}^{\mathrm{eff}}(\mathbf{x},t)\right) \quad \text{in } \Omega^{I}, \tag{6.37}$$

$$S_{\mathrm{w}}^{II} = S_{\mathrm{w}}^{II}\left(p_{\mathrm{w}}^{\mathrm{eff}}(\mathbf{x},t)\right) \quad \text{in } \Omega^{II}. \tag{6.38}$$

The average (effective) water content can be defined as the volume-weighted average of the water contents of the two materials:

$$\theta_{\mathrm{w}}^{\mathrm{eff}} = w^{I}\theta_{\mathrm{w}}^{I} + w^{II}\theta_{\mathrm{w}}^{II}. \tag{6.39}$$

An example of the effective water content as a function of the effective capillary pressure is shown in Fig. 6.2.

The effective storage coefficient is written as:

$$\begin{aligned} C_{\mathrm{wp}}^{\mathrm{eff}} &= \beta_{\mathrm{w}}\,\theta_{\mathrm{w}}^{\mathrm{eff}} + w^{I}\,\phi^{I}\,\frac{\mathrm{d}S_{\mathrm{w}}^{I}}{\mathrm{d}p_{\mathrm{w}}} + w^{II}\,\phi^{II}\,\frac{\mathrm{d}S_{\mathrm{w}}^{II}}{\mathrm{d}p_{\mathrm{w}}} \\ &= \beta_{\mathrm{w}}\,\theta_{\mathrm{w}}^{\mathrm{eff}} + w^{I}\,\frac{\mathrm{d}\theta_{\mathrm{w}}^{I}}{\mathrm{d}p_{\mathrm{w}}} + w^{II}\,\frac{\mathrm{d}\theta_{\mathrm{w}}^{II}}{\mathrm{d}p_{\mathrm{w}}}. \end{aligned} \tag{6.40}$$

Taking into account that the average porosity is equal to:

$$\phi^{\mathrm{eff}} = w^{I}\phi^{I} + w^{II}\phi^{II}, \tag{6.41}$$

it is also possible to define a large-scale average water saturation as:

$$S_{\mathrm{w}}^{\mathrm{eff}} = \frac{\theta_{\mathrm{w}}^{\mathrm{eff}}}{\phi^{\mathrm{eff}}}. \tag{6.42}$$

Note that the effective saturation cannot be obtained by simple averaging of the saturations in the two materials, except for the case when both materials have the same porosity.

The effective permeability tensor $\mathsf{k}_{\mathrm{w}}^{\mathrm{eff}}$ is defined using auxiliary variables χ_1, χ_2 and χ_3, corresponding to the three spatial directions. The auxiliary variable for each direction χ_m, $m = 1, 2, 3$, is the solution to a boundary value problem defined for the periodic cell. The problem is specified as follows [24]:

$$\frac{\partial}{\partial y_i}\left[k_{\mathrm{w},ij}^{I}\left(p_{\mathrm{w}}^{\mathrm{eff}}\right)\frac{\partial}{\partial y_j}\left(\chi_m^{I}+y_m\right)\right]=0 \quad \text{in } \Omega^{I}, \tag{6.43}$$

$$\frac{\partial}{\partial y_i}\left[k_{\mathrm{w},ij}^{II}\left(p_{\mathrm{w}}^{\mathrm{eff}}\right)\frac{\partial}{\partial y_j}\left(\chi_m^{II}+y_m\right)\right]=0 \quad \text{in } \Omega^{II}, \tag{6.44}$$

with the continuity conditions at the background-inclusion interface:

$$\chi_m^{I} = \chi_m^{II}, \tag{6.45}$$

$$\left[k_{\mathrm{w},ij}^{I}\left(p_{\mathrm{w}}^{\mathrm{eff}}\right)\frac{\partial}{\partial y_j}\left(\chi_m^{I}+y_m\right)\right]m_{\Gamma,i} = \left[k_{\mathrm{w},ij}^{II}\left(p_{\mathrm{w}}^{\mathrm{eff}}\right)\frac{\partial}{\partial y_j}\left(\chi_m^{II}+y_m\right)\right]m_{\Gamma,i}, \tag{6.46}$$

where $\mathbf{y}$ is a local spatial variable associated with a periodic cell, $k_{\mathrm{w},ij}^{I}$ denotes component ij of the tensor $\mathsf{k}_{\mathrm{w}}^{I}$ and $n_{\Gamma,i}$ is the ith component of the unit vector normal to the interface. At the outer boundaries of the cell, periodic boundary conditions for χ_m are specified. Moreover, the average value of χ_m should equal zero. In order to satisfy this condition, and on the other hand to ensure a unique solution of the problem, the value of χ_m is set to 0 at an arbitrary point in the periodic cell. Note that in the above equations the effective water pressure is a parameter, rather than a variable. The problem must be solved assuming a specific value of $p_{\mathrm{w}}^{\mathrm{eff}}$ and the corresponding piecewise-uniform distribution of the water saturations and permeabilities.

The solution for each spatial direction allows to compute entries in the corresponding column of the effective permeability tensor:

$$k_{\mathrm{w},mi}^{\mathrm{eff}} = \frac{1}{|\Omega|}\left[\int_{\Omega^{I}} k_{\mathrm{w},ji}^{I}\left(p_{\mathrm{w}}^{\mathrm{eff}}\right)\frac{\partial}{\partial y_j}\left(\chi_m^{I}+y_m\right)\mathrm{d}\Omega + \int_{\Omega^{II}} k_{\mathrm{w},ji}^{II}\left(p_{\mathrm{w}}^{\mathrm{eff}}\right)\frac{\partial}{\partial y_j}\left(\chi_m^{II}+y_m\right)\mathrm{d}\Omega\right], \tag{6.47}$$

where $|\Omega|$ denotes the volume of the periodic cell. One can obtain the large-scale permeability function by solving the local boundary value problem (6.43)–(6.46) for a number of values of p_{w} from the range of interest and using interpolation to estimate the components of the effective tensor for intermediate values of the capillary pressure. While it is possible to compute the upscaled absolute permeability tensor (assuming $p_{\mathrm{w}}^{\mathrm{eff}} = p_{\mathrm{c}}^{\mathrm{eff}} = 0$), is not possible to express the upscaled total water permeability as a product of a tensor absolute permeability and a scalar relative permeability function, except for the case when the relative permeability functions are the same in both materials.

The model described above is consistent with other models developed for the assumption of local capillary equilibrium for either two-phase flow or Richards equation, e.g. [1, 11, 30, 35]. As shown by Neuweiler and Eichel [31], if the gravitational force is more important at the local scale, the homogenized model has a similar form, but differs in the definition of effective parameters. However, even in such a case, the model obtained for capillary-dominated flow remains a reasonable approximation.

It should be noted that the method to compute $\mathsf{k}_{\mathrm{w}}^{\mathrm{eff}}$ resulting from homogenization is equivalent to the solution of a steady flow equation with periodic boundary condition, as described in Sect. 5.3.3. Thus, it can be concluded that the use of periodic conditions in upscaling is valid when assumptions underlying the homogenization theory, in particular the existence of REV and the separation of scales, are satisfied. On the other hand, for any specific value of the effective capillary pressure the effective permeability tensor can be estimated using approximate formulae, for instance those based on the effective medium theory or Cardwell and Parsons bounds. The advantage of such methods is that they are much simpler to implement than the method based on the solution of local boundary value problem, albeit at the cost of lower accuracy.

6.3.2 Weakly Permeable Inclusions: Local Equilibrium

If the inclusion-background diffusivity ratio is of the order ε, the characteristic time of flow in inclusions is longer than in the background material, but still significantly shorter than the observation time at the macroscopic scale. Application of the homogenization procedure leads to a model characterized by a uniform value of the zero-order water pressure $p_{\mathrm{w}}^{*(0)}$, corresponding to $p_{\mathrm{w}}^{\mathrm{eff}}$ in the whole periodic cell, and consequently to a local capillary equilibrium model [39, 42]. The homogenized equation has the same form as Eq. (6.34):

$$C_{\mathrm{wp}}^{\mathrm{eff}} \frac{\partial\, p_{\mathrm{w}}^{\mathrm{eff}}}{\partial\, t} - \nabla \left[\frac{\mathsf{k}_{\mathrm{w}}^{\mathrm{low}}}{\mu_{\mathrm{w}}} \nabla \left(p_{\mathrm{w}}^{\mathrm{eff}} - \rho_{\mathrm{w}}^{\mathrm{eff}}\, \mathbf{g} \right) \right] = 0, \tag{6.48}$$

with the effective storage coefficient $C_{\mathrm{wp}}^{\mathrm{eff}}$ defined by Eq. (6.40). However, the effective permeability $\mathsf{k}_{\mathrm{w}}^{\mathrm{low}}$ is obtained from a different local boundary value problem. Since the normal water flux in the interface condition Eq. (6.23) is scaled by a factor of ε, it is neglected at the zero order of approximation. The auxiliary variables χ_m are defined only in the part of the periodic cell corresponding to the background material (Ω^I):

$$\frac{\partial}{\partial y_i}\left[k_{\mathrm{w},ij}\left(p_{\mathrm{w}}^{\mathrm{eff}}\right)\frac{\partial}{\partial y_j}\left(\chi_m^I + y_m\right)\right] = 0 \quad \text{in } \Omega^I \tag{6.49}$$

with a zero-flux condition at the background-inclusion interface:

$$\left[k_{\mathrm{w},ij}^I\left(p_{\mathrm{w}}^{\mathrm{eff}}\right)\frac{\partial}{\partial y_j}\left(\chi_m^I + y_m\right)\right] n_{\Gamma,i} = 0. \tag{6.50}$$

The resulting effective permeability tensor is computed from the formula:

$$k_{\mathrm{w},mi}^{\mathrm{eff}} = \frac{1}{|\Omega|}\int\limits_{\Omega^I} k_{\mathrm{w},ji}^I\left(p_{\mathrm{w}}^{\mathrm{eff}}\right)\frac{\partial}{\partial y_j}\left(\chi_m^I + y_m\right)\mathrm{d}\Omega. \tag{6.51}$$

The above formulation represents a lower limit case of the definition for moderately heterogeneous media, given by Eqs. (6.43)–(6.47). The limit is obtained when the ratio $k_{\mathrm{w}}^{II(c)}/k_{\mathrm{w}}^{I(c)} \to 0$. In such a case, the contribution of the permeability of inclusions to the effective permeability, given by the second integral in Eq. (6.47), is negligible, and the auxiliary variable χ can be defined only on the Ω^I part of the periodic cell. The interface condition Eq. (6.46) becomes Eq. (6.50). If the background material is isotropic then for any value of the large-scale water pressure the resulting effective permeability tensor can be written as:

$$k_{\mathrm{w},ij}^{\mathrm{low}}\left(p_{\mathrm{w}}^{\mathrm{eff}}\right) = B_{ij}^{\mathrm{low}}\, k_{\mathrm{w},ij}^I\left(p_{\mathrm{w}}^{\mathrm{eff}}\right), \tag{6.52}$$

where the components of the tensor, $B_{ij}^{\mathrm{low}} < 1$, are constant for a given geometry of the periodic cell.

Note that while the inclusions are considered impermeable for the purposes of computing the effective permeability, they are sufficiently permeable to ensure fast equilibration of the water pressure locally within a periodic cell, and thus contribute to the storage term, which has the same form in the present model as in the case of moderately heterogeneous media, described in the previous section.

6.3.3 Weakly Permeable Inclusions: Local Non-Equilibrium

For the permeability ratio of the order of ε^2, the characteristic time of flow in a single inclusion is approximately the same as the characteristic time of flow in the connected background material at the macroscopic scale:

$$\mathcal{O}\left(\frac{L^2}{D_{\mathrm{h}}^{I(c)}}\right) = \mathcal{O}\left(\frac{l^2}{D_{\mathrm{h}}^{II(c)}}\right). \tag{6.53}$$

In other words, the large-scale response of the system appears before the pressure in all inclusions reaches equilibrium with the surrounding background material. Accordingly, homogenization leads to a two-scale local non-equilibrium model [25]. The governing equation for flow at the macroscopic scale is written as follows:

$$w^I\, C_{\mathrm{wp}}^I\, \frac{\partial\, p_{\mathrm{w}}^{\mathrm{eff}}}{\partial\, t} - \nabla\left[\frac{\mathsf{k}_{\mathrm{w}}^{\mathrm{low}}}{\mu_w}\left(\nabla p_{\mathrm{w}}^{\mathrm{eff}} - \rho_{\mathrm{w}}^{\mathrm{eff}}\,\mathbf{g}\right)\right] + T_{\mathrm{w}}^{\mathrm{v}} = 0. \tag{6.54}$$

The primary variable in the above equation, $p_{\mathrm{w}}^{\mathrm{eff}}$, represents the water phase pressure in the background material, which at the zeroth order of approximation can be considered uniform in Ω^I part of the periodic cell. The first term in Eq. (6.54) represents the contribution of the background material to the storage capacity of the heterogeneous medium:

$$w^I\, C_{\mathrm{wp}}^I\, \frac{\partial\, p_{\mathrm{w}}^I}{\partial\, t} = w^I\, \frac{\partial\, \theta_{\mathrm{w}}^I}{\partial\, t}. \tag{6.55}$$

On the other hand, the water pressure in the inclusions is not equilibrated with the pressure in the background material. At any point $\mathbf{x}$ of the large-scale domain, the evolution of the water pressure $p_{\mathrm{w}}^{II}(\mathbf{x}, \mathbf{y}, t)$ in the associated periodic cell can be described by the following equation:

$$C_{\mathrm{wp}}^{II}\, \frac{\partial\, p_{\mathrm{w}}^{II}}{\partial\, t} - \frac{\partial}{\partial y_i}\left[\frac{k_{\mathrm{w},ij}^{II}}{\mu_w}\frac{\partial p_{\mathrm{w}}^{II}}{\partial y_j}\right] = 0 \quad \text{in } \Omega^{II}. \tag{6.56}$$

Note that the equation for local flow in inclusions does not account for gravity, according to the assumption on the local dominance of the capillary forces. The boundary condition for Eq. (6.56) is:

$$p_{\mathrm{w}}^{II}(\mathbf{x}, \mathbf{y}, t) = p_{\mathrm{w}}^{\mathrm{eff}}(\mathbf{x}, t) \quad \text{on } \Gamma, \tag{6.57}$$

which results from the assumed continuity of the water pressure at the material interface.

The non-equilibrium transfer term $T_{\mathrm{w}}^{\mathrm{v}}$ describes volumetric water transfer between the background material and inclusions. Since the inclusions are disconnected from each other, by virtue of the mass conservation principle the integral of the normal

water flux over the interface Γ is equal to the rate of change of the mass of water in the inclusions:

$$
\begin{aligned}
T_{\mathrm{w}}^{\mathrm{v}} &= -\frac{1}{|\Omega|}\int\limits_{\Gamma}\left[\frac{k_{\mathrm{w},ij}^{II}}{\mu_{\mathrm{w}}}\frac{\partial}{\partial y_j}\,p_{\mathrm{w}}^{II}\right] n_{\Gamma,i}\,\mathrm{d}\Gamma \\
&= \frac{1}{|\Omega|}\int\limits_{\Omega^{II}} C_{\mathrm{wp}}^{II}\,\frac{\partial\, p_{\mathrm{w}}^{II}}{\partial\, t}\,\mathrm{d}\Omega = \frac{1}{|\Omega|}\int\limits_{\Omega^{II}}\frac{\partial\,\theta_{\mathrm{w}}^{II}}{\partial\, t}\,\mathrm{d}\Omega \\
&= \frac{1}{|\Omega|}\frac{\partial}{\partial\, t}\int\limits_{\Omega^{II}}\theta_{\mathrm{w}}^{II}\,\mathrm{d}\Omega = w^{II}\,\frac{\partial\bar{\theta}_{\mathrm{w}}^{II}}{\partial\, t},
\end{aligned}
\tag{6.58}
$$

where $\bar{\theta}_{\mathrm{w}}^{II}$ is the average water content in the inclusion. The term $T_{\mathrm{w}}^{\mathrm{v}}$ can be considered as the non-equilibrium part of the storage term, which complements the equilibrium part given by Eq. (6.55). The local distribution of the pressure and saturation in inclusions is obtained from the solution of the local flow equation Eq. (6.56).

The model is characterized by a coupling of large-scale and small-scale variables. Its solution domain consists of a large-scale domain associated with the variable x (in general three-dimensional), coupled with a set of local domains (in general also three-dimensional), corresponding to inclusions associated with each point of the large scale domain. Note that it is not necessary to solve the local flow equation (6.56) for each inclusion present in the physical domain—the equation must be solved only at the nodes of the numerical grid covering the large-scale domain (see Sect. 6.5).

The effective permeability tensor $\mathsf{k}_{\mathrm{w}}^{\mathrm{low}}$ is defined by the same local boundary value problem for the auxiliary variable χ as given by Eqs. (6.49)–(6.50). It means that the large-scale permeability of the heterogeneous medium does not depend on the permeability of inclusions. Still, the inclusions are sufficiently permeable to contribute to the storage properties of the heterogeneous medium at the chosen time scale. However, in contrast to the model described in the previous section, the equilibration of capillary pressure is not instantaneous, which leads to the appearance of the non-equilibrium term $T_{\mathrm{w}}^{\mathrm{v}}$.

Models of the same type were also obtained by other authors using the periodic homogenization method [2–4, 10, 18]. They are sometimes called distributed-microstructure models, e.g. [13]. As mentioned in Chap. 5, such models represent the most detailed form of the double-porosity models. Other double-porosity models can be considered as their simplifications, see for instance the discussion by Zimmerman et al. [45]. Taking into account the fact that the gravity force is absent from the local flow equation (6.56) and that the condition at the interface is uniform in space, for an isotropic medium one can assume that the local flow is essentially radial. It can be described by a one-dimensional equation with respect to a spatial coordinate representing the distance from the nearest interface point. This leads to the same description of the non-equilibrium water transfer as in the MINC model. Such a formulation is strictly equivalent to the homogenization result for circular or spherical

inclusions, while for other shapes it represents a reasonably accurate approximation [21, 41, 43]. A further simplification is possible if the locally variable water pressure and saturation in inclusions are replaced by average values, corresponding to the centre of inclusion. The gradient of the water pressure at the outer of inclusion can be then roughly approximated as a difference between the interface value (equal to the value in the background material) and the average value in inclusion, divided by a characteristic dimension of inclusion. In this way the first-order transfer term is obtained, as given by Eq. (5.44). The error caused by inaccurate approximation of the gradient is partially compensated for by introducing correction factors or adjusting the relative permeability at the interface, as discussed in Sect. 5.4.2. Thus, the model obtained by homogenization fits well into the framework of double-porosity single-permeability models. These models are based on the assumption that field-scale flow between weakly permeable regions (matrix blocks or inclusions) is negligible. As shown by Lewandowska et al. [25], the double-porosity single permeability model can be also used to describe flow in media with connected weakly permeable regions, provided that the contrast in hydraulic diffusivities is of the order of ε^2. In such a case the dynamics of water in the weakly permeable regions is determined mostly by the fluid transfer from and to the highly permeable system. In the numerical example shown in [25], the model described above was more accurate than the double-porosity double-permeability formulation of Gerke and van Genuchten [16], which accounts for large-scale flow in the matrix domain, but uses first-order approximation for the non-equilibrium transfer term. However, from practical point of view, the double permeability model has an advantage of flexibility (at the cost of reduced accuracy), since it can be used both in conditions close to saturation, when the flow is dominated by highly permeable fractures or macropores, and in drier conditions, where most of the moisture transfer takes place in the weakly permeable regions.

6.3.4 Quasi-Impermeable Inclusions

Yet another model arises when the permeability ratio is much smaller than ε^2. The flow in inclusions is then so slow compared to the flow in the background material, that its influence can be neglected both in the storage term and in the effective permeability. The resulting limit model has the following form:

$$w^I C^I_{\mathrm{wp}} \frac{\partial p^{\mathrm{eff}}_{\mathrm{w}}}{\partial t} - \nabla \left[\frac{\mathsf{k}^{\mathrm{low}}_{\mathrm{w}}}{\mu_{\mathrm{w}}} \left(\nabla p^{\mathrm{eff}}_{\mathrm{w}} - \rho^{\mathrm{eff}}_{\mathrm{w}} \mathbf{g} \right) \right] = 0, \tag{6.59}$$

where the effective permeability is defined as in the previous two models, Eqs. (6.49)–(6.50). Similarly as in the case of local non-equilibrium model, described in the previous section, the principal variable $p^{\mathrm{eff}}_{\mathrm{w}}$ corresponds to the pressure in the background material Ω^I. The model given by Eq. (6.59) is valid for the assumption that the observation time is of the order of the time of flow in the background material

at large-scale. If long-time processes are to be simulated, then the observation time corresponding to the flow in inclusions should be chosen, which would lead to a local non-equilibrium model, accounting for the evolution of the water pressure in inclusions.

6.3.5 Highly Permeable Inclusions

When the inclusions are much more permeable than the background, the unsaturated flow can be described with a homogenized equation of the following form [23, 27]:

$$C_{\mathrm{wp}}^{\mathrm{eff}} \frac{\partial\, p_{\mathrm{w}}^{\mathrm{eff}}}{\partial\, t} - \nabla \left[\frac{\mathsf{k}_{\mathrm{w}}^{\mathrm{high}}}{\mu_{\mathrm{w}}} \left(\nabla p_{\mathrm{w}}^{\mathrm{eff}} - \rho_{\mathrm{w}}^{\mathrm{eff}}\, \mathbf{g} \right) \right] = 0. \tag{6.60}$$

As it was in the case of moderately heterogeneous medium, local equilibrium conditions prevail, because the characteristic time of flow is much shorter for inclusions than for the background. Accordingly, the effective storage coefficient $C_{\mathrm{wp}}^{\mathrm{eff}}$ is defined by Eq. (6.40). However, the effective permeability tensor is defined differently than for the moderately heterogeneous case. The auxiliary variable χ_m, $m = 1, 2, 3$ is defined only on the part of the periodic cell corresponding to the background material Ω^I:

$$\frac{\partial}{\partial y_i} \left[k_{\mathrm{w},ij}^{I} \left(p_{\mathrm{w}}^{\mathrm{eff}} \right) \frac{\partial}{\partial y_j} \left(-\chi_m^I + y_m \right) \right] = 0 \quad \text{in } \Omega^I. \tag{6.61}$$

At the inclusion-background interface a Dirichlet condition is specified:

$$\chi_m = y_m \quad \text{on } \Gamma, \tag{6.62}$$

while at the outer boundaries of the cell periodic boundary conditions are imposed for χ_m. The components of the effective permeability tensor are then computed as follows:

$$k_{\mathrm{w},mi}^{\mathrm{high}} = \frac{1}{|\Omega|} \int\limits_{\Omega^I} k_{\mathrm{w},ji}^{I} \left(p_{\mathrm{w}}^{\mathrm{eff}} \right) \frac{\partial}{\partial y_j} \left(-\chi_m^I + y_m \right) \mathrm{d}\Omega. \tag{6.63}$$

Similarly to the case of weakly permeable inclusions, if the background material is isotropic then the effective permeability tensor can be written as:

$$k_{\mathrm{w},ij}^{\mathrm{high}} = B_{ij}^{\mathrm{high}}\, k_{\mathrm{w},ij}^{I} \left(p_{\mathrm{w}}^{\mathrm{eff}} \right), \tag{6.64}$$

where the components of the tensor, $B_{ij}^{\mathrm{high}} > 1$, are constant for a given geometry of the periodic cell. Thus, the effective permeability does not depend on the perme-

ability of inclusions, only on the permeability of the background material and the local geometry. It can be shown [42] that the definition of the effective permeability presented above can be obtained as a limit case of the formulation for moderately heterogeneous media, Eqs. (6.43)–(6.47). As the inclusion-background permeability ratio tends to infinity, the term $\nabla(-\chi_m + y_m)$ approaches zero in the inclusion domain Ω^{II}, which implies $\chi_m \to y_m$. Consequently, the boundary problem can be solved only in Ω^I domain, with the condition at the interface given by Eq. (6.62). A similar formulation for the effective permeability was obtained by other authors in the case of two-phase flow in media with highly permeable inclusions [32, 33].

6.4 Generalized Formulation

As shown in the preceding sections, the form of the large-scale model and the definition of the effective permeability depends on the assumed permeability ratio between inclusions and background. Figure 6.3 summarizes all the large-scale models described above. However, the permeability of each material is a nonlinear function of the water pressure and it is possible that the permeability ratio will be highly variable even during a single flow event in a heterogeneous medium. For instance, at large negative values of p_w clay is much more permeable than sand, while in the range of values close to zero the permeability of sand is larger by several orders of magnitude. The model applicable for a specific range of pressure values may be not useful outside this range. Thus, in view of the possible practical application of the results of homogenization it is necessary to consider the possible transitions between various models.

It has been already mentioned that the definitions of the effective permeability tensor for the cases of weakly and highly permeable inclusions, $\mathsf{k}_\mathrm{w}^\mathrm{low}$ and $\mathsf{k}_\mathrm{w}^\mathrm{high}$, represent the limit cases of the formulation developed for moderately heterogeneous media, $\mathsf{k}_\mathrm{w}^\mathrm{eff}$. They are obtained when $k_\mathrm{w}^{II(c)}/k_\mathrm{w}^{I(c)} \to 0$ and $k_\mathrm{w}^{II(c)}/k_\mathrm{w}^{I(c)} \to \infty$, respectively. Thus, the definition applicable for moderately heterogeneous media can be used for the whole range of permeability ratios. Consequently, a continuous transition exists between the model for moderately heterogeneous media, Eq. (6.34), and the local equilibrium models for media with weakly permeable inclusions, Eq. (6.48), or highly permeable inclusions, Eq. (6.60). These transitions are indicated by white arrows in Fig. 6.3.

On the other hand, the local non-equilibrium model, Eq. (6.54), includes the model for quasi-impermeable inclusions, Eq. (6.59), and the local equilibrium model for weakly permeable inclusions, Eq. (6.48), as special cases. In all three models the effective permeability tensor is defined by the same local boundary value problem, Eqs. (6.49) and (6.50), which does not take into account the permeability of inclusions. The models differ in the contribution of inclusions to the storage term. The most general formulation is represented by the non-equilibrium model, where the change in the amount of water stored in inclusions is obtained by solving the local

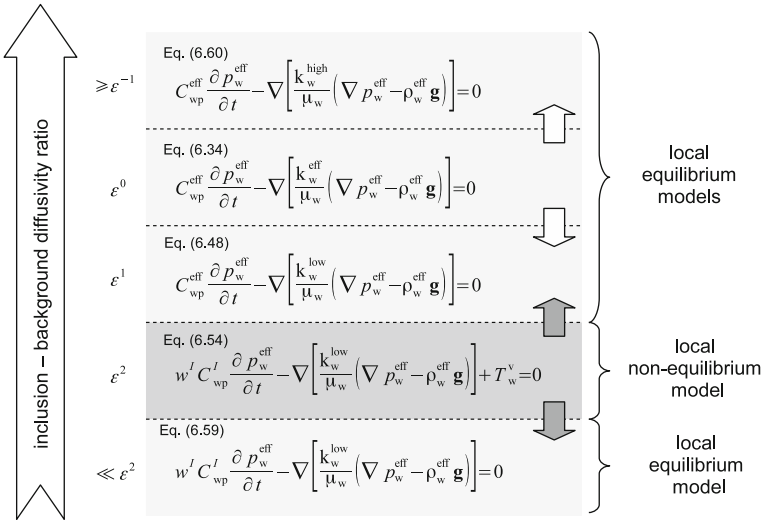

Fig. 6.3 Summary of various large-scale models with their domains of validity, *arrows* indicate possible transition between models. Modified with permission from [42]

flow equation, Eq. (6.56), and integrating either the volume of water in the inclusion or the flux at the interface Γ, according to Eq. (6.5). If the permeability of inclusions tends to zero, the changes in the local distribution of the pressure and saturation in inclusions, caused by the changes of the pressure at the interface, are insignificant. Thus, the non-equilibrium part of the storage term, associated with inclusions, becomes:

$$\frac{1}{|\Omega|}\int\limits_{\Omega^{II}} C_{\mathrm{wp}}^{II}\,\frac{\partial\, p_{\mathrm{w}}^{II}}{\partial\, t}\,\mathrm{d}\Omega \approx 0. \tag{6.65}$$

Consequently, the model for quasi-impermeable inclusions, Eq. (6.59), is obtained.

The second limit case of the local non-equilibrium model arises when

$$k_{\mathrm{w}}^{II(c)} \rightarrow k_{\mathrm{w}}^{I(c)}.$$

At the local scale, the characteristic time of flow in the inclusion becomes comparable with the time of flow in the background material and it can be assumed that the water pressure inside each inclusion equilibrates instantaneously with the pressure in the background material via the interface condition Eq. (6.57), so

$$p_{\mathrm{w}}^{II}(\mathbf{x},\mathbf{y},t) \rightarrow p_{\mathrm{w}}^{\mathrm{eff}}(\mathbf{x},t).$$

Thus, the non-equilibrium part of the storage term can be written as:

$$\frac{1}{|\Omega|}\int\limits_{\Omega^{II}} C_{\mathrm{wp}}^{II}\,\frac{\partial\, p_{\mathrm{w}}^{II}}{\partial\, t}\,\mathrm{d}\Omega \approx w^{II}\,C_{\mathrm{wp}}^{II}\,\frac{\partial\, p_{\mathrm{w}}^{\mathrm{eff}}}{\partial\, t} = w^{II}\,\frac{\partial\,\theta_w^{II}\left(p_{\mathrm{w}}^{\mathrm{eff}}\right)}{\partial\, t} \tag{6.66}$$

and the local equilibrium model for weakly permeable inclusions, Eq. (6.48), is recovered. The possible transitions between various models are indicated by dark arrows in Fig. 6.3.

In view of the above considerations, a generalized model for all values of the permeability ratio can be proposed in the following form [42]:

$$w^{I}\,C_{\mathrm{wp}}^{I}\,\frac{\partial\, p_w^{eff}}{\partial\, t} - \nabla\left[\frac{\mathsf{k}_{\mathrm{w}}^{\mathrm{eff}}}{\mu_{\mathrm{w}}}\,\nabla\left(p_{\mathrm{w}}^{\mathrm{eff}} - \rho_{\mathrm{w}}^{\mathrm{eff}}\,\mathbf{g}\right)\right] + T_{\mathrm{w}}^{\mathrm{v}} = 0, \tag{6.67}$$

where Q is the non-equilibrium part of the storage term associated with inclusions and obtained from the local flow equation (6.56) and the effective permeability tensor $\mathsf{k}_{\mathrm{w}}^{\mathrm{eff}}$ includes both background and inclusions permeabilities according to Eqs. (6.43)–(6.47). For weakly permeable inclusions, the definition of the effective permeability becomes equivalent to the definition given by Eqs. (6.49) and (6.50), while the non-equilibrium term $T_{\mathrm{w}}^{\mathrm{v}}$ accounts for the local variability of the pressure and saturation in inclusions. For moderate heterogeneity or highly permeable inclusions, the influence of inclusions on the effective permeability is captured, while the local distribution of the pressure in inclusions obtained from the local flow equation quickly reaches the equilibrium state at the scale of a single periodic cell. Thus, all the cases shown in Fig. 6.3 are represented.

The model requires an initial condition for the large-scale pressure $p_{\mathrm{w}}^{\mathrm{eff}}$ as well as an additional initial condition for the pressure in inclusions $p_{\mathrm{w}}^{II}(\mathbf{x}, \mathbf{y}, t = 0)$. The boundary conditions for the large-scale equation are specified in the same way as for the standard Richards equation (Sect. 2.3.2), for instance, as Dirichlet conditions (pressure or saturation in the background material) or Neumann conditions (water flux across the external boundary of the domain). The boundary condition for the local flow equations is given by the continuity of pressure at the interface, Eq. (6.57).

6.5 Numerical Implementation

Numerical implementation of the generalized model is performed in two stages:

1. Computation of the effective permeability function $\mathsf{k}_{\mathrm{w}}^{\mathrm{eff}}\left(p_{\mathrm{w}}^{\mathrm{eff}}\right)$ defined by the local boundary value problem, Eqs. (6.43) and (6.44).
2. Solution of the large-scale flow equation, Eq. (6.65), coupled with the solution of the local-scale flow equations in inclusions, Eq. (6.56).

The examples presented in this chapter were computed with numerical codes EFFCOND [40] (already mentioned in Chap. 5) and DPOR-2D [43, 44], developed by the author. EFFCOND solves the local boundary value problem for effective

conductivity in a three dimensional rectangular domain. The two porous materials are assumed locally isotropic and can be characterized by different relative permeability functions. The domain is covered with a uniform rectangular grid and the elliptic partial differential equation is solved with cell-centred finite volume scheme. The code allows to solve the local boundary value problem for a number of values of the capillary pressure from a user-specified range, creating an effective permeability function in tabulated form, which is then used as input to the numerical code DPOR-2D. During the solution of the large-scale equation, the components of the effective permeability tensor for any given value of the capillary are interpolated linearly from the table.

The code DPOR-2D solves the coupled flow equations for the field-scale domain and inclusions. In principle such type of coupling can be handled in three different ways:

- Full coupling implies that the discrete equations for the large-scale flow and local flow are assembled into one large system of $N \times (1 + M)$ unknowns, where N is the number of nodes in the large-scale domain and M is the number of nodes in the interior of an inclusions.
- Iterative coupling means that in each time step the large-scale equation and the local-scale equations are solved separately in such a way that one iteration of the large-scale equation follows one iteration of the local equations, and each solution is used to update the other one until a specific convergence criterion is met.
- Sequential coupling consists in solving for each time step first the large-scale equation, with the values of the non-equilibrium term from the previous step, and then solving the local-scale equations with the updated values of the interface conditions. Thereafter the solution proceeds to the next time step.

In the code DPOR-2D an iterative coupling procedure was applied in order to avoid the necessity to solve discrete equations with large number of unknowns. On the other hand, preliminary analysis showed that sequential coupling leads to convergence problems, due to strong interdependencies between the large-scale and local equations. In the numerical code, several simplifying assumptions were introduced with respect to the more general formulation presented above:

- large-scale problem is two-dimensional, in either cartesian or radial coordinates,
- local flow in inclusions can be described using the MINC approximation,
- large-scale permeability tensor is diagonal,
- permeability of inclusions is scalar,
- flow is incompressible.

For the large-scale domain, a uniform rectangular grid is used, Fig. 6.4. The large-scale equation is discretized in space using the vertex-centred finite volume approach with two-point flux estimation. The discretization with respect to time is carried out with first-order implicit Euler scheme. The non-equilibrium transfer $T_{\mathrm{w}}^{\mathrm{v}}$ is expressed in terms of the average water content in the inclusions $\bar{\theta}_{\mathrm{w}}^{II}$, computed from the local-scale flow equation:

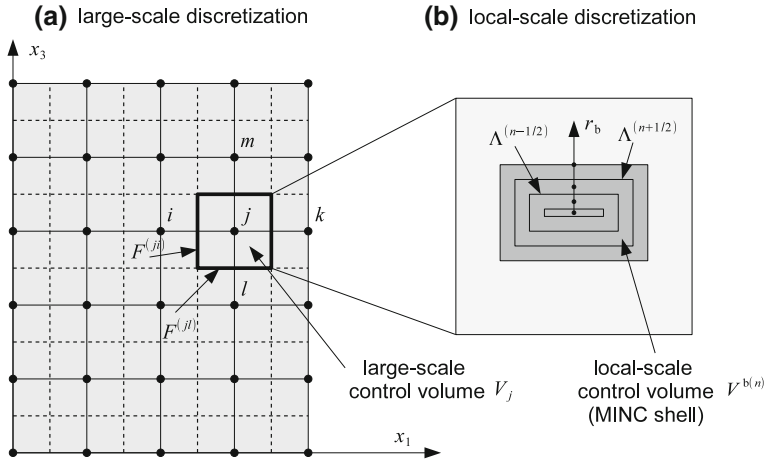

Fig. 6.4 Spatial discretization of the large-scale and local domains used in DPOR-2D numerical code

$$T_{\mathrm{w}}^{\mathrm{v}(j,\tau+1)} = w^{II}\,\frac{\bar{\theta}_{\mathrm{w}}^{II(j,\tau+1)} - \bar{\theta}_{\mathrm{w}}^{II(j,\tau)}}{\Delta t}\,. \tag{6.68}$$

This yields the following discretization scheme for the upscaled equation:

$$\begin{aligned} w^{I}\,|V^{(j)}|\,\frac{\theta_{\mathrm{w}}^{I(j,\tau+1)} - \theta_{\mathrm{w}}^{I(j,\tau)}}{\Delta t} + w^{II}\,|V^{(j)}|\,\frac{\bar{\theta}_{\mathrm{w}}^{II(j,\tau+1)} - \bar{\theta}_{\mathrm{w}}^{II(j,\tau)}}{\Delta t} \\ + Q_{\mathrm{w}}^{(ji,\tau+1)} + Q_{\mathrm{w}}^{(jk,\tau+1)} + Q_{\mathrm{w}}^{(jl,\tau+1)} + Q_{\mathrm{w}}^{(jm,\tau+1)} = 0, \end{aligned} \tag{6.69}$$

where i, j, k, l and m are node indices and τ is time level index. In the above equation both θ_{w}^{I} and $\bar{\theta}_{\mathrm{w}}^{II}$ depend on the value of the main variable $p_{\mathrm{w}}^{\mathrm{eff}}$. In the first case, the value of θ_{w}^{I} is calculated directly from the capillary function for the background material. In the second case, $\bar{\theta}_{\mathrm{w}}^{II}$ is obtained from the solution of the local-scale flow equation describing flow in an inclusion associated with the node j of the large-scale grid, with the coupling condition at the interface, Eq. (6.57). The water fluxes at the control volume faces are approximated using two-point finite difference formulae, e.g.:

$$Q_{\mathrm{w}}^{(ji,\tau+1)} = -\left|F^{(ji)}\right|\,\frac{k_{\mathrm{w},11}^{\mathrm{eff}(ji)}}{\mu_{\mathrm{w}}}\left(\frac{p_{\mathrm{w}}^{\mathrm{eff}(j,p+1)} - p_{\mathrm{w}}^{\mathrm{eff}(i,p+1)}}{\Delta x_1^{(ji)}}\right), \tag{6.70}$$

$$Q_{\mathrm{w}}^{(jl,\tau+1)} = -\left|F^{(jl)}\right|\,\frac{k_{\mathrm{w},33}^{\mathrm{eff}(jl)}}{\mu_{\mathrm{w}}}\left(\frac{p_{\mathrm{w}}^{\mathrm{eff}(j,\tau+1)} - p_{\mathrm{w}}^{\mathrm{eff}(l,\tau+1)}}{\Delta x_3^{(jl)}} + \rho_{\mathrm{w}}^{(jl)}\,g\right), \tag{6.71}$$

where $|F^{(ji)}|$ and $|F^{(jl)}|$ denote the areas of the corresponding control volume faces, while $k_{\mathrm{w},11}^{\mathrm{eff}(ji)}$ and $k_{\mathrm{w},33}^{\mathrm{eff}(jl)}$ are the average inter-nodal permeabilities. For the sake of simplicity, in the examples presented here the inter-nodal relative permeability is computed using the arithmetic mean approach. Other, more accurate approaches, as the ones discussed in Chap. 4, could be used if necessary. Note, however, that in the case of methods based on the integration of the relative permeability function, the integral of the function (flux potential Φ_{p}) must be computed and tabulated at the preprocessing stage, since the large-scale relative permeability obtained from homogenization cannot be described by a closed analytical formula and is in general different for each spatial direction.

At each point of the large-scale domain, an additional equation for the local flow in a representative inclusion must be solved. While Eq. (6.56) describes a three dimensional problem, in the numerical implementation a simplified one-dimensional formulation was applied, following the MINC approach, discussed previously. The spatial discretization of a single inclusion is presented in Fig. 6.4b. In a discrete form the local flow equation for node n in an inclusion can be written as follows:

$$\left|V^{\mathrm{b}(n)}\right| \frac{\theta_{\mathrm{w}}^{II(n,\tau+1)} - \theta_{\mathrm{w}}^{II(n,\tau)}}{\Delta t} + Q_w^{\mathrm{b}(n+1/2,\tau+1)} - Q_w^{\mathrm{b}(n-1/2,\tau+1)} = 0, \tag{6.72}$$

where the fluxes are approximated by the following algebraic formulae:

$$Q^{\mathrm{b}(n+1/2,\tau+1)} = \left|\Lambda^{(n+1/2)}\right| \frac{k_{\mathrm{w}}^{(n+1/2,\tau+1)}}{\mu_{\mathrm{w}}} \left(\frac{p_{\mathrm{w}}^{II(i+1,\tau+1)} - p_{\mathrm{w}}^{II(i,\tau+1)}}{\Delta r_{\mathrm{b}}} \right), \tag{6.73}$$

where $|\Lambda^{(n+1/2)}|$ is the area of the boundary between adjacent nested gridblocks in the MINC discretization. Again, in the above formula the inter-nodal relative permeabilities $k_{\mathrm{w}}^{(n+1/2,\tau+1)}$ are computed as algebraic averages of the nodal values. More accurate results could be obtained with improved averaging formulae for the relative permeability, as presented in Chap. 4. However, in the numerical simulations presented in this chapter the results were not sensitive to the choice of permeability averaging scheme, due to fine grid spacing in inclusions.

The iterative coupling procedure applied at each time step is shown schematically in Fig. 6.5. The iterations are started with the values of the large-scale pressure $p_{\mathrm{w}}^{\mathrm{eff}}$ taken from the previous time step, or extrapolated from two previous time steps. Then the local equations are solved at each macroscopic node j to obtain the new approximation of the water content in the inclusions, using $p_{\mathrm{w}}^{\mathrm{eff}(j,\tau+1,\upsilon)}$ as the boundary condition. The resulting values are then integrated for each inclusion and used to compute the residuum of Eq. (6.69). The local-scale equations are then solved once again using a perturbed value of the macroscopic water pressure $p_{\mathrm{w}}^{\mathrm{eff}(j,\tau+1,\upsilon)} + \upsilon$ in order to obtain the perturbed values of the water content in inclusions, which are then used to estimate the derivative of the non-equilibrium term with respect to the main variable $p_{\mathrm{w}}^{\mathrm{eff}}$. The derivative is added to the jacobian matrix for the large-

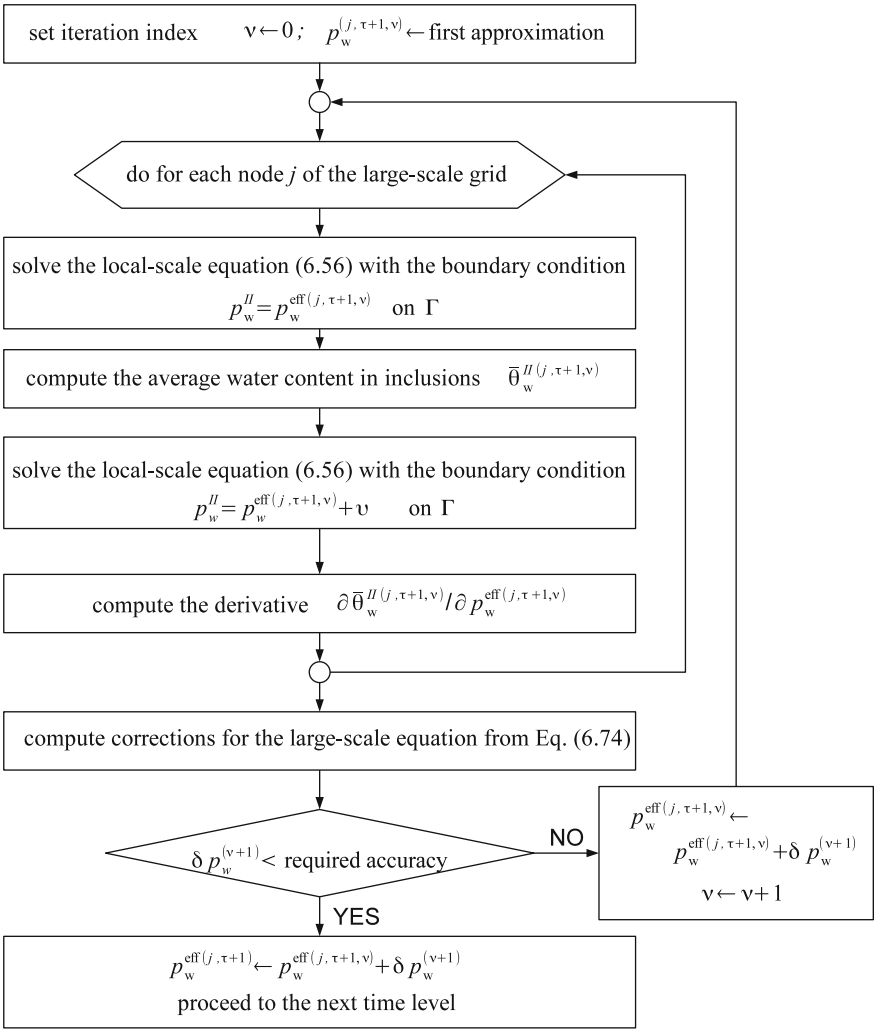

Fig. 6.5 Coupled solution of the large-scale and local-scale equations for a single time step

scale equation **J**. Then a single iteration for the discretized large-scale equation is performed:

$$\mathbf{J}^{(\nu)}\, \delta\mathbf{p}^{(\nu+1)} = -\mathbf{P}^{(\nu)}\ , \tag{6.74}$$

where $\delta\mathbf{p}$ is the vector of corrections to the nodal values of the effective water pressure and **P** is the vector of the residuals of discrete equations (6.69). It is possible to use either full jacobian, according to the Newton method, or an approximation in the form of modified Picard method, where the derivatives of the relative permeability over the water pressure are neglected (see Sect. 3.3.2). The latter option was used in this

work. If the corrections are smaller than the prescribed error tolerance, the iterations are terminated. Otherwise, the local flow equations are solved using the updated values of the effective pressure as the boundary condition and the iterative process is continued. This solution scheme was initially developed for macroscopically one-dimensional problems (DPOR-1D code, described in detail in [39]) and later extended to two dimensions [44]. It was shown to be convergent and reliable in a number of applications [25, 43, 44].

6.6 Comparison with Darcy-Scale Numerical Solutions

In order to illustrate the influence of inclusion-background diffusivity ratio, a number of numerical simulations were carried out for a model heterogeneous medium shown in Fig. 6.6. The scale parameter is $\varepsilon = 0.1$, which is often considered as the maximum value for which the homogenization approach is applicable [7]. The two porous materials are isotropic and characterized by the same capillary and relative permeability functions, the only difference being the absolute permeabilities. While such an assumption is not likely to be fulfilled in a real-life case, it allows to clearly distinguish between various flow regimes by keeping the ratio of permeabilities constant for each simulation (application of the model to flow in real heterogeneous porous media is described in the next section). The hydraulic functions are given by the van Genuchten–Mualem model, Eqs. (2.17), (2.40) and (2.41) with the following parameters: $p_g = 2,500\,\text{Pa}$, $n_g = 1.8$ and $m_g = 1 - 1/n_g$. The porosity is $\phi = 0.4$, the residual air saturation $S_{ra} = 0$ and the residual water saturation $S_{rw} = 0.1$. The absolute permeability of the background material is $k_s = 3 \times 10^{-12}\,\text{m}^2$. Eight sets of simulations were performed, each with a different value of the absolute permeability in inclusions, so that the values of the inclusion-background diffusivity ratio $\mathscr{R}_d$ (in this case equal to the permeability ratio) were equal to 10^3, 10^1, 1, 10^{-1}, 10^{-2}, 10^{-3}, 10^{-4} and 10^{-6}, respectively.

For each value of the inclusions permeability, three simulations were performed: two fine-scale solutions based on the two-phase model and the Richards equation, respectively, and an upscaled solution based on the model described in the previous section. The fine-scale solutions were carried out on a uniform dense grids of 20 elements in the horizontal direction and 200 elements in the vertical direction, with explicit representation of the heterogeneous structure of the medium. The upscaled solution was obtained on a numerical grid of 1 by 50 elements. While an apparently more logical choice would be to associate each periodic cell with a single element of the macroscopic model, this would result in a coarse grid of only 10 elements in the vertical direction, leading to significant errors in the spatial discretization of fluxes, as discussed in Chap. 4. As the upscaled model represents a continuum description of the behaviour of an heterogeneous system, the choice of the spatial discretization is in principle independent of the actual size of the periodic cell, although for real-life field-scale applications one would expect grid elements to be significantly larger than the periodic cell.

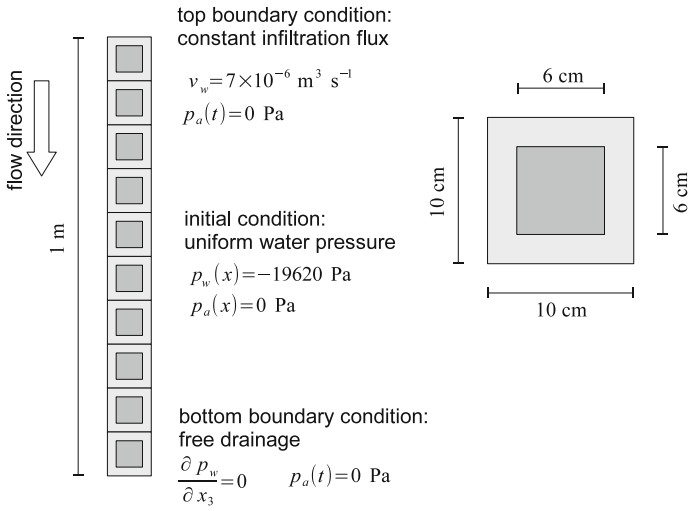

Fig. 6.6 Structure of heterogeneous medium used in numerical examples

Figure 6.7 shows the relationship between the ratio of inclusion to background permeability and the ratio of effective permeability to the background permeability for the considered geometry of periodic cell, as obtained with the general formulation of the local boundary value problem, Eqs. (6.43)–(6.47). Note that the effective permeability is the same for each spatial direction. The symmetry of the plot in the logarithmic scale can be clearly seen. For the permeability of inclusion smaller or larger than the permeability of background by a factor of 100 or more, the effective permeability–background permeability ratio becomes constant. It means that the effective permeability is a linear function of the background permeability and is not affected by the permeability of inclusions. This result is consistent with the discussion of the upscaled models for weakly permeable and highly permeable inclusions presented earlier in this chapter.

In each simulation the same set of initial and boundary conditions was used, which corresponds to infiltration in a dry soil column with free drainage at the bottom, as shown in Fig. 6.6. The value of the infiltration flux was chosen in such a way that the medium remains unsaturated even for the smallest considered value of the effective permeability, corresponding to the inclusion-background diffusivity ratio of 10^{-6}.

The results obtained with various models are compared in terms of the volumetric water flux observed at the outflow of the column in function of time, which can be called breakthrough curve, by analogy to the experiments on solute transport. The breakthrough curves for highly permeable inclusions ($\mathscr{R}_\mathrm{d} = 10^3$ and $\mathscr{R}_\mathrm{d} = 10^1$) are shown in Fig. 6.8, together with the results for homogeneous medium ($\mathscr{R}_\mathrm{d} = 1$). It can be seen that the differences between the two-phase and Richards models are negligible for all three permeability ratios. Moreover, the results obtained with the upscaled model are very close to the Darcy-scale solutions. As the

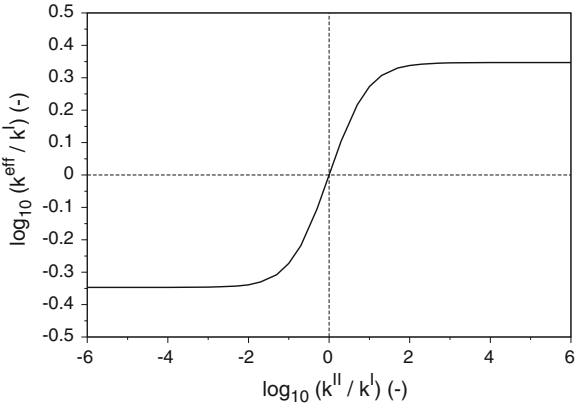

Fig. 6.7 Relation between the inclusion-background permeability ratio and the effective permeability –background permeability ratio

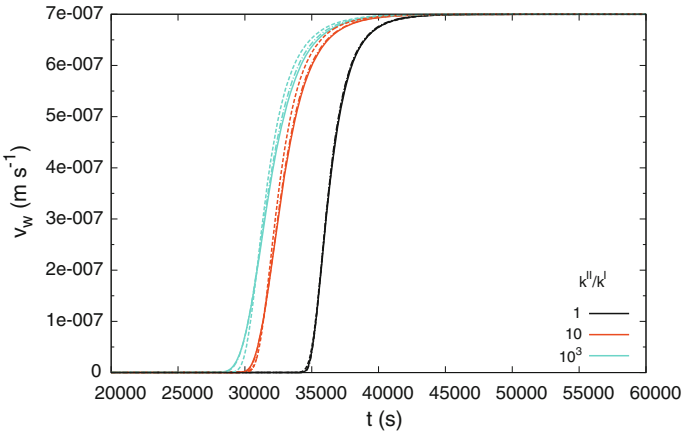

Fig. 6.8 Evolution of the volumetric water flux at the outflow for homogeneous medium and highly permeable inclusions. *Solid lines*—Darcy-scale Richards model, *dash-dot lines*—Darcy-scale two-phase model, *dashed lines*—generalized upscaled model

inclusion-background permeability ratio increases, the outflow from the column starts earlier, but the shape of the breakthrough curve remains unchanged. In fact, for all three values of the permeability ratio the homogenization predicts that local equilibrium conditions prevail at the scale of a single periodic cell.

Figure 6.9 show the distribution of the water saturation in the heterogeneous medium for various permeability ratios. These results are obtained with the Darcy-scale solution of the Richards equation. Since the capillary function is the same for both materials, the variability of the saturation results from the variability of the water pressure. Comparing the results for homogeneous medium, $\mathcal{R}_\mathrm{d} = 1$, with the results for $\mathscr{R}_\mathrm{d} = 10^3$ one can note that in the latter case the saturation in the domain is

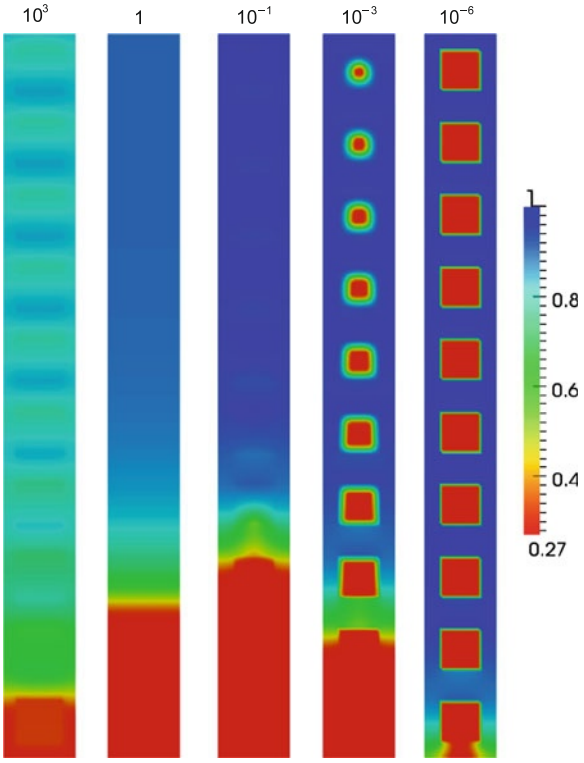

Fig. 6.9 Distribution of the water saturation in the heterogeneous medium obtained from the fine scale solution of the Richards equation for different values of the hydraulic diffusivity ratio $\mathscr{R}_\mathrm{d}$

lower, because the effective permeability is higher and the value of the permeability necessary to transmit the infiltrating water flux corresponds to a lower saturation. Moreover, for highly permeable inclusions one can see that the saturation is not uniform in the inclusions, but the variations are relatively small. This can be checked in Fig. 6.10a, which shows profiles of the water saturation along the vertical symmetry axis of the column obtained with different models for $t = 21,600\,\mathrm{s}$. In the case of the upscaled model, the saturation in the background and the average saturation in inclusions are both shown. It can be seen that the saturation profile obtained from the Darcy-scale solution (solid line) shows oscillations. These oscillations are caused by the action of gravity force at the local scale. In each inclusion the lower part is more saturated than the upper part. This effect is not represented in the upscaled model, which neglects local-scale gravity effects. Despite this simplification, the profile of the average saturation in the background material and in the inclusions, represented by the dashed and dotted line, respectively, follow the fine-scale profile with good accuracy. Moreover, in the upscaled model the values for background and inclusions virtually coincide with each other, indicating local equilibrium conditions.

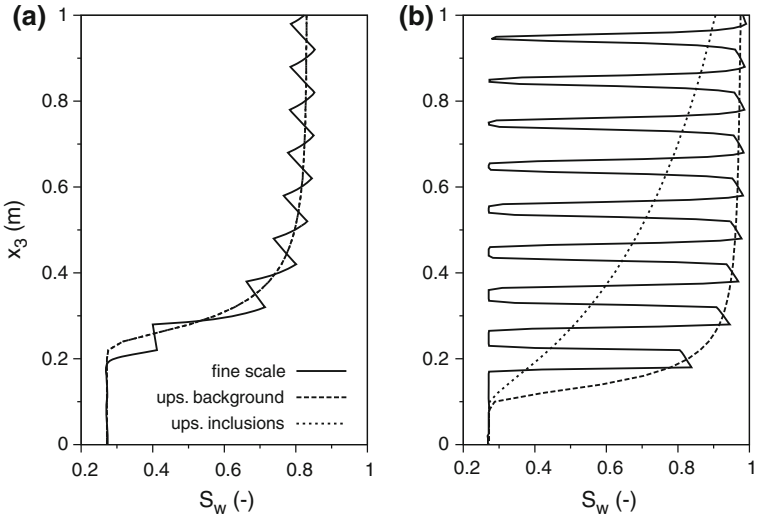

Fig. 6.10 Profiles of the water saturation along the vertical symmetry axis of the column obtained from the fine scale solution of the Richards equation and from the upscaled model: **a** $\mathscr{R}_\mathrm{d} = 10^3$, **b** $\mathscr{R}_\mathrm{d} = 10^{-3}$. In the upscaled model, the values for inclusions represent averages of the local distribution

The results for weakly permeable inclusions show a more varied behaviour in function of the permeability contrast, as shown in Fig. 6.11. For $\mathscr{R}_\mathrm{d} = 10^{-1}$ the breakthrough curve has the same shape as for the homogeneous medium, but the outflow is lagged in time due to a reduction of the effective permeability. However, as the permeability of inclusions decreases further, the outflow appears earlier, while the breakthrough curve is characterized by two distinct phases. In the first phase, the value of the flux increases rapidly, but does not reach the maximum (steady-state) value. The second phase is represented by a much slower, gradual increase of the flux towards its steady state value. Such effect is caused by local non-equilibrium conditions at the scale of a single periodic cell. During infiltration a part of the water bypasses the weakly permeable inclusions, contributing to the early outflow. However, the steady state cannot be reached until all inclusions reach capillary equilibrium with the surrounding matrix, and the water is no longer absorbed by the inclusions. The permeability of inclusions is sufficiently low to prevent instantaneous equilibration of the pressures, but on the other hand it is sufficiently large to allow significant quantities of water to enter the inclusions. These effects become visible for $\mathscr{R}_\mathrm{d} = 10^{-2} = \varepsilon^2$ and are most pronounced for $\mathscr{R}_\mathrm{d} = 10^{-3} = \varepsilon^3$. They are still significant, though to a lesser extent, for $\mathscr{R}_\mathrm{d} = 10^{-4} = \varepsilon^4$. However, for $\mathscr{R}_\mathrm{d} = 10^{-6} = \varepsilon^6$ the breakthrough curve regains the steep shape similar to the case of homogeneous medium, although the breakthrough appears at much earlier time. This can be explained by the fact that for very low permeability of inclusions the

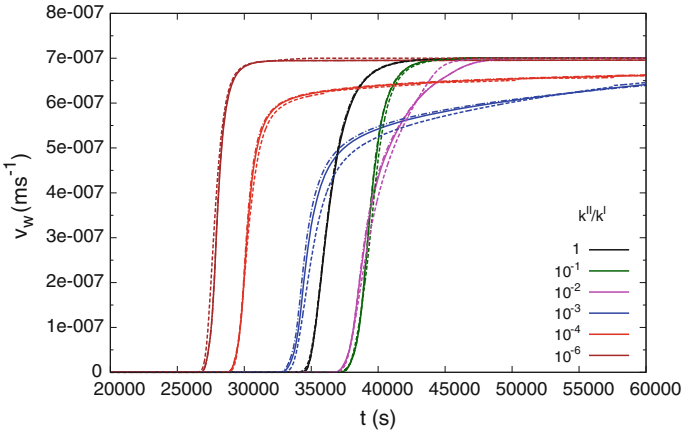

Fig. 6.11 Evolution of the volumetric water flux at the outflow for homogeneous medium and weakly permeable inclusions. *Solid lines*—Darcy-scale Richards model, *dash-dot lines*—Darcy-scale two-phase model, *dashed lines*—generalized upscaled model

actual amount of water that enters them is very small and most of the infiltrating water bypasses the inclusions and contributes to the outflow.

These observations are confirmed by Fig. 6.9, which shows the distribution of the water saturation for the permeability ratios $\mathscr{R}_\mathrm{d} = 10^{-1}$, 10^{-3} and 10^{-6}. In the first case, differences in saturation between the background and inclusions appear only at the infiltration front and quickly disappear. In the second case, differences persist in all periodic cells, indicating local non-equilibrium of the water pressure. With time, the saturation in inclusions tends to the saturation in the background material, as local pressure equilibrium is approached. In the third case, the saturation in all inclusions remains practically equal to the initial saturation, as only very small amount of water enters the inclusions due to their low permeability.

It can be noted that also in the case of weakly permeable inclusions the solutions obtained using the Richards equation and the two-phase model for heterogeneous medium are virtually coinciding, Fig. 6.11. The generalized upscaled model follows the reference solutions with a reasonable accuracy. Some slight discrepancies arise for $\mathscr{R}_\mathrm{d} = 10^{-2}$ and 10^{-3}, possibly due to differences in the spatial grids used for the upscaled and fine-scale models. It should be also remembered that the scale separation parameter is $\varepsilon = 0.1$, which can be considered a limit value for applicability of homogenization, as mentioned earlier. It means that the effects of terms of the higher orders of ε, which were neglected in the upscaled equations, can be relatively important. This is also a possible explanation for the fact that the local non-equilibrium effects are the most pronounced for permeability ratio of 10^{-3}, and not 10^{-2} as predicted theoretically. These remarks notwithstanding, one can conclude that the upscaled model captures the important features of flow for the whole range of inclusion-background permeability ratio.

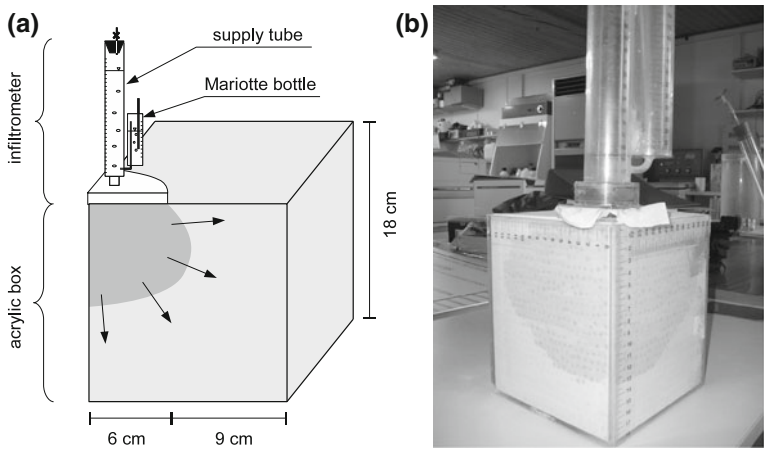

Fig. 6.12 Scheme **a** and photograph **b** of the experimental setup. Scheme not to scale. Figure **b** reproduced with permission from [26]

6.7 Comparison with Experiment

Experimental verification of the upscaled model is described in [26, 44]. The experiments were carried out at Laboratoire d'étude des Transferts en Hydrologie et Environnement (LTHE) in Grenoble, France. A model binary medium was created by embedding spheres made of sintered clay in fine sand in a quasi-periodic arrangement. The hydraulic characteristics of the two materials were obtained from independent tests performed on homogeneous samples. The resulting capillary and permeability functions were then used to compute the large-scale hydraulic functions, which in turn were applied in the numerical simulation of flow in heterogeneous medium.

6.7.1 Experimental Setup

The setup consisted of an acrylic box having dimensions 15 cm by 15 cm in the horizontal directions and 18 cm in the vertical direction, Fig. 6.12. The box was opened at the top and filled completely with a mixture of sand and spheres. The spheres were placed manually layer by layer, with the spheres in each layer touching each other, Fig. 6.13. After each layer was placed, the void space between the spheres was filled with sand and the medium was compacted. Both sand and spheres were in air-dry conditions. Three experiments were carried out and for each of them the box was filled anew with air-dry porous materials. Three additional tests were carried out for homogeneous sand, in order to provide data for independent estimation of the hydraulic parameters for sand. Also in this case, for each experiments the box was filled with air-dry material, keeping the same packing and compacting procedure.

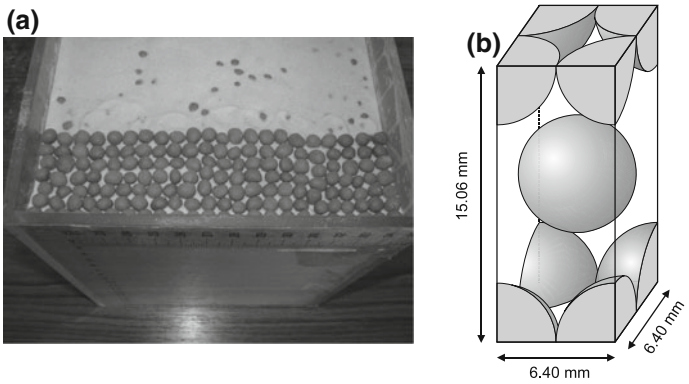

Fig. 6.13 Structure of the binary medium: **a** arrangement of spheres in sand, **b** periodic cell. Figure **a** reproduced with permission from [26], figure **b** reproduced with permission from [44]

At the top surface of the medium, a quarter-disc infiltrometer was placed in one of the corners of the box. The radius of the infiltrometer base was 6 cm. The infiltrometer allowed to impose a specific constant value of the water pressure at the contact between its base and the surface of the porous medium, while the amount of infiltrating water was measured at regular time intervals. The applied pressure head was $h_w = -8.5\,\text{cm}$ ($p_w = -834\,\text{Pa}$) in all experiments. The estimated measurement error in the water volume was $1.25\,\text{cm}^3$. The cumulative infiltration curves for homogeneous sand and double porosity medium are shown in Fig. 6.14 and the corresponding values of infiltration flux in Fig. 6.15. Moreover, the position of the wetting front on the vertical sides of the box and at the upper surface was observed. Due to limited amount of water in the supply tube, the wetting front never reached the bottom of the box nor the sides opposite to the infiltrometer. The observed wet zone had always a regular and symmetric shape, which suggested that axisymmetric conditions of the flow were preserved.

6.7.2 Material Parameters

Hostun HN38 sand [14] was used in the experiments. It has a relatively uniform grain distribution with the average grain size of 162 μm and 51 % of the particles (by weight) in the size interval between 100 and 200 μm. As shown in Table 6.1, in all experiments the porosity of the sand was very similar and close to 0.4 (the porosity was calculated assuming specific density of sand particles $2.65\,\text{g}\,\text{cm}^{-3}$). It was assumed that the sand can be characterized by van Genuchten capillary function and a power-type function for the relative permeability:

Table 6.1 Parameters of the experiments in sand and binary medium

	Sand			Binary medium		
	Minimum	Maximum	Average	Minimum	Maximum	Average
Volumetric fraction of sand	1.000	1.000	1.000	0.555	0.555	0.555
Porosity of sand	0.376	0.295	0.0	16215	2.27	0.56
Total time of the infiltration	0.376	0.295	0.0	16215	2.27	0.56
Total volume of the infiltrated water	0.376	0.295	0.0	16215	2.27	0.56

For each category minimum, maximum and average values of the three experiments are reported. Reproduced with permission from [44]

$$S_{ew} = \left[1 + \left(-p_w/p_g\right)^{n_g}\right]^{-m_g}, \tag{6.75}$$

$$\theta_w = \theta_{rw} + S_{ew}\,(\theta_{sw} - \theta_{rw}), \tag{6.76}$$

$$k_w = k_{sw}\,k_{rw}, \tag{6.77}$$

$$k_{rw} = (S_{ew})^{\eta_w}, \tag{6.78}$$

with $m_g = 1 - 2/n_g$ and η_w considered as an independent parameter. This model, advocated in a number of papers, e.g. [15, 22], was chosen based on preliminary tests, where it offered a better fit to experimental data than the most commonly used Brooks–Corey and van Genuchten–Mualem models.

The parameters of the hydraulic functions for sand were obtained partly from an inverse analysis of the infiltration experiments performed in homogeneous sand and partly from independent measurements or assumptions. The residual water content was assumed to be $\theta_{rw}^I = 0$, since the volumetric water content measured gravimetrically for air dry sand was below 0.001. The saturated water content was set to $\theta_{sw}^I = 0.342$, which was the value measured in previous one dimensional experiments on the same sand [28], with very similar porosity. The saturated water content is smaller than the porosity by about 13 %, due to pore-scale air trapping. The assumed value of θ_{sw}^I is also consistent with the value measured in the radial flow experiments after the end of infiltration at the soil surface, which was 0.314. As the latter value corresponds to the capillary pressure head of 8.5 cm, imposed by the infiltrometer, one should expect it to be lower than θ_{sw}^I.

It is well known that the parameter fitting based only on the cumulative infiltration curve often leads to problems with finding a unique set of parameters, because some of the parameters may be highly correlated with each other, e.g. [17]. In order to reduce the number of parameters determined by inverse analysis, the exponents n_g and η_w were set to fixed values $n_g = 7$ and $\eta_w = 7$. It was found by a trial and error procedure that such values best represent the sharp transition between wet and dry zones observed in the experiments. The remaining parameters, k_{sw} and $\alpha_g = 1/p_g$, were obtained by numerical solution of an inverse problem. This consisted in minimizing the sum of squared differences between measured and computed values of the cumulative infiltration for all measurement times. The objective function was minimized using Marquard–Levenberg algorithm [34] integrated with the forward solution by DPOR-2D code for homogeneous sand. The numerical solution for

Table 6.2 Hydraulic parameters of sand and sintered clay [44]

	ϕ (–)	θ_{sw} (–)	θ_{rw} (–)	p_g (Pa)	n_g (–)	m_g (–)	η_w (–)	k_{sw} (m^2)	K_{sw} (m s^{-1})
Sand	0.392	0.342	0.0	2964	7.00	0.71	7.00	1.20e − 11	1.18e − 4
Clay	0.376	0.295	0.0	16215	2.27	0.56	–	1.17e − 14	1.15e − 7

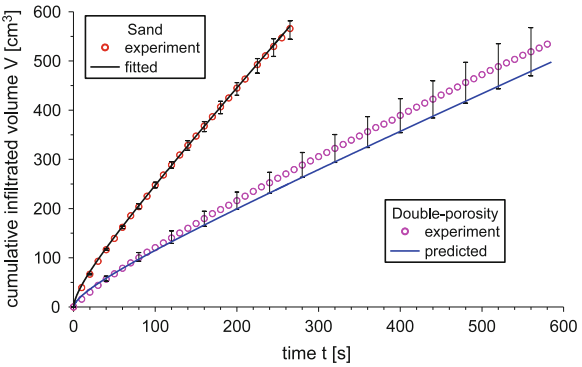

Fig. 6.14 Cumulative amount of infiltrated water as a function of time, for homogeneous sand and double-porosity medium, as obtained from the experiments and numerical simulations. Modified with permission from [44]

infiltration in homogeneous sand was based on the Richards equation (two-phase model was not applied in the analysis of this experiment). The initial condition was assumed to be $p_w = -98,100$ Pa (water pressure head $h_w = -1,000$ cm). At the part of the boundary in contact with the infiltrometer, the water pressure was $p_w = -834$ Pa ($h_w = -8.5$ cm). Other boundaries were considered impermeable for water. A uniform grid with spacing equal to 0.5 cm in both vertical and radial direction was used, with adaptive time step in the range from 10^{-12} to 1 s.

The resulting values of the sand parameters are summarized in Table 6.2. The cumulative infiltration curve corresponding to the fitted parameters is shown in Fig. 6.14. It can be seen that a very good fit is obtained. For the purposes of comparison, another inverse solution was carried out, where four parameters were fitted, i.e. k_{sw}, p_g, n_g and η_w. This resulted in a fit which was even better in terms of the cumulative infiltration curve, but very inaccurate with respect to the observed position of the wetting front [44]. For this reason, the second solution is not shown here.

The characteristics of the sintered clay, of which the spheres were made, were taken from an earlier paper [28], which describes experiments on quasi one dimensional flow in a similar binary medium. The clay spheres were produced manually in a pottery workshop, and thus showed some slight variations in shape and size. Their average diameter was 6.4 mm, with minimum and maximum measured values of 4.3 and 9.4 mm. The origin of the clay was La Bisbal, Spain. It was washed and sintered at temperature of 1,000°C, following an old traditional technology. The porosity of the sintered clay measured with mercury porosimeter was $\phi^{II} = 0.376$ with the

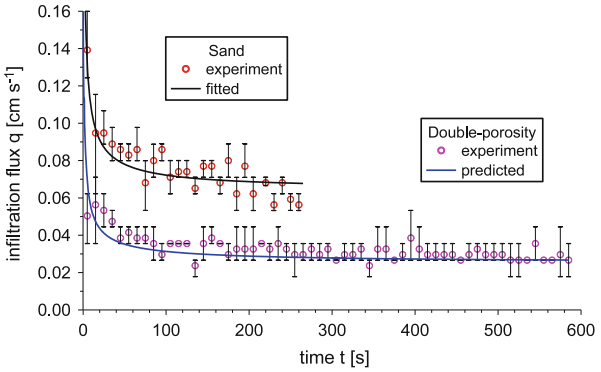

Fig. 6.15 Cumulative amount of infiltrated water as a function of time, for homogeneous sand and double-porosity medium, as obtained from the experiments and numerical simulations. Modified with permission from [44]

average pore size around 0.7 μm, the specific skeleton density $\rho_s^{II} = 3.01\,\mathrm{g\,cm^{-3}}$ and the dry bulk density $\rho_d^{II} = 1.88\,\mathrm{g\,cm^{-3}}$. Additional saturation tests were performed to determine the saturated water content in clay. The average saturated water content obtained from these test was $\theta_{sw}^{II} = 0.295$, which is significantly less than the measured porosity. The residual water content was assumed to be $\theta_{rw}^{II} = 0$.

In order to determine the hydraulic parameters of the sintered clay, an infiltration experiment was carried out using a cylinder made of the same material as the spheres [28]. The standard van Genuchten–Mualem hydraulic model was chosen, as given by Eqs. (2.17), (2.40) and (2.41). The parameters k_{sw}, $\alpha_g = 1/p_g$ and n_g were obtained by numerical optimization procedure based on minimizing the difference between simulated and measured values of the cumulative infiltration. The parameter fitting procedure was carried out using HYDRUS 1D computer program [37]. The obtained values are listed in Table 6.2. Note that the permeability of the sintered clayey material is significantly larger than the values reported for natural clay soils, e.g. [12].

The periodic cell characterizing the heterogeneous medium at the Darcy scale is shown in Fig. 6.13b. The spheres are touching each other in each horizontal layer, whereas the vertical distance between layers was based on the volumetric fraction of the spheres $w^{II} = 0.445$. For such an arrangement the effective permeability tensor is diagonal. The values of the permeability in vertical and radial directions were computed from the solution of the local boundary value problem, Eqs. (6.43) and (6.44), for the geometry shown in Fig. 6.13b. They are plotted in Fig. 6.16. It can be seen that the anisotropy is relatively small. Moreover, the effective permeability function for both spatial directions follows the shape of the permeability function for sand, i.e. it is determined mostly by the permeability of the background material.

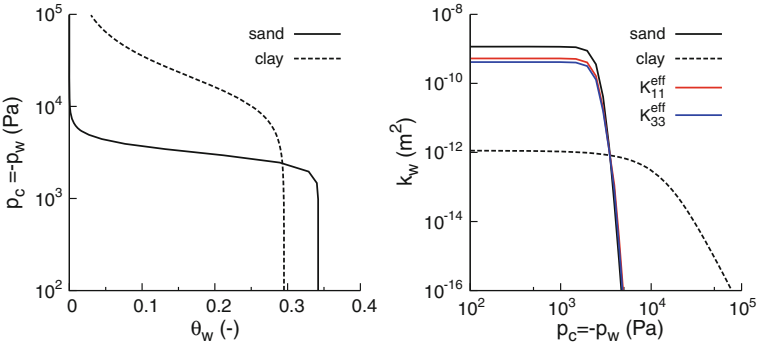

Fig. 6.16 Capillary and permeability functions for the sand, clay and composite material used in the experiments

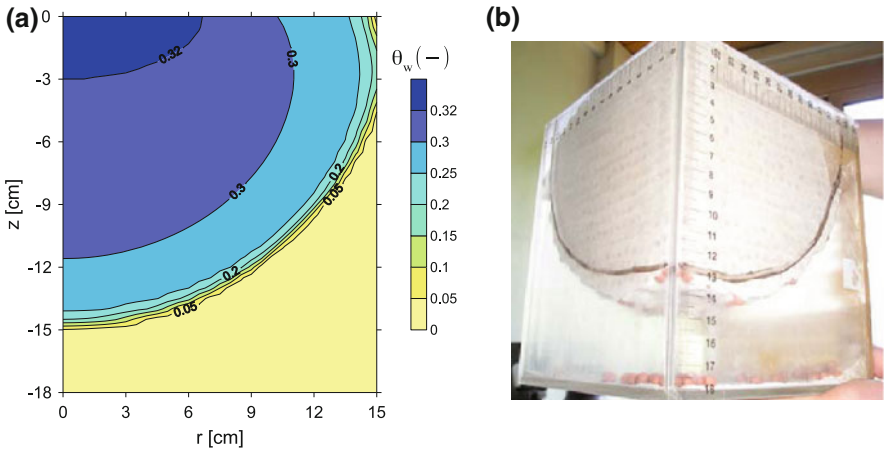

Fig. 6.17 **a** Distribution of the average water content in the heterogeneous medium (sand and spheres) at the end of the infiltration obtained from the numerical simulation using upscaled model; **b** corresponding range of the wet zone observed in the experiment. Modified with permission from [44]

6.7.3 Results

The parameters of the two materials and the effective permeability function were used as input to the upscaled model. Numerical solution was carried out for a uniform grid with spacing 0.5 cm in each direction. The spherical inclusions were discretized using 10 concentric shells for each inclusions, with uniform spacing of 0.032 cm. Other parameters were the same as in the inverse analysis for homogeneous sand.

As shown in Fig. 6.14, the cumulative infiltration curve predicted by the upscaled model is in a relatively good agreement with the experimental results. While falling slightly below the average of the experimental curves, it is still within the range of

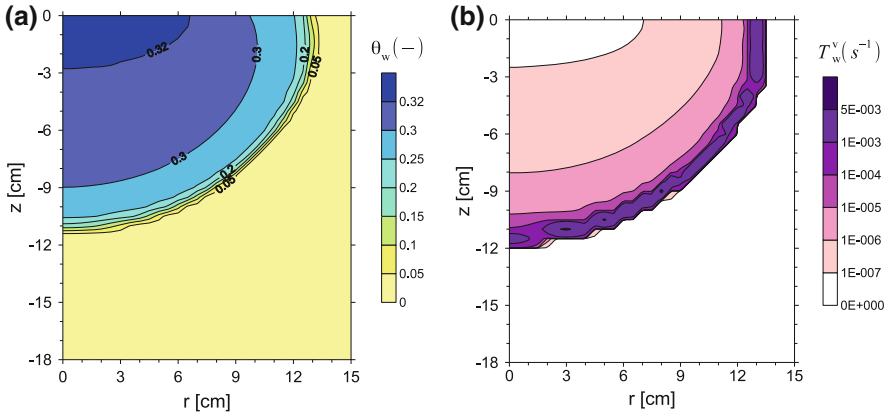

Fig. 6.18 **a** Distribution of the average water content at t=330 s and **b** the corresponding values of the non-equilibrium transfer term, as obtained from the numerical solution. Modified with permission from [44]

the measured values, indicated by the vertical bars. This is confirmed by the analysis of the instantaneous infiltration flux shown in Fig. 6.15, where similar agreement between the measured and computed values is observed. Furthermore, one can compare the distribution of the average water content in the domain obtained from the numerical solution with the range of the wet zone observed at the end of the infiltration, Fig. 6.17. The water content shown in Fig. 6.17a represents an average for the sand and spheres at a given point of the large-scale domain. Since the water content was not measured in the experiments, the comparison can be only qualitative. The sharp transition zone between dry and wet part of the domain seen in Fig. 6.17a approximately corresponds to the observed extent of the wetted "bulb" outlined in Fig. 6.17b, although the latter one is smaller by about 1–2 cm in each direction. While the agreement between simulations and observations can be further improved by adjusting one or more parameters of the upscaled model, such results are not presented here as the main objective of this analysis was to test the predictive capability of the homogenization approach.

Figure 6.18 shows distribution of the average volumetric water content at an earlier stage of the infiltration, $t = 330$ s and the corresponding spatial distribution of the background–inclusion water transfer intensity $T_{\mathrm{w}}^{\mathrm{v}}$. The transfer intensity is shown in terms of volume of water per volume of porous medium per second. It can be seen that the zone of the highest intensity of the water transfer corresponds to the wetting front. This zone is relatively narrow, while behind the infiltration front the intensity significantly diminishes. This suggests that water pressure tends to equilibrate relatively quickly and the non-equilibrium phenomena are limited to the vicinity of the wetting front, even though the inclusion-background intrinsic permeability ratio is of the order of 10^{-3}. However, the difference in intrinsic permeability is not enough to ensure significant non-equilibrium effects, since the latter ones are influenced by

the relative permeability and specific water storage functions of the two materials. In this case, it seems that the actual contrast in hydraulic diffusivities is not sufficiently large to produce prolonged non-equilibrium water transfer. While the water transfer intensity obtained from the numerical simulation cannot not be verified by direct comparison with measurements, the numerical results are generally consistent with the experiment.

References

1. Amaziane B, Bourgeat A, Koebbe J (1991) Numerical simulation and homogenization of two-phase flow in heterogeneous porous media. Transp Porous Media 6(5–6):519–547. doi:10.1007/BF00137848
2. Arbogast T (1993) Gravitational forces in dual-porosity systems: I. Model derivation by homogenization. Transp Porous Media 13(2):197–203. doi:10.1007/BF00654409
3. Arbogast T (1993) Gravitational forces in dual-porosity systems: II. Computational validation of the homogenized model. Transp Porous Media 13(2):205–220. doi:10.1007/BF00654410
4. Arbogast T, Douglas J, Hornung U (1990) Derivation of the double porosity model of single phase flow via homogenization theory. SIAM J Math Anal 21:823–836
5. Auriault JL (1983) Effective macroscopic description for heat conduction in periodic composites. Int J Heat Mass Transf 26:861–869
6. Auriault JL (1991) Heterogeneous medium: is an equivalent macroscopic description possible? Int J Eng Sci 29(7):785–795. doi:10.1016/0020-7225(91)90001-J
7. Auriault JL, Boutin C, Geindreau C (2009) Homogenization of coupled phenomena in heterogeneous media. Wiley, Hoboken
8. Bensoussan A, Lions JL, Papanicolaou G (1978) Asymptotic analysis for periodic structures. North-Holland, Amsterdam
9. Bielski W (2005) Nonstationary flows of viscous fluids through porous elastic media: homogenization method. Publ Inst Geophys Pol Acad Sci A-29(388):1–147
10. Bielski W, Telega J (1997) Effective properties of geomaterials: rocks and porous media. Publ Inst Geophys Pol Acad Sci A-26(285):1–120
11. Braun C, Helmig R, Manthey S (2005) Macro-scale effective constitutive relationships for two phase flow processes in heterogeneous porous media with emphasis on the relative permeability-saturation relationship. J Contam Hydrol 76(1–2):47–85. doi:10.1016/j.jconhyd.2004.07.009
12. Das B (2008) Advanced soil mechanics. Taylor and Francis, London
13. Douglas J, Peszyńska M, Showalter R (1997) Single phase flow in partially fissured media. Transp Porous Media 28(3):285–306. doi:10.1023/A:1006562120265
14. Flavigny E, Desrues J, Palayer B (1990) Le sable d'Hostun RF: note technique. Revue française de géotechnique 53:67–69
15. Fuentes C, Haverkamp R, Parlange JY (1992) Parameter constraints on closed-form soil-water relationships. J Hydrol 134(1–4):117–142. doi:10.1016/0022-1694(92)90032-Q
16. Gerke H, van Genuchten M (1993) A dual-porosity model for simulating the preferential movement of water and solutes in structured porous media. Water Resour Res 29(2):305–319. doi:10.1029/92WR02339
17. Hopmans J, Šimůnek J, Romano N, Durner W (2002) Inverse methods. In: Dane JH, Topp GC (eds) Methods of soil analysis. Part 4: physical methods, soil science society of America, Inc., Madison, Wisconsin, pp 963–1007
18. Hornung U (1991) Homogenization of miscible displacement in unsaturated aggregated soils. In: Dal Masse G and Dell'Antonio GF (ed) Composite media and homogenization theory, Birkhäuser, Boston, pp 143–153

19. Hornung U (ed) (1997) Homogenization and porous media. Springer, New York
20. Jikov V, Kozlov S, Oleinik O (1994) Homogenization of differential operators and integral functionals. Springer, Berlin
21. Lai CH, Liu CW (2001) Accuracy examination of the multiple interacting continua approximation. Proc Natl Sci Counc Repub China (A) 25(1):35–39
22. Lassabatere L, Angulo-Jaramillo R, Soria Ugalde J, Cuenca R, Braud I, Haverkamp R (2006) Beerkan estimation of soil transfer parameters through infiltration experiments–BEST. Soil Sci Soc Am J 70(2):521–532. doi:10.2136/sssaj2005.0026
23. Lewandowska J, Auriault JL (2004) Modeling of unsaturated water flow in soils with highly permeable inclusions. Comptes Rendus Mecanique 332(1):91–96
24. Lewandowska J, Laurent JP (2001) Homogenization modeling and parametric study of moisture transfer in an unsaturated heterogeneous porous medium. Transp Porous Media 45(3):321–345. doi:10.1023/A:1012450327408
25. Lewandowska J, Szymkiewicz A, Burzyński K, Vauclin M (2004) Modeling of unsaturated water flow in double-porosity soils by the homogenization approach. Adv Water Resour 27(3):283–296. doi:10.1016/j.advwatres.2003.12.004
26. Lewandowska J, Butlańska J, Angulo-Jaramillo R (2005) Etude expérimentale de l'infiltration bi-dimensionelle d'eau dans un modèle à double porosité. Milieux poreux et transfers hydriques—Bulletin du Groupe Francophone Humidimétrie et Transferts en Milieux Poreux 51:50–55
27. Lewandowska J, Szymkiewicz A, Auriault JL (2005) Upscaling of Richards equation for soils containing highly conductive inclusions. Adv Water Resour 28(11):1159–1170. doi:10.1016/j.advwatres.2005.03.006
28. Lewandowska J, Szymkiewicz A, Gorczewska W, Vauclin M (2005) Infiltration in a double-porosity medium: experiments and comparison with a theoretical model. Water Resour Res 41(2):W02,022. doi:10.1029/2004WR003504
29. Łydżba D (2002) Zastosowania metody asymptotycznej homogenizacji w mechanice gruntów i skał (Applications of asymptotic homogenisation method in soil and rock mechanics). Prace naukowe Instytutu Geotechniki i Hydrotechniki Politechniki Wroclawskiej, Oficyna Wydawnicza Politechniki Wroclawskiej, Wroclaw
30. Neuweiler I, Cirpka O (2005) Homogenization of Richards equation in permeability fields with different connectivities. Water Resour Res 41:W02009. doi:10.1029/2004WR003329
31. Neuweiler I, Eichel H (2006) Effective parameter functions for the Richards equation in layered porous media. Vadose Zone J 5(3):963–977. doi:10.2136/vzj2005.0127
32. Panfilov M (2000) Macroscale models of flow through highly heterogeneous porous media. Kluwer, Dordrecht
33. Panfilov M, Quintard M, Bertin H (1997) Macroscale two-phase flow through porous media with highly permeable inclusions. In: Dmitrievski A, Panfilov M (eds) Proceedings of the international conference "Porous media: physics, models, simulations", World Scientific, Singapore, pp 297–324
34. Press W, Teukolsky S, Vetterling W, Flannery B (1992) Numerical recipes in C: the art of scientific programing. Cambridge University Press, Cambridge
35. Quintard M, Whitaker S (1988) Two-phase flow in heterogeneous porous media: the method of large scale averaging. Transp Porous Media 3(4):357–413. doi:10.1007/BF00233177
36. Sanchez-Palencia E (1980) Non-homogeneous media and vibration theory. Lecture notes in physics, vol 127. Springer, Berlin
37. Šimnek J, Šejna M, Saito H, Sakai M, van Genuchten M (2008) The HYDRUS-1D software package for simulating the one-dimensional movement of water, heat and multiple solutes in variably-saturated media. Version 4.0. Department of Environmental Sciences, University of California Riverside, Riverside, California
38. Strzelecki T (ed) (1996) Mechanika osrodków niejednorodnych. Teoria homogenizacji, Dolnośląskie Wydawnictwa Edukacyjne, Wroclaw
39. Szymkiewicz A (2004) Modeling of unsaturated water flow in highly heterogeneous soils. PhD thesis, Université Joseph Fourier, Grenoble

40. Szymkiewicz A (2005) Calculating effective conductivity of heterogeneous soils by homogenization. Arch Hydro-Eng Environ Mech 52(2):111–130
41. Szymkiewicz A (2008) Modelowanie przeplywu wody w utworach o podwójnej porowatosci (Modeling water flow in double porosity geological formations). Biuletyn Państwowego Instytutu Geologicznego 431:251–258
42. Szymkiewicz A, Lewandowska J (2006) Unified macroscopic model for unsaturated water flow in soils of bimodal porosity. Hydrol Sci J 51(6):1106–1124
43. Szymkiewicz A, Lewandowska J (2008) Micromechanical approach to unsaturated water flow in structured geomaterials by two-scale calculus. Acta Geotechnica 3(1):37–47. doi:10.1007/s11440-007-0049-5
44. Szymkiewicz A, Lewandowska J, Angulo-Jaramillo R, Butlańska J (2008) Two-scale modeling of unsaturated water flow in a double-porosity medium under axi-symmetric conditions. Can Geotech J 45(2):238–251. doi:10.1139/T07-096
45. Zimmerman R, Hadgu T, Bodvarsson G (1996) A new lumped-parameter model for flow in unsaturated dual-porosity media. Adv Water Resour 19(5):317–327. doi:10.1016/0309-1708(96)00007-3

Chapter 7
Flow in Binary Media with Heterogeneous Air-Entry Pressure

The upscaled models presented in Chap. 6 are based on the assumption that the Richards equation is a valid model of water flow at the local (Darcy) scale. This, however, is not necessarily the case, especially during transition between unsaturated and water-saturated conditions in porous media showing distinct and locally variable values of the entry pressure. As the continuity of the air phase and its connection to the atmosphere may be lost, the assumptions underlying the Richards model no longer hold, and the description should be based on the full two-phase flow model. This chapter presents the development of an upscaled model which accounts for heterogeneity in the air entry pressure and which is applicable to capillary-dominated flow in media showing moderate permeability contrast. It is shown that, after appropriate modification, the upscaled Richards equation shows a better agreement with the reference two-phase model than the non-upscaled Richards equation solved for explicitly represented heterogeneous structure. The following presentation is based on papers [8, 9].

7.1 Upscaled Model of Two-phase Capillary Flow

7.1.1 Basic Assumptions

The porous medium is characterized by the same binary structure as considered in Chap. 6, see Fig. 6.1, i.e. it is composed of a continuous background material, denoted by superscript I and disconnected inclusions, denoted by superscript II. Furthermore, it is assumed that the condition of separation of scales, given by Eq. (6.1), is satisfied. At the local scale, the flow of water and air in each region is described by Eqs. (2.50)–(2.51), with the storage terms written according to Eq. (2.52):

A. Szymkiewicz, *Modelling Water Flow in Unsaturated Porous Media*,
GeoPlanet: Earth and Planetary Sciences, DOI: 10.1007/978-3-642-23559-7_7,

$$\theta_{\mathrm{w}}^{I} c_{\mathrm{w}} \frac{\partial p_{\mathrm{w}}^{I}}{\partial t} + \rho_{\mathrm{w}}^{I} \frac{\partial \theta_{\mathrm{w}}^{I}}{\partial t} - \nabla \left[\rho_{w}^{I} \frac{\mathsf{k}_{\mathrm{w}}^{I}}{\mu_{\mathrm{w}}} \left(\nabla p_{\mathrm{w}}^{I} - \rho_{\mathrm{w}}^{I} \mathbf{g} \right) \right] = 0 \quad \text{in } \Omega^{I}, \tag{7.1}$$

$$\theta_{\mathrm{a}}^{I} c_{\mathrm{a}} \frac{\partial p_{\mathrm{a}}^{I}}{\partial t} + \rho_{\mathrm{a}}^{I} \frac{\partial \theta_{\mathrm{a}}^{I}}{\partial t} - \nabla \left[\rho_{a}^{I} \frac{\mathsf{k}_{\mathrm{a}}^{I}}{\mu_{\mathrm{a}}} \left(\nabla p_{\mathrm{a}}^{I} - \rho_{\mathrm{a}}^{I} \mathbf{g} \right) \right] = 0 \quad \text{in } \Omega^{I}, \tag{7.2}$$

$$\theta_{\mathrm{w}}^{II} c_{\mathrm{w}} \frac{\partial p_{\mathrm{w}}^{II}}{\partial t} + \rho_{\mathrm{w}}^{II} \frac{\partial \theta_{\mathrm{w}}^{II}}{\partial t} - \nabla \left[\rho_{w}^{II} \frac{\mathsf{k}_{\mathrm{w}}^{II}}{\mu_{\mathrm{w}}} \left(\nabla p_{\mathrm{w}}^{II} - \rho_{\mathrm{w}}^{II} \mathbf{g} \right) \right] = 0 \quad \text{in } \Omega^{II}, \tag{7.3}$$

$$\theta_{\mathrm{a}}^{II} c_{\mathrm{a}} \frac{\partial p_{\mathrm{a}}^{II}}{\partial t} + \rho_{\mathrm{a}}^{II} \frac{\partial \theta_{\mathrm{a}}^{II}}{\partial t} - \nabla \left[\rho_{a}^{II} \frac{\mathsf{k}_{\mathrm{a}}^{II}}{\mu_{\mathrm{a}}} \left(\nabla p_{\mathrm{a}}^{II} - \rho_{\mathrm{a}}^{II} \mathbf{g} \right) \right] = 0 \quad \text{in } \Omega^{II}, \tag{7.4}$$

where c_{w} and c_{a} are the compressibility coefficients of water and air. The conditions at the interface Γ vary, depending on the saturation of the two materials, as discussed in the following sections. Similarly to the previous chapter, the characteristic time of the process is chosen as the time of flow at the macroscopic scale in the background material. However, in contrast to the previous chapter, the analysis is limited to the case when the permeabilities of the two materials are of the same order of magnitude.

As far as the local balance of driving forces is considered, we assume that at the scale of a single periodic cell the capillary forces dominate over the viscous and gravitational forces. These conditions can be quantified by two dimensionless numbers. The Bond number $\mathscr{R}_{\mathrm{g}}$ represents the ratio of gravitational to capillary forces, while the capillary number $\mathscr{R}_{\mathrm{c}}$ represents the ratio of viscous to capillary forces, e.g. [2]:

$$\mathscr{R}_{\mathrm{g}} = \frac{\left(\rho_{\mathrm{w}}^{(c)} - \rho_{\mathrm{a}}^{(c)} \right) g^{(c)} l_{\mathrm{g}}}{p_{\mathrm{c}}^{(c)}} = \mathscr{O}(\varepsilon) \ll 1, \tag{7.5}$$

$$\mathscr{R}_{\mathrm{c}} = \frac{\mu_{\alpha}^{(c)} v_{\alpha}^{(c)} l_{\mathrm{c}}}{k_{\mathrm{s}}^{(c)} p_{\mathrm{c}}^{(c)}} = \mathscr{O}(\varepsilon) \ll 1, \tag{7.6}$$

where the superscript (c) denotes characteristic values. The characteristic length for the Bond number l_{g} can be assumed equal to the vertical dimension of a single heterogeneity (inclusion), while the length in the capillary number l_{c} can be taken as the dimension of the heterogeneity in the direction of the flow. A more detailed discussion of the role of dimensionless numbers in upscaling of two-phase flow can be found in [2, 3, 7].

The form of the upscaled model depends on the continuity of the non-wetting fluid across the material interface Γ between the background material and inclusions. One can distinguish three cases, which are described in the following paragraphs.

7.1.2 Capillary Flow without Entry Pressure Effects

If both air and water are mobile at either side of the material interface, one can assume that the pressures in each of the phases (and consequently also the capillary pressure) are continuous across the background-inclusion interface:

$$p_{\mathrm{w}}^{I} = p_{\mathrm{w}}^{II} \quad \text{on } \Gamma, \tag{7.7}$$

$$p_{\mathrm{a}}^{I} = p_{\mathrm{a}}^{II} \quad \text{on } \Gamma. \tag{7.8}$$

Moreover, the continuity of normal mass fluxes across the interface can be assumed:

$$-\rho_{\mathrm{w}}^{I} \frac{\mathsf{k}_{\mathrm{w}}^{I}}{\mu_{\mathrm{w}}} \left(\nabla p_{\mathrm{w}}^{I} - \rho_{\mathrm{w}}^{I}\,\mathbf{g}\right) \mathbf{n}_{\Gamma} = -\rho_{\mathrm{w}}^{II} \frac{\mathsf{k}_{\mathrm{w}}^{II}}{\mu_{\mathrm{w}}} \left(\nabla p_{\mathrm{w}}^{II} - \rho_{\mathrm{w}}^{II}\,\mathbf{g}\right) \mathbf{n}_{\Gamma} \quad \text{on } \Gamma, \tag{7.9}$$

$$-\rho_{\mathrm{a}}^{I} \frac{\mathsf{k}_{\mathrm{a}}^{I}}{\mu_{\mathrm{a}}} \left(\nabla p_{a}^{I} - \rho_{\mathrm{a}}^{I}\,\mathbf{g}\right) \mathbf{n}_{\Gamma} = -\rho_{\mathrm{a}}^{II} \frac{\mathsf{k}_{\mathrm{a}}^{II}}{\mu_{\mathrm{a}}} \left(\nabla p_{\mathrm{a}}^{II} - \rho_{\mathrm{a}}^{II}\,\mathbf{g}\right) \mathbf{n}_{\Gamma} \quad \text{on } \Gamma. \tag{7.10}$$

where $\mathbf{n}_{\Gamma}$ is the unit vector normal to the interface Γ.

For the above interface conditions, Saez et al. [6] derived a homogenized model of the following form:

$$\theta_{\mathrm{w}}^{\mathrm{eff}}\, c_{\mathrm{w}} \frac{\partial p_{\mathrm{w}}^{\mathrm{eff}}}{\partial t} + \rho_{\mathrm{w}}^{\mathrm{eff}} \frac{\partial \theta_{\mathrm{w}}^{\mathrm{eff}}}{\partial t} - \nabla \left[\rho_{\mathrm{w}}^{\mathrm{eff}} \frac{\mathsf{k}_{\mathrm{w}}^{\mathrm{eff}}}{\mu_{\mathrm{w}}} \left(\nabla p_{\mathrm{w}}^{\mathrm{eff}} - \rho_{\mathrm{w}}^{\mathrm{eff}}\,\mathbf{g}\right) \right] = 0, \tag{7.11}$$

$$\theta_{\mathrm{a}}^{\mathrm{eff}}\, c_{\mathrm{a}} \frac{\partial p_{\mathrm{a}}^{\mathrm{eff}}}{\partial t} + \rho_{\mathrm{a}}^{\mathrm{eff}} \frac{\partial \theta_{\mathrm{a}}^{\mathrm{eff}}}{\partial t} - \nabla \left[\rho_{\mathrm{a}}^{\mathrm{eff}} \frac{\mathsf{k}_{\mathrm{a}}^{\mathrm{eff}}}{\mu_{\mathrm{a}}} \left(\nabla p_{\mathrm{a}}^{\mathrm{eff}} - \rho_{\mathrm{a}}^{\mathrm{eff}}\,\mathbf{g}\right) \right] = 0. \tag{7.12}$$

This model can be regarded as a two-phase counterpart of the upscaled Richards equation with local equilibrium, described in Sect. 6.3.1. The pressures in each fluid phase is uniform within a unit cell at the zeroth order of approximation. Consequently, the phase densities are also uniform, their values corresponding to the phase pressures, $\rho_{\alpha}^{\mathrm{eff}} = \rho_{\alpha}\left(p_{\mathrm{c}}^{\mathrm{eff}}\right)$. Moreover, the capillary pressure:

$$p_{\mathrm{c}}^{\mathrm{eff}} = p_{\mathrm{a}}^{\mathrm{eff}} - p_{\mathrm{w}}^{\mathrm{eff}}$$

is uniform in a periodic cell, i.e. local capillary equilibrium conditions occur. However, the saturations and phase contents are different in each of the two regions, because the background material and inclusions are characterized by different $p_{\mathrm{c}} - S_{\mathrm{ew}}$ curves. The effective (average) porosity and volumetric phase contents are defined similarly as in the case of the upscaled Richards equation:

$$\phi^{\mathrm{eff}} = w^{I}\,\phi^{I} + w^{II}\phi^{II}, \tag{7.13}$$

$$\theta_{\alpha}^{\mathrm{eff}} = w^{I}\,\theta_{\alpha}^{I}\left(p_{\mathrm{c}}^{\mathrm{eff}}\right) + w^{II}\theta_{\alpha}^{II}\left(p_{\mathrm{c}}^{\mathrm{eff}}\right), \tag{7.14}$$

$$S_{\alpha}^{\mathrm{eff}} = \theta_{\alpha}^{\mathrm{eff}}/\phi^{\mathrm{eff}}. \tag{7.15}$$

In order to simplify the presentation, it is assumed that the residual saturations of air and water are zero in each material, i.e. the saturations can change in the whole range of values between 0 and 1:

$$0 \leq S_\alpha^\iota \leq 1, \tag{7.16}$$

$$0 \leq \theta_\alpha^\iota \leq \phi, \tag{7.17}$$

where $\iota = 1, 2$ is the index of porous material. This assumption does not reduce the generality of the model and the case with non-zero residual saturations is described in [8].

The effective permeability tensors for each phase depend on the effective capillary pressure. They are defined in a similar way as the effective water permeability in the case of upscaled Richards equation, Eqs. (6.43)–(6.47). For the chosen value of the effective capillary pressure, a corresponding piecewise-constant distribution of the phase permeability is assumed, with $\mathsf{k}_\alpha^I\left(p_\mathrm{c}^\mathrm{eff}\right)$ in the background material and $\mathsf{k}_\alpha^{II}\left(p_\mathrm{c}^\mathrm{eff}\right)$ in the inclusions. Next, the local boundary value problem, Eqs. (6.43)–(6.46), is solved for each spatial direction m to obtain the corresponding auxiliary variable χ_m, which has to satisfy periodic boundary conditions. Based on these results, the entries of the effective tensor are computed from Eq. (6.47). The same procedure applies to water and air phases. Note that the formulation of the local boundary value problem implies that the local permeability values are larger than zero in inclusions as well as in the background material, i.e. the fluid is mobile everywhere in the periodic cell. This is consistent with the assumed conditions at the interface Γ, Eqs. (7.7)–(7.10). If both materials are isotropic, instead of the solution of the elliptic boundary value problem, simplified approaches can be used to compute the components of the effective tensor for the given pair of scalar values $k_\alpha^I\left(p_\mathrm{c}^\mathrm{eff}\right)$ and $k_\alpha^{II}\left(p_\mathrm{c}^\mathrm{eff}\right)$. However, the procedure outlined above seems more accurate for complex geometries [1, 2].

7.1.3 Infiltration with Entry Pressure Effects

The model described above is valid on condition that both fluid phases are present and mobile on both sides of the interface. If the capillary functions in both inclusions and background do not show air entry pressure (as is the case, for instance, with the van Genuchten model), the air phase disappears from the system for the same value of $p_\mathrm{c} = 0$ in both materials. However, if the capillary functions have distinct entry pressures, which are different in each material, one of the materials becomes fully saturated at a value of the capillary pressure for which the other material remains unsaturated. In such a case an extended capillary pressure continuity condition must be used at the interface Γ, as discussed in Sect. 2.3.3. The effect of this change on the upscaled model depends on whether the flow is of infiltration or drainage type and whether the entry pressure is higher in the background or in inclusions. This

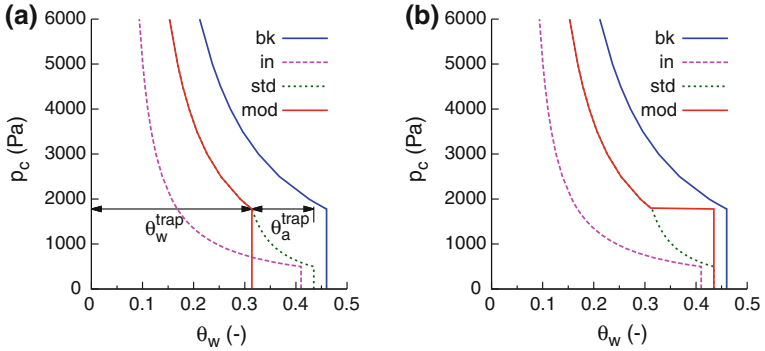

Fig. 7.1 Upscaled capillary functions for heterogeneous medium with coarse-textured inclusions: **a** infiltration, **b** drainage, (*bk*) background material, (*in*) inclusions, (*std*) standard upscaling method, (*mod*) modified upscaling method accounting for the air entry pressure effects

problem was analyzed for flow in one-dimensional layered medium by [4, 10] and for a multidimensional medium with inclusions by [8].

First, infiltration in a medium with higher entry pressure in the background is considered, $p_e^I > p_e^{II}$. Since the entry pressure is in general inversely proportional to the characteristic size of the pores, the inclusions can be regarded as having coarser texture (larger pores) compared to the finer background material. Initially the medium is dry, which corresponds to a large value of the capillary pressure. As the water infiltrates, the capillary pressure decreases and the saturation in both materials increases. When the value of the entry pressure of the background p_e^I is reached, this material becomes fully saturated with water. However, the water content in inclusions is still below its maximum value, due to the differences in shape of the capillary functions. This is shown schematically in Fig. 7.1a. If capillary equilibrium conditions hold at the Darcy scale, the inclusion becomes surrounded with fully water saturated fine material and the connectivity of the air phase is lost. In contrast, the water phase remains connected throughout the medium, and the continuity of its pressure and normal flux can be assumed at the material interfaces. The difference between the air pressure in inclusions and the pressure in the water phase does not exceed the entry value for the background material, so the air remains trapped in inclusions. The threshold value of the effective water content, which corresponds to the effective capillary pressure equal to the entry pressure of the background, can be written as:

$$\theta_w^{trap} = w^I \phi^I + w^{II} \phi^{II} S_w^{II}\left(p_e^I\right) < \phi^{eff} \tag{7.18}$$

and the corresponding effective water saturation is:

$$S_w^{trap} = \theta_w^{trap}/\phi^{eff} < 1. \tag{7.19}$$

The corresponding values for the air phase:

$$\theta_{\mathrm{a}}^{\mathrm{trap}} = \phi^{\mathrm{eff}} - \theta_{\mathrm{w}}^{\mathrm{trap}}, \tag{7.20}$$

$$S_{\mathrm{a}}^{\mathrm{trap}} = 1 - S_{\mathrm{w}}^{\mathrm{trap}}, \tag{7.21}$$

can be considered as the field-scale residual air content and saturation, respectively. Note that these residual values result only from the presence of material heterogeneities, since the pore-scale residual saturations are neglected here. The actual value of the field-scale residual air content depends on the shapes of the capillary functions of the porous materials, as shown in Fig. 7.1a.

Even if the water pressure increases further, the air phase cannot leave the inclusions. This is in contrast to the model described in the previous section, where further decrease of the capillary pressure results in the corresponding decrease of θ_{a}^{II} and $\theta_{\mathrm{a}}^{\mathrm{eff}}$ and the increase of the wetting phase permeability, computed from the solution of the cell problem. Such approach does not take into account the fact that the non-wetting phase cannot leave the inclusions, because it cannot overcome the entry pressure in the background material. In order to include this effect, the interface conditions (7.7)–(7.10) and the upscaled equations should be modified.

In the simplified case of incompressible flow ($c_{\mathrm{w}} = c_{\mathrm{a}} = 0$) the interface conditions can be specified as follows:

$$p_{\mathrm{w}}^{I} = p_{\mathrm{w}}^{II} \quad \text{on } \Gamma, \tag{7.22}$$

$$p_{\mathrm{c}}^{II} = p_{\mathrm{e}}^{I} \quad \text{on } \Gamma, \tag{7.23}$$

where p_{e}^{I} is the entry pressure of the background material, while for the normal fluxes the following condition holds:

$$-\frac{\mathsf{k}_{\mathrm{w}}^{I}}{\mu_{\mathrm{w}}}\left(\nabla p_{\mathrm{w}}^{I} - \rho_{\mathrm{w}}^{I}\,\mathbf{g}\right)\mathbf{n}_{\Gamma} = -\frac{\mathsf{k}_{\mathrm{w}}^{II}}{\mu_{\mathrm{w}}}\left(\nabla p_{\mathrm{w}}^{II} - \rho_{\mathrm{w}}^{II}\,\mathbf{g}\right)\mathbf{n}_{\Gamma} \quad \text{on } \Gamma, \tag{7.24}$$

$$-\frac{\mathsf{k}_{\mathrm{a}}^{II}}{\mu_{a}}\nabla\left(p_{\mathrm{a}}^{II} - \rho_{\mathrm{a}}^{II}\,\mathbf{g}\right)\mathbf{n}_{\Gamma} = 0 \quad \text{on } \Gamma. \tag{7.25}$$

Note that the air phase pressure is undefined in the background material. With these boundary conditions, the upscaled equation for water becomes:

$$-\nabla\left(\rho_{\mathrm{w}}^{\mathrm{eff}}\,\frac{\mathsf{k}_{\mathrm{w}}^{\mathrm{trap}}}{\mu_{\mathrm{w}}}\left(\nabla p_{\mathrm{w}}^{\mathrm{eff}} - \rho_{\mathrm{w}}^{\mathrm{eff}}\,\mathbf{g}\right)\right) = 0, \tag{7.26}$$

where $\mathsf{k}_{\mathrm{w}}^{\mathrm{trap}}$ is the effective wetting phase permeability obtained from the solution of the local boundary value problem with the relative permeability $k_{\mathrm{rw}}^{I} = 1$ in the background material and $k_{\mathrm{rw}}^{II} = k_{\mathrm{rw}}^{II}\left(p_{\mathrm{e}}^{I}\right)$ in the inclusions. Equation (7.26) describes steady flow, because the water saturation cannot increase any further and the fluids are incompressible. Since the background becomes impermeable with respect to the

non-wetting phase, the corresponding effective permeability becomes $\mathsf{k}_{\mathrm{a}}^{\mathrm{eff}} = 0$. Note that this result cannot be obtained from the solution of the cell problem, because the problem becomes ill-posed when the permeability in any part of the cell is equal to zero. The air content in inclusions is constant:

$$\theta_{\mathrm{a}}^{\mathrm{eff}} = \theta_{\mathrm{a}}^{\mathrm{trap}} = const. \tag{7.27}$$

The capillary pressure in inclusions remains constant and equal to the entry pressure in the background material. Thus, any increase in the water pressure will cause the same increase of the air pressure and the air saturation in inclusions will remain constant. In reality, air can dissolve in water or move upwards in form of small bubbles, but these long-term processes are not accounted for by the present model, based on two-phase immiscible formulation.

If the compressibility of the fluids is taken into account, the model becomes more complex, since the air saturation in inclusions can change due to the compressibility. The relevant upscaled equations can be written as:

$$\theta_{\mathrm{w}}^{\mathrm{eff}}\, c_{\mathrm{w}} \frac{\partial p_{\mathrm{w}}^{\mathrm{eff}}}{\partial t} + \rho_{\mathrm{w}}^{\mathrm{eff}} \frac{\partial \theta_{\mathrm{w}}^{\mathrm{eff}}}{\partial t} - \nabla \left[\rho_{\mathrm{w}}^{\mathrm{eff}} \frac{\mathsf{k}_{\mathrm{w}}^{\mathrm{trap}}}{\mu_{\mathrm{w}}} \left(\nabla p_{\mathrm{w}}^{\mathrm{eff}} - \rho_{\mathrm{w}}^{\mathrm{eff}} \mathbf{g} \right) \right] = 0, \tag{7.28}$$

$$\theta_{\mathrm{a}}^{II}\, c_{\mathrm{a}} \left(\frac{\partial p_{\mathrm{w}}^{\mathrm{eff}}}{\partial t} + \frac{\partial p_{\mathrm{c}}^{II}}{\partial t} \right) + \rho_{\mathrm{a}}^{II} \frac{\partial \theta_{\mathrm{a}}^{II}}{\partial t} = 0. \tag{7.29}$$

Equation (7.29) states that the mass of the air phase trapped in inclusions should remain constant. Note that the local capillary function is used instead of an upscaled one. The change in saturation is driven by the change in the macroscopic wetting phase pressure. A positive change in $p_{\mathrm{w}}^{\mathrm{eff}}$ causes an increase of the non-wetting phase pressure in inclusions and consequently an increase in the density of the non-wetting fluid. In order to keep the mass constant, the increase in density should be balanced by a decrease of volume occupied by the fluid, which means in turn that the capillary pressure decreases. On the other hand, if $p_{\mathrm{w}}^{\mathrm{eff}}$ decreases, the capillary pressure in inclusions is expected to increase. It can even reach values higher than the entry pressure in the background, which enables the non-wetting fluid to move from inclusions to the background. In this case one should switch again to the model with two continuous phases, described in the previous section. Note also that the saturation change in inclusions due to the compressibility is assumed to be small and its influence on the effective permeability tensor for the water phase is neglected.

7.1.4 Drainage with Entry Pressure Effects

As the second case, drainage in a medium with disconnected coarse inclusions is analyzed. The medium is initially fully saturated with the wetting phase ($S_{\mathrm{w}} = 1$) and starts to be invaded by the non-wetting phase. However, the drainage is possible

only after the critical capillary pressure p_e^I is reached. In the range of capillary pressures below that value, the upscaled equations have the following form:

$$\theta_w^{\text{eff}} c_w \frac{\partial p_w^{\text{eff}}}{\partial t} - \nabla \left[\rho_w \frac{\mathbf{k}_s^{\text{eff}}}{\mu_w} \left(\nabla p_w^{\text{eff}} - \rho_w^{\text{eff}} \mathbf{g} \right) \right] = 0, \tag{7.30}$$

$$\theta_a^{\text{eff}} = 0 = const, \tag{7.31}$$

where the effective permeability of the wetting phase is equal to the effective intrinsic permeability of the medium.

Initially, there is no capillary equilibrium between inclusions and background, because the capillary pressure in each material is equal to its entry pressure. Once the entry pressure for the matrix is exceeded, the non-wetting phase from the injection zone starts invading the system. As soon as there is a connected path of the non-wetting phase between the injection zone and inclusions, the capillary pressure in inclusions increases, until it equilibrates with the surrounding background material, with the corresponding non-wetting phase saturation in inclusions much larger than the one in the background. This can be represented by a discontinuity in the effective capillary curve, Fig. 7.1b. The water content is constant and equal to the porosity for $p_c^{\text{eff}} < p_e^I$. If the capillary pressure increases by a very small value above the entry pressure of the background, the average water content within a unit cell decreases rapidly to the value corresponding to the capillary equilibrium conditions, because the inclusions desaturate quickly. Such behavior is confirmed by physical experiments on heterogeneous media with disconnected coarse-textured inclusions [11].

Comparing this result with the one obtained for infiltration, one can note that the presence of disconnected coarse inclusions causes a hysteretic behaviour of the heterogeneous medium in the range of capillary pressures below the entry pressure of the background material p_e^I. The upscaled capillary and permeability functions are different for infiltration and drainage, as shown in Fig. 7.1a, b. In contrast, application of the standard upscaling procedure based on the assumption of local capillary equilibrium for the whole range of pressures leads to a unique capillary curve for both infiltration and drainage, shown by dotted lines in Fig. 7.1. In the range of capillary pressures above the entry pressure of the background material, all three curves are the same.

The hysteresis results from the presence of material heterogeneities at the Darcy scale and occurs even if locally each of the materials is characterized by a unique capillary curve for infiltration and drainage. The presented approach can be also used when each of the material exhibits hysteresis in its local scale capillary curve. In this case, the method of computing the effective parameters remains the same, but different local scale functions should be used as input, depending on the process which is to be simulated.

The numerical implementation of the upscaled model with entry pressure effects depends on the formulation used in the numerical code to solve the effective equations. As mentioned in Chap. 3, two approaches are possible, i.e. either the principal variables are the pressures of the two fluids and the phase content and permeabilities

are calculated as functions of the pressure difference (capillary pressure) or the principal variables are one of the pressures and one of the saturations and the capillary pressure and permeabilities are calculated as the functions of the saturation. In the first case, one should remember that when the capillary pressure is below the critical value $p_c^{\text{eff}} < p_e^I$, Eqs. (7.14)–(7.15) are no longer valid because the air phase content is either constant or changes very slightly due to the compressibility. In the second case, one should remember that during infiltration the value of the wetting phase content cannot exceed the critical value $\theta_w^{\text{trap}} = \phi^{\text{eff}} - \theta_a^{\text{trap}}$. During the drainage one has to deal with a discontinuous capillary function. For the purposes of consistent numerical solution, it can be replaced by a continuous capillary curve, with linear variation of $\theta_{\text{w}}^{\text{eff}}$ between p_c^{eff} and $p_c^{\text{eff}} + \upsilon$, where υ is a small number (similar technique for the unsaturated flow equation was used by [11].

Finally, one has to consider an inverse heterogeneity pattern, i.e. fine-textured inclusions with high entry pressure embedded in a continuous coarser background with low entry pressure. During infiltration in such a medium the air phase disappears in inclusions earlier than in the background. Consequently, there is no trapping effect and the standard upscaling procedure can be used for the effective capillary and water permeability functions. In the range of capillary pressures below the entry pressure p_e^{II}, the inclusions are impermeable to air, and the cell problem used to define the effective air permeability must be modified. The auxiliary variable χ is defined only in the background material, while the material interface is considered impermeable. The resulting formulation would be the same as the cell problem describing water permeability in a medium with weakly permeable inclusions, described in Sect. 6.3.2.

The same observation regarding the air permeability holds for drainage. Since the medium starts to drain as soon as the entry pressure of the coarse material is exceeded, there is no discontinuity in the resulting capillary curve. Until the value of the entry pressure for inclusions is reached, the saturation in inclusions remains equal to one, but the effective water content decreases, due to the drainage of the continuous coarse-textured background. In this range the inclusions must be considered as impermeable to air. If the difference in the shape of the capillary curves of the two materials is very large, for high values of the capillary pressure a phenomenon of water phase trapping in fine inclusions may occur, as pointed out by [5]. Since the coarse background is virtually impermeable for water in the range of capillary pressures around the entry pressure of the inclusions, the changes of the capillary pressure in the background (e.g. due to evaporation) are not reflected by the changes of the water saturation in inclusions, because mobile water phase cannot enter the coarse material. Analysis of such phenomena would require accounting for evaporation and vapor transfer and is beyond the scope of this work.

7.1.5 Modified Richards Equation

The above analysis has important implications for the Richards equation. The latter approach differs from the full two-phase model in two important aspects. First,

the volume of water entering or leaving a porous domain is not balanced with the corresponding volume of air which must be displaced by water or replace water, respectively. Second, the water content (or saturation) and permeability are defined as functions of the water pressure, which is assumed to be equal to the negative of the capillary pressure. Thus, it is not possible to describe the air entry effects discussed above using the Richards equation as the model of flow at the Darcy scale.

Consider, for instance, horizontal two-dimensional incompressible flow in a domain containing a single centrally placed inclusion, with entry pressure lower than at the background. Initially, the capillary pressure is equal to the entry pressure in the background material, and the air is at atmospheric pressure ($p_a = 0$). If the water pressure is uniformly increased along the boundaries of the cell, the water pressure in the interior will equilibrate with the new value, due to the continuity of the water phase. According to the two-phase flow model, the pressure of the air in the inclusion will increase by the same value, while the capillary pressure and saturation will remain the same, because the air cannot leave the inclusion through the fully water-saturated background material. However, in the Richards equation the new capillary pressure, taken as the negative of the water pressure, will be smaller than the entry pressure in the background and the corresponding water saturation in the inclusions will increase. Since the increase in water saturation is not balanced with a decrease in air saturation, the result will be such that some amount of water enters the inclusion. If the boundary water pressure is increased to $p_w = 0$, the whole domain will eventually become fully water-saturated.

Differences between the Richards model and the two-phase model are also apparent for drainage of initially fully water-saturated medium with coarse inclusions. Since in the Richards approach the capillary pressure, and consequently the water saturation, depends uniquely on the water pressure, as soon as the water pressure becomes smaller than $(-p_e^{II})$, i.e. the negative of the entry pressure in inclusions, the saturation in inclusions decreases. According to the two-phase model, the drainage cannot start until p_w falls below $(-p_e^{I})$ which is the negative of the entry pressure for the fine-textured background.

In order to overcome this deficiency of the Richards equation, a different approach can be adopted. In this approach, the Richards equation is used not as a Darcy-scale model, but as an upscaled model, with the effective capillary and permeability functions which account for the entry pressure effects in the same way as it was presented for the full two-phase model in the preceding sections. Such a model does not result from a direct upscaling of the Darcy-scale Richards equation. Rather, it should be regarded as a simplification of the two-phase model which is introduced only at the field scale, after the entry pressure effects have been taken into account.

7.2 Numerical simulations

In order to illustrate the application of the modified Richards equation, two numerical examples are presented. They concern two-dimensional flow in a heterogeneous medium with inclusions characterized by lower air-entry pressure than the

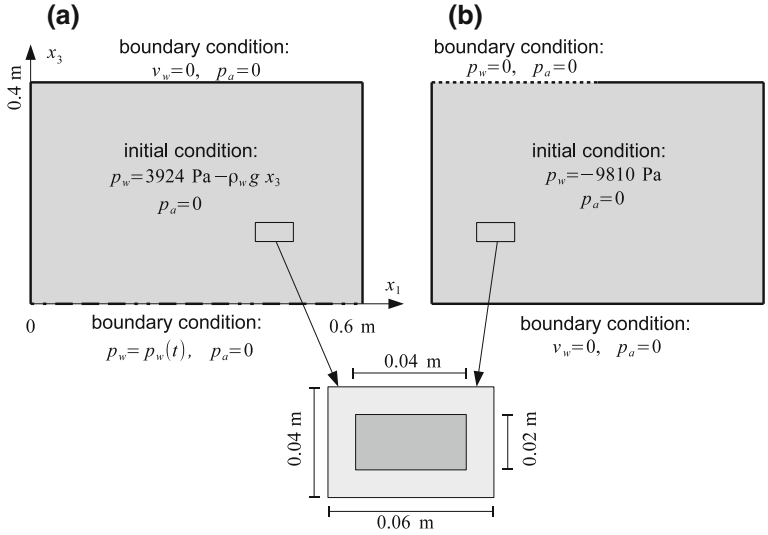

Fig. 7.2 Geometry and boundary conditions used in the numerical example: **a** water table fluctuation, **b** infiltration in a dry soil

background. For each example, several numerical simulations are provided, based on different models. First, the two-phase model and the Richards equation are solved for the homogeneous background material without inclusions, in order to evaluated the differences between these two approaches due to factors other than material heterogeneity. These solutions are denoted as 2PH-BK and RE-BK, respectively. Next, Darcy-scale solutions are provided for a heterogeneous medium containing inclusions, again using both the two-phase model and the Richards equation. They are denoted as 2PH-DAR and RE-DAR, respectively. Finally, two forms of upscaled Richards equation are solved. The first one is based on the standard approach, which assumes the continuity of the capillary pressure in the periodic cell in the whole range of its values, with the effective parameters defined as in Sect. 7.1.2. This solution is denoted as RE-UPS-1. The second upscaled solution takes into account the air-entry pressure effects, which lead to air trapping during infiltration and retardation of drainage in inclusions, as described in Sects. 7.1.3 and 7.1.4. This solution is referred to as RE-UPS-2.

7.2.1 Geometry and Material Parameters

In each of the two examples, the flow takes place in the same two-dimensional domain represented by a rectangle of 60 by 40 cm, Fig. 7.2. The heterogeneous domain contains 100 inclusions of the dimensions 4 by 2 cm arranged in a regular pattern in the

Table 7.1 Hydraulic parameters of porous media used in numerical examples

	ϕ (–)	S_{rw} (–)	S_{ra} (–)	p_e (Pa)	n_b (–)	k_s (m^2)
Background	0.4	0.0	0.0	1,200	1.5	1e−11
Inclusions	0.4	0.0	0.0	400	2.5	1e−10

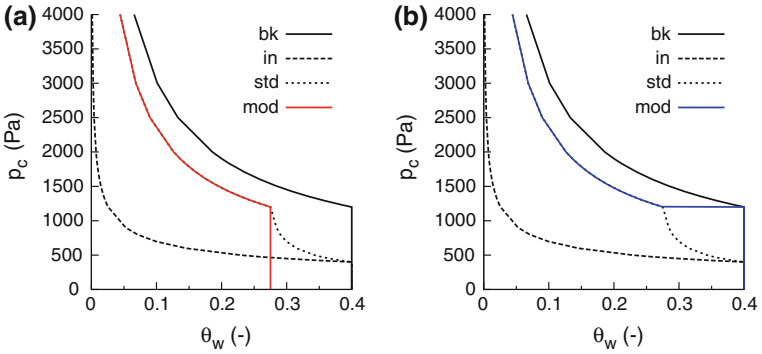

Fig. 7.3 Capillary functions used in the numerical examples: **a** infiltration, **b** drainage, (*bk*) background material, (*in*) inclusions, (*std*) standard upscaling method, (*mod*) modified upscaling method accounting for the air entry pressure effects

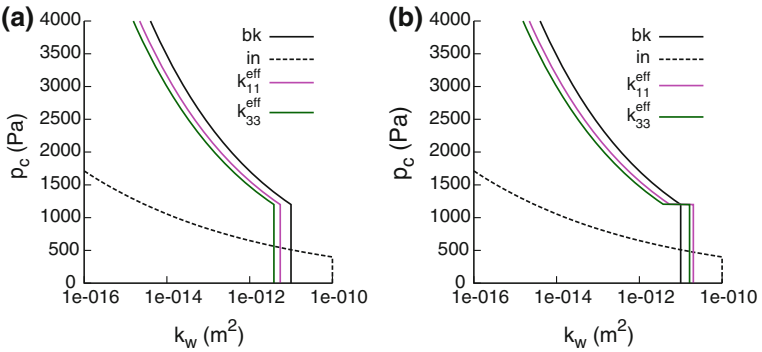

Fig. 7.4 Water permeability functions used in the numerical examples: **a** infiltration, **b** drainage, (*bk*) background material, (*in*) inclusions. The effective permeability in *horizontal* and *vertical* direction is shown only for the modified method

background material, so that the scale parameter $\varepsilon = 0.1$ for both horizontal and vertical direction. The two porous materials are characterized by Brooks–Corey–Burdine hydraulic functions. Their parameters are listed in Table 7.1. The capillary functions and the relative permeability functions for the wetting phase are shown in Figs. 7.3 and 7.4. Both materials are characterized by a sharp decrease of the water saturation above the air-entry pressure, which is typical for uniformly sized pores.

7.2.2 Example 1: Fluctuating Water Table

The considered flow process consists of two stages. At the beginning of the simulation, the domain is fully saturated with water and the position of the water table corresponds to the top of the domain, Fig. 7.2a. The water pressure is distributed hydrostatically from $p_w = 0$ at the top to $p_w = 3924\,\text{Pa}$ at the bottom. In the first phase the water table is gradually lowered until it reaches the bottom of the domain. This is represented by a linear decrease of the water pressure from the initial value at $t = 0$ to the value $p_w = 0$ at $t = 1200\,\text{s}$. The latter value of the pressure is kept constant at the bottom until $t = 7200\,\text{s}$, allowing the water to drain from the domain under the action of the gravity force. Next, the upward infiltration stage begins. The water table is gradually risen to its initial position. Accordingly, the pressure at the bottom increases linearly from $p_w = 0$ at $t = 7200\,\text{s}$ to $p_w = 3924\,\text{Pa}$ at $t = 8400\,\text{s}$. This value remains constant till the end of the simulation at $t = 9600\,\text{s}$. The top of the domain and the vertical edges are considered impermeable for water. For the air flow equation, the initial condition is $p_a = 0$ in the whole domain and a constant boundary value $p_a = 0$ is also imposed at all external boundaries, which represents unobstructed contact with atmospheric air.

The Darcy-scale numerical simulations for heterogeneous domain were performed on a uniform rectangular grid consisting of 60 (horizontal) by 40 (vertical) elements. For the assumed set of boundary conditions the upscaled problems become essentially one-dimensional in the vertical direction, and were solved as such, using 40 elements along x_3 axis. The same approach was applied to solve the flow equations in a homogeneous medium (without inclusions).

The results obtained with different models are compared in terms of the average water saturation of the domain, which changes in function of time, as shown in Figs. 7.5 and 7.6. The average water saturation is obtained by dividing the total volume of water in the domain by the total volume of the pores. The drainage and infiltration phases can be easily distinguished as they correspond to the decrease and increase in the average saturation, respectively. In the solutions for homogeneous material, Fig. 7.5, the average water saturation at the end of the drainage–infiltration sequence becomes equal to the initial saturation, i.e. $S_w = 1$. There are virtually no differences between the two-phase model and the Richards equation. In contrast, the presence of inclusions gives rise to significant discrepancies in the results obtained with these two models. In RE-DAR solution the drainage starts earlier than in the 2PH-DAR solution and the amount of drained water is larger, which corresponds to smaller saturation in the domain at the end of drainage phase. The Richards equation does not take into account the fact that drainage of inclusions is only possible if the air is able to reach them, i.e. if the air-entry pressure in the background material is exceeded. The evolution of the average saturation shown in Fig. 7.5 is consistent with the distribution of the local saturation in the domain at $t = 960\,\text{s}$, $t = 7200\,\text{s}$ and $t = 8160\,\text{s}$ shown in Figs. 7.7, 7.8 and 7.9, respectively. It can be seen that according to the Richards equation some inclusions become drained even though the background material around them remains fully saturated. In the 2PH-DAR model, the entry

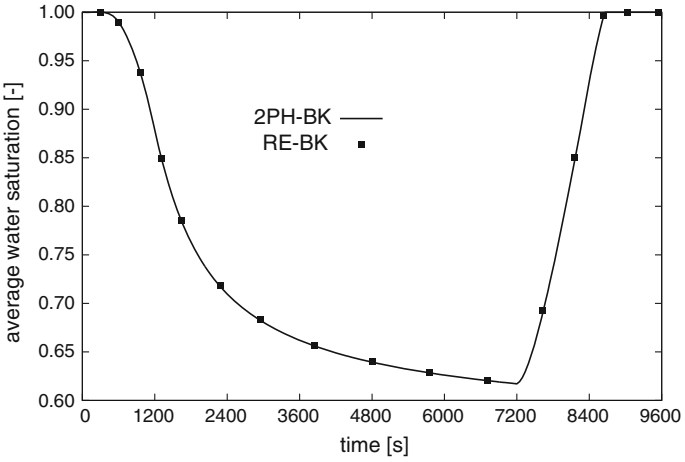

Fig. 7.5 Example 1: Evolution of the average water saturation in homogeneous background material without inclusions according to the two-phase solution (2PH-BK) and the Richards model (RE-BK)

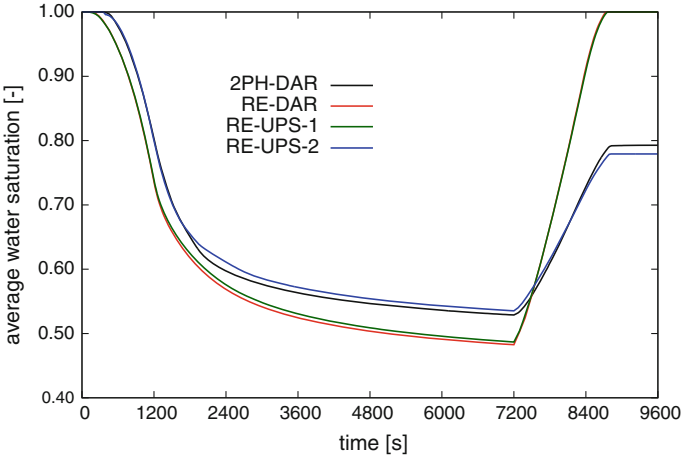

Fig. 7.6 Example 1: Evolution of the average water saturation in heterogeneous domain according to Darcy-scale two-phase solution (2PH-DAR), Darcy-scale Richards model (RE-DAR), Richards model upscaled in the standard way (RE-UPS-1) and the modified upscaled Richards model (RE-UPS-2)

pressure effects are correctly taken into account and the inclusions remain fully saturated in the lower part of the domain, where the difference between the air pressure and the water pressure does exceed the air entry pressure of the background material.

In the second phase of the flow, which corresponds to upward infiltration, the differences between the two-phase model and the Richards equation become even more

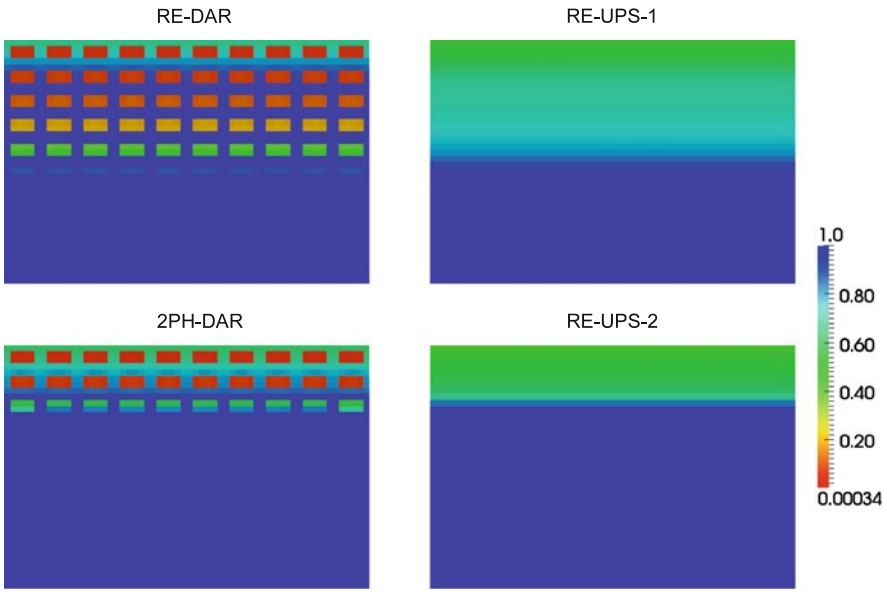

Fig. 7.7 Example 1: Distribution of the water saturation at $t = 960\,\mathrm{s}$, notation as in Fig. 7.6

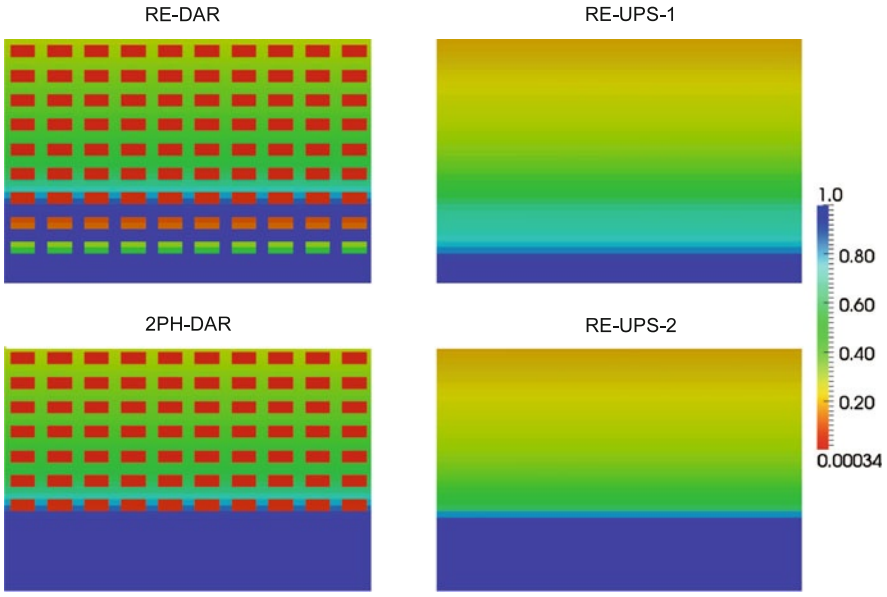

Fig. 7.8 Example 1: Distribution of the water saturation at $t = 7200\,\mathrm{s}$, notation as in Fig. 7.6

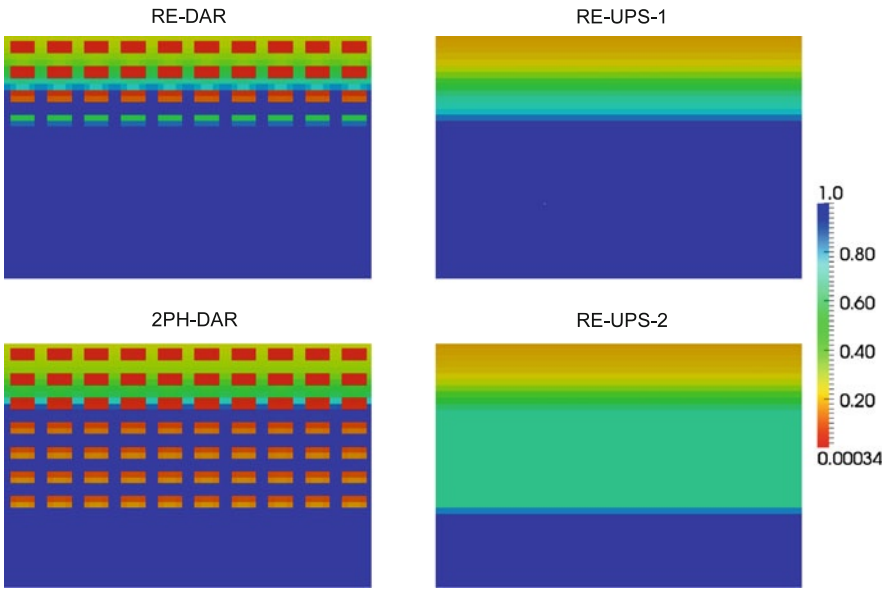

Fig. 7.9 Example 1: Distribution of the water saturation at $t = 8160\,\mathrm{s}$, notation as in Fig. 7.6

pronounced. According to the 2PH-DAR solution, as the water table is risen the background material in the whole domain becomes fully saturated, before the previously drained inclusions reach full saturation. The blocking of flow paths for air leads to trapping of large quantities of air in the inclusions. The inclusions remain unsaturated till the end of the simulation. In contrast, RE-DAR solution shows that all inclusions become fully saturated at the end of the simulation. While there are some unsaturated inclusions immediately behind the wetting front in the background material, they are quickly filled with water, as can be seen in Fig. 7.9. Thus, the Richards equation predicts a reversible drainage–infiltration process, which is similar to the one observed for homogeneous medium, Fig. 7.5. On the other hand, the two-phase flow model describes a reversible phenomenon only in the case of homogeneous medium, while in the presence of coarse-textured inclusions the initial fully water-saturated state is not recovered.

As can be seen from Fig. 7.6, the upscaled model based on the standard approach, RE-UPS-1, follows very closely the solution of Darcy-scale Richards equation, RE-DAR. This proves the accuracy of the homogenization approach, but both solutions are far from the two-phase solution, which should be considered as the reference point. In contrast, the modified approach, RE-UPS-2, is in a reasonable agreement with the 2PH-DAR model, and correctly captures the irreversibility of the drainage–infiltration cycle. This suggest that the Richards equation can be used to describe unsaturated water flow in porous media showing heterogeneity with respect to the air entry pressure, on condition that the effective functions are appropriately modified.

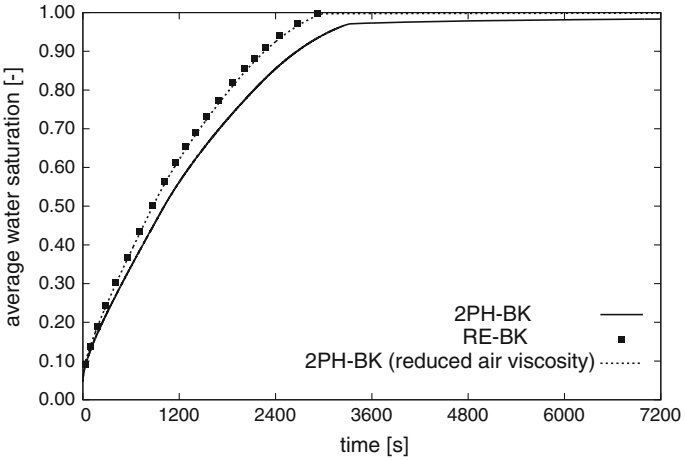

Fig. 7.10 Example 2: Evolution of the average water saturation in homogeneous domain

7.2.3 Example 2: Two-Dimensional Infiltration

The second example represents two-dimensional downward infiltration in an initially dry porous medium, Fig. 7.2b. The initial value of the water pressure is $p_w = -9810\,\text{Pa}$ (water pressure head of $h_w = -1\,\text{m}$) and the air is at atmospheric pressure $p_a = 0$. At the left part of the top boundary, the water pressure is instantaneously risen to the value $p_w = 0$, while the air pressure is kept at atmospheric value, which implies full water saturation. All other boundary segments are considered impermeable for water and open for the atmospheric air ($p_a = 0$). Since the upscaled problem is also two-dimensional, all numerical simulations were performed on the same grid of 60 by 40 elements.

In contrast to the previous example, some differences between the two-phase model and the Richards model can be noticed even for homogeneous medium. The corresponding values of the average saturation in the background material without inclusions are shown in Fig. 7.10. The Richards equation predicts a slightly faster infiltration rate than the two-phase model, while at the end of the simulation the domain becomes wholly water-saturated according to both approaches. As the boundaries are open for air flow, the discrepancy seems to be caused by the viscous resistance to air flow. In fact, decreasing the air viscosity by two orders of magnitude leads to a perfect matching, as shown in Fig. 7.10.

The evolution of average water saturation in heterogeneous medium is plotted in Fig. 7.11, while Figs. 7.12 and 7.13 show the spatial distribution of the water saturation in the domain for two intermediate times. In Fig. 7.11 it can be seen that the presence of inclusions leads to a much larger discrepancy between the Richards and two-phase solutions in terms of the evolution of the average water saturation. In the first case, the whole domain becomes fully water-saturated at the end of

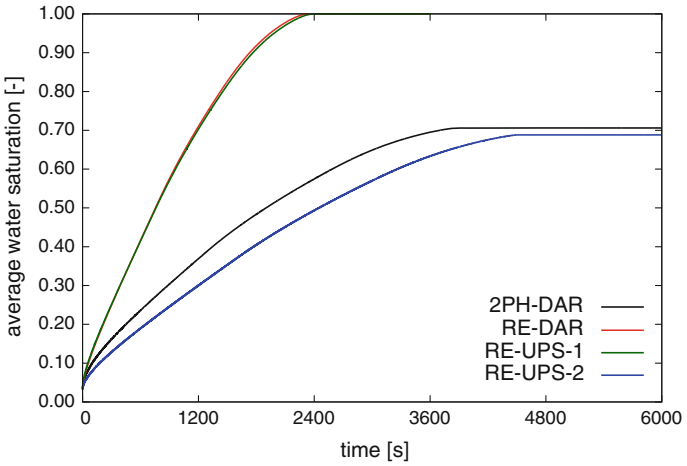

Fig. 7.11 Example 2: Evolution of the average water saturation in heterogeneous domain, notation as in Fig. 7.6

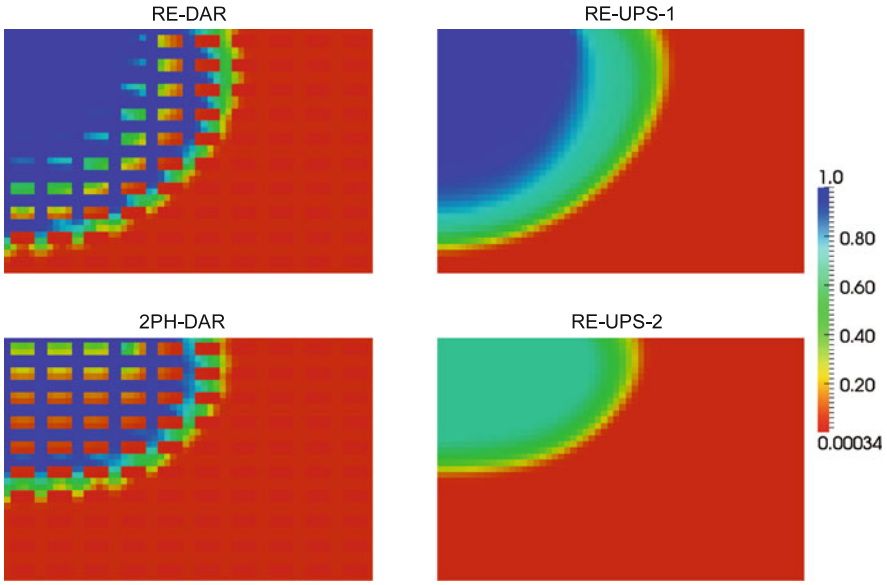

Fig. 7.12 Example 2: Distribution of the water saturation at $t = 540\,\mathrm{s}$, notation as in Fig. 7.6

the simulation. In the second case, only the background material saturates, while a significant amount of air is trapped in the inclusions. Thus, the final steady-state average saturation is 0.706 according to the two-phase flow model and the infiltration rate represented by the slope of the saturation curve is significantly smaller than in the Richards model.

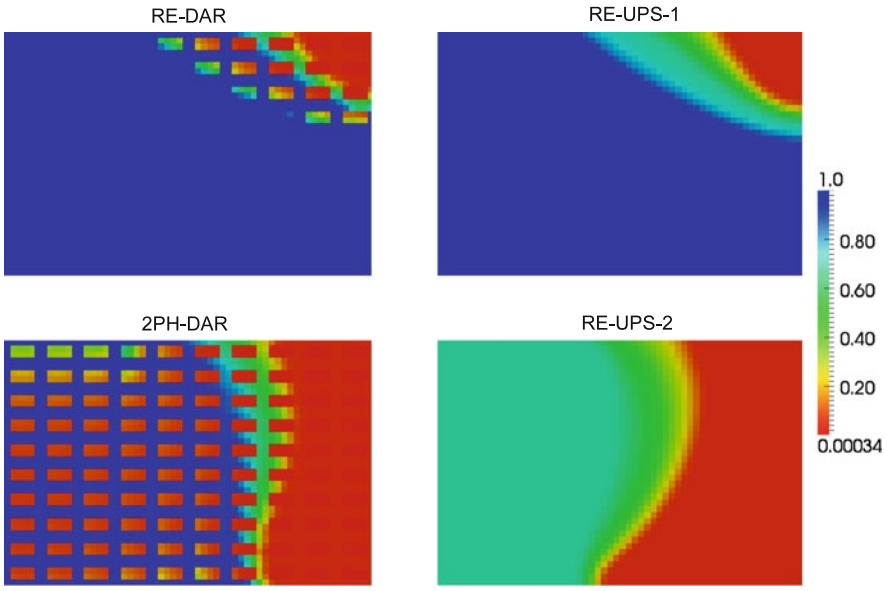

Fig. 7.13 Example 2: Distribution of the water saturation at $t = 1800$ s, notation as in Fig. 7.6

As far as the upscaled models are considered, one can see that RE-UPS-1 follows the corresponding Darcy-scale solution of the Richards equation (RE-DAR) very closely. In contrast, the difference between the two-phase model and the modified Richards equation RE-UPS-2 is significantly larger than in the previous example, although a qualitative agreement can be observed. While the final steady state saturation of RE-UPS-2 (0.688) is only slightly smaller than the corresponding saturation obtained from 2PH-DAR, more pronounced differences are observed in the infiltration rate, which is lower in the RE-UPS-2 approach. A possible reason for these discrepancies may be a more important role played by gravity and viscous forces, compared to the previous test case. A closer examination of Fig. 7.13 reveals that the saturation in inclusions at the end of simulation is not uniform. In particular, the inclusions close to the infiltration boundary have much higher saturation than the value corresponding to the entry pressure in the background material $S_w = 0.064$. The actual values reach locally 0.578. In the initial stages of the infiltration, the viscous and gravitational forces are important and the capillary equilibrium assumption does not hold for the periodic cells close to the infiltration boundary. Since the water saturation is higher than the one predicted from the capillary equilibrium model, the equivalent permeability of the cell with respect to water is also significantly increased. Consequently, the water infiltration according to 2PH-DAR solution proceeds faster than in the RE-UPS-2 approach, based on the assumption of local capillary equilibrium. Nevertheless, the modified upscaled model RE-UPS-2 is considerably closer to the reference two-phase solution than either the Darcy-scale Richards equation or the upscaled Richards equation without entry pressure effects.

References

1. Braun C, Helmig R, Manthey S (2005) Macro-scale effective constitutive relationships for two phase flow processes in heterogeneous porous media with emphasis on the relative permeability-saturation relationship. J Contam Hydrol 76(1–2):47–85. doi:10.1016/j.jconhyd.2004.07.009
2. Eichel H, Helmig R, Neuweiler I, Cirpka O (2005) Upscaling of two-phase flow processes in porous media. In: Das D, Hassanizadeh S (ed) Upscaling multiphase flow in porous media, Springer, New York, pp 237–257
3. Jonoud S, Jackson M (2008) New criteria for the validity of steady-state upscaling. Transp Porous Media 71(1):53–73. doi:10.1007/s11242-007-9111-x
4. Mikelic A, van Duijn C, Pop I (2002) Effective equations for two-phase flow with trapping on the micro scale. SIAM J Appl Math 62(5):1531–1568. doi:10.1137/S0036139901385564
5. Quintard M, Whitaker S (1988) Two-phase flow in heterogeneous porous media: The method of large scale averaging. Transp Porous Media 3(4):357–413. doi:10.1007/BF00233177
6. Saez A, Otero C, Rusinek I (1989) The effective homogeneous behavior of heterogeneous porous media. Transp Porous Media 4(3):213–238. doi:10.1007/BF00138037
7. Stephen K, Pickup G, Sorbie K (2001) The local analysis of changing force balances in immiscible incompressible two-phase flow. Transp Porous Media 45(1):63–88. doi:10.1023/A:1011850618324
8. Szymkiewicz A, Helmig R, Kuhnke H (2011) Two-phase flow in heterogeneous porous media with non-wetting phase trapping. Transp Porous Media 86(1):27–47. doi:10.1007/s11242-010-9604-x
9. Szymkiewicz A, Helmig R, Neuweiler I (2012) Upscaling unsaturated flow in binary porous media with air entry pressure effects. Water Resour Res 48:W04522. doi:10.1029/2011WR010893
10. van Duijn C, Eichel H, Helmig R, Pop I (2007) Effective equations for two-phase flow in porous media: the effect of trapping at the micro-scale. Transp Porous Media 69(3):411–428. doi:10.1007/s11242-006-9089-9
11. Vasin M, Lehmann P, Kaestner A, Hassanein R, Nowak W, Helmig R, Neuweiler I (2008) Drainage in heterogeneous sand columns with different geometric structures. Adv Water Resour 31(9):1205–1220. doi:10.1016/j.advwatres.2008.01.004

Chapter 8
Summary

The flow of water through porous media in partially saturated conditions is an important, and on the other hand complex problem, relevant to several disciplines of science and engineering. The present book is a contribution to this field of research, which particularly focuses on the problem of numerical solution of the flow equations and on capturing the influence of Darcy-scale material heterogeneities in the field-scale models of water flow in unsaturated porous media.

A general background to the mathematical modeling of flow in porous media was given in Chap. 2. The two-phase flow of water and air in the unsaturated zone was discussed, as well as the simplified, and more widely used Richards approach, which neglects the air flow, assuming instantaneous equilibration of the air pressure with the atmosphere. In each case the flow is described by nonlinear partial differential equations of parabolic type. The nonlinearity results from complex relationships between the capillary pressure, saturations and permeabilities of the two fluid phases, which can be represented by several types of analytical functions.

In practical applications, the unsaturated flow equations usually must be solved using numerical methods. This is performed in several stages. Spatial discretization using finite difference, finite element or finite volume approach transforms a partial differential equation into a system of ordinary or algebraic differential equations with respect to time. Next, implicit temporal discretization results in a system of nonlinear algebraic equations for each time step. The system must be solved iteratively, and the subsequent corrections to the vector of unknowns are obtained from the solution of a system of linear algebraic equations, arising for each iterations. In Chap. 3 basic numerical techniques relevant to each of those stages were outlined and the similarities and differences between various available approaches were discussed. The numerical scheme based on vertex-centred finite volume discretization, used in the following chapters, was presented in more detail.

One aspect of the numerical solution of the Richards equation, which received particular attention in Chap. 4, was the problem of approximation of the relative conductivity between adjacent nodes of the numerical grid. A number of averaging schemes available in the literature were compared and evaluated. The performance of

A. Szymkiewicz, *Modelling Water Flow in Unsaturated Porous Media*,
GeoPlanet: Earth and Planetary Sciences, DOI: 10.1007/978-3-642-23559-7_8,

simple methods, like arithmetic, geometric or upstream averaging is highly dependent on the form of relative permeability function, boundary conditions of the problem and node spacing. The relationship between the value of the average permeability and the interplay of capillary and gravity forces was explored in the framework of the so-called Darcian approach. The Darcian averaging is based on consideration of steady-state flow between adjacent nodes. A method of this type, proposed by the author in an earlier paper, was comprehensively evaluated. It was shown to be a viable alternative to other existing methods, offering accurate approximation for a wide range of relative permeability functions and grid sizes.

Another important issue related to the modeling of water flow in the unsaturated zone is the upscaling, i.e. the development of models which describe in the average terms large-scale behaviour of media showing small-scale heterogeneity. This work focused on upscaling from Darcy scale to field scale and a brief overview of the problem was presented in Chap. 5. The importance of factors such as local heterogeneity pattern, separation of scales, existence of the representative elementary volume and balance of capillary, viscous and gravity forces was discussed. The following Chaps. 6 and 7 focused more specifically on upscaling of flow in a porous medium composed of disconnected inclusions embedded in a continuous background material. The upscaled models obtained with the periodic homogenization approach were presented. The main point was to show that even if a relatively simple flow model is assumed at the Darcy scale, the large-scale flow in a heterogeneous medium may have non-standard characteristics.

In Chap. 6 the influence of inclusion–background diffusivity ratio was analyzed. The results of a numerical experiment indicated qualitative differences between the media with weakly permeable and highly permeable inclusions. In the former case, the increase of inclusions' diffusivity led to a monotonic acceleration of the infiltration process. In contrast, for weakly diffusive inclusions the large scale response of the system was strongly related to the actual value of the diffusivity ratio, measured with regard to the scale parameter ε. Depending on this value, the outflow can be either retarded or accelerated in comparison to the homogeneous medium. Theoretical analysis showed that for the diffusivity ratio of ε^2 the flow is dominated by local non-equilibrium of the capillary pressure at the scale of a single representative elementary volume, leading to prolonged water transfer between inclusions and background. This process is represented by an additional "memory" term arising in the large scale equation. A generalized upscaled equation was discussed, which is suitable for the whole range of the inclusion–background diffusivity ratio. A preliminary experimental verification of this model was also described.

Chapter 7 deals with the heterogeneity in the air entry pressure. This important parameter represents the value of the capillary pressure below which the air phase loses its connectivity and cannot flow. If the entry pressure in inclusions is lower than in the background material, two types of phenomena can be expected. First, during infiltration some amount of air becomes trapped in the inclusions, as it cannot overcome the entry pressure to move through the water-saturated background. Second, if the medium is initially fully water-saturated the drainage of inclusions cannot start earlier than the drainage of the background material, because only then

the air phase can form connected paths through the medium. These two cases cannot be represented by the standard Richards equation, and significant differences were observed in the Darcy-scale numerical solutions of the Richards equation and the reference two-phase model. Such differences do not occur for a homogeneous medium. The performance of the Richards equation can be greatly improved by introducing upscaled capillary and permeability functions which account for the entry pressure effects and show quasi-hysteresis in the range of capillary pressures below the entry pressure of the background material. It is important to stress that the hysteresis results purely from the heterogeneous structure of the medium at Darcy scale, and not from the pore scale effects, which are neglected in the analysis.

In the author's view, several issues considered in this book offer perspectives for further research. For instance, the performance of the improved method for inter-nodal permeability averaging should be evaluated more thoroughly for multidimensional problems, involving unstructured grids and anisotropic media. Moreover, an attempt can be made to extend the presented approach to the case of two-phase flow, by adding viscous forces to the capillary–gravity balance. There are also numerous possibilities for further development of the presented upscaling approach. They include a more general formulation, which would account for both local non-equilibrium of the fluid pressures, discussed in Chap. 6, and air-entry effects, considered in Chap. 7. Another direction would be to introduce a more realistic local-scale description, encompassing hysteresis in the hydraulic functions of each material, inter-phase mass transfer and deformations of the solid skeleton. Finally, the need for a comprehensive experimental verification of the upscaling approaches must be emphasized.